1-1-2021

Dynamic Characterization of Bio-Inspired Functionally Graded Polymer Infused Metallic Foams for Blast and Impact Hazard Mitigation

Damian Stoddard

University of Mississippi

DYNAMIC CHARACTERIZATION OF BIO-INSPIRED FUNCTIONALLY GRADED

POLYMER INFUSED METALLIC FOAMS FOR BLAST AND IMPACT HAZARD

MITIGATION

A Dissertation
presented in partial fulfillment of requirements
for the degree of Doctor of Philosophy
in the Department of Mechanical Engineering
University of Mississippi

by

Damian Stoddard

December 2021

ABSTRACT

Current vehicular crashworthy systems and body armor designs are effective in protecting personnel and equipment from disaster due to their energy absorbing characteristics. However, little is understood about how to replicate naturally occurring designs through man-made techniques, and the role of functional grading to further improve the performance of such protective systems. This research investigates an advanced material system analogous to a bio-inspired functionally graded material that will serve as a protective system for the mitigation of dynamic events such as low-velocity impact and/or blast loading.

In this research, two types of polymer infused metallic foams, functionally graded to mimic naturally occurring designs, are integrated as core material in a sandwich composite configuration. Closed cell foams from Cymat with three density variations was used to construct sandwich structures with six functionally graded configurations. These sandwich structures mimic conventional armor designs and functional graded armor designs. Additionally, open cell foams from Duocel with two density variations were used, with and without polymer infusion, to construct eight functionally graded panels. Low density polyurethane foam was used as the polymeric infusion material.

Experimental analysis was conducted using a quasi-static, low-velocity impact machine, direct compression impact, Split Hopkinson Pressure Bar, and blast tube. The dynamic properties of six variations of conventional design and eight configurations of functionally graded metallic foams, four of which are infused with polymer resin, were evaluated. This research also serves to

advance the knowledge of the effects of polymer infusion into metallic foam systems and how this can alter the dynamic performance. Computational modeling was conducted using ABAQUS/CAE to model the dynamic behavior of base material and sandwich structure used in blast samples. This can be used in advancing current knowledge on dynamic performance of new bio-inspired functionally graded configurations that can be implemented into or replace current designs for shock and impact hazard mitigation.

DEDICATION

This dissertation is dedicated to everyone that has helped me on my journey to completing

my doctoral research. In particular, my mother and father Dr. Mary and Dr. Marcus Stoddard that

instill in me an appreciation for education. My sisters Dr. Shana, Carmella, Dr. Erica, and Serena

Stoddard that help push me to finish my goal. My wife Dr. Okoia and two sons Levi and Gabrielle

Stoddard that helped give me the dedication and focus to finish. I would also like to dedicate this

to Matt Lowe, Dr. Mantena, Dr. Raj, and Dr. Matt Nelms that helped guide me when I first became

a graduate student.

LIST OF ABBREVIATIONS AND SYMBOLS

SHPB	Split Hopkinson Pressure Bar
RD	Relative Density
σ_s	Sample Stress
P	Applied Force
ε_s	Sample Strain
E	Energy Absorption
U_1 and U_2	Displacement of Incident and Transmission Bar, Respectively
L_s	Length of Sample
$\varepsilon_i, \varepsilon_r,$ and ε_t	Incident, Reflected, and Transmission Strain, Respectively
P_1 and P_2	Incident and Transmission Bar Force, Respectively
C_o	Elastic Wave Speed of Incident and Transmission Bar
E_b	Elastic Modulus of Bar Material
t	time
p	Pressure
S	Cross Sectional Area
u	Particle Velocity
ρ	Density
γ	Adiabatic Expansion Coefficient
M	Mach Number

U_+ and U_-	Particle Velocity
$E_{deformation}$	Deformation Energy
ρ_{rd}	Relative Density
ρ_A	Areal Density

ACKNOWLEDGEMENTS

Without the continuous effort, advice, and support of my advisor Dr. P. Raju Mantena, Professor of Mechanical Engineering, this thesis would not be possible. I would also like to acknowledge my appreciation for my Ph.D. committee members, Dr. A. M. Rajendran, Chair and Professor of Mechanical Engineering, Dr. John O'Haver, Professor of Chemical Engineering and Director of Center for Mathematics and Science Education, and Dr. Shan Jiang, Assistant Professor for serving on my Ph.D. committee as well as guidance throughout the Ph.D. process.

I would also like to acknowledge Matt Lowe, Mechanical Engineering Machine Shop Supervisor, for modifications to experimental setups as well as manufacturing of samples and discussion on solutions for any issues that arose during testing. In addition, I would like to thank an acknowledge the undergraduate researcher that helped during testing.

TABLE OF CONTENT

ix

x

LIST OF TABLES

LIST OF FIGURES

CHAPTER I: INTRODUCTION

1.1 Background and Motivation

In combat scenarios protective armor for the combatants, military equipment, supplies, etc. is necessary to ensure safety. Typical armor protection includes metallic, ceramic, polymer, and composite materials. Protective systems such as the armor used on a M1 Abrams Tank are made of rolled homogenous steel under a composite armor layer. Depleted uranium (David, 2014) can be retrofitted with reactive armor to mitigate armor piercing munitions and urban combat (Writer, 2019). This armor can sustain substantial dynamic force keeping occupants safe from harm by having various layers of different materials to help dissipate the energy. Other armored vehicles are also able to sustain damage from shrapnel, projectiles, etc. during combat scenarios. Figure 1 (Alamy, 2019) shows typical damage sustained from bullets and shell fragments. This type of armor, however, has no self-healing capabilities and once the protective system is damaged it loses its ability to resist the next dynamic event.

Figure 1. Damage to Armored Vehicle Caused by Bullets and Shell Fragments (Alamy, 2019)

Other armor systems made of composite materials are used as protective plates on body armor to resist projectile penetration. These plates are typically Kevlar and are able to dissipate energy due to the woven fabric configuration. Ballistic vests of this nature come in different levels of protection and can absorb the energy from a projectile. While the ballistic plate may stop the projectile, a lot of energy is still transferred to the user and can result in bruising, broken ribs, and behind armor blunt trauma (BABT), which can be fatal (Shield Technology Inc., 2018). Another drawback to the conventional ballistic vest is they do not protect a large surface area, as in the case during an insurgent attack on an Abu Ghraib Prison. Figure 2 (Multi-National Corps - Iraq Publ, 2005) shows laceration to an armor plate worn by Marine Lance Corporal Joseph Arale during the

attack. While the plate was able to stop shrapnel from an explosion he still sustained wounds to his lower back.

Figure 2. Ballistic Vest Lacerations Caused by Shrapnel (Multi-National Corps - Iraq Publ, 2005)

Another infamous event where nearly 3000 people lost their lives was the attack on the World Trade Center and the Pentagon. The pentagon was hit by American Airline Flight 77 which resulted in significant structural damage and loss of life to personal and passengers. Events such as this can cause significant damage with the current conventional designs, which is why extensive research is needed to develop protective systems for mitigating the immense energy caused by such dynamic events. Figure 3 shows the aftermath at the impact location on the Pentagon (Defense, 2019).

Figure 3. Structural Damage of the Pentagon During the Sep. 11th Attack (Defense, 2019)

This type of damage is not limited to just military structures. Numerous terrorist attacks have resulted in immense damage to civilian buildings, such as the 1993 Bombay Bombing. In this attack 13 explosive devices were detonated targeting civilian locations such as hotels, office buildings, markets etc. (Karkaria, 2015) which caused large damage to structures in Mumbai (Figure 4).

Figure 4. Blast Damage to Century Bazaar Worli During the 1993 Bombay Bombings (Alamy, 2008)

1.2 Relevant Background Research

The need for more advanced protective systems is especially relevant in today's world. This need has given rise to numerous research ideas on understanding, developing, and improving existing or new ideas on protective systems for personnel, vehicles, and structures. A growing field within this topic is bioinspired armor designs which attempt to replicate known biological systems that have desirable properties. These bioinspired designs have prompted numerous investigations on the best armor designs and the limitations of each design. This section reviews bioinspired designs, metallic foams, and the effects of functional grading in optimizing armor designs subjected to low-velocity impact, high strain-rate, and blast loading.

1.2.1 Bioinspired Armor Design

McKittrick, et al., (2010) reviewed several mammalian structures and established relationships between mechanical properties and emphasized the relationship between the structure and energy absorption mechanisms to serve as a guide for bio-inspired composite designs. The first material studied was bone (cancellous and compact) and antler, which have similar structures. The cancellous bone has a density of approximately 0.4 g/cm^3 and is composed of interconnected platelets and rods. This bone is trabecular (spongy) and pourous in nature and is surrounded by a dense outer layer (compact) with higher density ~ 2 g/cm^3. Figure 5 gives a depiction of different hierarchical structures for bone and antler.
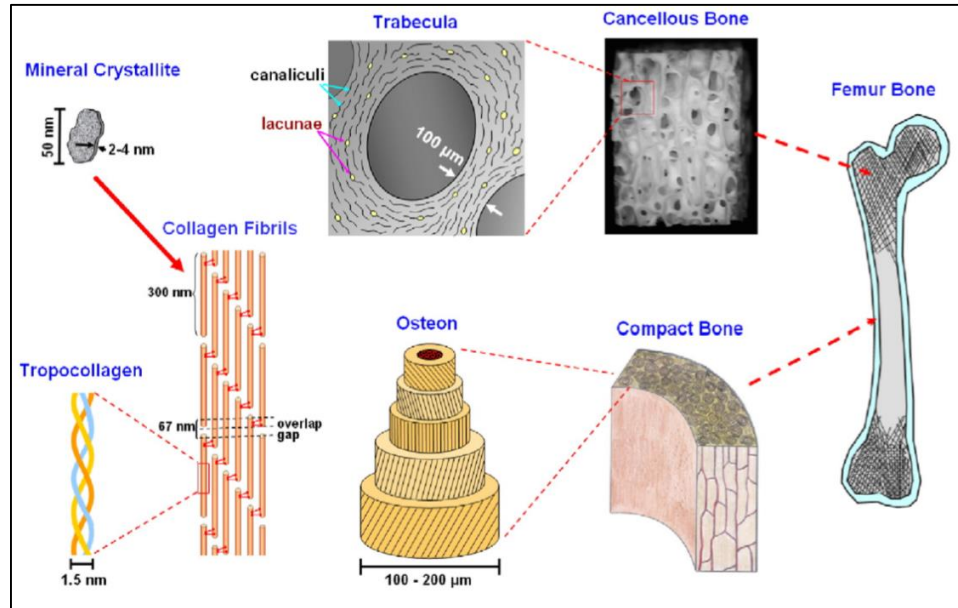
Figure 5 Hierarchical Bone Structure (McKittrick, et al., 2010)

Another structure characterized in this study was tooth and tusk. Similar to the bone structure the tooth and tusk properties vary through the thickness. Characterization of hardness variations were obtained and revealed a three times increase in hardness when comparing the dentin (inner layer) to the enamel (outer layer). A schematic of a typical tooth along with hardness values is shown in Figure 6.
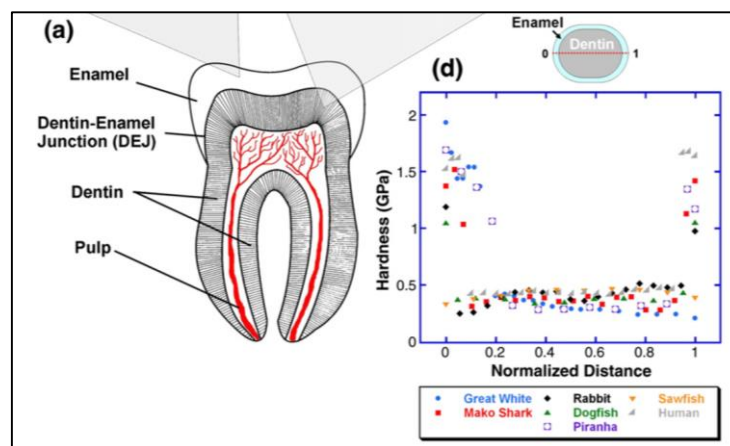
Figure 6. Tooth Enamel and Dentin Hardness Relationship (Edited from s (McKittrick, et al., 2010))

6

Another notable finding was variation in the mechanical properties with respect to orientation. This variation in properties was observed in horns, when comparing the radial and longitudinal stress-strain response at various strain-rates. It was observed that in the longitudinal direction as strain-rate increased compressive strength increased. However, the energy absorption at strain to failure decreased with increasing strain-rate. With respect to the radial direction an increase in strength was observed. Two notable variations in stress-strain response of the horn was observed. When strain-rate was increased from 0.0001 sec^{-1} to 1 sec^{-1} an increase in strength and energy absorption was observed and typical stress-strain shape remained relatively constant. However, when increasing the strain rate to 950 sec^{-1} the stress-strain response varied drastically reflecting a typical brittle response with low strain to failure. Figure 7 shows the typical compressive stress-strain response of horn in both radial and longitudinal directions.
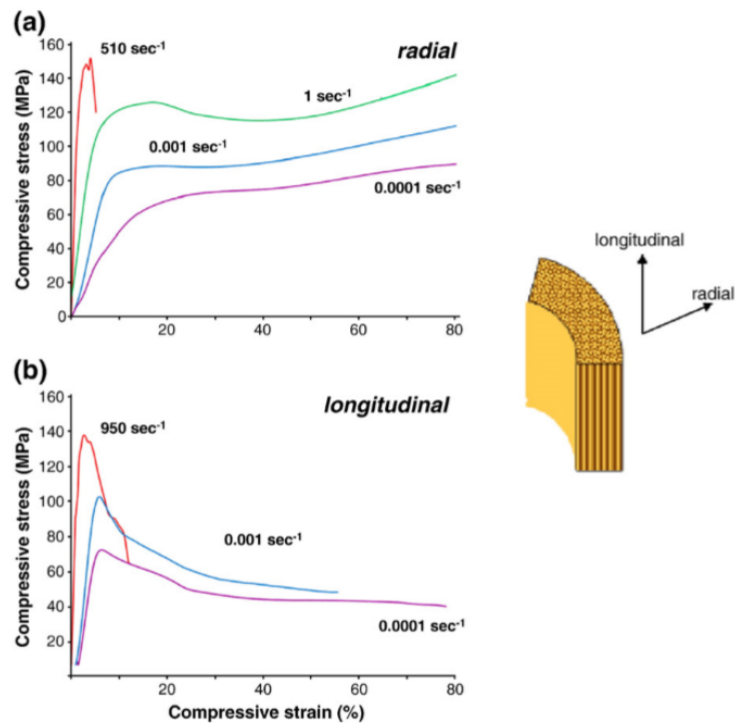
Figure 7. Radial and Longitudinal Stress-Strain at Various Strain Rates (Edited from (McKittrick, et al., 2010))

A summary of the property variation for typical bio-materials is shown in Figure 8. In this figure the relationship between cross sectional area and mineral content, porosity, Elastic Modulus, and Compressive strength can be seen.
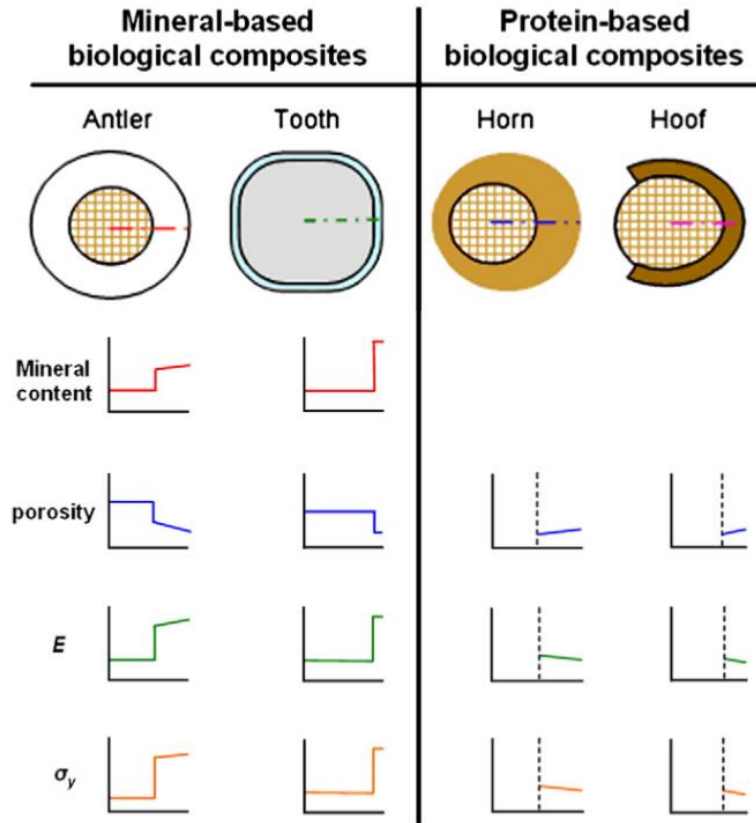
Figure 8. Variation in Properties with Respect to Cross Sectional Area (McKittrick, et al., 2010)

A variation in the properties of different structures is believed to increase their energy absorption in an impact scenario. From this knowledge a bio-inspired design can be developed to mimic bio-structures and hopefully achieve similar increases in energy absorption.

Biomaterials such as alligator gar fish scales, known as exoskeletons, have been known to exhibit desirable impact mitigating properties such as high strength, light weight, and toughness (Wegst & Ashby, 2004). The mechanical properties of fish scales vary through the thickness, and is thought to cause the high strength and light weight characteristics of the material. These

desirable properties stemming from functional gradation (variation in properties through the thickness) of the material exoskeleton facilitates improved absorption of energy (Nelms, 2018). From these materials engineers and researchers can develop better energy dissipative composite configurations for use as armor in military applications, protect individuals, and equipment.

Metallic foams are a specific type of cellular materials that have large volumes of void content which reduces the overall weight of the component. These can be manufactured from various materials, in both open and closed cell configurations (Figure 9 A, B).
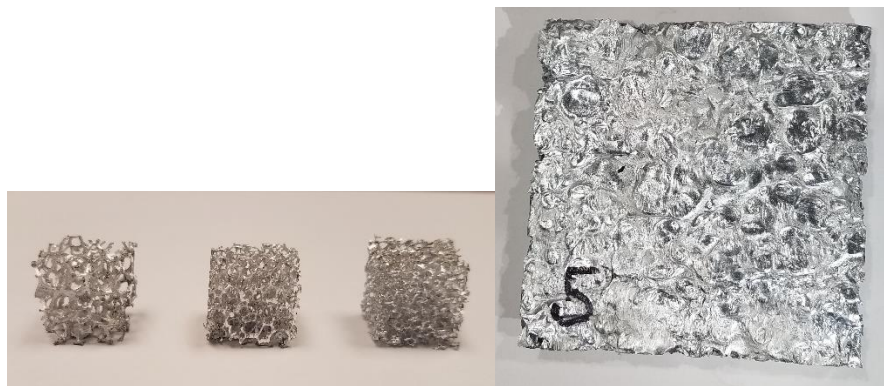
Figure 9. (A) Open Cell Aluminum Foam with Various Relative Density, and (B) Closed Cell Aluminum Foams

Open cell foams have voids visible from the outer surface of the materials whereas closed cell foams do not. The open cell foams can be porous and nonporous for various applications. In recent years, considerable research has been done to understand the mechanical properties of these materials and how utilization of these materials can lead to lighter and stronger engineering designs.

Huang et al. (2011) investigated the ballistics response of functionally graded bioinspired armor design similar to horse forelimb bone. Simulation of a ballistic projectile made of steel was done to compare the baseline response of uniform density foams. Coupon protection point (center back surface) was observed to have an overall decreasing acceleration as foam density was

9

increased from 350 kg/m^3 to 1370 kg/m^3. Utilizing this information along with known structure of the horse forelimb, an optimized design was constructed and experimentally tested. Comparisons were made between uniform density coupons (520 kg/m^3, and 770 kg/m^3) and enhanced bone-inspired coupons. The bone-inspired design was constructed of four different relative density foams (470 kg/m^3, 850 kg/m^3, 520 kg/m^3, 1260 kg/m^3) and a protection side made of a steel plate (7800 kg/m^3). The response of the low density uniform allowed for complete penetration of the projectile. The highest uniform density foam only allowed for 80% penetration, while the bone-inspired design only allowed for 44% penetration. This remarkable increase in ballistic mitigation is largely due to the variation in density of the coupon. The experimental response of the coupons is consistent with the simulation conducted in the same study. Based on this evidence it is speculated that a panel made of similar design would be more resistant to blast loading.

A similar study by Chintapalli et al. (2014) studied the puncture resistance of segmented glass which allows for a flexible armor. Design of the armor is fabricated to mimic armor consistent with fish, armadillo, and crocodile whose armor is embedded with hard plates over a soft substrate. This design has proven to be resilient to impact loading due to the variation in material properties through the thickness of the armor, (Nelms, 2018). To replicate this design, armor made of segmented hexagonal glass plates and a soft silicone rubber substrate with 1/63,000 the stiffness of the glass plates was fabricated. Test samples were impacted with a 25 µm steel tip equipped with a 110 N load cell. Loading rate of the steel tip was 0.005 m/s at the center of the hexagonal glass plate. Results of the bio-inspired design were compared against a continuous glass piece with a soft substrate backing. The glass piece showed a different failure pattern than the hexagonal armor design. The load-displacement response of the uniform continuous glass

piece increases load and then has an abrupt failure. By comparison, the hexagonal piece has a slightly lower initial load-displacement response caused by separation of the hexagonal glass piece from the composite. However, the armor is still able to resist loading of the separated piece and develop an increase in overall load carrying capability. Another advantage to the segmented armor design is that failure of one hexagonal piece has a minimal effect on other sections. Another observation made during testing is two distinctly different failure mechanics, tablet fracture and tablet tilt, which produced different resistance to penetration. Several variations in hexagonal glass piece sizes were tested and resulting data showed that a 70% increase in resistance when sectioned armor was compared with continuous armor.

Other investigators have taken a different approach and combined additive manufacturing with bio-inspired designs. Variations of single isolated scales non-overlapping, overlapping, overlapped stagger, simplified elasmoid, simplified ganoid, topologically interlocked, and full ganoid arrays were 3D printed and tested for puncture resistance. Results of this study show that simple array and a single isolated scale have low puncture resistance and that the array has low flexural compliance while the single isolated scale has a high compliance. Flexural compliance was defined as derivative of the force over the deflection. Other configurations such as simplified elasmoid and ganoid had high puncture resistance and low flexural compliance. It was also observed that the ganoid array, similar to fish scales provided a wide range of puncture resistance and flexural compliance. Similar observations were seen by Porter et al. (2017) and rotation, bending, and frictional sliding was shown to have a large influence on penetration resistance. It is possible that these designs can be applied to man-made armor designs, and would allow for better protection from penetration during highly energetic events.

A study conducted on bio-inspired sandwich structures by Yang et al (2017) explored the geometric dependency of various designs using a finite element simulation (FEM). Sandwich structure of aluminum with varying core geometric configurations (triangle core, single sinusoidal core, double sinusoidal core) were compared and showed slight variations in response to quasi-static compression. The initial peak force before a decrease in strength was observed for triangular core (1436 N) had the highest (about 1.4x and 5.7x) peak load, followed by the single sinusoidal core, and the double sinusoidal core. However, it was also observed that the specific energy absorption (SEA) was the highest when a double sinusoidal core was used. This hints that there is an ideal core configuration that will achieve the maximum specific energy absorption. Numerical simulations were conducted and parameter for the number of waves and amplitude of the waves was analyzed. It was found that six waves obtained the highest SEA and increasing beyond this number decreased the SEA.

Utilizing the knowledge obtained from other researchers, a bio-inspired functionally graded polymer infused metallic foam design is proposed for shock and impact mitigation applications. These designs have several variations to optimize for impact and blast mitigation. Two porous metallic foams with relative densities were infused with a polymeric material

1.2.2 Low-velocity Impact - Background Research

Low-velocity impact characteristics are used to understand and compare different materials for their impact resistance. Several types of impact test configurations can be done to obtain mechanical properties such as fracture toughness, or qualitative properties such as the SEA of a material which allows for the comparison of different material systems under the same loading conditions. This section provides an overview of experimental and computational work performed on functional graded and non-graded aluminum composites, like the type proposed in this research.

A study conducted on comparing the low-velocity impact SEA of 6063 aluminum foam and pure aluminum foam by Liu, et al. (2013) revealed two steps during the impact event, initial compression and gradual crushing. Specimens were subjected to 150 J of impact energy and impact velocity of 2.53 m/s. Quasi-static compression was also performed which showed that when comparing foams with density 0.26-0.29 g/cm^3 to 0.45-0.48 g/cm^3 an approximate 5x increase of SEA was observed. When comparing the different density foams in the low-velocity loading condition it was observed that an increase in SEA was obtained for increasing density for both the 6063 aluminum foam and the pure aluminum foam. It was also observed that when the density of the foams is between 0.2-0.25 g/cm^3 the SEA is nearly identical and beyond this threshold the 6063 aluminum foam SEA begins to be higher than the pure aluminum foam. At a density of 0.436 g/cm^3 the 6063 foam has a 1.55x higher SEA than the pure foam. Utilizing this information, it can be hypothesized that an ideal type of foam material within different alloys of aluminum and different densities to achieve the most ideal SEA.

A similar study performed by Yu et al. (2008) revealed multiple failure modes in quasi-static and dynamic three-point bend testing performed on sandwich composite constructed of LF21 aluminum face sheets (equivalent to 3003 aluminum) and closed cell aluminum foams (Hong Bo Company). The failure modes observed in the quasi-static testing revealed face sheet yielding, indentation, core shear, and face sheet yielding crack. The failure mode observed during the dynamic loading conditions were observed to be tensile crack, core shear crack, and debonding between face sheet and foam core, indentation. Comparisons were made between the experimental results and a modified Gibson model McCormack et al. (2001) to accommodate the unsymmetrical deformation and the cylindrical loading head. Comparison between the experimental results and

model showed similar trends for the experimental load-displacement curve and the simulated response.

A recent study by Li et al. (2019) investigates the effects of core thickness, core relative density, and indenter tip. These investigations revealed that as core thickness and relative density are increased energy absorption increases as well. The core thickness and density range tested in this investigation were from 10-33 mm and 0.05-0.275 g/cm^3, respectively. Comparison of the three indenters (conical noses, flat ended, and hemispherical noses) revealed that samples subjected to the hemispherical indenter had the highest energy absorption, followed by the flat ended indenter and the conical noses. This again gives valuable information about the penetration resistance to different projectiles. Utilization of this information could help improve dynamic models of ballistics or blast events where protective systems are subjected to projectiles of various size and shape. When comparing the absorption (hemispherical and conical noses) an increase of approximately 2x was observed.

Another investigation on functional graded sandwich composite constructed of unidirectional glass fiber/polypropylene with an aluminum foam cores conducted by Reyes (2008) compared the response of unidirectional and woven configurations. Panels configured of 0°/90°/0°/90° unidirectional and aluminum core composites and woven glass fiber with aluminum core material were subjected to low-velocity impact to understand the effects of fiber orientation. Results of this investigation revealed unidirectional fibers provided the highest strength. It was also observed that at different impact energy, two failure modes (bending and shear) converged at 20 J.

A study conducted by Fang et al. (2015) developed 3D mesoscopic model of closed-cell aluminum foams. Size and shape of closed-cell configurations were generated using an algorithm

and Weibull distribution of measured size distribution of the pores to accurately reflect typical close-cell foams. Once 3D models were generated from a FORTRAN code, quasi-static and dynamic simulation were performed using LS-DYNA. Simulation for both quasi-static and dynamic show good agreement in the stress-strain response. The numerical simulation resulted in slightly higher stress-strain response than the experimental curves. Simulation at various impact velocities showed an increase in energy absorption with increasing impact velocity from 40 m/s to 160 m/s. Another simulation conducted shows that as strength of the cell wall is increased the plateau typically seen in compression of foams increased as well. The effect of porosity was also a parameter analyzed in this study and it revealed that as porosity is increased from 71.1% to 81.1%, energy absorption decreases by about 1/2x when the same cell-wall strength and impact velocity conditions are applied.

A recent study by Qin, et al., (2017) compared simulation of dynamic three-point bend tests using FEM to analytical solutions. Analysis was performed using ABAQUS/Explicit Version 6.11. Face sheets were modeled using J_2 flow stress theory of plasticity and foams were modeled as a continuum. The plastic crushable behavior was modeled using Deshpande-Fleck model (Deshpande & Fleck, 2000). Impact force vs. total deflection was compared for the analytical solution and revealed that the FEM and analytical solution were in agreement, and the most ideal cases being when G* = 400, and $\bar{h}$ = 0.05, where G* is dimensionless parameter and $\bar{h}$ = the ratio of the thickness of the face sheets and core thickness. Three stages were observed during impact. Stage I is a localized denting phase, Stage II characterized by a combined localized denting and global deformation of the beam, and Stage III is a global deformation phase. Jumps in response were observed for theoretical solutions and it is argued that this is due to the acceleration of the striker depends on sub beam at Stage I and Stage II, and the basic beam at Stage III.

A study performed by Daniel, (2010), characterized several fiber reinforced composites in various loading scenarios. Aluminum honey comb and other core materials were also tested to obtain the stress-strain relationship. It was observed that as density increases strength increases and strength increases with increasing strain-rate. Utilizing a semi-empirical criteria (Olsson, 1998), a relationship between the ratio impactor mass to specimen mass, average frequency of impact pulse, impact velocity compared to wave propagation velocities in samples and strain rate, a model using energy balance can be obtained. From the energy balance an equation of motion can be obtained and used to predict the vertical deflection and the maximum load. Similar analysis was attempted in this research to validate whether this model is applicable for composites made of aluminum foam.

1.2.3 High Strain-Rate Split Hopkinson Pressure Bar - Background Research

Split Hopkinson Pressure Bar (SHPB) is an apparatus used for characterizing the high strain-rate response of materials subjected to compressive, tensile, or torsional loading conditions. Dynamic mechanical properties such as ultimate compressive strength and specific energy can be obtained. This section discusses recent research related to SHPB testing specifically on metallic foams.

A study conducted on closed-cell Alulight with 0.17-0.4 relative density and open-cell Duocel with relative density of 0.07 foams by Deshpande & Fleck (2000), compared the quasi-static and dynamic response of aluminum foams. Dynamic strain-rates ranged from 1000/s-5000/s. The resulting stress-strain curve yielded three distinct regions; an initial linear elastic region, followed by a yield point, then a plateau region, and finally a rapid increase in strength as cells begin to collapse. A transmission bar made of PMMA was used to increase the signal strength in the transmission region. Based on results it was stated that no strain-rate sensitivity was

observed when comparing quasi-static and dynamic stress-strain response despite an increase shown in the response shown for samples of relative density 0.17. Results obtained in this investigation also show that the plateau strength is rate insensitive.

A similar study conducted in 2009 Edwin Raj et al., (2009) on the high strain-rate response of closed-cell aluminum foams manufactured by Alulight and Cymat reported conflicting results from the previous results found in Deshpande & Fleck (2000). Relative density ranges between 0.062 to 0.373 were tested in quasi-static compression and dynamic loading conditions. Energy density and plateau strength for quasi-static and dynamic testing were obtained to compare the effect of strain rate at various relative densities. Comparison between the quasi-static and dynamic stress-strain response reveals an increase in energy density and plateau strength. This comparison was made between 0.001/s and 1000/s. Another phenomenon observed is that as relative density increases the plateau strength increases, which is consistent with low-velocity testing results. No densification was observed in both test methods and no explanation was given to underline the reason.

Another study conducted on open and closed-cell foams manufactured by Alporas by Dannemann & Lankford Jr., (2000) compare the stress-strain response at varying strain-rates. Relative densities (7.4% and 15%) for closed-cell Alporas foams and Duocel foams with relative density of 7% were subjected to high strain-rate loading. The higher relative density Alporas foam had 2-3 mm pore size and the lower density had cell sizes approximately 4-7 mm. Resulting data all show variance with results of Deshpande & Fleck, (2000), but it is stated that this could be due to difference in material and processing methods. Stress-strain response of the Duocel foams showed a slight increase in response with increasing strain rate from 9.5×10^{-4}/s to 1.2×10^{3}. Peak stress of the Alporas closed-cell foams was found to be approximately 1.5 MPa as compared to

2.6 MPa at 1×10^{-3}/s and $1.36 \times 10^{\wedge 3}$s respectively, for the 0.07 relative density samples. The 0.15 relative density samples exhibited a similar increase in peak stress, and plateau stress as the 0.07 samples. This increase was observed to be approximately 2.3x when compare the quasi-static at strain-rates of 1×10^{-3}/s. and 4.26×10^{2}/s. Final results show that after normalizing the plateau stress at various strain-rates an increase in strength was observed for Alporas foams.

Characterization of stress-strain response of aluminum foams at intermediate strain-rates was performed by Yang, et al., (2013) performing experiments within strain-rate rages of 40/s - 585/s. FEM was conducted at similar strain-rate as experimental testing. Stress-strain response of experimental samples is consistent with other literature that show FEM simulation can accurately predict the stress-strain response of aluminum foams. Also similar to several models of aluminum foam for low-velocity and SHPB the FEM results give a slight over prediction of the response of the foams.

The effects of heat treatment on crushing behavior and energy absorption of aluminum foams was studied by Wang et al. (2009). Three heat treatment variations were studied in this article; untreated (as received from the manufacture), T6-Strengthing, and Age-Hardened for two alloys Al-Mg-Si and Al-Mg. Quasi-static and high strain-rate compression was performed and yielded typical stress-strain response for aluminum foams having a linear elastic region followed by yielding, plateau region, and densification region. The T6-Strengthing samples gave a higher stress-strain response versus the Age-Hardened samples until the densification region of the compression, and the non-treated samples exhibited the lowest response in all regions for Al-Mg-Si samples. The same trend was not observed when comparing the high strain-rate response. The T6 samples exhibited the highest response in all regions at a strain-rate of 2000/s, followed by the Age-Hardening samples and control group. Strain rate sensitivity was observed in all samples.

Samples made of alloy Al-Mg results in similar quasi-static stress-strain response. Slight strain-rate sensitivity was exhibited by all heat treatment, however little variation in response was observed due to heat treatment.

A study that implemented a slightly different approach was performed by Merrett et al. (2013), conducted direct impact of aluminum foams in two configurations, dynamic forward and dynamic reverse. The variation in the testing configuration was achieved by changing the location of the foam to be attached to the striker rod or the end cap. Specimens were bonded to the striker and back plate using polypropylene adhesive, no face sheets were used due to them potentially causing premature fragmentation seen in research conducted by Langdon, et al., (2010). Results from the experimentation show increase in stress-strain response when compared to quasi-static for both configurations. Variation in densification region initiation was also observed. Samples in the forward configuration (foam bonded to output bar) had smaller strain to densification, when compared to quasi-static, and an even larger strain needed for densification was observed for the reverse configuration. Further comparison revealed an increase in dynamic plastic collapse stress and plateau stress, consistent with previously mentioned articles.

An investigation of the directional dependency of aluminum foams was studied by Peroni et al. (2013), who explored the response at different orientations. SHPB testing was performed on three axes relative to the plate orientation with the Z direction samples being through the thickness of the plate, and the X and Y being transverse to the Z and normal to each other. It was found that samples did not exhibit the typical stress-strain regions of linear elastic, yield, plateau, and densification seen in other studies. High scatter was also observed due to the non-homogenous structure tested. Ultimately no large anisotropy was observed in samples tested. No strain-rate effects were observed for the strain rates tested between 100/s – 300/s.

An innovative study performed on polymer filled auxetics using SHPB was conducted by Fı́la, et al. (2017) who studied the effects of infusing polymer into an auxetic structure. Unlike typical foam structures, samples in this study were 3D printed using additive manufacturing techniques and had consistent repeating structure. 316L-0407 austenitic stainless steel alloy, was used in this study and infused with ordnance gelatine. This was selected due to it low viscosity during preparation, which provided uniform distribution into auxetic structures. A second set of samples was filled with low expansion polyurethane foams, and a third unfilled control group all tested using an SHPB system. Three internal configuration were compared 2D re-entrant, 3D re-entrant, and 2D missing rib. Comparison of SEA yielded an increase when comparing quasi-static and SHPB responses. Comparison of the different core configuration shows that the SEA increases when comparing 2D re-entrant, 3D re-entrant, and 2D missing rib with the later having the highest SEA. Comparison of the non-filled and filled samples showed an increase in SEA with the samples infused with the gelatine having the highest SEA overall. Increases as high as 70% were seen when comparing quasi-static and dynamic response, and increases as high as 40% for filled when compared to non-filled. This unique phenomenon is the main focus of this research.

1.2.2 Blast Loading - Background Research

Highly energetic events such as blast loading are of great interest for armor design. Armor that has been manufactured to with stand other dynamic events such as ballistics or low-velocity impact may not necessarily be efficient at mitigating blast loads. Because of this it is essential that in-depth investigations be done on the capabilities of armor designs in such loading situations. This section reviews several articles that are relevant to the proposed research.

Blast resistance of PVC foam core sandwich composites with aluminum face sheets was studied by Hassan et al. (2012). PVC composites with 20 mm thickness were bonded to 1.7 mm

aluminum face sheets using a fast-curing contact adhesive. Five density foams were used in this investigation; 60, 80, 100, 130, and 200 kg/m^3, all of which had increasing mechanical properties as density increased. A Disc of PE4 explosive was detonated 90 mm from the sample surface. Based on visual inspection no sign of fracture was observed in the 60 kg/m^3 panels. This type of failure is consistent with plastic membrane stretching identified by Abdullah (2008). Debonding between aluminum face sheets and foam core was observed in other density foam composites, and the extent of the damage propagated to clamping regions. Plastic deformation of the aluminum face sheets was also observed. Another important failure characteristic that was observed was crack initiations (Mode I) and propagation at the tensile surface of the composite panels for higher density foams, however the energy absorbed due to this specific failure type was low in comparison to other failure modes. It was also noted that when comparing similar impulse of 11.2 Ns, lower density foams did not exhibit cracking making them a more ideal component for energy absorption when weight is considered. Using numerical simulations in ABAQUS, individual energy absorption of each sandwich panel component (front face sheet, core, and back face sheet) was obtained and compared with the impulse the panels were subjected to. Based on resulting simulations as impulse increases core material energy absorption decreases, front face sheet absorption increases, and bottom face sheet increases for lower density foams. The same is true for the higher density foams with the exception that the back face sheet increases in energy dissipation. Final conclusions show that most of the energy absorbed during blast loading was due to plastic deformation of skin and core material, and Mode I fracture becomes more pronounced as core density is increased.

Another study that investigated the blast response of closed-cell aluminum foams observed the response of metallic foams subjected to blast loading in a curved configuration as opposed to

a flat panel. This study performed by Jing et al. (2014), conducted blast testing on panels with two curvatures (500 mm and 250 mm). Two thin LY-12 aluminum face sheets were bonded to aluminum foams using commercially available adhesive (HY-914). Three variations of face sheet thickness were used, 0.5 mm, 0.8 mm, and 1.0 mm, and three relative densities were used, 11%, 15%, and 18%. Blast experimentation was done using a four bar ballistic pendulum system. Based on inspection of samples after experimentation several prominent failure mechanisms are noted. The different types of failure mechanisms are specific to each component of the sandwich composites. Front face sheets exhibited indentation, transverse tearing, and petal-like tearing. Core material (aluminum foams) exhibited crushing and shear failure. While rear face sheets exhibited gross inelastic deformation, gross inelastic deformation with tensile tearing, and transverse shear failure. Delamination was also observed between face sheets and core material. Based on experimental results it was observed that as impulse strength increased center point deflection increased for all sandwich composites, and as face sheet thickness increased center point deflection decreased. Ultimately it was observed that the curved sandwich composites with smaller radius exhibited less resistance to blast than those with larger radius. It is believed that this is due to difference in dominant deformation mechanisms.

Analytical and experimental comparison for energy during blast tube experimentation is presented by Wang & Shukla (2010). In this article an explanation of the energies associated with a blast event (incident energy and remaining energy) are discussed and compared with experimental results. This analytical analysis was done for a single panel of homogenous material (aluminum). Details of the analytical equations are discussed in more detail later in this prospectus. Utilization of the incident and reflected wave ultimately allows for the energies to be theoretically calculated. For comparison with experimental results, the deformation energy and

work done to deform panel must be evaluated using the deflection-time of the panel and the force-time data from pressure sensor located near the specimen surface. From these two signals the force-deflection can be obtained, and integration of this curve allows for the absorbed energy to be calculated. Experimental validation was completed using a homogenous 6061 aluminum sheet subjected to blast loading. Deflection of the panel was captured using a high speed camera at a recording frame rate of 70 µs/frame (≈14,300 Frames Per Second (FPS)). Pressure sensor located ~0.02 m and 0.18 m from the sample surface were used to record the pressure profile during the blast event. Velocity of the shock wave was used using the pressure profiles from the two pressure sensors. Typical pressure profiles show two jumps in pressure for each sensor. The first jump being the incident shock and the second being the reflected shock. Verification of the pressure sensor was done by placing a third transducer mounted in a thick steel plate at the surface of blast wave impact and comparing with pressures recorded transducer 1 and 2. An overlap of the incident and reflected pressure was observed, which prevents the use of the waves directly. Due to the repeatability of shock profiles in a shock tube test the incident profile can be obtained by testing without a sample present and recording pressure signals. This allows for the energy absorption to be estimated for a longer time span. This simplification does add error to the estimation of energy absorbed by samples during blast loading, however due to the consistent particle velocity the methods are still feasible.

A similar study performed on functional graded styrene acrylonitrile foams was performed by Wang et al. (2009). In this study two configurations of functionally graded sandwich composites (A300/A500/A800 and A500/A300/A800) made of three styrene acrylonitrile foam densities with E-Glass/Vinyl Ester skings were subjected to blast loading to better understand the effect of density sequence of energy absorption. The exact setup previously mentioned in Wang

& Shukla, (2010) was used. A300, A500, and A800 styrene acrylonitrile foams of density 58.5 kg/m^3, 92 kg/m^3, and 150 kg/m^3, and compressive strength 32 MPa, 64 MPa, 117 MPa, respectively were used in this study. Visual inspection of samples post testing exhibited several failure mechanisms. Cracking in the core was observed near the supports, delamination between core and skins, and core compression was also observed. Core compression was most pronounced in lowest density foam. Using the same analysis presented in Wang & Shukla, (2010) the total energy absorbed was analyzed for both configurations, which yielded no difference in total energy absorbed. Configuration of A300/A500/A800 showed no structural collapse while the second configuration did exhibit collapse. This variation in damage was used to justify that the first configuration was better at absorbing energy than the later. Based on comparison of the deformation energy and the total energy loss it was concluded that 25% of total energy was transferred to the panels, with the remaining 75% being dissipated as other form of energy. Based on comparison of this experiment and previous bio-inspired design it is possible that the variation in density was not large enough to observe a pronounced difference in the response.

To expand on the knowledge of functionally graded composites, another study introduced polyurea intermediate layers into configuration 1 described in Wang et al. (2009) at the front and back surface of the A300/A500/A800 styrene foam sandwich composites. Gardner et al. (2012) introduced a polyurea layer 6.35 mm thick in between the E-Glass/Vinyl Ester face sheet and styrene acrylonitrile foams to improve the blast mitigation of sandwich panels. 3D digital image correlation (DIC) was used to observe the back surface full field strain and mid-line strain, and 2D DIC was used to observe the out of plane deformation at each interface, later used for energy analysis. Similar analysis by Wang et al. (2009) and Wang & Shukla (2010) revealed that samples with polyurea located at the back surface allowed for stepwise compression of foams reducing the

24

transmission of the blast waves and lowering the back surface deflection, which resulted in a better structural composite. It was also observed that when polyurea interlayer was added to the front side of sandwich composite it prompted failure. Based on this analysis it was surmised that having low density foams located near the front surface and with increasing density towards the back surface is more idyllic to mitigate blast loading.

Attempts to improve the blast mitigation properties of foam filled sandwich composites was conducted by Yazici et al. (2015). This investigation coupled two previous investigations Yang et al. (2017) and Fı´la, et al. (2017)) to try and improve the blast capabilities of steel sandwich composites with sinusoidal core framework by infusing low-density polyurethane foam. The corrugated core framework had five layers that were filled or left unfilled in six configurations, F1-F5, F4-F5, F3-F4-F5, F3, F2-F4, and F1-F3-F5, where F denotes filled and the number denotes the layer. FEM analysis was also done to compare experimental responses with computational results which use Johnson-Cook model to model the response of steel, and foam components were modeled using a compressible hyper-elastic solid with time dependent mechanical properties and hysteresis being ignored. Evolution of deflection was monitored using a high speed camera at 20,000 fps. Several conclusions were drawn from the resulting analysis. A noteworthy conclusion drawn from analysis was that back side filling was more effective at reducing the back surface deflection, even to that of a fully filled core. This was also observed in a numerical simulation by Liu et al. (2014) that was conducted on functionally graded sandwich composites. The main difference between the two studies is that no steel corrugated layer was used in the later, only different relative density foams. It was also observed that the functionally graded sheets showed improved mitigation response over conventional sandwich composites with one solid core.

A continuation of the previous investigation prompted two more investigations of foam filled steel sandwich composites by Yazici et al. (2014) and Karen et al. (2016). In both investigations, numerical simulation for corrugated steel sandwich composites was done. The first investigation tested three configuration of corrugated sandwich composites, non-filled, foam filled corrugate steel core, and foam core. Similar test method, procedure, and analysis were used as described in Wang et al. (2009) and Wang & Shukla, (2010). Experimental results were compared with FEM models which used Johnson-Cook strain hardening model for the steel components and hyper-elastic compressible solid model discussed in Yazici et al. (2015). Comparison of results yielded several conclusions related to the scope of the proposed research. Notable conclusion drawn from numerical simulations is that the fully filled foam core exhibited the smallest back surface deflection, and FEM simulation using ABAQUS matched experimental results. It was also observed that increasing the thickness of the skins and corrugated core reduced the benefit of the foam filled sandwich composite. The later investigation expanded on the former and sought to optimize the filling sequence of the corrugated core using a hybrid evolutionary optimization algorithm. Using similar modeling techniques 2D and 3D simulation were performed. Utilization of the method developed in Karen et al. (2016) can be used to optimize properties such as energy absorption, and best improvement in back face deflection was observed in simple supported configurations.

1.3 Objective of Research

Biological composites have been known to have advantageous properties not easily replicated by manmade materials. These have also been shown to have superior energy dissipative properties due to the functional gradation of the mechanical properties of the material. The specific

goal of this research is to develop a manmade analogy for biomaterials using functionally graded metallic foams with varying relative densities; both for understanding the low-velocity, high strain-rate, and blast response of metallic foams, and further improving the energy dissipation characteristics of these functionally graded materials by infusing the porous foams with a polymer resin.

The materials investigated in this research are porous aluminum 6101-T6 metallic foams with two relative densities with and without infusion of polymeric material, and three nonporous 6101-T6 aluminum metallic foams that are currently used in military applications. The dynamic mechanical testing techniques that were employed in this study are low-velocity impact, split Hopkinson pressure bar, and blast tube. This serves to give a wide range of loading conditions, as well as, fundamental knowledge of the material behavior at various strain-rates. Finite element modeling of the high strain-rate response was performed using a commercially available software (ABAQUS/LS-Dyna). The primary objective of this research is to develop a functionally graded composite with and without polymeric infusion; test the dynamic response of these bioinspired designs, compare the energy absorption with conventional materials used in military applications, identify failure mechanisms associated with each type of loading case, and understand how polymeric resin infusion influences the energy dissipative characteristics of such functionally grade composites. The secondary objective is to model the high strain-rate SHPB response of such materials for optimizing their energy absorption capabilities in sandwich structures.

As stated, the finite element modeling was performed using a commercially available software (ABAQUS/LS-Dyna) for evaluating SHPB high strain-rate response of the metallic foams. Computational models have simplified metallic foam samples imported into the model for comparison to experimental response of metallic foams.

1.4 Research Significance

Not much is reported on the blast response of open-cell foams subjected to dynamic loading, and to date no research appears to have been conducted on functionally graded polymer infused metallic foams with random structures. Similar studies have been conducted on polymer filled auxetics and sinusoidal corrugated steel core structures filled with polymers or foams respectively Fı´la, et al. (2017), Yazici et al. (2014), and Yaziciet al. (2015) metallic. These studies, however, have repeating internal structure as opposed to a random structure. The subtle change in core framework could have more pronounced effects of functional grading and improvement of dynamic mitigation properties. Another significance of this research is that this compiled data will be beneficial for modeling of complex sandwich composites with random core structure as opposed to a repeating one.

The effects of functional grading are still not well understood. Information gathered in this dissertation will provide necessary experimental background information for further understanding of these types of complex systems. This research will also provide a basis for comprehending the response of functionally graded polymer infused metallic foams subjected to dynamic loading and for comparison with analytical models. Another significance is an understanding of how the response of these complex functionally graded polymer infused metallic foams change in different loading scenarios such as low-velocity impact and high energy blast loading.

Significance 1: Investigating the performance of sandwich composites with porous open-cell foams and comparison with conventional configurations under low-velocity impact, SHPB high strain-rates and blast loading.

Significance 2: Investigating the performance of polymer filled open-cell aluminum foams and comparison with conventional configurations as well as non-filled configurations under low-velocity impact, SHPB high strain-rates and blast loading.

Significance 3: Investigating the high strain-rate SHPB response of non-filled closed and filled open cell foams.

Significance 4: Model SHPB and blast loading cases and compare with experimental results.

Significance 5: Investigating the effect of stacking sequence on the response of non-filled and filled open cell aluminum foams under low-velocity and blast loading.

Significance 6: Investigating different failure mechanisms under low-velocity, SHPB high strain-rates and blast loading.

Significance 7: Providing a robust experimental data set for comparison with analytical models.

1.5 Scope of Research

The research scope is primarily focus on experimental characterization of dynamic properties of open-cell foams, polymer filled open-cell foams, and studying the effects of functionally grading such core materials on the dynamic properties of composite structures. Based on preliminary results, sample configurations were made into sandwich structures. Several testing methods (low-velocity, direct compression impact, SHPB, and shock tube) were implemented to

characterize the dynamic response of sandwich composites or core materials. Modeling was done on quasi-static, high strain-rate SHPB, and blast loading cases.

The functional grading manufacturing method was also a focus of this investigation. The specific method used for infusing porous metallic foams with resins consisted of mixing appropriate volumes of polyurethane foam and infusing into metallic foams in wooden molds. The method for bonding layers of aluminum foams together used in this study was using conventional high strength aerosol adhesive. Six variations of the conventional closed cell aluminum foams used in current armor designs were manufactured, and eight variations (four non-filled and four resin infused variations) of functionally graded composites were fabricated.

Direct impact testing was done to understand the compressive impact behavior of each functionally graded metallic foam configuration with and without infusion. Energy absorption dynamic properties was compared to obtain the energy dissipation of each configuration.

Low-velocity punch shear response of different functionally graded core materials or sandwich composites was a major scope of this work. Energy absorption was analyzed to obtain which configuration dissipates the most energy.

SHPB of all baseline materials (various relative densities for non-filled and resin infused configurations) were evaluated in dynamic compression to understand the high strain-rate behavior of individual foams. Rate effects, energy absorption, critical components of stress-strain relationship, etc., were an important focus for SHPB analysis. Information from resulting data can be used to advance computational modeling and further understand metallic foam/polymer composite dynamic behavior.

Blast loading was performed on rectangular beam specimens to compare the response of each configuration. The scope of this was to include DIC analysis to obtain necessary parameters for analytical model comparison, DIC analysis of side view, and energy absorption characteristics.

ABAQUS models was developed to compare the computational analysis for each dynamic testing configuration (SHPB and blast loading). Models served as comparative tools but will not be the focal point of this research. Samples were 3D CT scanned or representative volumes of the metallic foams was attempted to be imported into ABAQUS or LS-Dyna for direct comparison of experimental and computational results. Limitation for computational modelling responding to processing resources did not enable CT scan to be used in finite element modeling. As a results simplified models were used to understand some of the dynamic phenomena present in SHPB and blast loading. Figure 10 shows an image of a typical 3D CT scanned sample. Models were performed and then fine-tuned if good agreement between experimental and computational is not observed. Comparison between experimental and computational models were made to better understand key phenomena in experimental results.
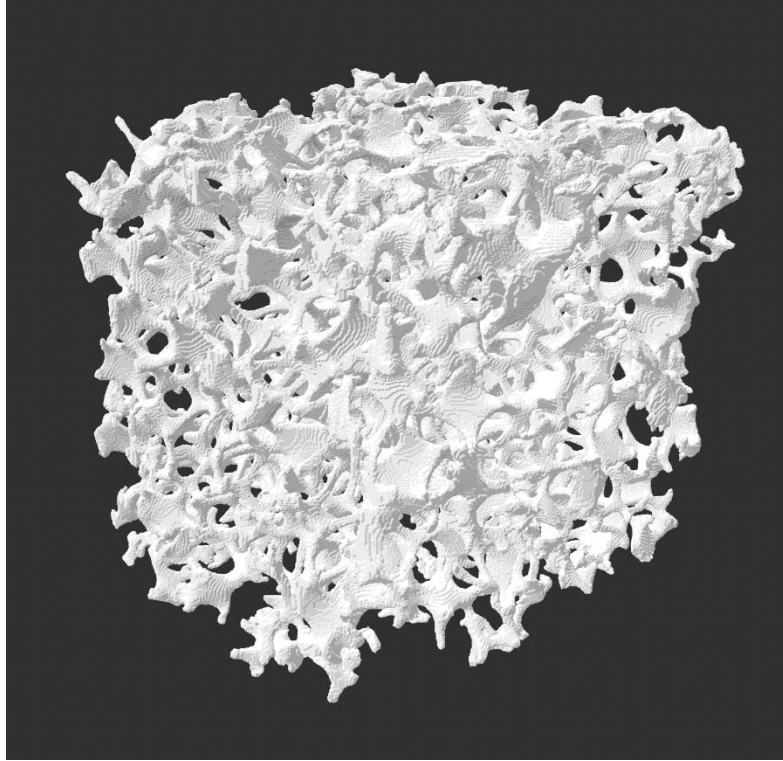
Figure 10: 3D CT Scan of Aluminum Foam

1.6 Organization of Dissertation

Chapter 1 explains the background research needed to get a general idea of the methods and analysis currently available to analyze sandwich composites, compare different material systems, and compare experimental results with analytical results. It also provides a guide for how this specific project is constructed, fusing several different ideas obtained from previous research by other investigators. Chapter 1 also gives basic background on the material systems that was investigated in this study.

Chapter 2 explores the theory used to obtain experimental results and modeling results. It discusses in detail the five different testing systems, quasi-static testing, low-velocity impact, direct impact compression, SHPB, and blast tube experimentation. It also covers in detail the

experimental analysis used for quasi-static, low-velocity impact, direct impact compression, SHPB, and blast tube testing methods.

Chapter 3 provides details of all experimental setups used to test base material and functionally graded non-infused, and infused composites. Analysis on maintaining the same areal density for porous metallic foams are discussed. Detailed fabrication procedure for composite panels are also given in this section.

Chapter 4 covers the experimental results for quasi-static compression testing on samples. The major focus is obtaining stress-strain diagrams that can be used to compare with dynamic stress-strain curves. It also serves as a tool to compare the response of infused variations compared to non-infused. Finite element simulations on simplified sample geometry are used to obtain information related to failure mechanisms.

Chapter 5 reports all experimental results obtained from low-velocity impact testing. The major focus of this section will be on energy absorption of the non-filled and resin infused functionally graded metallic foams and comparing the different configurations. The secondary discussion will discuss the failure mechanisms observed during experimentation. This chapter also compares the response of similar closed-cell metallic foams already in use for similar energy absorption applications.

Chapter 6 presents results for direct compression impact testing of functionally graded materials. The energy absorption and dynamic behavior of each material is experimentally characterized to obtain stress-strain relations, energy absorption as well as failure mechanisms.

In Chapter 7 experimental results from SHPB testing are presented. These results primarily focus on energy absorption characteristics of each individual configuration and compare the response of each. This section also compares results obtained using conventional SHPB

techniques with DIC techniques. Computational models of simplified geometry are presented and compared to experimental results to obtain insight on phenomena present during experimentally testing.

Chapter 8 covers the results obtained from blast tube testing. Primary focus is on the energy absorption of each composite and comparing the response of different relative density composites, comparing non-filled and filled aluminum foam composites. Comparisons are also made with conventional composites made of closed-cell metallic foams already in use in similar applications. Comparison of FEA models with experimental results are discussed along with explanations of any deviations if present.

Chapter 9 covers the novelty of research conducted and potential applications of the composites investigated in this research investigation will be given. Summary of the results and conclusions that can be drawn from the resulting analysis will be discussed in this chapter. Ideas for future investigations and recommendations to further the understanding of non-filled and resin infused metallic foams for shock and impact hazard mitigation will also be given in this section. Concluding remarks and recommendation for future research.

CHAPTER II: THEORY/ANALYSIS

2.1 Quasi-Static and Direct Impact Theory/Analysis

Quasi-static compression is used to determine mechanical properties of various materials. In this study the stress and strain response of metallic foam and metallic/polymer foam composites are obtained. Current methods for obtaining stress are typically designed for solid materials and not high porosity foams. However, to understand the bulk response of the metallic foam quasi-static analysis was obtained using conventional uniaxial stress and strain formulation. The approximate sample stress was calculated using equation 1.

$$\sigma_s = \frac{P}{A} \qquad\qquad eq. 1$$

Current methods also do not allow for obtaining strain of the metallic framework strand, but rather the global strain of the entire metallic foam sample. Strain was calculated using simple uniaxial strain formulation (eq.2).

$$\varepsilon_s = \frac{\Delta L}{L_o} \qquad\qquad eq. 2$$

The stress and strain calculated for the bulk material does not accurately reflect the strain of individual metallic foam framework. In essence, the metal strands that make up the of metal framework are potentially at a high or lower state of stress than the calculated global stress and strain depended on the deformation at that particular location.

Direct impact is a means of testing materials at intermediate strain-rates when compared to quasi-static and SHPB Similarly, direct impact compression also has no provisions to obtain stress

and strain for individual metal strand within the foam framework. For this reason, global stress and strain were obtain using equations 1 and 2.

2.2 Low-Velocity Theory/Analysis

Low velocity impact testing was performed to observed the punch shear behavior of Cymat and Duocel metallic foams and Duocel/polymer composite materials. Low velocity impact testing was performed using ASTM D3763 (ASTM Standard, 2018) as a guiding tool to obtain accurate results. Critical for accurate results, the impact velocity was set to achieve a velocity slowdown of between 5-20% for all tested materials. Uniform testing protocols were used for same material but are not consistent when comparing Cymat and Duocel foams due to velocity slowdown criteria. During experimentation load-displacement is monitored and a corresponding load-displacement curve is produced. Resulting energy absorption is calculated from numerical integration of load-displacement curves using equation 3.

$$E = \int_0^x P(x)dx \hspace{4cm} eq.(3)$$

Damage initiation energy was calculated up to peak load and puncture propagation energy was calculated from peak load to signal end plateau. Signal end plateau was defined as the region of the load-displacement curve were the signal reached a constant force. Figure 11 (Pramanik & Mantena, 2009) depicts the damage initiation energy and puncture propagation energy regions of the load-displacement and energy-displacement curves, respectively, associated with the low-velocity impact test.
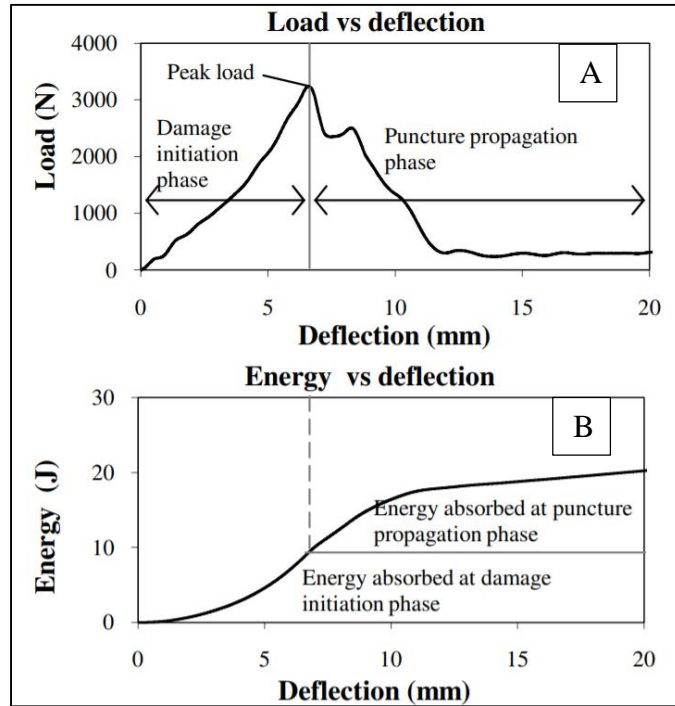
Figure 11: (A) Damage Initiation, Puncture Propagation Energy for Load-Displacement, and (B) Energy-Displacement Regions (Pramanik & Mantena, 2009)

2.3 Split Hopkinson Pressure Bar Theory/Analysis

Split Hopkinson Pressure Bar (Fig. 12) testing facilitates the high strain-rate dynamic stress-strain behavior of materials to be characterized. The capabilities of materials tested using this method can be obtained and used for dynamic simulations as well as practical applications. This method involves a striker that is propelled with compressed air towards and impacts an incident bar, which generates an elastic compressive stress pulse (incident wave).
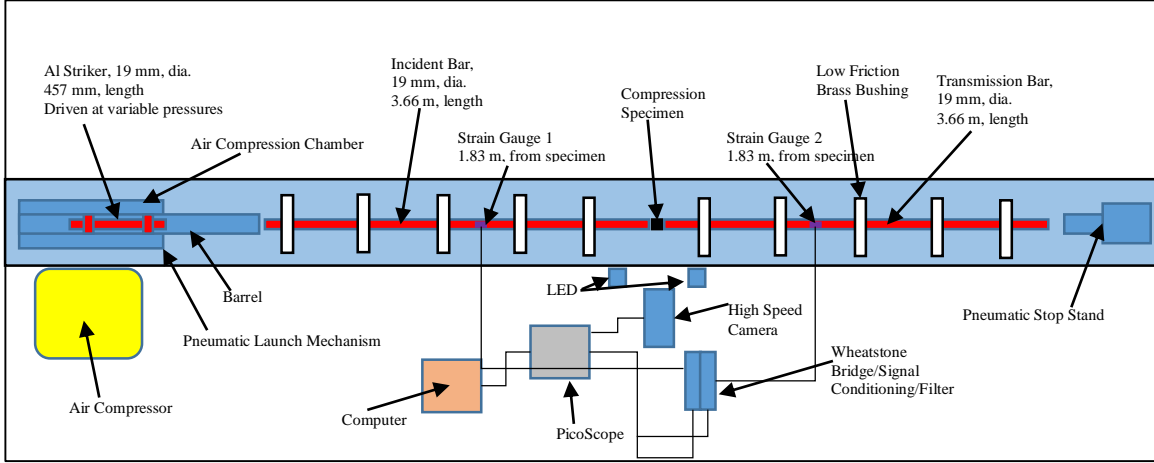
Figure 12. Split Hopkinson Pressure Bar System Schematic (Not to Scale)

Traditionally the incident wave is rectangular, unless a pulse shaper is used (Pramanik B. , 2014). Pulse shapers are typically used to prevent undesired failure in samples caused by non-stress equilibrium. Once the compressive wave has reached the sample's initial surface, located between the incident and transmission bar, due to impedance mismatch, based on cross sectional area or material mismatch, the incident wave separates into a reflected and transmitted wave. Based on the elastic properties of the bar material dynamic properties of the sample material can be found. Displacement of bar ends of incident and transmission bars can be calculated using equations 4 and 5, respectively.

$$U_1 = \int_0^t C_o \varepsilon_1 dt \qquad eq.4 \qquad\qquad U_2 = \int_0^t C_o \varepsilon_2 dt \qquad eq.5$$

From bar end displacement sample strain can be calculated using uniaxial strain equations (eq. 6).

$$\varepsilon_s = \frac{U_1 - U_2}{L_s} \qquad\qquad eq.6$$

Combining equations 3-5 provides a relationship between the three stress waves (incident, reflected, and transmitted) and sample strain (eq. 7).

$$\varepsilon_s = \frac{C_o}{L_s} \int_0^t (\varepsilon_i - \varepsilon_r - \varepsilon_t) dt \qquad\qquad eq.7$$

During dynamic SHPB high strain-rate wave propagation force equilibrium must be maintained (Frew, Forrestal, & Chen, 2002) for valid results. Since the incident and transmission bar remain elastic during compression the force on each end of the bar can be calculated using uniaxial stress formulation and Hooke's law (Chen & Song, 2011). Force at incident bar and transmission bar end nearest to sample surface are shown in equations 8 and 9, respectively.

$$P_1 = E_b A_b (\varepsilon_i + \varepsilon_r) \qquad eq.\,8 \qquad\qquad P_2 = E_b A_b \varepsilon_t \qquad eq.\,9$$

Setting equation 8 and 9 to be equal (dynamic force equilibrium) reduces to equation 10, which can then be further used to simplify equation 7 to relate sample strain to the reflected stress wave (eq. 11).

$$\varepsilon_i + \varepsilon_r = \varepsilon_t \qquad\qquad eq.\,10$$

$$\varepsilon_s = \frac{-2C_o}{L_s} \int_0^t \varepsilon_r dt \qquad\qquad eq.\,11$$

From equation 11 the sample strain-rate can be obtained by taking the time derivative (eq. 12). Sample stress can be obtained from relating applied force to the cross sectional area of the sample (eq. 13)

$$\dot{\varepsilon}_s = \frac{-2C_o}{L_s} \varepsilon_r(t) \qquad\qquad eq.\,(12)$$

$$\sigma_s = E_b \frac{A_b}{A_s} \varepsilon_t(t) \qquad\qquad eq.\,(13)$$

The elastic wave analysis allows for stress-strain to be calculated at every time instance during experimentation. Numerical integration of stress-strain curve allows for energy density to be obtain and compared at varying strain-rate and material composition.

2.4 Shock Tube Theory/Analysis

Shockwaves are caused by highly energetic disturbances that cause it to propagate through a medium at or the sound speed of the medium. The shockwave carries internal energy that can subject surrounding object to abrupt changes in pressure, and propagates at or above the sound speed of the medium (Anderson, 2012). A shock tube is a device that is designed to simulate a shockwave event at an engineering scale. Conventional design consists of a driver section and a driven section of compressed fluid separated by a diaphragm or high speed valve. Upon diaphragm burst or high speed valve actuation a planar shockwave propagates at or above the sound speed of the medium towards a sample. Before the shockwave reaches the sample (Fig. 13) the location of the shockwave creates two separate sections, the driven gas (in front of the shockwave) and driver gas (behind the shockwave). The driven gas has not been disturbed while the driver gas is a high pressure disturbance with internal energy that propagates at a speed U_+. Once the shock front propagates and impacts the sample surface a reflected shockwave is generated and propagates at a speed U_-. This will again create two sections (Fig. 13(B)) however, the gas in front of the planar reflected shockwave still remains the driver section and the gas behind is disturbed gas (Wang & Shukla, 2010). The properties of the different sections created by the shock front can be defined by physical parameter of the gases where u is the particle velocity, p is the pressure, c is the sound velocity, ρ is the density, τ is the specific volume, and e is the specific (internal energy) (Wang & Shukla, 2010).
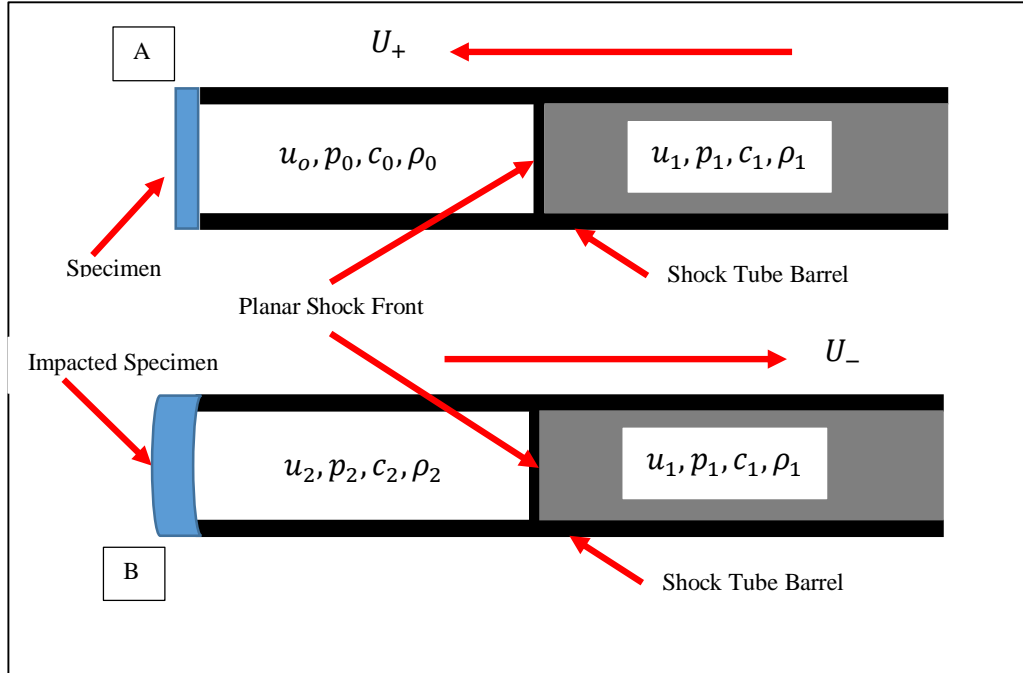
Figure 13. Incident and Reflected Shock Front Schematic

From the three sections the among of energy stored can be separated into the internal energy, translational energy, and the work done by the gas over a time span of d*t* during the experimental loading conditions with a cross sectional area of *S*, pressure *p(t)*, particle velocity *u(t)*, and γ is adiabatic exponent of the gas (Wang & Shukla, 2010). The work done by the gas, internal energy, and translational energy can be defined as (Wang & Shukla, 2010),

$$dE_{Work\ Done} = p(t) \cdot S \cdot |u(t)| dt \qquad eq.(14)$$

$$dE_{internal} = \frac{p(t) \cdot S \cdot |u(t)|}{\gamma - 1} dt \qquad eq.(15)$$

$$dE_{translational} = \frac{1}{2} \rho(t) \cdot S \cdot |u(t)|^3 dt \qquad eq.(16)$$

Integration of equation 14-16 allows for the incident energy and remaining energy to be calculated using equations 17 and 18 (Wang & Shukla, 2010). Subscripts 1 and 2 denote incident and reflected respectively.

$$E_{incident} = \int S \cdot |u_1(t)| \left[\frac{\gamma \cdot p_1(t)}{\gamma - 1} + \frac{1}{2} \rho_1(t) \cdot |u_1(t)|^2 \right] dt \qquad eq.(17)$$

$$E_{incident} = \int S \cdot |u_2(t)| \left[\frac{\gamma \cdot p_2(t)}{\gamma - 1} + \frac{1}{2} \rho_2(t) \cdot |u_2(t)|^2 \right] dt \qquad eq.(18)$$

During experimentation the cross sectional area of the shock tube is known and the pressure profile are captured using transducers. However, the velocities of the gas particles, density, and sound speed are not known and therefore must be calculated. A polytropic gas whose compression or expansion can be described by the polytropic process. The physical parameters of the gas can be defined by equations 19-22.

$$\rho \tau = 1 \qquad\qquad eq.(19)$$

$$e = \frac{1}{\gamma - 1} p \tau \qquad\qquad eq.(20)$$

$$\rho c^2 = \gamma p \qquad\qquad eq.(21)$$

$$p = A \rho^\gamma \qquad\qquad eq.(22)$$

Where, A corresponds to a reversible process of the initial state of the gas during an adiabatic process. The initial pressure jump caused by the shock wave can be obtained from laws of physics equations (conservation of mass, momentum, and energy) and the particle velocity relative to the planar shock front, v. Combining equation 19 with conservation of mass and momentum yield the following relationships.

$$(\tau_1 + \tau_0)(p_1 - p_0) = v_0^2 - v_1^2 \qquad\qquad eq.(23)$$

$$\frac{(p_0 - p_1)}{(\tau_0 - \tau_1)} = \rho_0 v_0 = \rho_1 v_1 \qquad\qquad eq.(24)$$

$$\frac{(p_1 - p_0)}{(\rho_1 - \rho_0)} = v_0 v_1 \qquad\qquad eq.(25)$$

From resulting equation 23 and conservation of energy the Hugoniot relationship can be obtained (eq. (26)).

$$H(\tau_1, p) = e_1 - e_0 + \frac{1}{2}(\tau_1 - \tau_0)(p_1 - p_0) = 0 \qquad eq.(26)$$

The specific energy e and specific volume τ are unable to be measured during the shock wave loading of the samples and as a result the Hugoniot relationship must be modified with parameters that can be obtained during experimentation. Modification of equation 26 by substitution of equation 20 allows the following relationship to be derived.

$$\frac{p}{p} = \frac{\tau_0 - \mu^2 \tau_1}{\tau_1 - \mu^2 \tau_0} \qquad eq.(27)$$

Combining equation 21, 24, and 27 yields the following relationship, where $\mu^2 = (\gamma - 1)/(\gamma + 1)$ and M is the Mach number.

$$\frac{p}{p} = (1 + \mu^2)M_0^2 - \mu^2 \quad Eq.(28(A)) \qquad or \qquad \frac{p}{p} = (1 + \mu^2)M_1^2 - \mu^2 \qquad eq.(28(B))$$

Combining equations 21, 25, and conservation of energy yield a relationships between adiabatic exponent of the gas, velocity of the shock fronts (U_+ and U_-), particle velocities and sound speed.

$$(1 - \mu^2)(U_+ - u_0)^2 - (u_1 - u_o)(U_+ - u_0) = (1 - \mu^2)c_0^2 \qquad eq.(29(A))$$

$$(1 - \mu^2)(U_+ - u_1)^2 - (u_0 - u_1)(U_+ - u_1) = (1 - \mu^2)c_1^2 \qquad eq.(29(B))$$

From the above equations particle velocity, sound speed, and density of the different section during the shock loading event can be obtained.

The deformation energy of the sample can be obtained using high speed camera images to obtain the sample deflection and the pressure profile for the reflected wave which cause the panel to deform. Combination of the two allows for the load-displacement data to be obtained and integrated to find the deformation energy of the sample. The deflection of the panel can be treated as a beam bending deflection is the displacement through the width of the sample are the same

(Wang & Shukla, 2010). The shape of the front surface deflection pattern can be obtained using curve fitting methods and from the resulting curve fit equation the displacement at any point along the front surface can be obtained. As previously stated the deformation energy can be obtained from integration of the pressure-deflection curve at all points within the loading area (eq. (30)).

$$E_{deformation} = \oint_{S_{shock\ tube}} \left(\int p_2(t) dl_{deformation} \right) dS \qquad eq.(30)$$

CHAPTER III: MATERIALS AND EXPERIMENTAL SETUP

3.1 Material Description

3.1.1 Metallic Foam

Duocel metallic foams are porous foams with an interconnected framework (solid struts) of a base metal material. The framework resembles a pattern formed by bubbles of various size that form a 3D structure with multi facet that form a polyhedral of 14 sides (tetrakaidecahedron, Fig. 14). After solidification of the metallic foam thin membranes between the metal struts are removed through a reticulation process (ERG Materials and Aerospace, 2020). This process results in an open cell, porous, and isotropic metallic foam. This foam is more ideal for mitigation of dynamic events in all direction versus corrugated or auxetic structures due to its isotropic nature.
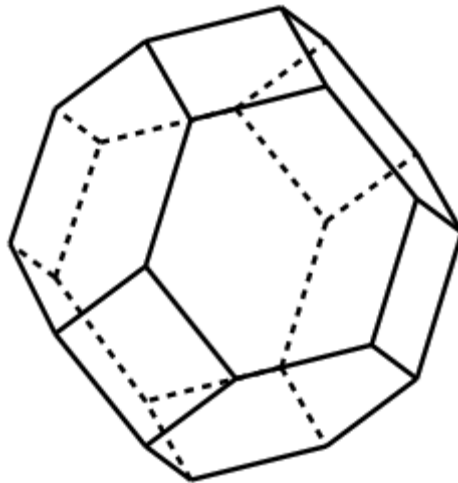
Figure 14. Tetrakaidecahedron Framework (Weaire, 2009)

Metallic foams are characterized by three specifications (pore size, relative density, and base metal) that help to guide the specific application or use. The pore size characterizes how

45

many pores per unit length are found in each metallic foam. Depending on the type of base material typical pores per inch (PPI) can range from 5-40 PPI for metal and 5-100 PPI for carbon and ceramic foams (ERG Materials and Aerospace, 2020). Metallic strut length, cross sectional area, pore diameter, size, and fluid flow through the metal framework are directly relatable to the PPI of the foam. In this study 40 PPI was used for all Duocel metallic foams. While the highest PPI is more restrictive in terms of permeability of a fluid during initial SHPB testing it was observed that the higher PPI metallic foam exhibited the highest plateau strength (Fig. 15). Due to this fact the higher PPI was selected for consideration in this study.
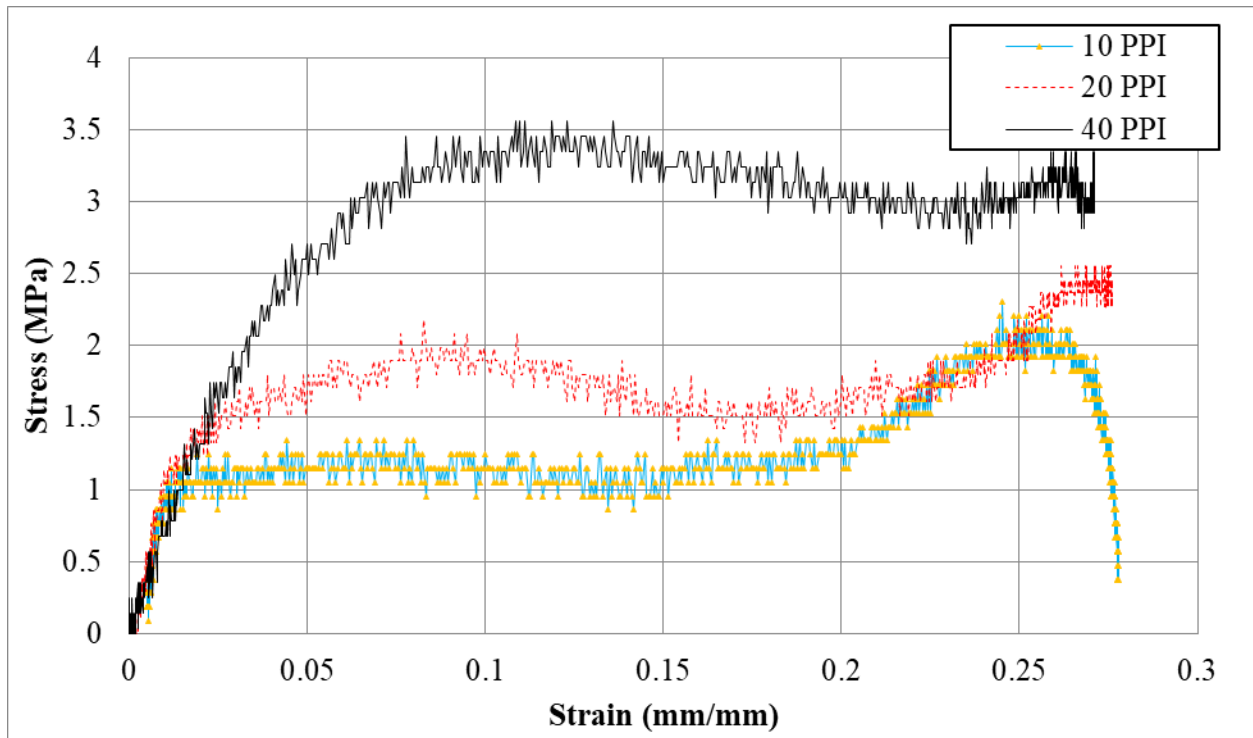
Figure 15. Comparison of Dynamic Stress-Strain for 6101-T6 Aluminum Foam

The relative density of a foam is defined as the ratio of the density of the foam and base metal material (eq. 31). For Duocel foam the relative density can range from 2-15%. The relative density controls the strut cross section shape and actual size.

$$\rho_{RD} = \frac{\rho_{Metal\ Foam}}{\rho_{Base\ Material}} \qquad eq.\,(31)$$

46

The strut structure is the primary driver for the mechanical properties of the metallic foam. As a result, the relative density controls the energy absorption of any component made of these types of foams. The strut cross sectional area of different relative densities can be seen in Figure 16.
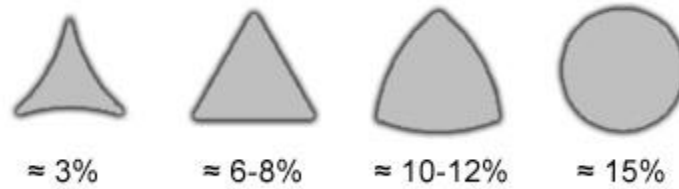
Figure 16. Metallic Framework (Struts) of Difference Relative Densities (ERG Materials and Aerospace, 2020)

The base material used during the metallic foam manufacturing process is melted to a liquid state, foamed, and then reticulated leaving a metal framework made of struts. The metallic struts have no discontinuities within and the overall framework is porous due to the foaming process. The base material used in this process directly dictates the performance and properties of the metallic foam. The combination of pore size, relative density, and base material can be used to tailor the metallic foam for specific applications. Aluminum (6101-T6) metallic foam with relative densities 4-6% and 10-14% were selected for this study due to its low cost and weight.

3.1.2 Foam-iT!™ 3lb Polyurethane Foam

Polyurethane is a class of polymers made from various starting materials. This causes distinctly different chemical compositions of polyurethane. For this study expanding, low density polyurethane foam from Smooth-On were used as an infusion material. The chemical additive in the mixture consist of 4,4' Methylene bis(phenylisocyanate) (MDI), Benzene, 1,1'-methylenebis[4-isocyanato-] homopolymer, and Methylenediphenyl diisocyanate. Combination of the aforementioned chemicals allows for a solid structure of polyurethane to be formed after expansion. Depending on the initial composition of the constituents' components the density of

the resultant foam can be altered. For this study a 48 kg/m^3 (3lb/ft^3) polyurethane foam was used. The idea behind using a lower density foam by comparison to previous studies (Fı′la, et al., 2017), is to minimize the additional weight while simultaneously providing additional resistance to the deformation of the metal framework. The Foam-iT 3 has a volumetric expansion of 18 times the original mix volume. Consideration should be taken during batching procedures since the pot life of the material is 60 seconds, which provides a short duration to infuse the polymer inside of the metallic framework. The additional mass caused by the filler (polyurethane foam) should provide a sufficient resistance to strut deformation during compression and provide additional strength for energy absorption.

3.2 Polymer Infusion Process/Functionally Graded Configurations

3.2.1 Polymer Infusion Process

A simple infusion technique was used during this study for infusing the pure metallic foam samples. This infusion technique was kept simple for one primary factor, the pot life of the polyurethane foam. Once mixed the pot life for Foam-iT 3 (60 sec) is significantly shorter than most polymer resins. This pot life prevents any complex method from being implemented with the available resources. After approximately 1.5-2 minutes the polyurethane foam becomes extremely viscous and cannot be poured into the metallic foam framework. For this reason, the two-part mixture was vigorously mixed for approximately 15-30 seconds and then poured directly into the metallic foam located in a wooden mold (Fig. 17(A)). Also for this reason two personnel are required for the infusion process. Personnel one mixes the resin and continuously pours the mixture into the metallic foam and ensure even distribution of the resin, while the second personnel

further distributed the resin over the entire surface area using a flat scrapping device (Fig. 17(B)). This further ensures that the resin permeates the entire metallic foam.
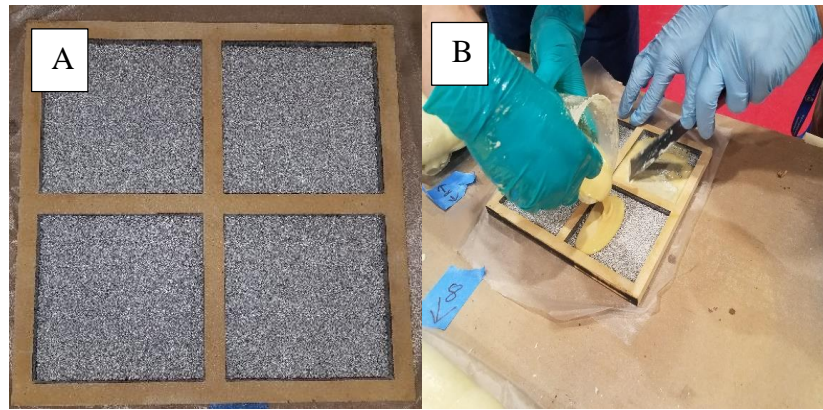
Figure 17. (A) Wooden Molds for Infusion Process, (B) Two Personnel Infusion Technique

The wooden mold prevented expansion in the transverse directions at the edge of each sample panel. This was done help ensure that full infusion (Fig. (18(A)) of the metallic panels was accomplished. Wooden mold cut out sections had consistent dimensions as the metallic foam panels and helped prevent the expanded polymer foam from lifting the panels, which can cause incomplete infusion of the metallic foam (Fig. 18(B)).
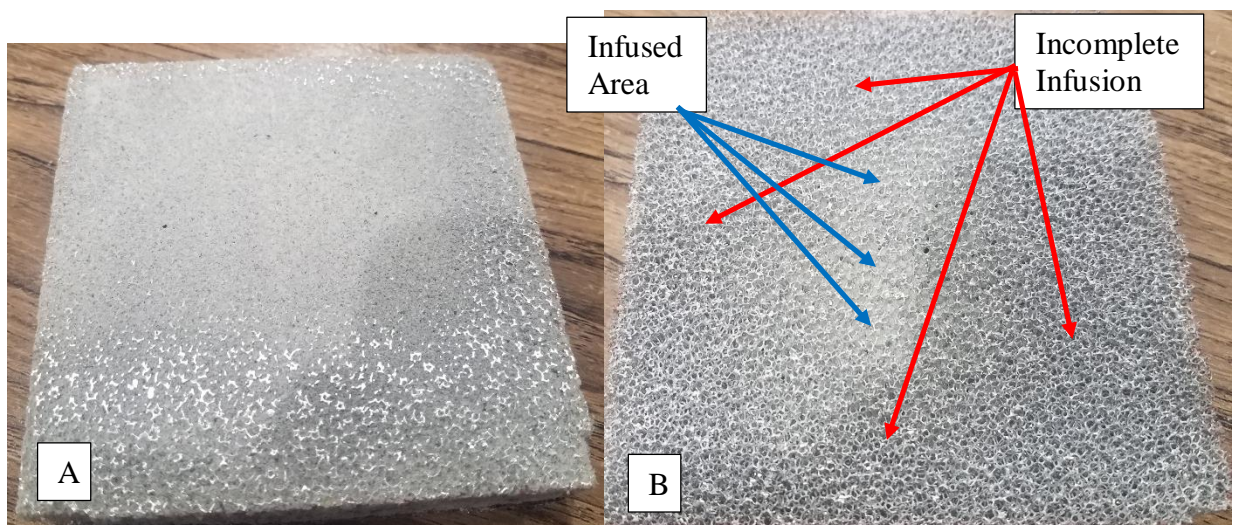
Figure 18. (A) Complete Infusion of Metallic Foam, (B)Incomplete Polymer Infusion of Metallic Foam Panel

Excess polymer resin was used to accomplish complete infusion of and was removed after 2-hour cure time of polyurethane foam. This caused a large amount of waste polyurethane foam to be present on each panel (Fig. 19). The excess material was removed initially with a band saw. Care was taken to ensure no damage to the metallic foam was induced during the cutting procedure. After initial removal of polyurethane excess, a surface grinder was used to reduce the pultrusion of the polymer material to be consistent with the original thickness of the metallic foam panel.

Figure 19. Excess Polyurethane Foam on Composite Panels

3.2.2 Functionally Graded Configurations

The advantages of functionally graded composites has been shown to help improve the energy absorption capabilities of materials in a wide range of applications ((Reyes, 2008), (Li, Zheng, & Yu, 2019), (Liu, Tian, Lu, & Liang, 2014), (Yazici, Wright, Bertin, & Shukla, 2015), (Yang, Ma, Shi, & Yang, 2017), (Sun, Wang, Wang, Xiao, & Li, 2018), (Gardner, Wang, Kumar, & Shukla, 2012)) and can be clearly seen for hazard mitigation. However, most have not tried to take advantages of using a hybrid metallic/polymer foam hybrid core material. By combining the advantages of functionally graded material and the composite response of a metal/polymer composite a more absorptive composite can be designed. This study focuses on the dynamic behavior Duocel metallic foams with and without polymer infusion. Quasi-static and SHPB

samples have no functional gradation (Foam-iT 3, 4-6% RD Duocel, 10-12% RD Duocel, 4-6%/Foam-iT composite, and 10-12%/Foam-iT composites) and only studies the changes due to infusion. Direct impact and low-velocity samples encompass the functionally graded composite with and without infusion, but without aluminum face sheets. The remaining experiment (blast loading) samples have the same functional gradation and infusion as direct impact and low velocity samples but have an aluminum face sheets.

Mechanical properties of the material were varied thorough the thickness of the core material by varying the relative density of the metallic foams. Two relative densities of metallic foams from Duocel (4-6% and 10-12% relative densities) have been selected for characterization. Comparison were made between panels of closed-cell aluminum foams (control panels used for military application, Cymat), non-polymer infused porous open-cell aluminum foams, and polymer infused porous open-cell aluminum foams. Figures 20 and 21 show the configuration for the low-velocity, direct impact, and blast panels control group, non-polymer infused, and polymer infused panels.
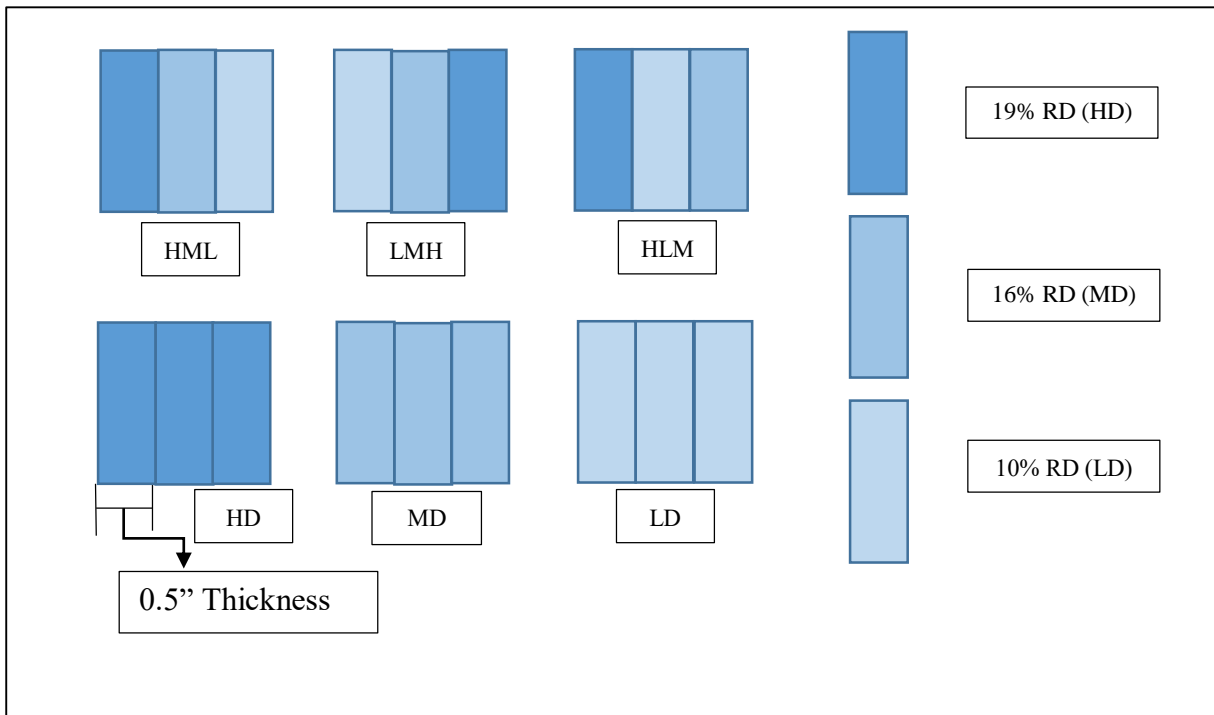
Figure 20. Sandwich Composite Core Configuration - Closed Cell Aluminum Foam Sandwich Composite Configuration for Control Group Using Three Relative Densities from Cymat Metallic Foams
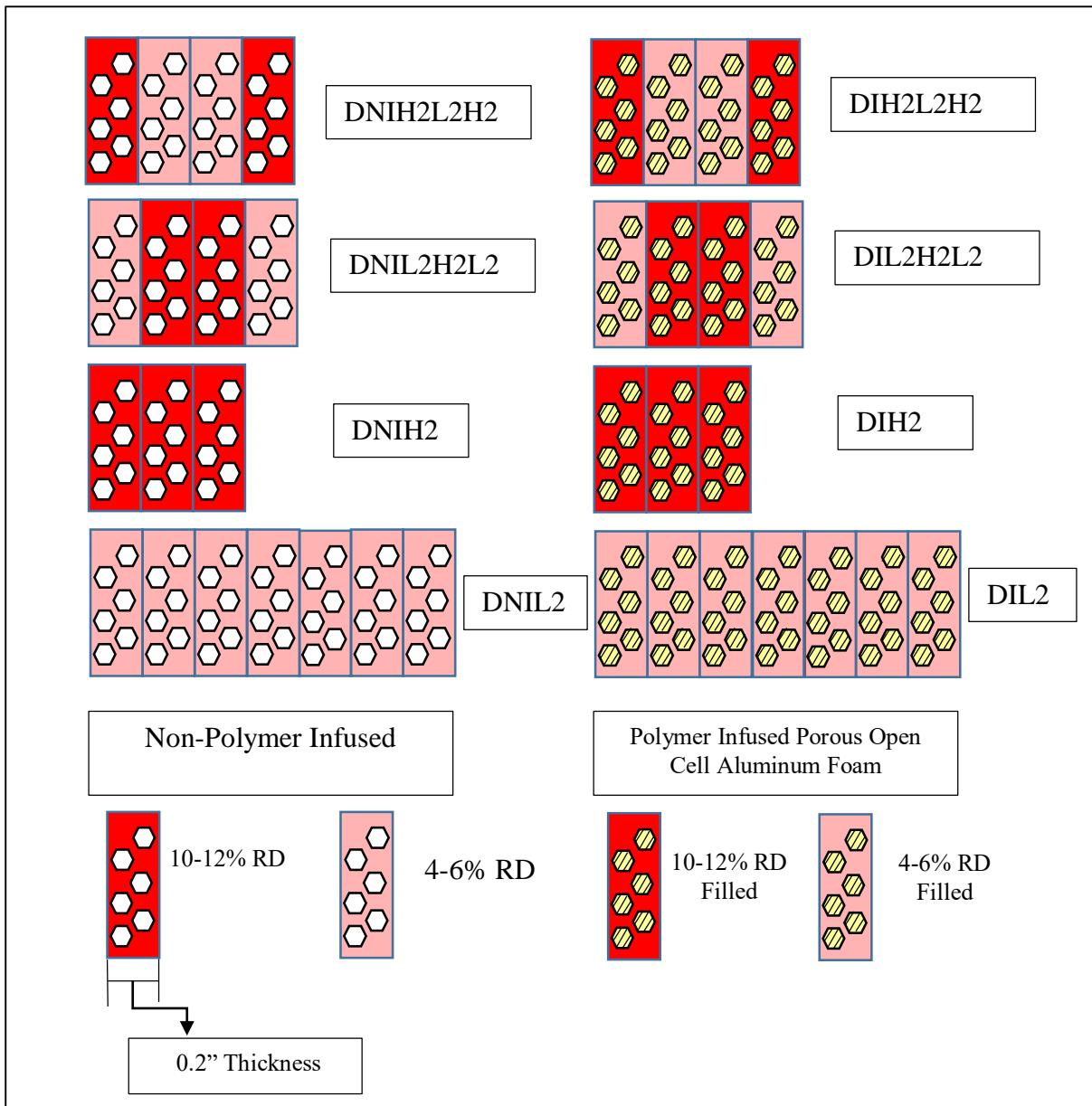
Figure 21. Sandwich Composite Core Configuration for Open Cell Non-Infused and Infused Aluminum Foam Sandwich Composite Configuration Using Two Relative Densities

As previously stated aluminum face sheets (1.27 mm), were only used during blast loading experiments. Samples were bonded using industrial grade 3M High Strength 90 Adhesive between each layer of the functionally graded structures. This bonding agent was selected due to its ability to bond various material as well as its' bonding strength. Weights were placed on top of bonded panels to ensure excellent adhesion between each layer of the panels.

3.3 Quasi-Static Experimental Setup

Quasi-static compression was conducted using an 810 MTS system (Fig. 22(A)). Experimentation was conducted using displacement control to achieve a strain-rate of 0.007/s (0.1 mm/s displacement rate). Fifteen samples of each base material was tested in quasi-static compression. A 5-kip load cell was used to obtain the applied force on the sample. Self-aligning compression platens (Fig. 22(B)) were used to prevent off axis compression during experimentation. Platens were aligned before each test by compressing both platens together with 2200 N. force. This ensured that the alignment of the platens was parallel to each other. Data was acquired at an acquisition rate of 2 Hz to remain uniform to camera acquisition rate.
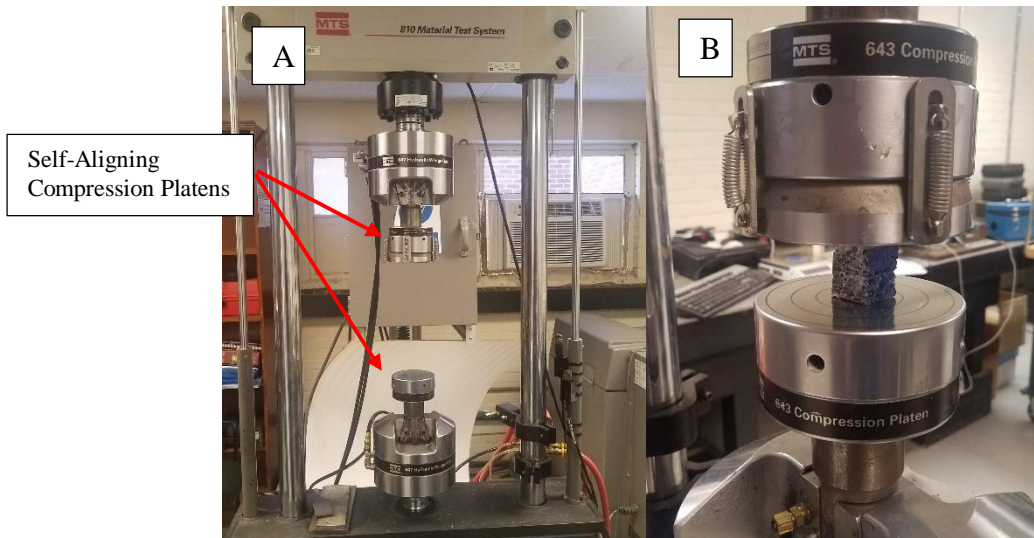
Figure 22. (A) 810 MTS Testing System (B), 643 Self Aligning Compression Fixture

Samples with dimensions 12.7 mm^3 (Fig 23) were used during compression testing. Cube samples were cut from a 101.6 mm x 101.6 mm x 12.7 mm plate of corresponding base material (Foam-it™ 3, 4-6% RD, and 10-12% RD) or composite material (4-6%/Foam-it and 10-12%/Foam-iT™). Dimensions used during compression testing were used to maintain consistency

when comparing quasi-static and SHPB dynamic compression results, and ensure that now size

affects or dissimilar failure mechanism were present.

Figure 23. Quasi-Static Compression and Split Hopkinson Pressure Bar Metallic Foam Samples

Digital image correlation setup was used to obtain uniaxial sample strain during

compression. A mvBlueFox 3-2, 2.4 Mpixel USB camera (Fig. 24) was used to capture uniaxial

specimen strain. Strain measurements were made on the flat end of compression platens using

ProAnalyst DIC software (Xcitex, Woburn, MA USA).

Figure 24. mvBlueFox 3-2 2.4 MPixel USB Camera

Line tracking was used to obtain XY coordinates for platen locations and corresponding strain was

calculated from initial length when top platen contacted the top of the sample surface. This

tracking technique reduced/minimized flickering typical for 2D DIC tracking. The line tracking

technique utilizes a binary image filter to process images into black and white (Threshold Binary,

Fig. 25(A) using a gray scale threshold that tracks the location of a transition between white/black or vice versa. This allow for smoother tracking of bar end locations due to the high contrast of the platen and background image. Platen tracking locations was obtained using a 10-15 pixel average location. In essence the threshold of where the DIC software obtains the white/black transition point must be at least 10-15 pixels wide for it to be considered the transition zone. This minimizes any effects of pixel flickering near the transition location, caused by the grey scale threshold binary filter. Tracked XY coordinates (Fig. 25(B)) for each platen end is exported and used to calculate global strain for each sample.
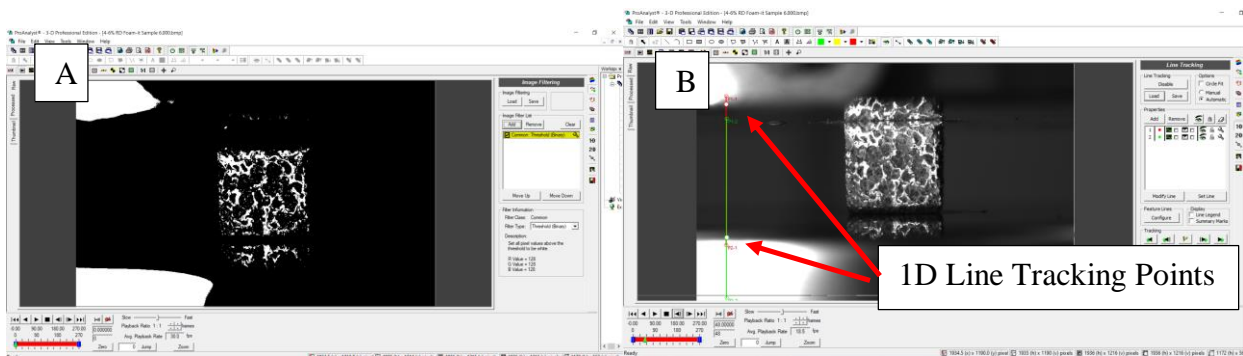
Figure 25. (A) Threshold Binary Image Filter (Black and White), (B) ProAnalyst(Xcitex) Digital Image Correlation 1D Line Tracking

3.4 Low-Velocity Experimental Setup

Low velocity experimentation was conducted using a CEAST 9450 low velocity impact machine, shown in Figure 26. The low velocity impact system is equipped with a velocity sensor, clamping fixture, and data acquisition system monitoring force output from strain gauged load cell.

Figure 26. Instron CEAST 9450 Low Velocity Impact Machine

ASTM 3763-18 (ASTM Standard, 2018) was used due to no suitable alternative method for testing impact resistance of metallic foam/metallic foam polymer composites. Low velocity samples for Duocel foams were 101.6 mm x 101.6 mm and 600 mm x 600 mm plates for Cymat. Impact velocity of 2.8 m/s and impact energy of 120 J was used to subject samples to punch shear loading with a 20 mm diameter steel hemispherical tup for Duocel metallic foam and Duocel/polymer composites. Cymat functionally graded and non-functionally graded samples were tested at an impact velocity of 6.3 m/s and impact energy of 600 J, with same size indenter tip. Impact velocity was monitored from a flag with known gap dimensions that obscures a laser at two points. Impact velocity slowdown was maintained between 5-20% to ensure samples were not overloaded as per ASTM 3763-18. Load-displacement data was captured at a data acquisition rate of 1 MHz with a 1400Hz Butterworth low pass filter.

A clamping fixture was used to stabilizes the samples during impact. The fixture was made from a high strength steel tubing with a 76 mm diameter hole for sample impact area (Fig 27). The clamping pressure used for Duocel metallic foam and Duocel/polymer composite was set to 300

kPa and 600 kPa for Cymat configurations. Clamping pressure was set to these levels to prevent premature failure in samples due to over clamping.
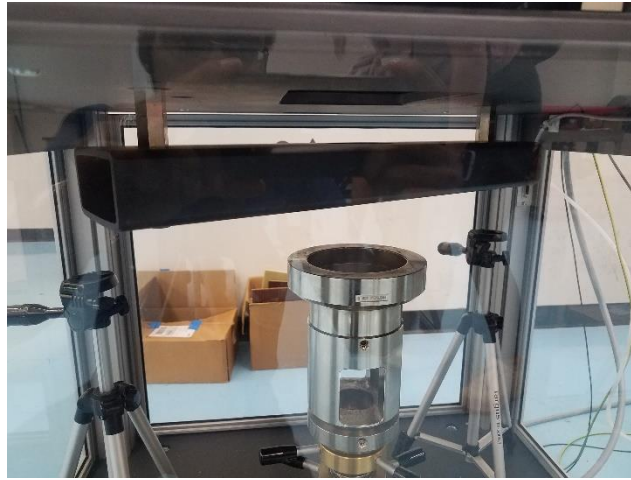
Figure 27. Low Velocity Clamping Fixture

3.5 Direct Impact Experimental Setup

Direct impact is a method of testing material at intermediate strain rates (100/s-1000/s). The current direct impact setup uses several components to apply compression to the surface of a sample. An aluminum (7075-T6) striker with diameter 37.7 mm, length 101.6 mm, and mass 320 grams was used to impact functional graded metallic foam and metallic/polymer foam composite previously shown in Figure 21 at various velocities. Materials configurations made with Cymat were not tested in this method. The reason behind this omission is the size of the void present in Cymat are approximately $1/3$ to $1/4$ of the diameter of the impact striker, which is smaller than the necessary size for valid results (Gibson & Ashby, 1997). Impact velocity (8 m/s – 30 m/s) was adjusted for each configuration until consistent strain-rate was achieved. While the impact energy is not consistent the strain-rate caused by the impact striker for each sample type was approximately 500/s. This allowed for comparable dynamic compressive behavior of the samples.

Samples were placed on a platen connected to a 9352A Force Lin High Impedance Load Cell, with 44.48 kN load capacity. Sample thickness for 3-layer, 4-layer, and 7-layer configuration were approximately 15.24 mm, 20.32 mm, and 35.56 mm respectively. Sample dimensions were cut to ensure a 1:1 aspect ratio (Length/Thickness) with the exception of the lowest density seven-layer configuration. These samples were cut with a 1.5 aspect ratio due to the cross sectional area of the impact striker (35.56 mm) and the overall thickness of the panels. The load cell is design with a quartz crystal sensor that is applicable for quasi-static and dynamic loading and is connected to a pneumatic stop stand. The load cell is connected to a 5165AK4 Charge Amplifier/Conditioning system with 24-bit resolution, and can output analog signals to remote data acquisition systems. A PicoScope with 16-bit resolution was used to acquire the analog signal at an acquisition rate of 8.92 MHz. This was done to better synchronize high speed photography with load data from the load cell by having a consistent trigger point and enough time resolution to obtain the exact moment of impact. A schematic of the direct impact setup can be seen in Figure 28.
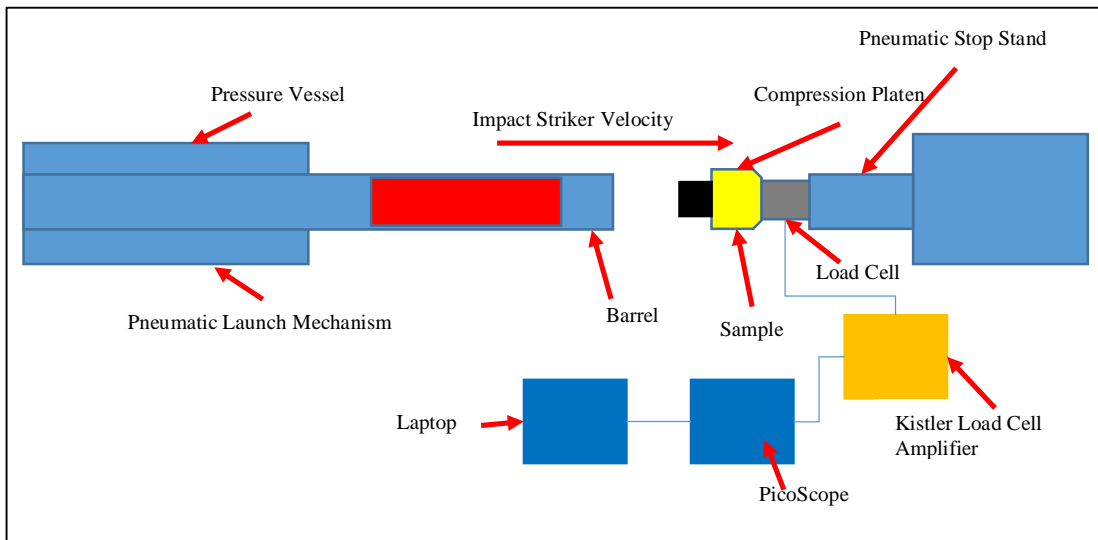
Figure 28. Direct Impact Setup Schematic

A digital image correlation setup was used to capture high speed photographs using a Shimadzu HPV2 high speed camera for each test to obtain sample strain and strain-rate during dynamic compression. LED lighting was used to illuminate the sample surface and impact striker. Digital image correlation setup and load cell acquisition were trigger from the rising edge of densification region of load-time data. This allowed the buffer feature for the camera and data acquisition system to be used in unison with the LED lighting to ensure capture of the compression event. High speed photographs were taken at a frame rate of 32 µs/frame, which allowed 30-55 frames (0.92 ms – 1.76 ms) to be captured depending on the sample thickness. After acquisition of high speed photograph ProAnalyst was used to capture sample strain at the moment of impact until complete compression using 1-D Line Tracking (Fig. 29).
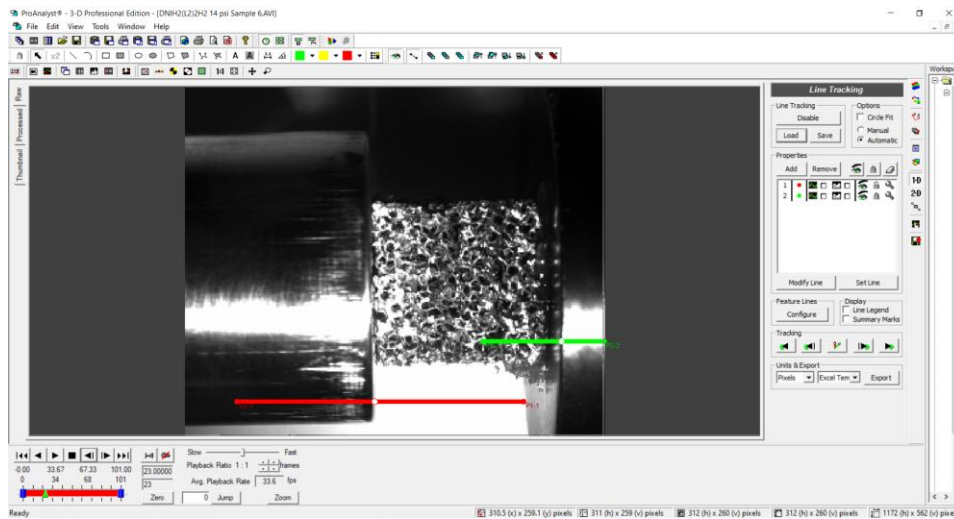
Figure 29. Digital Image Correlation of Direct Impact Samples Using 1-D Line Tracking

3.6 Split Hopkinson Pressure Bar Experimental Setup

A SHPB system located at the University of Mississippi Blast and Impact Dynamics Laboratory was used to test the dynamic performance of base materials of metallic foam and metallic/polymer foam composites (Fig. 12). The SHPB setup consists of two 3.66 m long 7075 aluminums (incident and transmission) bars with 19 mm diameter, and an impact striker of 457

mm was used to obtain high strain-rate dynamic compressive response of Foam-iT 3, metallic foam, and metallic/polymer foam composites with nominal dimensions of 12.7 mm³. Strain gauges with 350 Ω resistance (CEA-06-250UW0350) were mounted at the midpoint of each 3.66 m bar in a quarter Wheatstone bridge configuration in the axial direction, and were used to monitor the incident, reflected, and transmission wave during high strain-rate compression. A Vishay 2310B Signal Conditioning Amplifier was used to provide 15-volt excitation to the Wheatstone bridge as well as apply a wideband filter to the incoming analog voltage signals. Vishay signal conditioning amplifiers were also used to apply a voltage gain to the signals to achieve a conversion between bar strain and output voltage. A 135x gain and 1350x gain were applied to the incident and transmission bar respectively. The increased gain for the transmission bar was done to increase the visibility of the transmission signal which is often difficult to obtain for low-impedance materials (Chen, Zhang, & Forrestal, 1998). With current acquisition systems used in this study it was not necessary to use a hollow bar which are typically used for low-impedance materials (Chen, Zhang, & Forrestal, 1998). The current setup allowed for a low voltage noise level of the incoming signals (≈12 mV and ≈5 mV for incident and transmission signal respectively). Filtered voltage signals from the incident and transmission bridge were output to a 544D model PicoScope with 15-bit resolution for the set voltage range (±2 V and ±200 mV to ±500 mV for incident and transmission signals respectively). Acquisition rate was set to 25 MHz to ensure sufficient time resolution of voltage signals.

Digital image correlation was used to obtain global compressive strain of SHPB samples using a Shimadzu HPV-2 High speed camera to validate SHPB strain evolution. High speed camera and LED were positioned perpendicular to the sample thickness dimension (Fig. 12). Camera frame rates were set to 4 μs/frame to observe a 408 μs time span, allowing for full

compression event to be captured. High speed camera system was triggered using the data acquisition PicoScope's external trigger system to delay the high speed photography to just before the moment of the compressive stress wave reached the initial sample surface. Resulting high speed videos were post processed using ProAnalyst DIC software (Xcitex, Woburn, MA USA). Similar to quasi-static 1D Line Tracking feature was used to obtain global sample strain by tracking bar end displacements from post processed images. Typical DIC analysis video is shown in Figure 30 for compression samples.
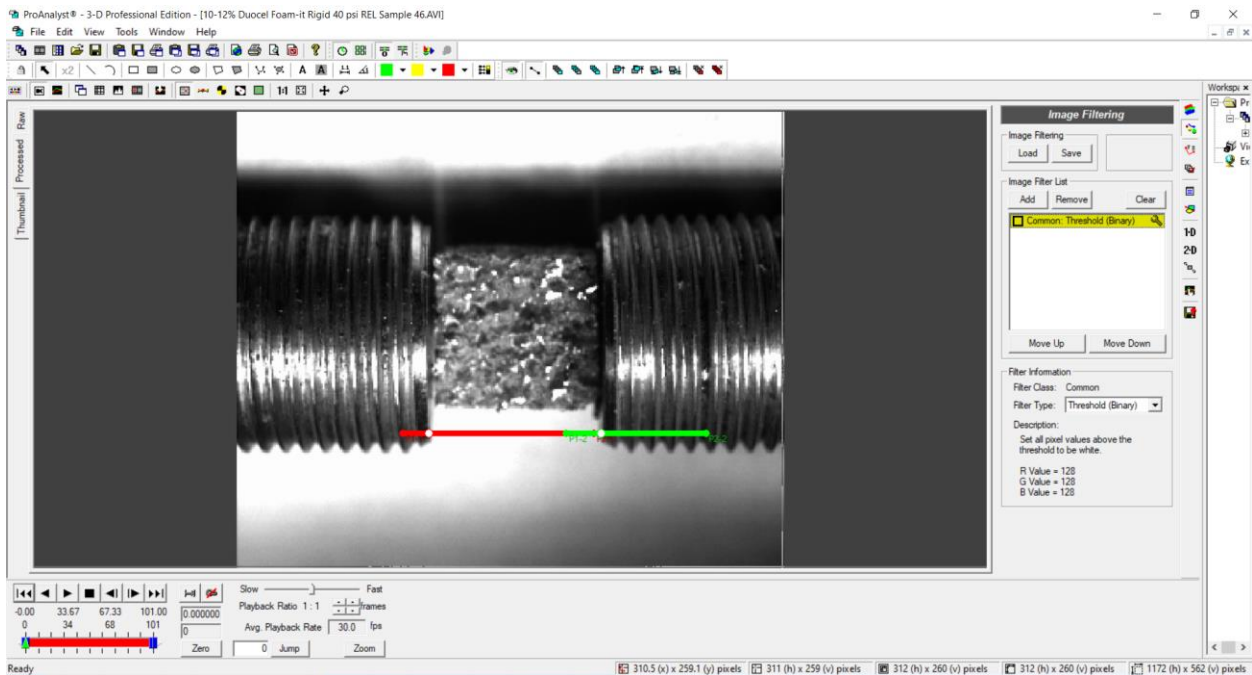
Figure 30. Split Hopkinson Pressure Bar ProAnalyst Digital Image Correlation 1-D Line Tracking

3.7 Shock Tube Experimental Setup

A variable pressure and driver volume section shock tube (Srushti Engineering Innovations PVT. LTD., 2020) equipped with a three high speed valves actuating system was used to subject 101.6 mm x 254 mm simply supported beam samples to shock loading (Fig. 31 and 32). Shock

tube volume for driver section was approximately 2040 cm^3 of nitrogen at a pressure of 3.5 MPa

and 4.2 MPa for Duocel and Cymat samples respectively.

Figure 31. Variable Pressure Shock Tube (Srushti Engineering Innovations PVT. LTD., 2020)
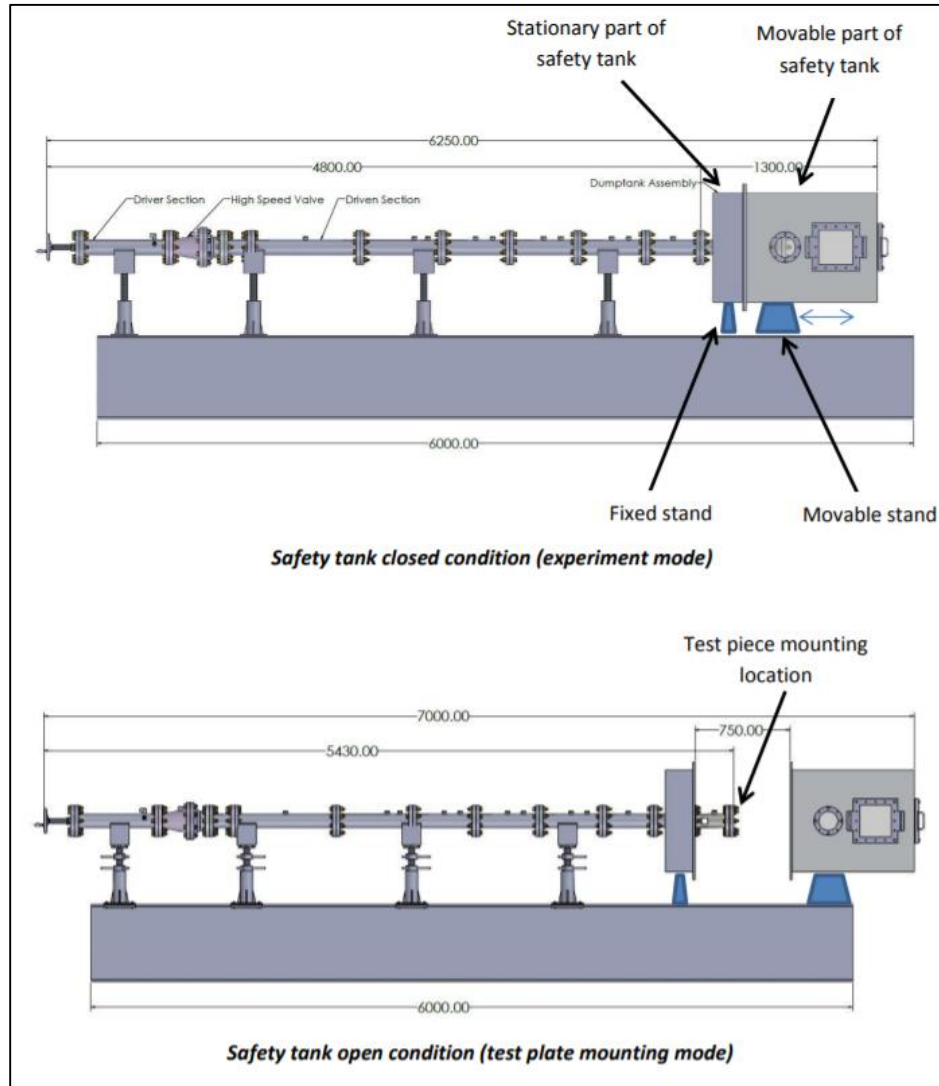
Figure 32. Shock Tube Experimental Setup((Srushti Engineering Innovations PVT. LTD., 2020)

Two Kulite HKS-HP-375-5000SG pressure transducers with 34 MPa maximum capacity were used to capture the incident and reflected shock pressure waves. Transducer were located approximately 125 mm (Fig. 33) apart with the close transducers to the sample being 6 mm away from its front surface. This allowed for reflected pressure from the sample surface to be obtained yielding from the transducer located nearest to the samples surface.
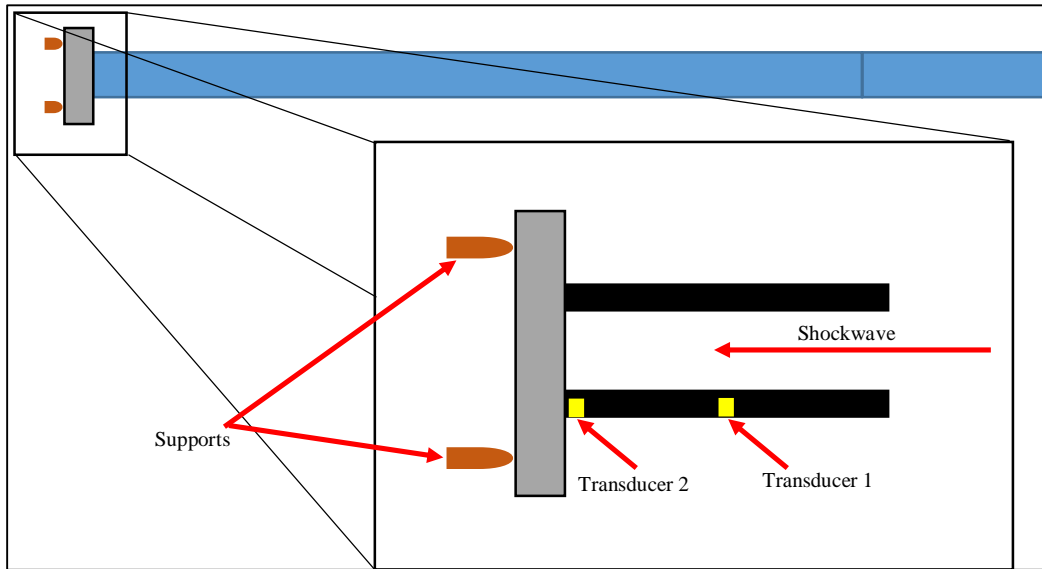
Figure 33. (A) Transducer Location Schematic, (B) Shock Tube Transducer Location

Transducers were connected to a Kulite KSC-2 signal conditioning and amplification systems which maintain signal noise at approximately ±5 mv. Signal pregain and postgain were set to 64x and 4x respectively to increase the signal output to a sufficiently level for synchronizing high speed camera and data acquisition using the reflected pressure wave. Transducer excitation voltage and maximum output voltage were set to 5 volts with a 10 kHz filter.

Beam samples subjected to shock loading were placed on a steel specimen holder located on the bottom bend fixture, which allowed for equal specimen overhang on top and bottom, to provide sufficient resistance. A fixture span of 152.4 mm (Fig. 34) was used and has been shown

to produce reliable and consistent results by other investigators Wang & Shukla (2010) and Wang, Gardner, & Shukla, (2009). Shock tube bend fixture was positioned such that the front surface of specimens was located at the edge of the shock tube barrel without inducing any bending.
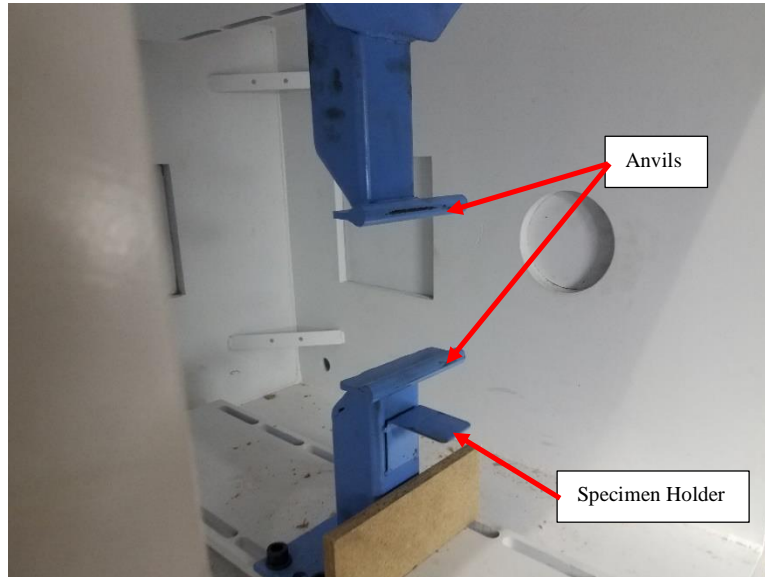
Figure 34. Shock Tube Bend Fixture

A Shimadzu HPV-2 high speed camera was used to obtain images of sample deformation at a rate of 16 μs/frame, allowing for a total capture time of 1.6 ms. Camera resolution is fixed at 312x260 pixel. High speed videos in conjunction with ProAnalyst software was used to obtain center point deflections using 1D line tracking feature (Fig. 35). This information provided a comparative analysis for computational simulations as well information on the compression of each layer during shock loading.
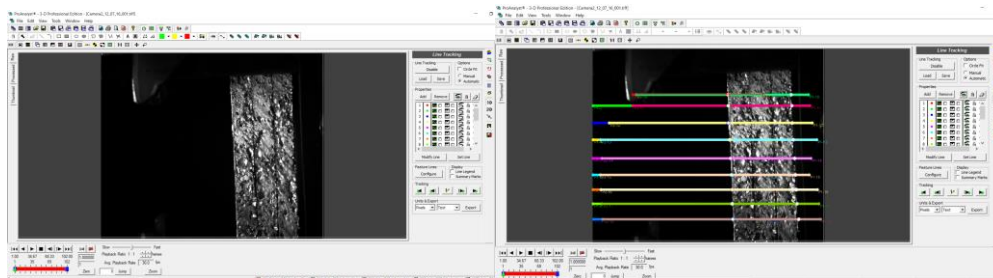
Figure 35. ProAnalyst (Xcitex) Digital Image Correlation Line Tracking Analysis for Shock Tube Beam Samples

CHAPTER IV: QUASI-STATIC TEST RESULTS/DISCUSSION

4.1 Quasi-Static Experimental Results/Discussion

Quasi-static compression was performed to understand the compressive response of the pure Foam-it!™ 3lb rigid polyurethane foam, 4-6% RD, 10-12% RD, 4-6% Al 6101-T6 metallic foam/Foam-it!™ composite, and 10-12% Al 6101-T6 metallic foam/Foam-it!™ composite materials, as well as, to serve as a baseline for comparison with the dynamic compression results. Global strain was obtained using an optical DIC technique previously mentioned in Chapter 3. Figure 36 shows typical compression of metallic foam specimens tested at a strain-rate of 0.007/s.
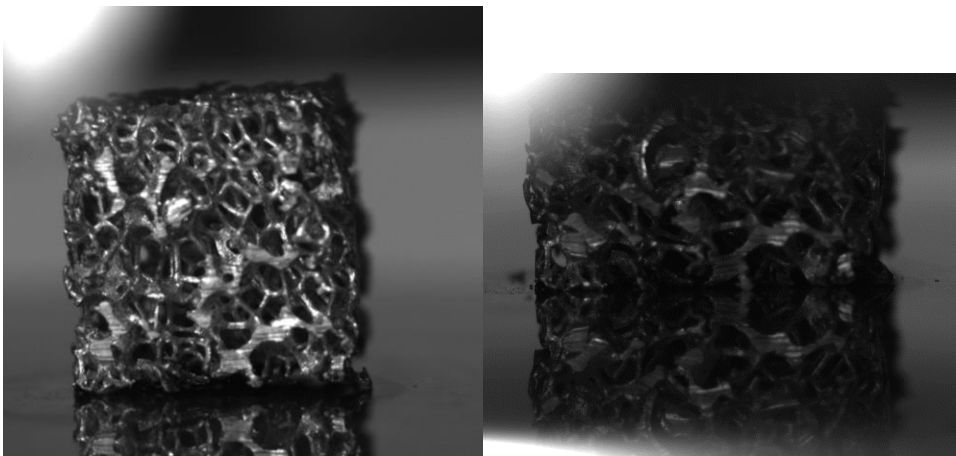
Figure 36. 10-12% Relative Density Quasi-Static Compression of Metallic Foam

Fifteen specimens of each material was tested to obtain the stress-strain relation in a quasi-static compression test for each material (Figure 37-46). Typical scatter of resulting compression testing was observed for all samples in the initial elastic region, plateau region, and densification

region for metallic foams.   Variations in stress-strain response can be attributed to the variation in the metallic framework void size and distribution. Deviation in stress-strain response were less pronounced in metallic/polymer foam composite configuration as compared to base materials due to a more homogenous/isotropic material makeup.
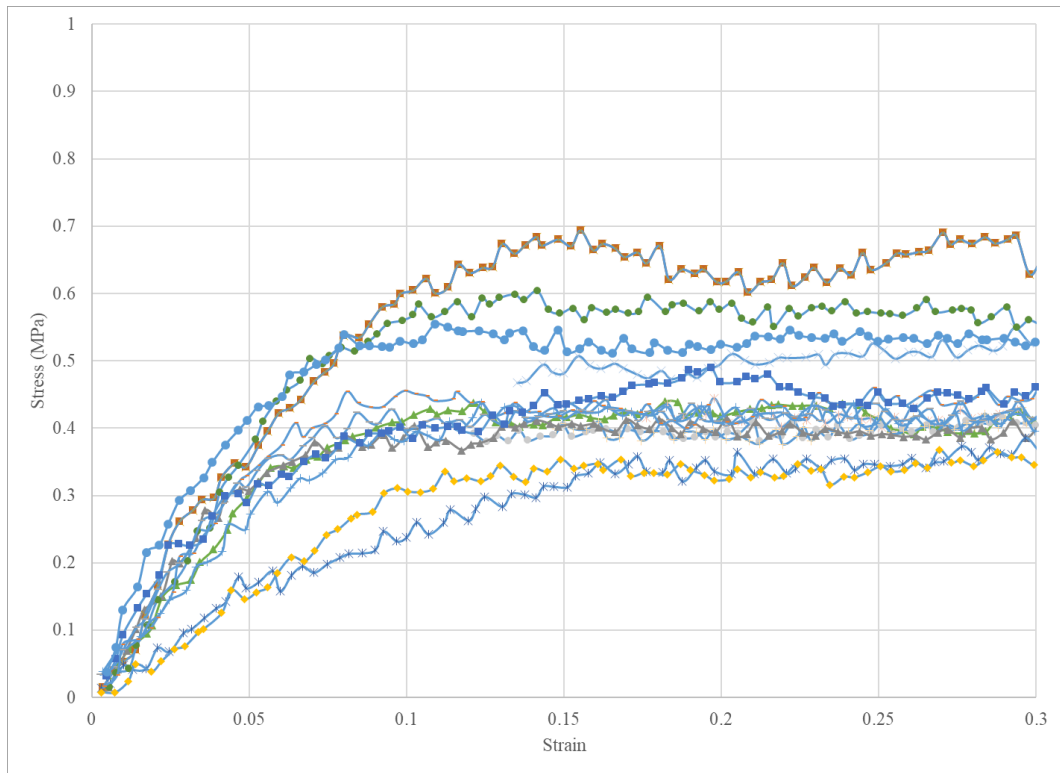
Figure 37. Foam-it 3!™ Stress-Strain Response (0-0.3)
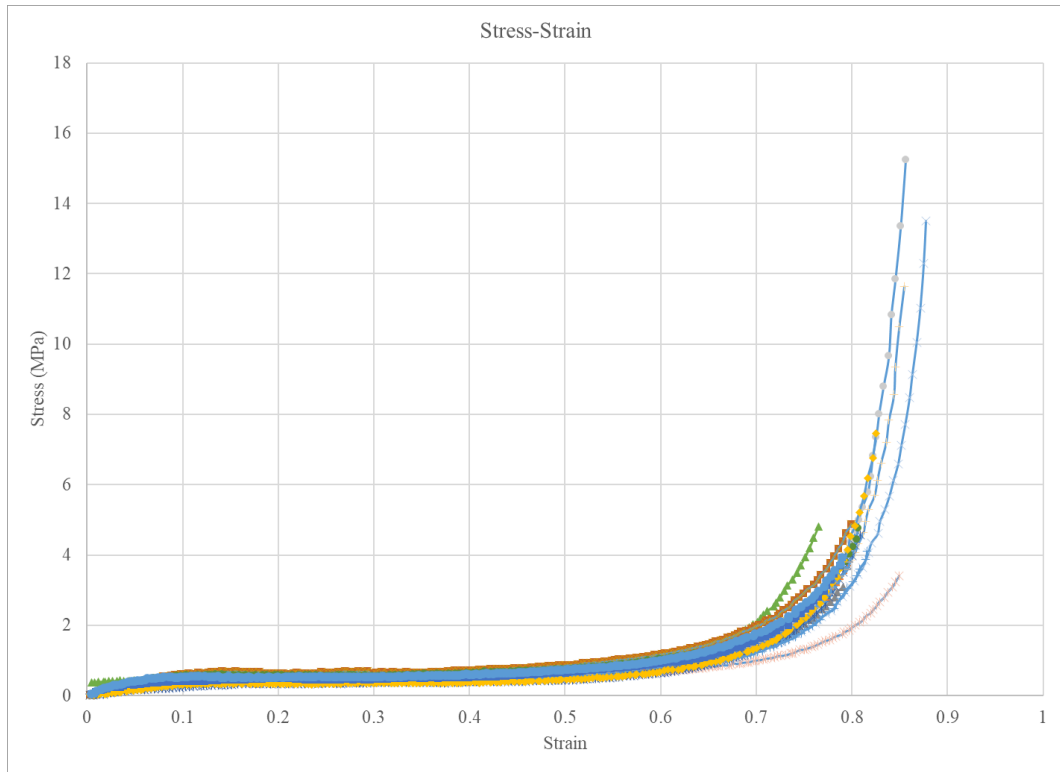
Figure 38. Foam-it 3!™ Quasi-Static Stress-Strain Response (Full)
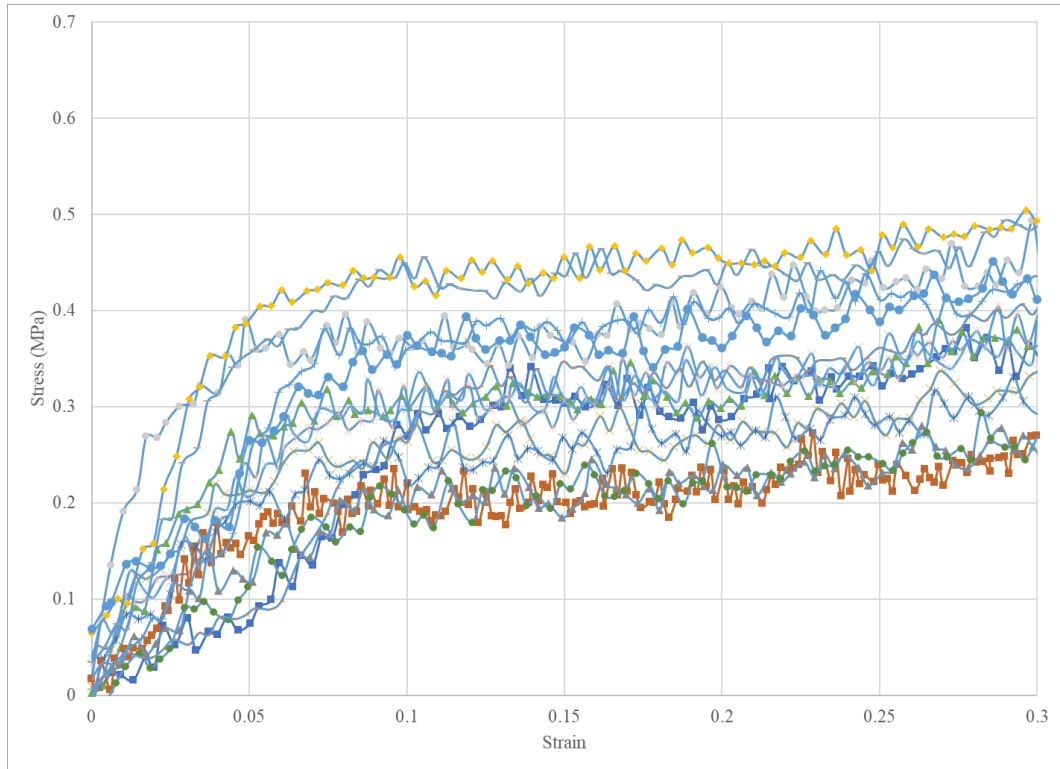
Figure 39. 4-6% Relative Density Duocel Foam Quasi-Static Stress-Strain (0-0.3)
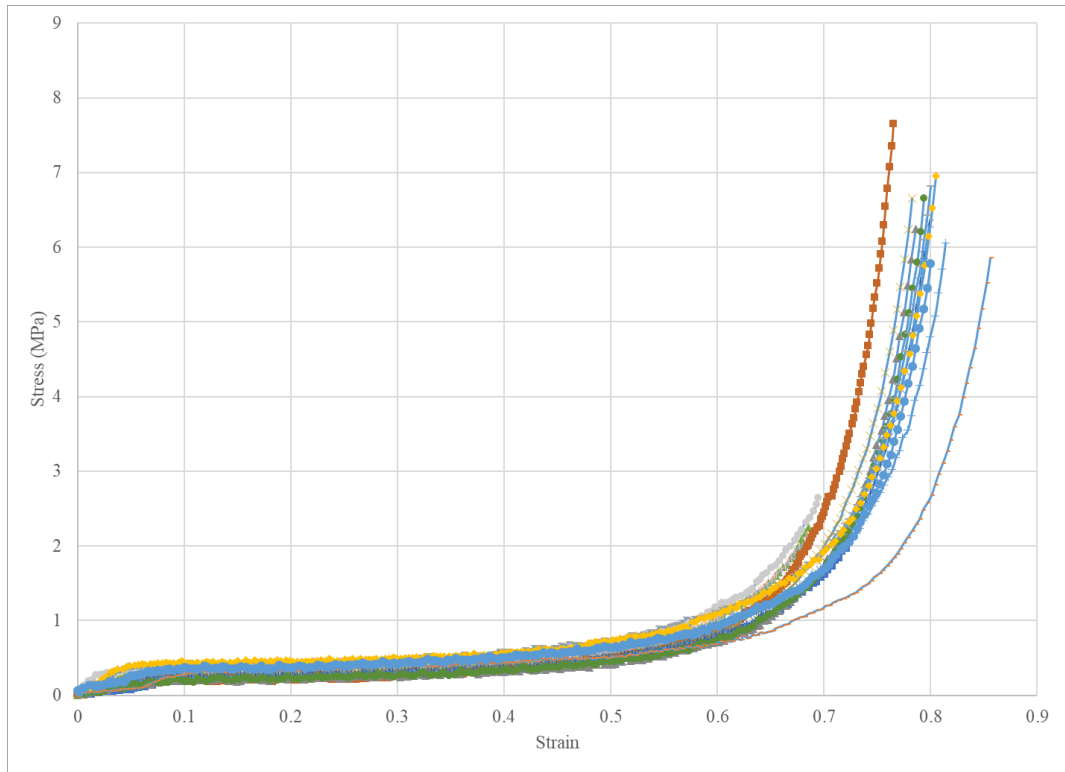
Figure 40. 4-6% Relative Density Duocel Foam Quasi-Static Stress-Strain (Full)
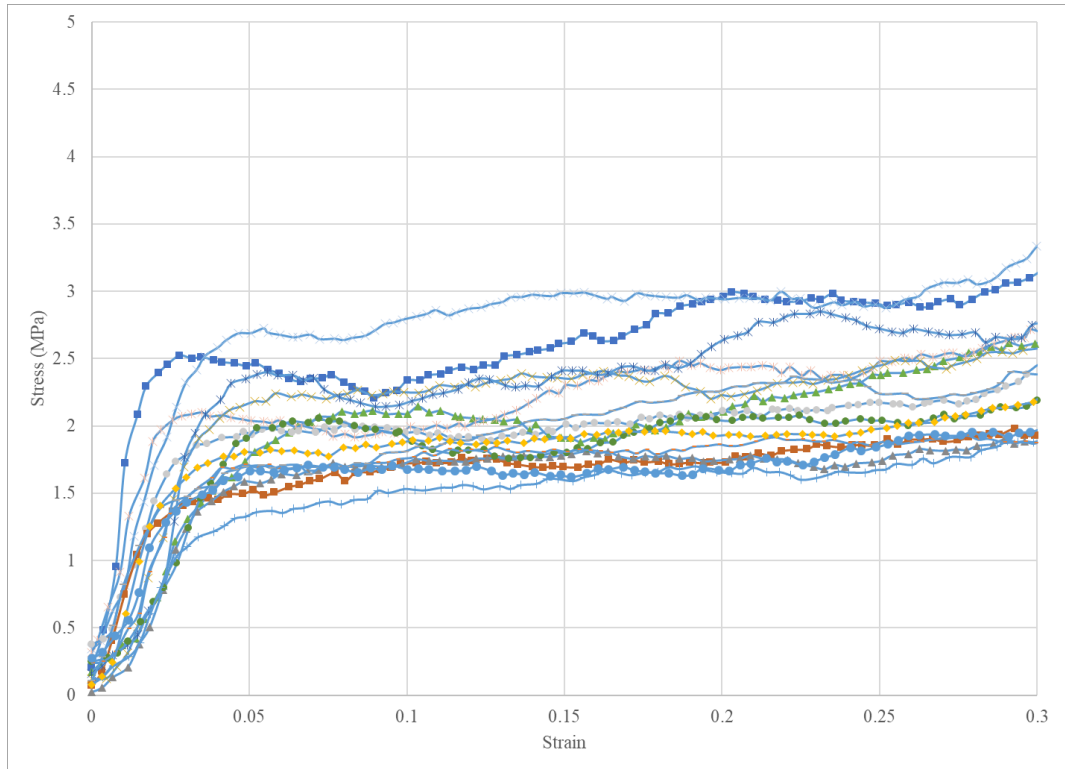
Figure 41. 10-12% Relative Density Duocel Foam Quasi-Static Stress-Strain (0-0.3)

70
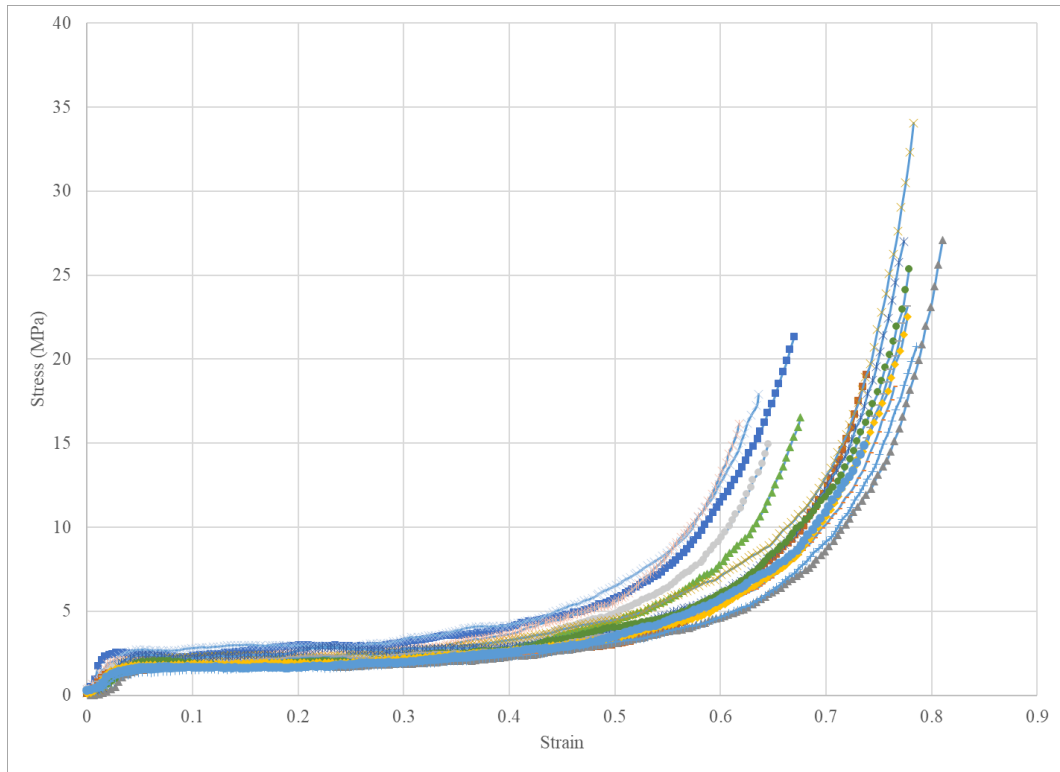
Figure 42. 10-12% Relative Density Duocel Foam Quasi-Static Stress-Strain (Full)
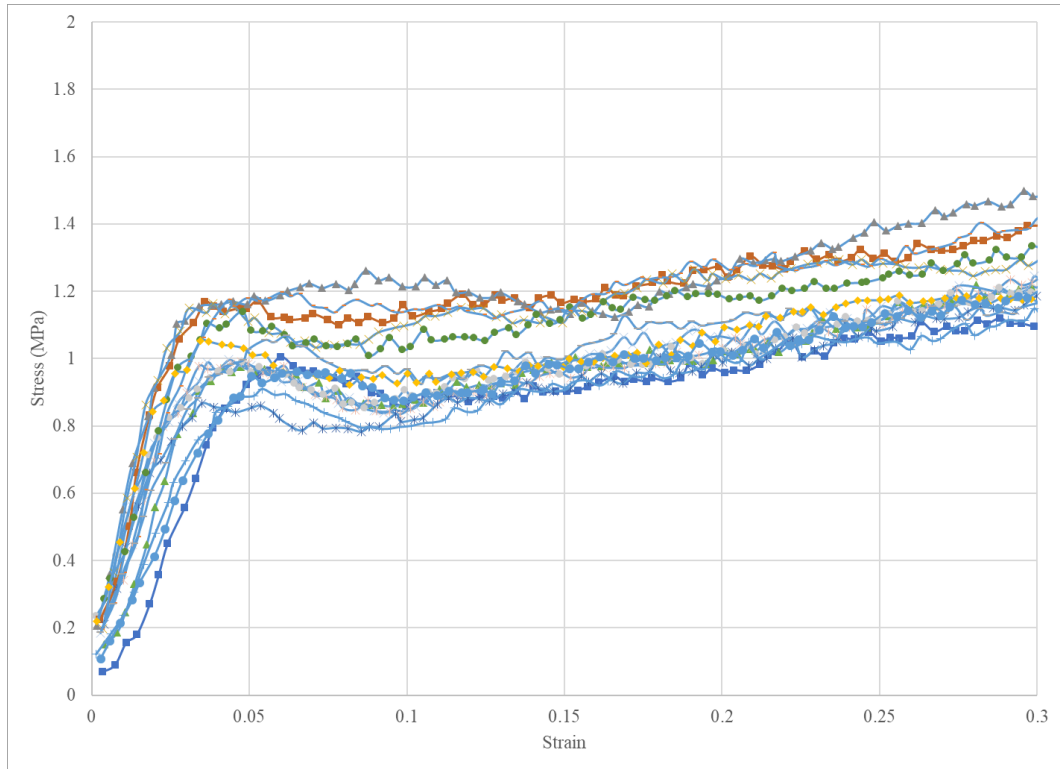
Figure 43. 4-6%/Foam-it!™ Composite Quasi-Static Stress-Strain (0-0.3)

71
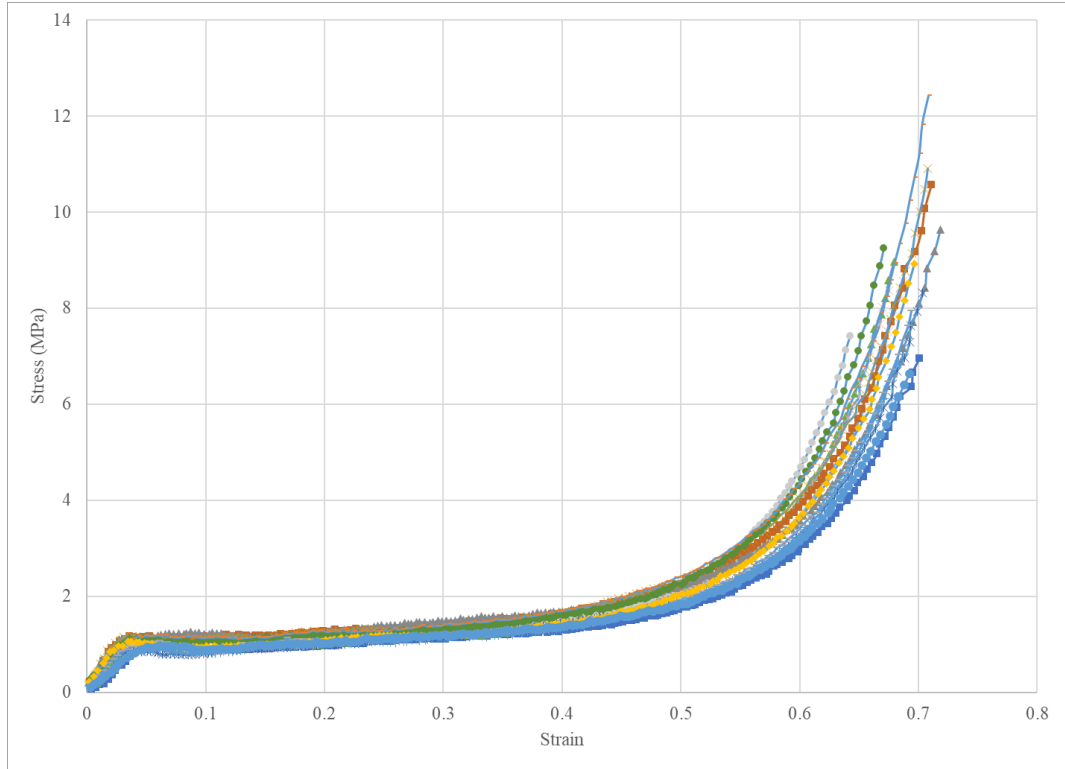
Figure 44. 4-6%/Foam-it!™ Composite Quasi-Static Stress-Strain (Full)
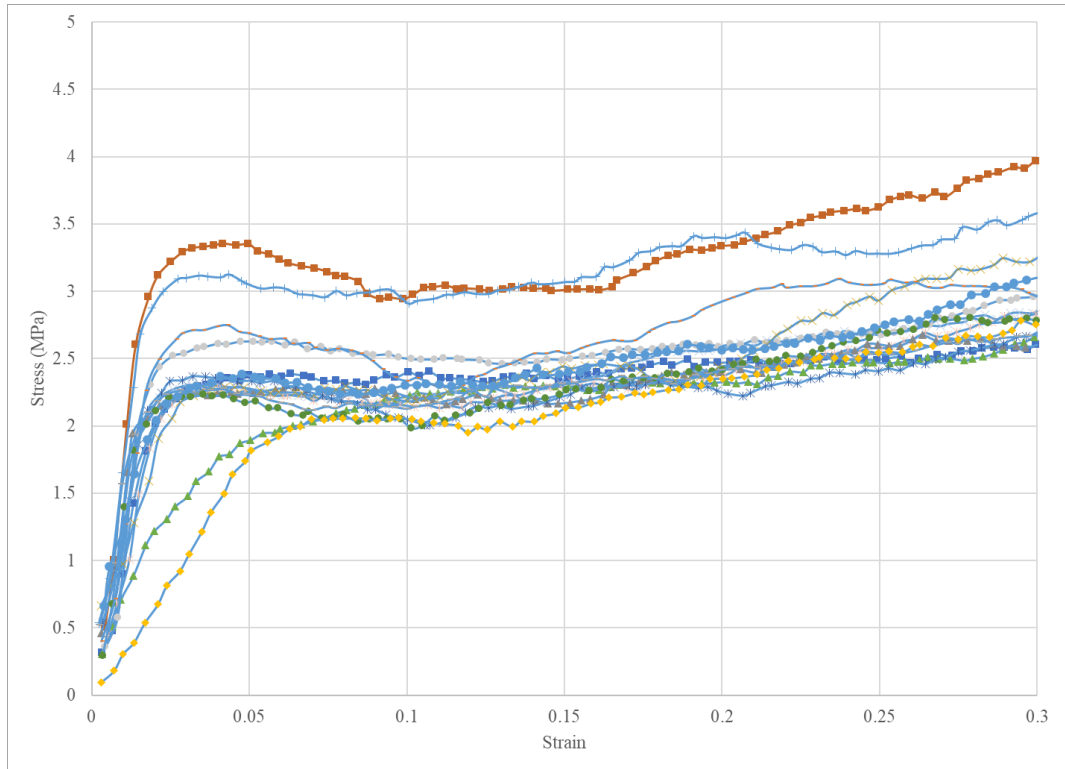
Figure 45. 10-12%/Foam-it!™ Composite Quasi-Static Stress-Strain (0-0.3)

72
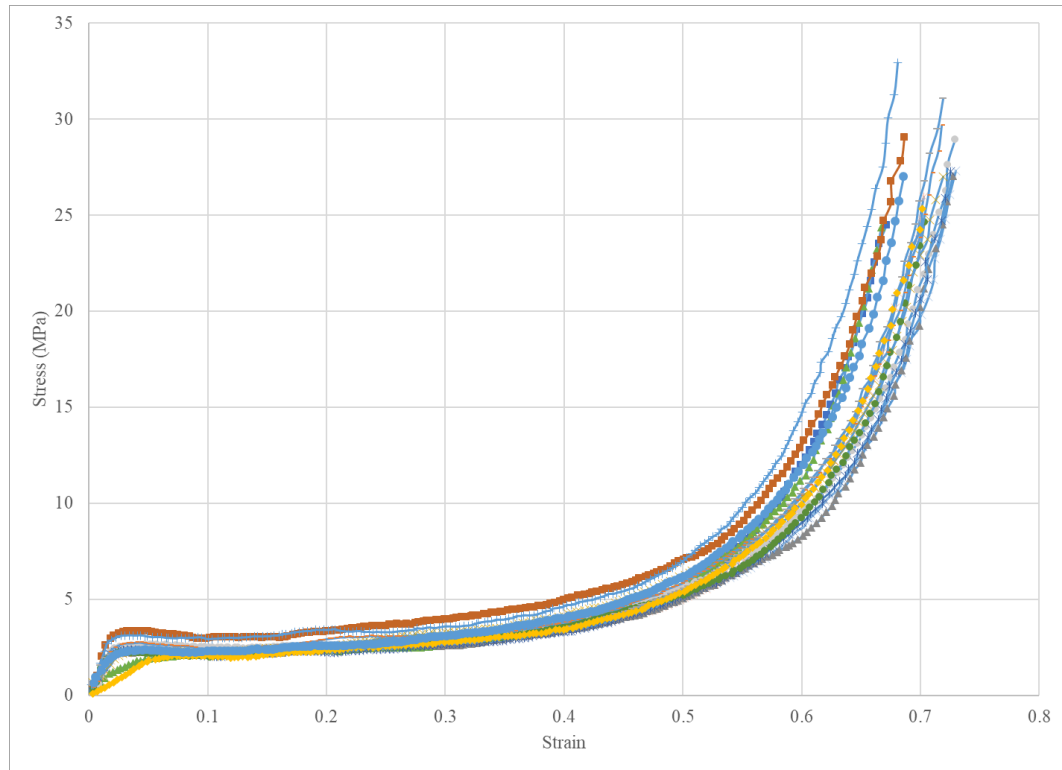
Figure 46. 10-12%/Foam-it!™ Composite Quasi-Static Stress-Strain (Full)

During compressive loading localized deformation zones were observed during quasi-static compression of all specimens, however the number of areas and prominence was greater in the base materials as compared to the infused composite materials. Comparison of quasi-static results for all materials can be seen in Figure 47. Results from compression testing show 10-12% Al 6101-T6 metallic foam/Foam-it!™ composite achieve the highest plateau strength of all materials. It was also observed that the Foam-it!™ 3lb and the 4-6% RD metallic foam had only slight differences in plateau strength. All composites made of metallic foam infused with Foam-it!™ 3lb exhibited a higher plateau strength than non-infused base metallic foam materials. Two factor contribute to the increase in strength; additional material providing strength in the composite in areas that would be void due to high porosity; and polymeric foam resisting metallic framework buckling. Based on rule of mixtures and quasi static average plateau strength (Gibson R. F., 2007) the estimated plateau strength for 4-6%/Foam-it!™, and 10-12% Foam-it!™ composites is 0.436-

0.438 MPa and 0.612-0.646 MPa, respectively. However, from experimental results the average plateau strength for 4-6%/Foam-it!™, and 10-12% Foam-it!™ composites was 1.1 MPa and 2.6 MPa, respectively. The increase strength within the plateau region is due to the aforementioned factors.
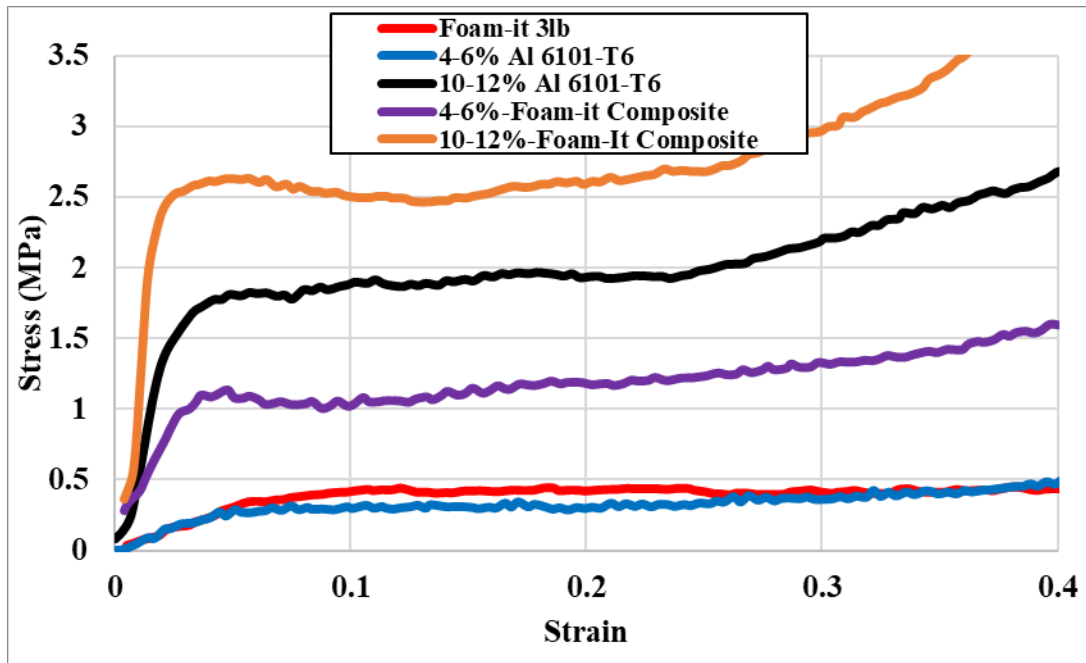
Figure 47. Quasi Static Stress-Strain Response of Foam-it!™ 3lb, 4-6% RD, 10-12% RD, 4-6% Al 6101-T6 metallic foam/Foam-it!™ Composite, and 10-12% Al 6101-T6 metallic foam/Foam-it!™ Composite

Average values for the plateau strength and specific energy of the samples at 10% strain and 20% strain are shown in Figures 48, 49, and 50 respectively. The plateau strength for quasi static samples is defined as the average strength from 10% strain to 30% strain. Increases in plateau strength were seen on both the 4-6% Foam-it!™ infused composite and 10-12% Foam-it!™ infused composite as compared to the based metallic foam. An increase of 233% and 22% in plateau strength was observed when comparing the 4-6% RD to the 4-6% Foam-it!™ infused composite, and 10-12% RD to the 10-12% Foam-it!™ infused composite. The substantial increase in strength of the 4-6% RD is believed to be due to the previously mentioned mechanism of

increased resistance to motion the metallic framework caused to the polyurethane infusion. The increase in strength of the 10-12% RD metallic foam is also likely due to the same mechanism, however with the increased volume of metal present in the 10-12% RD the effects of the polymeric foam are less pronounced. When comparing the specific strength dramatic increases were found when comparing the 4-6% RD to the 4-6% Foam-it!™ composite, but only a marginal increase and slight decrease were found for the 10-12% RD to 10-12% Foam-it!™ composite material at 10% and 20% strain respectively. The increase in specific energy of the 4-6% RD to its composite counterpart is 177%, and is again credited to added resistance to the metal framework. At 20% strain the specific energy increases to 150% of the base 4-6% RD metal foam. A 4.7% increase in specific energy at 10% strain and a negligible decrease (0.65%) in specific energy at 20% strain were observed when comparing the 10-12% RD to the 10-12% Foam-it!™ composite. The decrease in specific energy when comparing the 10-12% RD to the 10-12% Foam-it!™ composite at 20% strain is likely due to damage of the polyurethane foam which inevitably causes a drop in strength and resistance to the metal struts. It is also believed that the response of the metallic foam overshadows any additional resistance of the polymeric foam, and is why increases consistent with 4-6% RD and 4-6% Foam-it!™ composites were not seen in the 10-12% Foam-it!™ composite material. Using a higher density polymeric foam could potentially add enough resistance to the metal framework during compression while increasing the specific energy as in the case of the 4-6% RD metallic foam. Tabular representation of average plateau strength and specific energy can be seen in Table 1.
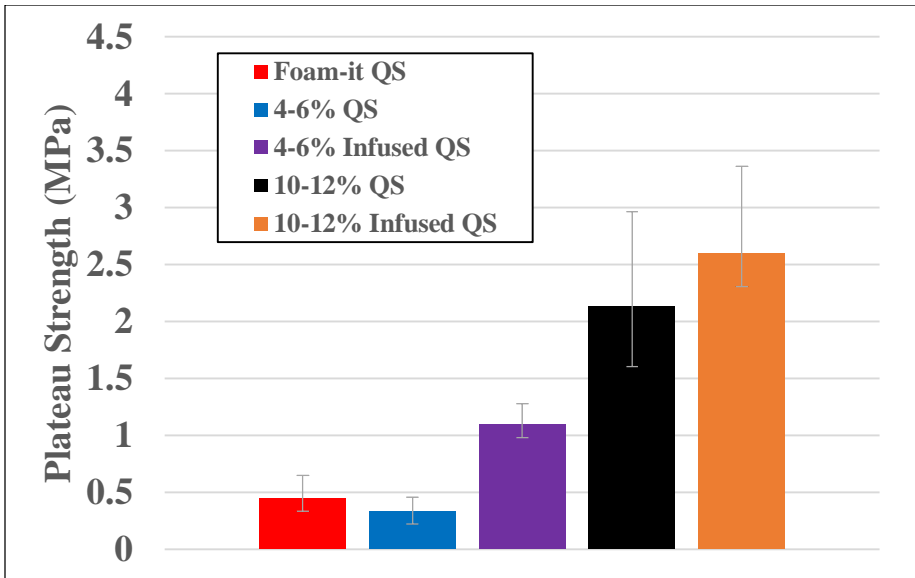
Figure 48. Quasi Static Plateau Strength
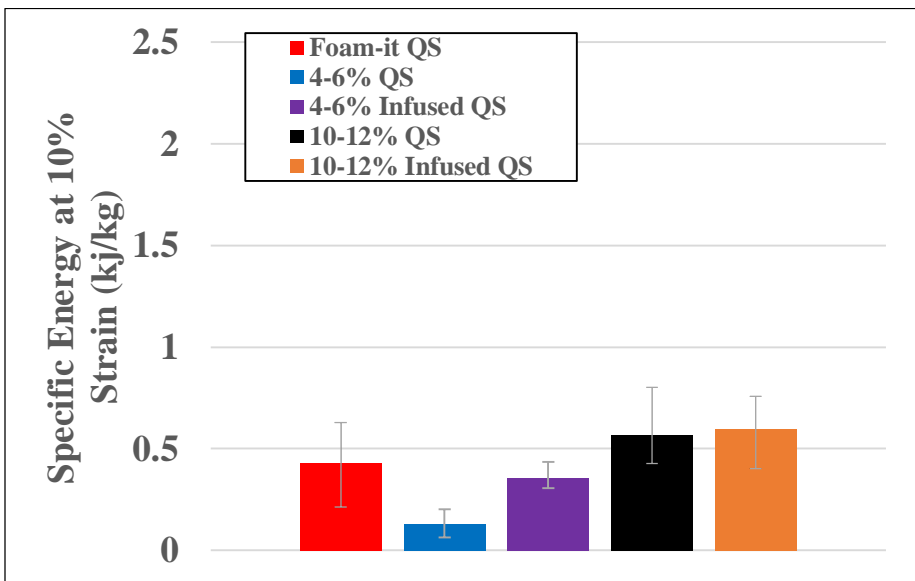
Figure 49. Quasi Static Specific Energy at 10% Strain
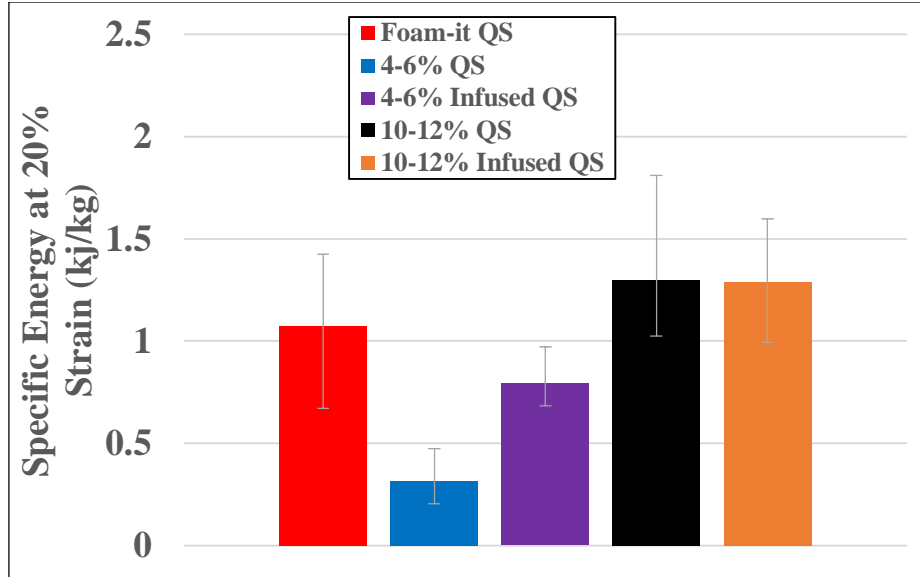
Figure 50. Quasi Static Specific Energy at 20% Strain

Table 1. Quasi-Static Density, Plateau Strength, and Specific Energy for Foam-it 3, 4-6% RD, 10-12% RD, 4-6% RD/Foam-it 3, and 10-12% RD/Foam-it 3

Material	Density (kg/m^3)	Plateau Strength (MPa) (0.1-0.3)	Specific Energy (KJ/Kg) (10% Strain)	Specific Energy (KJ/Kg) (20% Strain)	Specific Energy (KJ/Kg) (30% Strain)
Foam-it 3	68.7	0.44	0.43	1.07	1.74
4-6% RD	161.9	0.33	0.13	0.32	0.53
10-12% RD	281.4	2.13	0.57	1.30	2.09
4-6% RD/Foam-it 3	235.7	1.10	0.36	0.79	1.29
10-12% RD/Foam-it 3	350.7	2.60	0.60	1.29	2.08

4.2 Quasi-Static Computational Results/Discussion

Computational simulation using Abaqus CAE were conducted to illustrate phenomenon present in quasi-static loading. Four main configurations were used to correlation phenomenon observed in experimental quasi-static compression (localized deformation, isotropic behavior, increase in strength). The first had a non-staggered porosity configuration (Fig. 51(A)), the second had identical porosity however voids were not located directly in line with each other (Fig. 51(B)). The last configuration had randomly located porosity as well as variations in pore size (Fig. 51

77

(C)). The fourth configuration had different pore size (Fig. 51 (D)) located in a symmetric configuration. Additional configurations for infused variations were done with the non-staggered and staggered configurations to observed the effects of infusion on the quasi-static response of the composite materials.
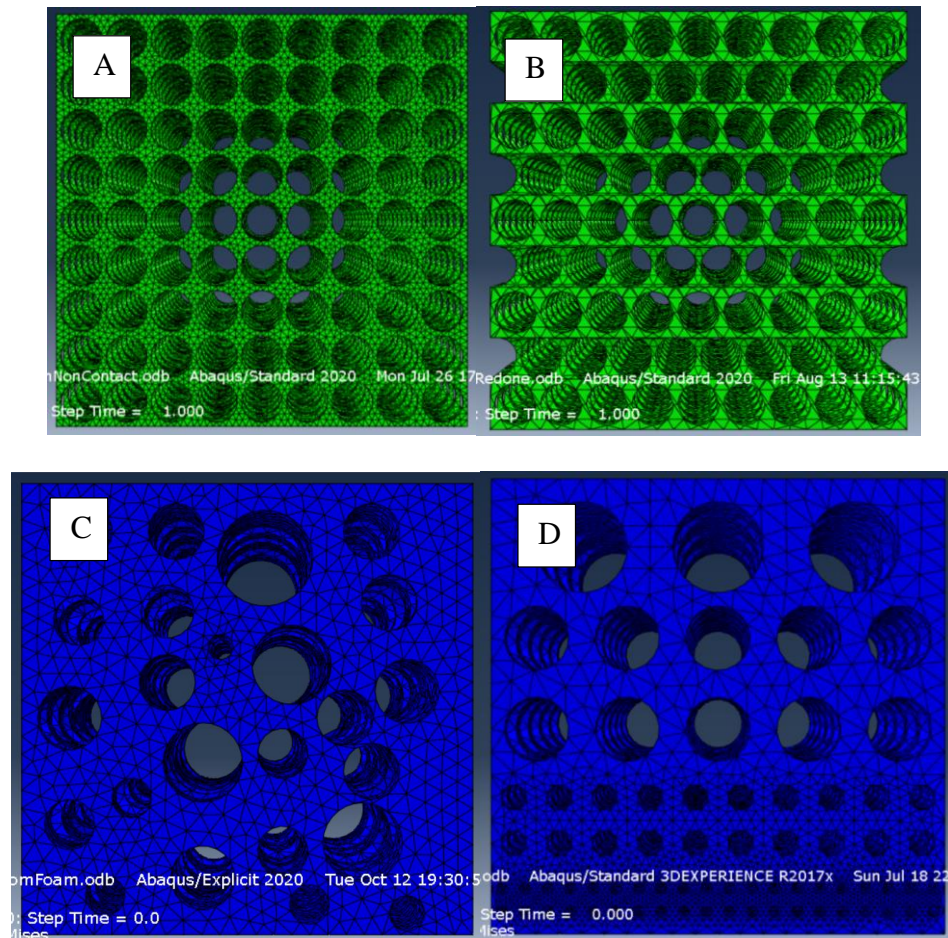
Figure 51. (A) Non-Staggered Configuration, (B) Staggered Configuration, (C) Random Porosity Configuration, (D) Variable Pore Size Configuration

All configurations used the same constitutive model parameters for aluminum with strain rate affects (Daoud, Jomma, Chatelain, & Bouzid, 2015). Model parameters can be seen in Table 2. A tabular constitutive relationship was used for infusion polymer from quasi static compression of Foam-it™ 3lb.

Table 2. Johnson Cook Parameters (Daoud, Jomma, Chatelain, & Bouzid, 2015)

A	B	C	n	m	Melting Temp.	Transition Temp.
250 MPa	79.7 MPa	0.0249	0.499	1.499	923 K	300 K

All samples had similar boundary conditions applied to the top and bottom surface (Fig. 52). The bottom surface was fixed in all direction, while the top surface had a known displacement applied to the surface to achieve a global strain of 0.5, with the exception of the variable pore size configuration.
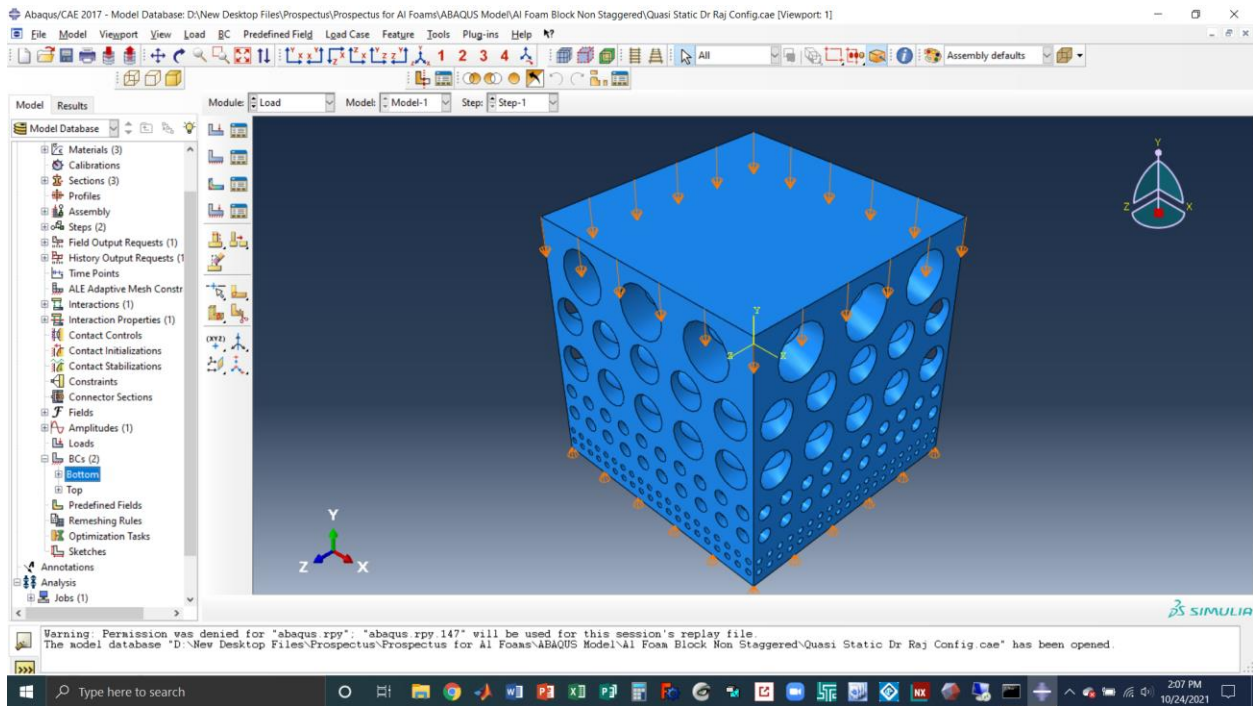
Figure 52. Abaqus Simulation Quasi Static Boundary Conditions

This was done due to computational errors that occurred with large strain computation. The comparison of simulations shows that with increasing disorder (i.e. random void location) an increase in isotropic behavior of the metallic framework as well as a decrease in overall stress within the framework is observed. This highlights why the behavior of the quasi-static samples did not exhibit any anisotropic behavior during compression. Stress levels for the non-staggered,

staggered, and random configuration of 398 MPa, 383 MPa, and 335 MPa at element located near the edges of voids (Fig. 53 A-E). However, at peak areas of the random configuration the stress level achieved a maximum of 533 MPa were observed. Based upon the resulting simulations it can be concluded.
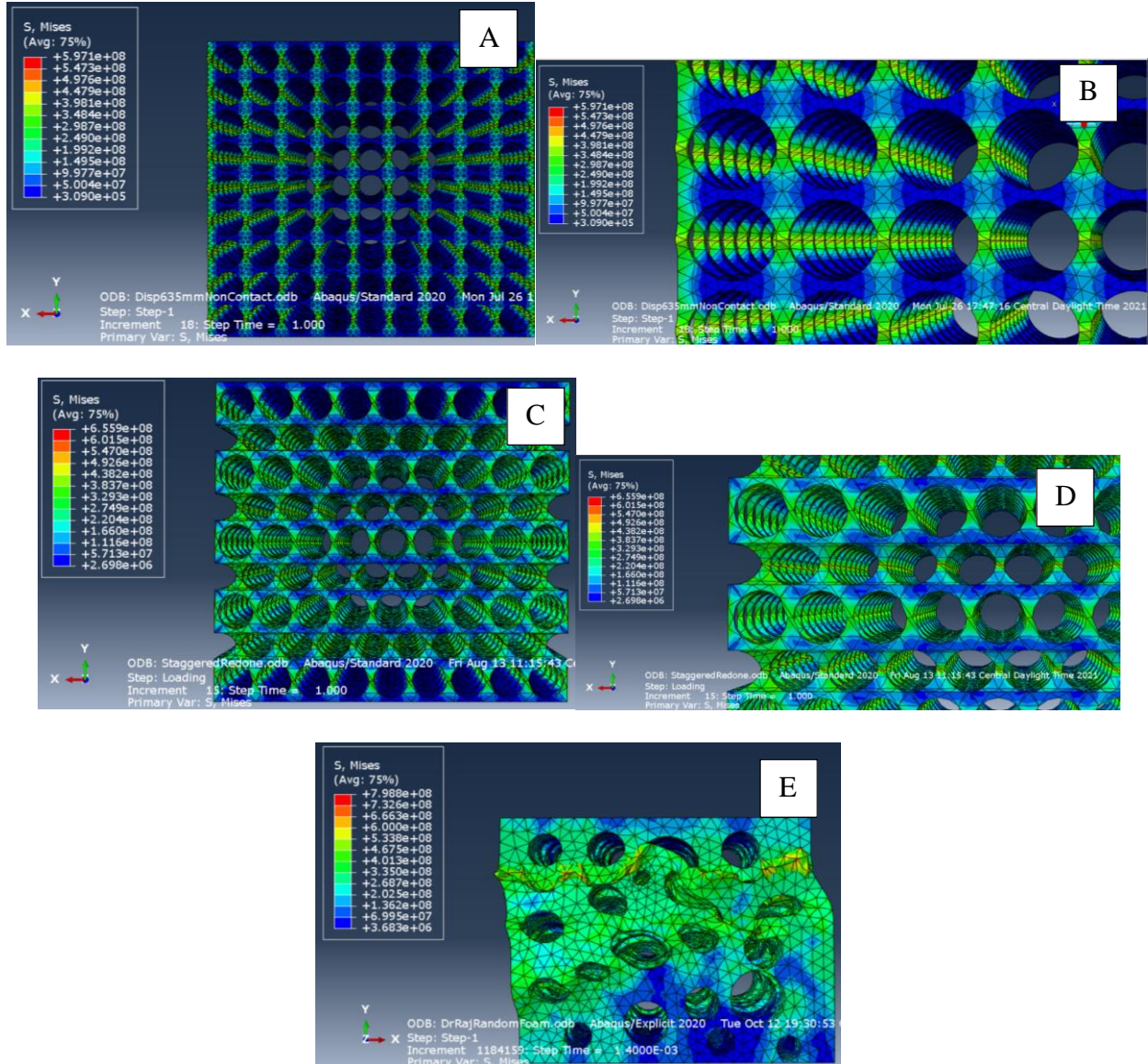
Figure 53. (A) Non-Staggered Von-Mises Stress, (B) Non-Staggered Von-Mises Stress at Pore Edge, (C) Staggered Von-Mises Stress, (D) Staggered Von-Mises Stress at Pore Edge, (E) Random Pore Von-Mises Stress Configurations

The variable pore size configuration simulation that was conducted at quasi static loading conditions revealed that deformation is localized at areas with the smallest cross sectional area transverse to the loading direction. In essence locations with less material to resist deformation deform more than areas with more material, irrespective of void size (Fig. 54 A-C). Stress levels all became more isotropic within areas with less transverse cross sectional area. Based on the quasi-static computational simulation it can be concluded that the isotropic behavior of the aluminum foam is due to the random pore size and location. It can also be concluded that localized deformation will occur in areas with minimal material.
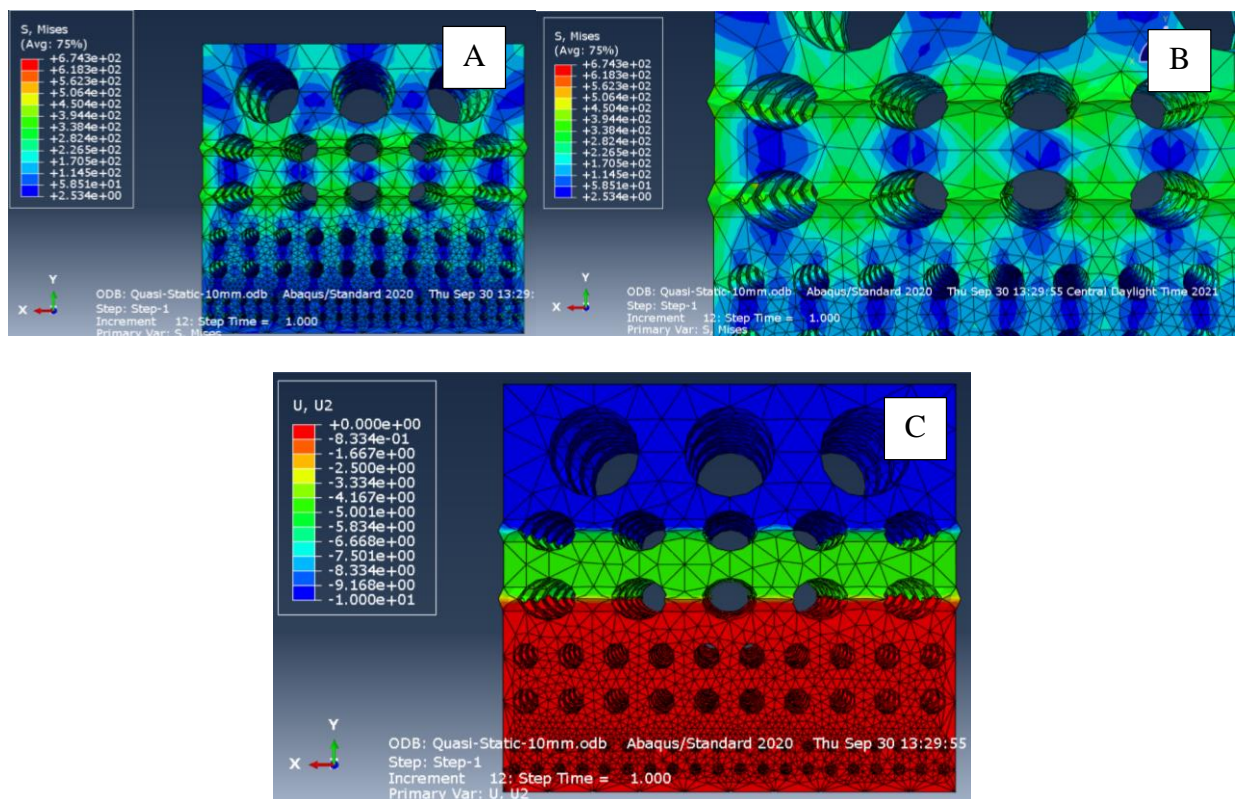
Figure 54. (A) Random Pore Size Von-Mises Stress, (B) Random Pore Size Von-Mises Stress at Pore Edge, (C) Displacement in the Y Direction for Quasi-Static Loading

The remaining two simulations for the infused variations revealed two key findings. The first is that with the infusion polymer present the stress levels in the metallic framework increases,

and the second is that when comparing the non-staggered and staggered configurations there is a decrease in strength. Infused non-staggered and staggered configuration exhibited 484 MPa and 445 MPa, respectively, at the edges of the pores; approximately a 21% and 16% increase in strength when compared to non-infused simulation (Fig. 55 A-D). From this it can be concluded that the infusion material aids in distribution of the stress such that more is able to flow through the metallic framework. Based on experimental observation it is also believed that the polymer foam material increases the resistance in the transverse direction (buckling) of the metallic framework. It was also observed that the staggered simulation exhibited slight shear deformation during compression. It is believed that this is not due to the material response but an artifact of the simulation not having exactly symmetric pore location due to simulation input resolution. From experimental analysis of the compression images no shear phenomenon was observed. From the analysis of all simulations it can be concluded that the infusion causes higher stress levels in the metallic framework which increase the compressive resistance of the material.
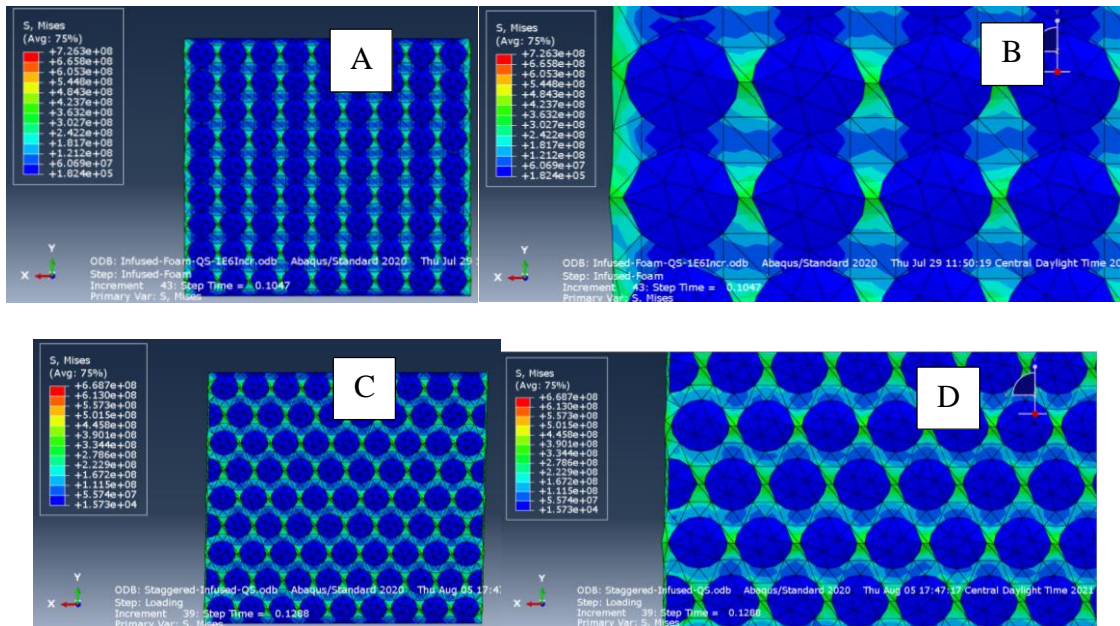
Figure 55. (A) Non-Staggered Infused Von-Mises Stress, (B) Non-Staggered Infused Von-Mises Stress at Pore Edge, (C) Staggered Infused Von-Mises Stress, (D) Staggered Infused Von-Mises Stress at Pore Edge

CHAPTER V: LOW-VELOCITY PUNCH SHEAR RESULTS/DISCUSSION

5.1 Areal Density

The areal density (also indicated as: mass thickness, area density, surface density) is a key parameter controlled in this study. With changing stacking sequences, it is crucial to maintain the amount of material located under the impact zone of the hemispherical tup to understand the role infusion and functionally gradation plays in the impact resistance of metallic foam and metallic/polymer foam composites. Areal density was calculated from the using equation 31 which relates the total mass of the material to the cross sectional area or density to the thickness of the material.

$$\rho_A = \frac{m}{A} = \rho l \qquad\qquad eq.\,(31)$$

The areal density was maintained by equating the functionally graded stacking sequences area density to the uniform metallic foam panels for the Duocel configurations. Area density was monitored before and after the infusion process to insure consistency. Table 3 shows the area density of all Duocel configurations. Based on results the area density did have a slight increase when comparing the non-infused configuration to the infused variations. This can be attributed to the density of the binding agent (3M Hi-Strength 90 Contact Adhesive) between each layer of the configuration, especially in the case of the 7-layer low density foams. Samples with DNI designation are panels made with Duocel Metallic Foam. Designations H and L indicate 10-12% and 4-6 % relative density metallic foam, respectively. The two located directly after L or H

indicates the thickness of the samples in tenth of inch. The remaining two located after a parenthesis indicates the number of layers.

Table 3. Areal Density for Non-Infused and Infused Metallic Foam Configurations

Panel Configuration	Nominal Thickness (mm)	Area Density (Kg/m^2)	Area Density (Kg/m^2) After Infusion	Percent Increase in Area Density
DNI(H2)3	15.24	5.3	X	X
DNI(L2)7	35.56	5.3	X	X
DNIH2(L2)2H2	20.32	5.1	X	X
DNIL2(H2)2L2	20.32	5.3	X	X
DI(H2)3	15.24	5.1	6.0	18
DI(L2)7	35.56	4.9	8.1*	42*
DIH2(L2)2H2	20.32	5.1	6.3	27
DIL2(H2)2L2	20.32	5.7	6.4	26

* Increase in area density due to increased volume of 3M adhesive

5.2 Duocel Functionally Graded Low-Velocity Results/Discussion

The response of pure metallic foam versus metallic foam/polymer materials was an increase in all impact properties (peak load, total energy absorption, damage initiation energy, and puncture propagation energy). However, what is most key to the increase in energy absorption is not the strength of the layers of the panels but the distance over which the material is mass is extended. Comparison necessary to arrive at the aforementioned conclusion are discussed in this chapter.

Several difference and similarities of results from low-velocity impact were observed during impact testing. Contrary to Mohan et al. (Mohan, Yip, Idapalapati, & Chen, 2011), load did not increase linearly to peak load. Metallic foams (Alporas) characterized in Mohan et al, were closed cell with RD 9.5%, and are open cell and porous in the present study. It is believed that the difference in cellular structure is the cause of discrepancy between the results. Similarly, to Mohan et al, long plateau regions were not observed with hemispherical indenter, with the exception of

non-infused samples with only 4-6% RD layers. Thickness of samples with 4-6% (35.5 mm) is the probable cause of this pronounced plateau region from 10-25 mm displacement. This was however, not observed in the composite variation of the 4-6% RD configuration. It is presumed that this is due to the less ability to collapse the cellular structure in the composite panels.

Analysis of load-displacement curve revealed several key similarities and differences when comparing stacking sequence and infusion type. Comparison of load-displacement curves (Figure 56, Figure 57) revealed a shift in displacement at peak load (15-20mm) for samples made with only 4-6% RD metallic foam (non-infused and infused) when compared to remaining configurations (10-15 mm). The increased displacement required to achieve maximum penetration load is likely due to the increased thickness of samples constructed of only 4-6% (non-infused and infused), which was done to achieve same nominal area density. This increase in thickness of metallic foams has been also shown to increase the plateau length, which can be attributed to increase volume of material compressed by hemispherical tup. Deviation in load-displacement of sample set for each configuration (Fig. 56, Fig. 57) show more scatter when comparing non-infused panels versus infused panels, and even more deviation when comparing uniform metallic foam RD panels to functionally graded configurations. Scatter observed in initial rise of load-displacement curves to peak load yielded higher deviation in functionally graded samples than constant metallic foam configurations. Variations in infused samples are potentially caused by inconsistent expansion of polymeric foam through the panels. The increase in scatter when comparing functionally graded samples to uniform samples is possibly caused by variation in the metallic foam RD and previously mentioned expansion inconsistencies.

Another key finding when evaluating non-infused versus infused configurations of similar stacking sequence show an increase in end displacement (Fig. 58-61). From this comparison it is clear that the infusion technique increases the ductility/displacement to punch through of metallic foam panels. This increase in displacement required to achieve full punch through of the panels adds to the overall energy absorption capabilities of the infused configuration compared to non-infused.

All variation of infused panels showed increase in peak load compared to similar non-infused configurations (Fig. 56-61). The increased peak load can be credited to the increase in material directly beneath the indenter tip. This improvement in strength will allow panels to absorb more energy due to penetration loading, potentially reducing damage to protected individuals/systems. Maximum peak load trend show that samples made from functionally graded samples with high density middle section (DNIL2H2L2 and DIL2H2L2) achieved highest peak load regardless of infusion technique, showing that stacking sequence does affect strength of functionally graded composites. Lowest peak load configurations (DNIH2L2H2 and DNIL2) reversed peak load trends in terms of overall peak load comparison. Without infusion DNIH2L2H2 had the third highest peak load with infusion it had the weakest peak load. Variation between DNIH2L2H2 and DNIL2 was approximately 135 N where variation of DIH2L2H2 and DIL2 were only 13 N. This show the capabilities of the infusion technique to increase the penetration strength of lower density metallic foams.
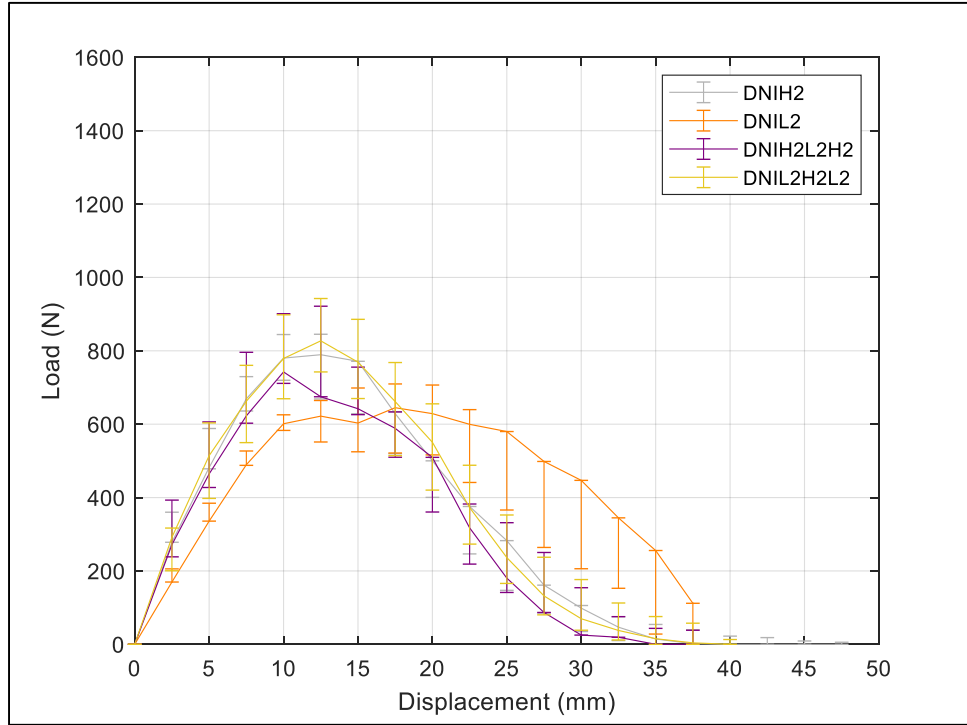
Figure 56. Load-Displacement for Non-Infused Metallic Foam Panels
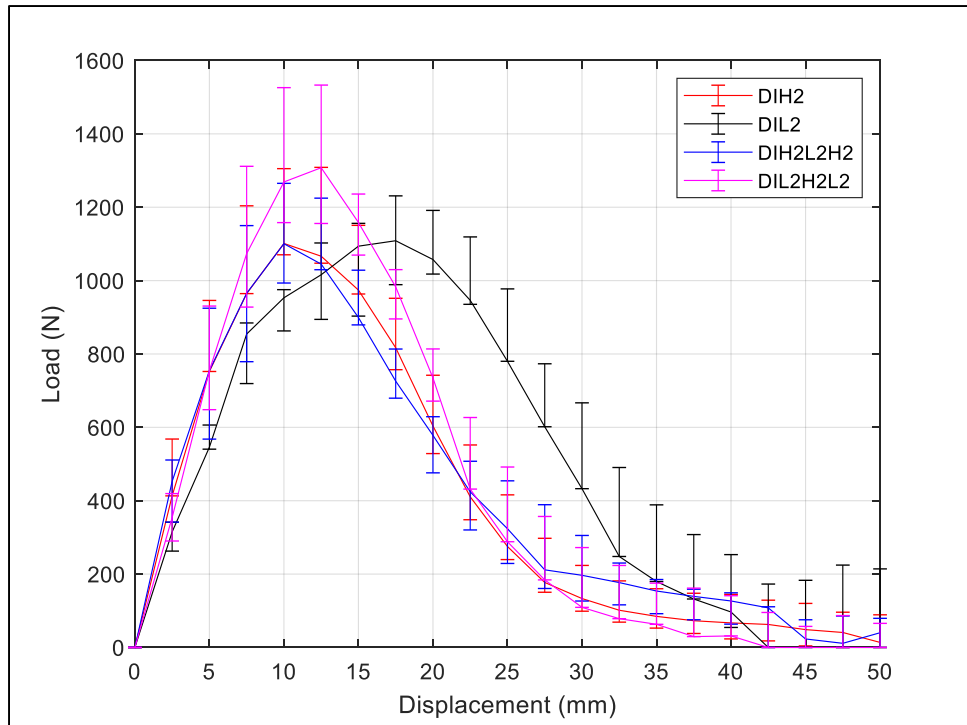
Figure 57. Load-Displacement for Infused Metallic Foam Panels

87
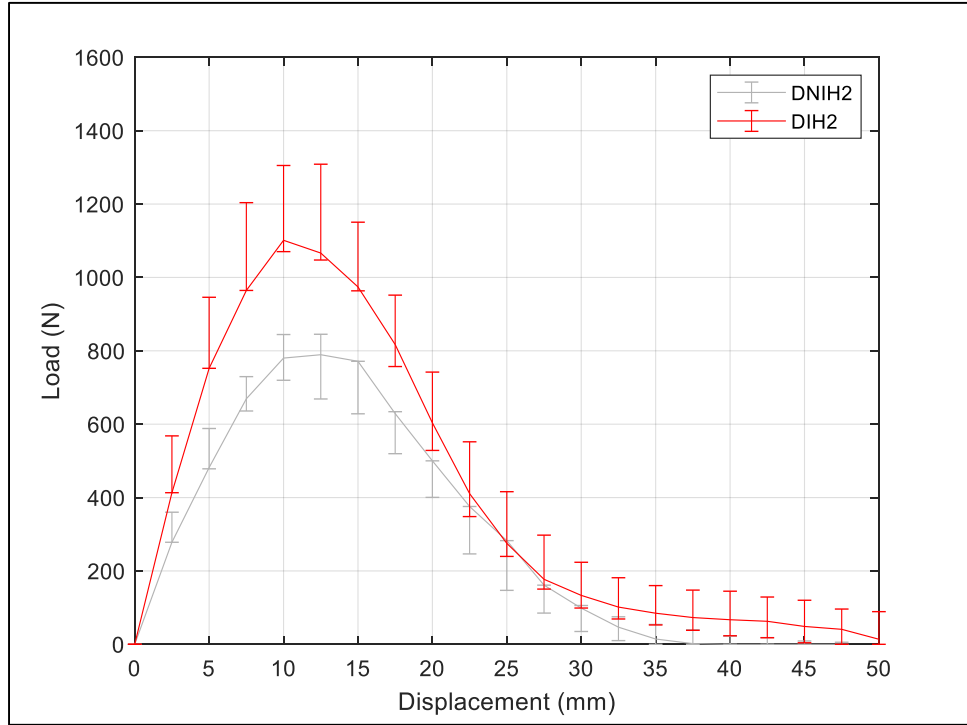
Figure 58. Load-Displacement for 3 Layer (DNI(H2)3/DI(H2)3) Non-Infused/Infused 10-14% Relative Density Metallic Foam
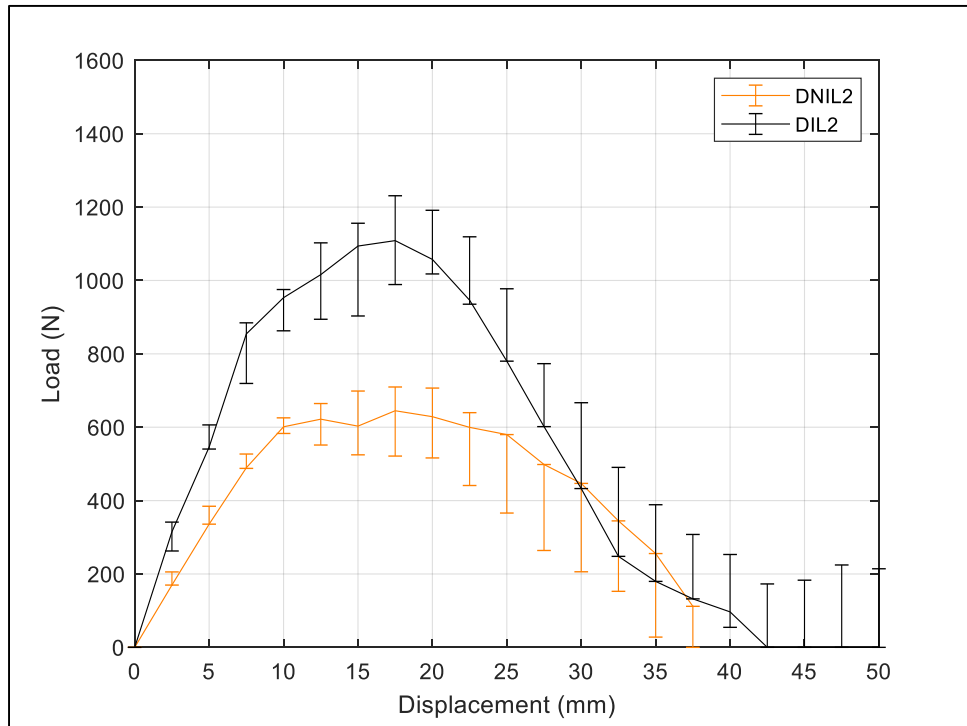
Figure 59. Load-Displacement for 7 Layer (DNI(L2)7/DI(L2)7) Non-Infused/Infused 4-6% Relative Density Metallic Foam
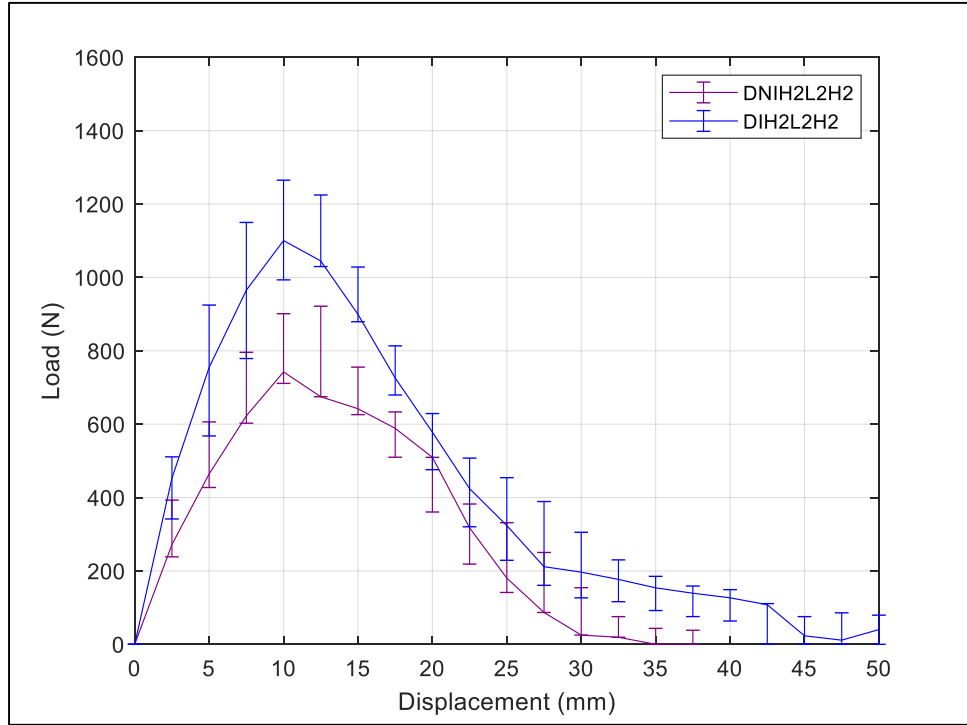
Figure 60. Load-Displacement for 4 Layer (DNIH2(L2)2H2/DIH2(L2)2H2) Non-Infused/Infused Functionally Graded Metallic Foam Panels
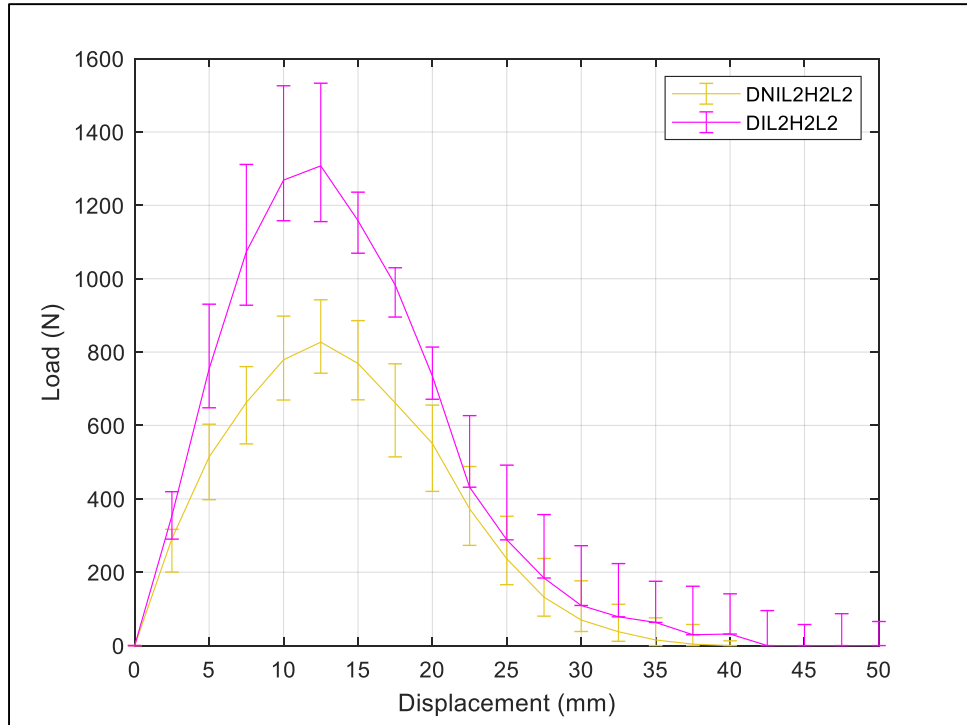
Figure 61. Load-Displacement for 4 Layer (DNIL2(H2)2L2/DIL2(H2)2L2) Non-Infused/Infused Functionally Graded Metallic Foam Panels

Evaluation of several key regions (peak load, total energy absorption, damage initiation energy, and puncture propagation energy) of load-displacement curve yielded increases in all categories of comparison. Damage initiation phase and puncture propagation phase are defined as the energy up to peak load and the energy from peak load to end displacement, respectively. Peak load was highest in L2H2L2 configuration (Fig. 62, Table 4) regardless of infusion technique, which can be credited to the ability of functional graded composites to increase strength with specific stacking sequence. Comparison of DNI samples to DI show substantial increases in peak load. Increases of 43%, 74%, 42%, and 58% (Table 5), were seen for H2, L2, H2L2H2, and L2H2L2 respectively, when comparing infusion technique.

Energy absorption of all configuration increase in all phases of total energy absorption, damage initiation energy, and puncture propagation energy (Table 5) when comparing non-infused sample to infused configurations. Total energy absorption of each material increased by considerable percentage (Fig. 63, Table 5), most notably the lowest metallic foam density (4-6%) configuration which had an increase of 106%. It is noteworthy that the density of the panels did increase (Table 1) the most but this is again credited to the increase volume of bonding agent required to combine layers of composite material. The lowest increase in total energy absorption was found in the panels made with only highest density metallic foam (10-14%). It is believed that this is due to the variation in density of the constituent materials being larger for composite made of highest density foams versus lowest density foam. It is plausible that the combination of 4-6% RD metallic foam and FOAM-iT!™ 3lb allows for enough resistance of motion of the metallic framework to be provided allowing more stress to be applied before catastrophic failure occurs. The highest energy absorption was observed in non-infused and infused samples made solely of 4-6% RD metallic foams framework. This points to the possibility that increasing the

90

volume over which the metallic foam is spread has a more pronounced effect on increasing the energy absorption due to the increased length of the zone of material loaded. In essence each sample has the same amount of material resisting the motion of the indenter, however when the volume of material is spread out over a large thickness it is able to absorb more energy than if it is amassed in a smaller volume/smaller thickness. Similar trends were found when comparing DNI samples to DI samples for damage initiation energy and puncture propagation energy (Fig. 64, 65). Consistent with total energy absorption composite panels made of lowest density metallic foam exhibited the largest increase in damage initiation and puncture propogation energy absorption capability (Fig. 64, Table 5). Increases of 108% and 104% were observed for DIL2 samples compared to DNIL2, respectively. Observation of remaining composite configurations revealed increases in damage initiation were not as high as puncture propagation energy. The increase in material present beneath the indenter tip is the most probable cause for this increase. The increased energy absorption when factoring the increase in composite density still demonstrates the ability of the composite material to absorb more energy without sacrificing the overall mass. Composite made of H2L2H2 exhibited the lowest increase in damage initiation energy (38%), but had sizeable increase in the propagation loading phase (88%).
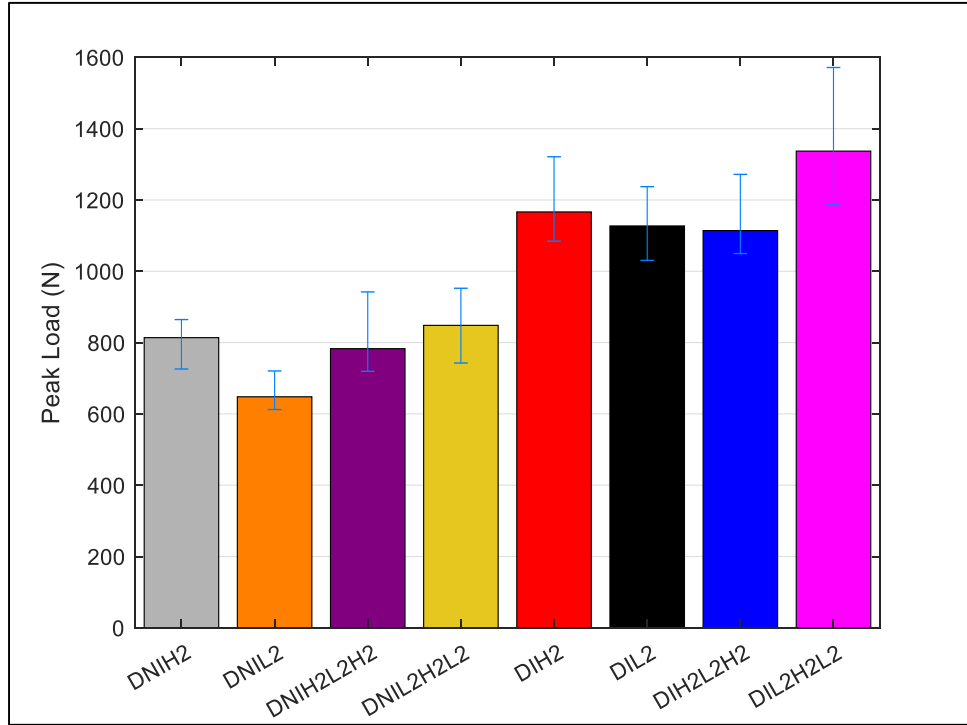
Figure 62. Peak Load(N) for Low Velocity Impact Duocel Panel Configurations
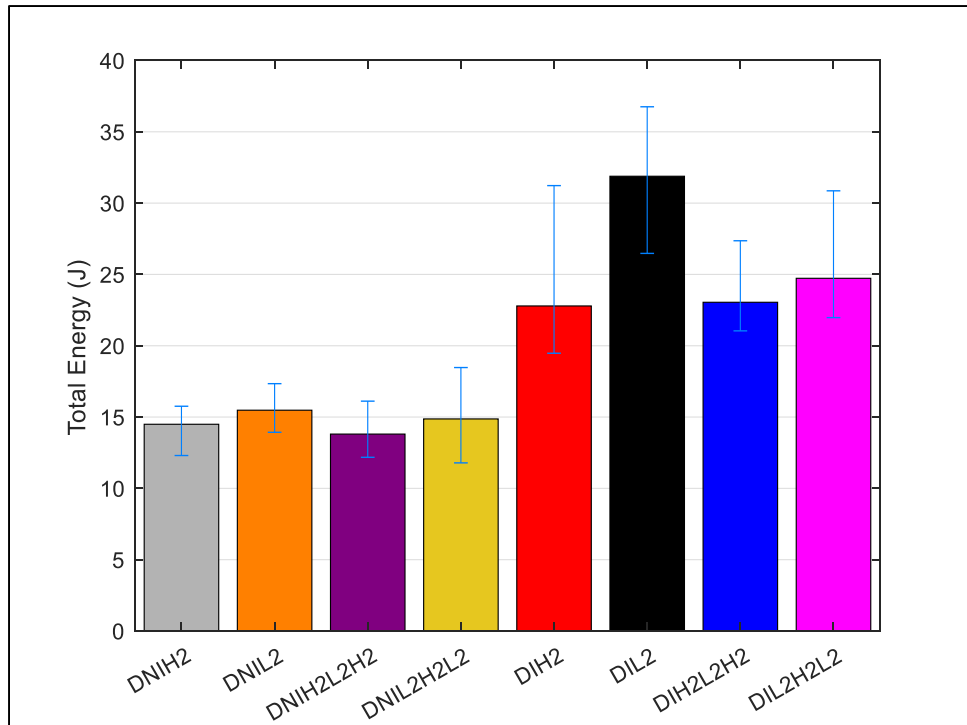
Figure 63. Total Energy Absorption for Non-Infused/Infused Metallic Foam Panels
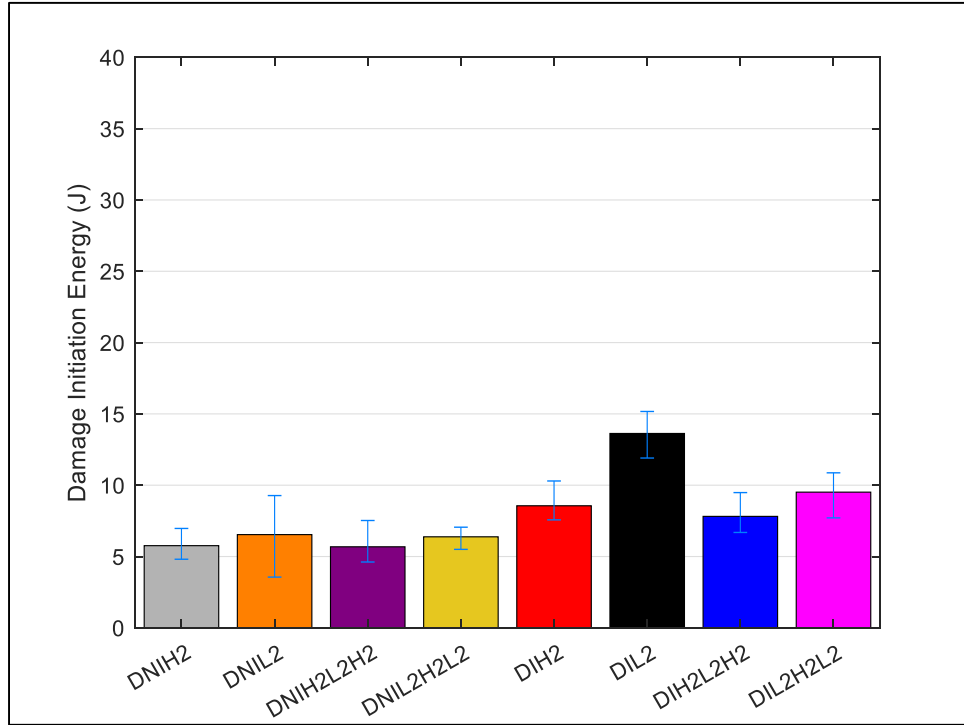
Figure 64. Damage Initiation Energy Absorption for Non-Infused/Infused Metallic Foam Panels
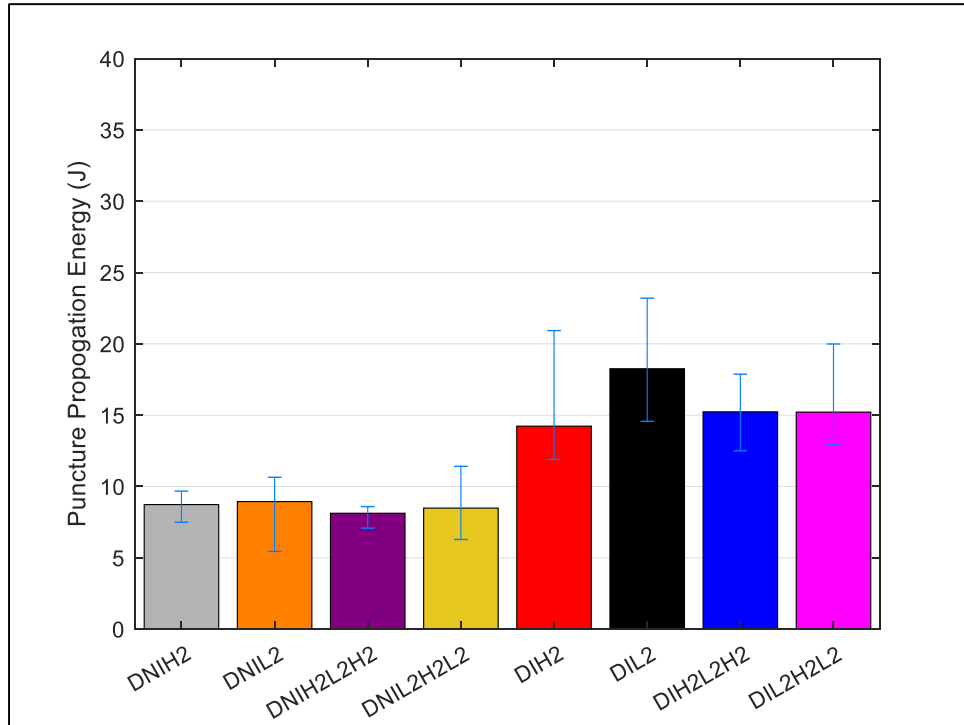
Figure 65. Puncture Propogation Energy Absorption for Non-Infused/Infused Metallic Foam Panels

Table 4. Peak Load, Total Energy Absorption, Damage Initiation Energy, and Puncture Propagation Energy for Low Velocity Non-Infused and Non-Infused Metallic Foam Configurations

Panel Configuration	Peak Load (N)	Total Energy (J)	Damage Initiation Energy (J)	Puncture Propagation Energy (J)
DNI(H2)3	814	14.49	5.76	8.73
DNI(L2)7	648	15.48	6.54	8.94
DNIH2(L2)2H2	783	13.81	5.68	8.12
DNIL2(H2)2L2	848	14.87	6.38	8.49
DI(H2)3	1166	22.79	8.56	14.23
DI(L2)7	1127	31.88	13.63	18.26
DIH2(L2)2H2	1114	23.05	7.82	15.23
DIL2(H2)2L2	1337	24.73	9.51	15.21

Table 5. Percentage Increase for Peak Load, Total Energy, Damage Initiation Energy, and Puncture Propagation Energy for Non-Infused Compared to Infused Metallic Foam Configurations

Panel Configuration	Peak Load (N) Percent Increase	Total Energy (J) Percent Increase	Damage Initiation Energy (J) Percent Increase	Puncture Propagation Energy (J) Percent Increase
DNI(H2)3-->DI(H2)3	43	57	49	63
DNI(L2)7-->DI(L2)7	74	106	108	104
DNIH2(L2)2H2-->DIH2(L2)2H2	42	67	38	88
DNIL2(H2)2L2-->DIL2(H2)2L2	58	66	49	79

Based on the findings of this study a functionally graded composite made with an optimal pure metallic foam RD and infused polymeric foam density could be used to achieve the most

desirable energy absorption capabilities. More investigation is needed to find the ideal ratio of metallic foam RD and polymeric foam density for ideal configuration as well as stacking sequence. It is however, from this study, preferable to place the higher density pure metallic foam panels near or at the mid-section of the panels when functionally graded configurations are used. Overall, a low density metallic foam/polymeric composite could provide substantially more protection in penetration loading condition. While the peak load of the lowest density isn't as desirable as other configurations, the overall ability of these infused composites to reduce energy of penetration is substantially higher than other configurations. As previously mentioned the energy absorption is based largely on the thickness of the panel rather than the strength of each layer. The capabilities of each configuration and additional configurations should be tested in other high energy loading conditions such as direct impact, ballistics, and shock loading to understand the capabilities of each configuration in different loading conditions.

Resulting analysis of low velocity punch shear impact testing revealed similar failure zone and patterns of non-infused and infused panels. Visual inspection of damage zone shows crushed metallic foam or metallic foam/polymeric foam composite material directly under the hemispherical impactor. Inspection of back surface of panels revealed fracture of metallic foam framework at various location near impact zone. Typical damage zones can be seen in Figure 66.
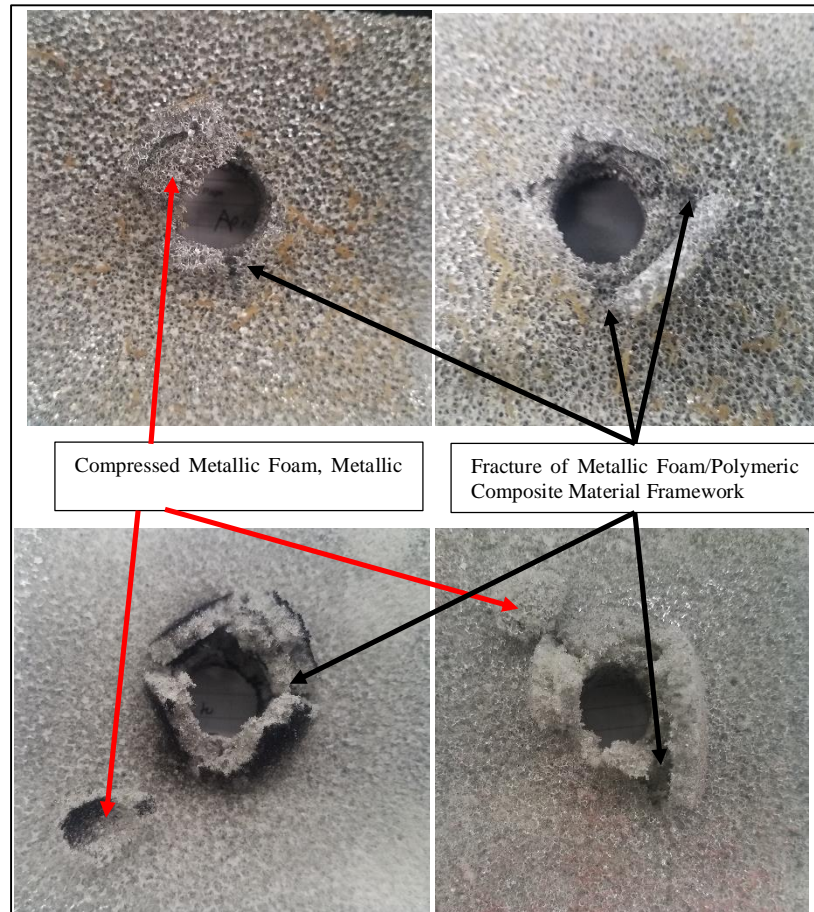
Figure 66. Damage Zone of Non-Infused Metallic Foam and Infused Metallic Foam Panels

5.3 Cymat Functionally Graded Low-Velocity Punch Shear Results/Discussion

Low-velocity punch shear testing was performed on Cymat closed cell 6061 aluminum foams for 6 configurations, three with consistent density layers and three functionally graded (Fig. 67) using an Instron 9450 low-velocity impact machine. A hemispherical tup was used to penetrate samples to induce punch shear failure. As previously stated, impact velocity of 6.3 m/s was set to achieve an impact energy approximately three times that of the energy to peak load and achieve a velocity slowdown no greater than 20%. Load and displacement data were recorded at a sampling rate of 1 MHz for the entire duration of the impact event. Energy absorption was calculated by

numerical integration of the area under the load-displacement curve for each sample and is the focus of the comparison for each configuration. Due to the large difference between the impact capabilities and variations in the testing procedure no comparisons were made between the Cymat and Duocel panels.

Figure 67. Cymat Non-Functionally Graded (A-C), Functionally Graded (D-F) Low Velocity Impact Panels

The response of Cymat low-velocity impact panels shows variations in the response due to penetration testing when comparing all configurations. The highest density (HD) metallic foam exhibited the highest response for peak load, total energy, damage initiation energy, and puncture propagation energy as compared to all other configurations (Fig. (54), Table 3), due to more material directly under the hemispherical loading tip. The trend when comparing high density, medium density (MD), and lowest density (LD) shows a decrease in all impact properties aforementioned, respectively. This comparison merely shows that the penetration of the Cymat panels with layer of same density will yield a response proportional to the density of the metallic foam. Configurations with intermediate layers with decreased density relative to the impact layer (High-Low-Medium Density (HLM), and High-Medium-Low (HML) showed an initial response consistent with the HD panels, however at approximately 7.5-15 mm displacement the load capacity of the panel decreases followed by an increase in force. The increase in force for HLM samples as compared to HML samples is significantly higher, due to the stacking sequence of the material. Configurations of Lowest-Medium-High (LMH) showed slight decreases in peak load

97

(6.8%, Fig. 68-69, Table 6) when compared to panels made with only high density closed cell metallic foam. The initial stiffness of the material is however vastly different with the high density panel exhibiting a considerable stiffer initial response. Based on the results it appears that the overall strength of the panels in terms of peak load properties is more related to the back surface layer as opposed to the initial strike face layer. Essentially having a high density material furthest away from the location of impact will achieve approximately the same peak load compared to uniform high density panel. It is plausible that material densification under the hemispherical tup above the highest density foam back layer cause additional resistance as more material is compacted before the tup reaches the first interface of the highest density back layer. In essence as the tup puncture through the layers of foam and propagates through the panel the compressed damaged foam provided additional resistance when penetrating through the high density back layer. Peak load for HLM and HML functionally graded panels fell slightly under the response of the medium density configuration. The response of all panels exhibited a vast range in response for the same panel. This is attributable to the inconsistent nature of the Cymat closed cell panels and the large void content.
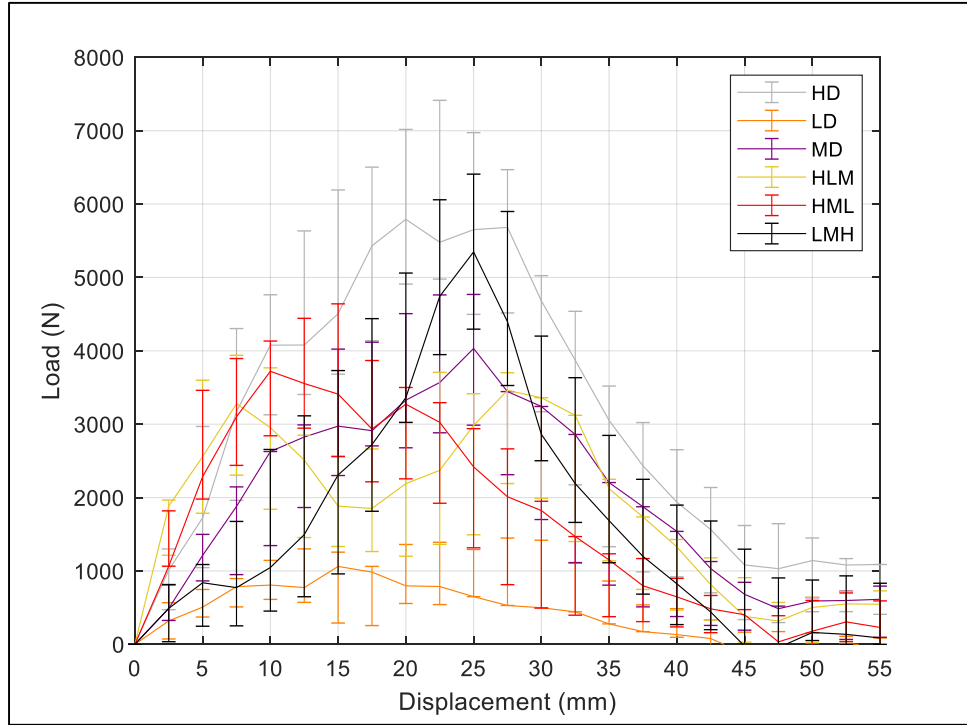
Figure 68. Load-Deflection for Cymat Low Velocity Impact Panels
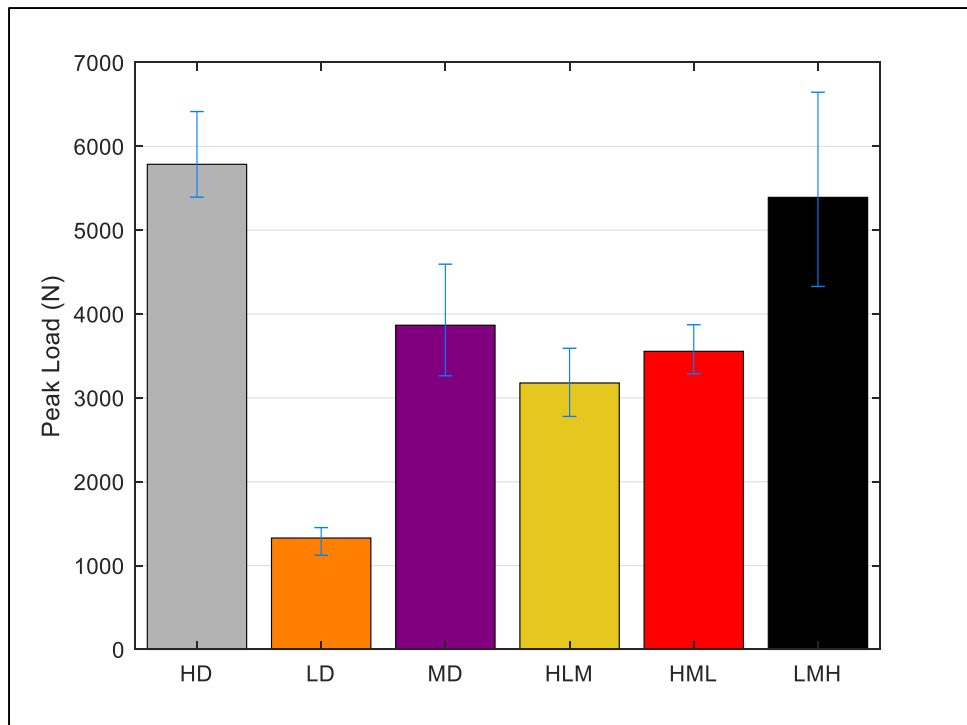
Figure 69. Peak Load for Cymat Low Velocity Impact Panels

99

Total energy absorption, damage initiation, and puncture propagation energy were highest in HD panels (Fig. 70-72) due to strength, damage initiation energy, and energy absorb during propagation phase (Fig. 68). Functionally graded variations HLM, HLM, and LMH exhibited similar total energy absorption to that of MD panels. Another conclusion that can be gleamed from total energy absorption when comparing functionally graded panels is that the layer furthest from the impact zone is more critical for energy absorption than the stacking sequence. Panels made in LMH, HLM, and HML show a decreasing trend in energy absorption. The common thread being the lower layer of the panel, however, the mode for which energy is being absorb are different in each case (Fig. 71, Fig. 72). HML panels exhibited highest propagation energy as compared to other functionally graded panels, due to plug formation (buildup of densified metallic foam) (Rajaneesh, Sridhar, & Rajendran, 2014) (Markaki & Clyne, 2000) on indenter tip causing more resistance during penetration. The increased propagation energy absorption comes at the cost of damage initiation energy. In essence the functionally graded panels absorb approximately the same total of energy (Table 6) however the failure mechanism changes with stacking sequence.
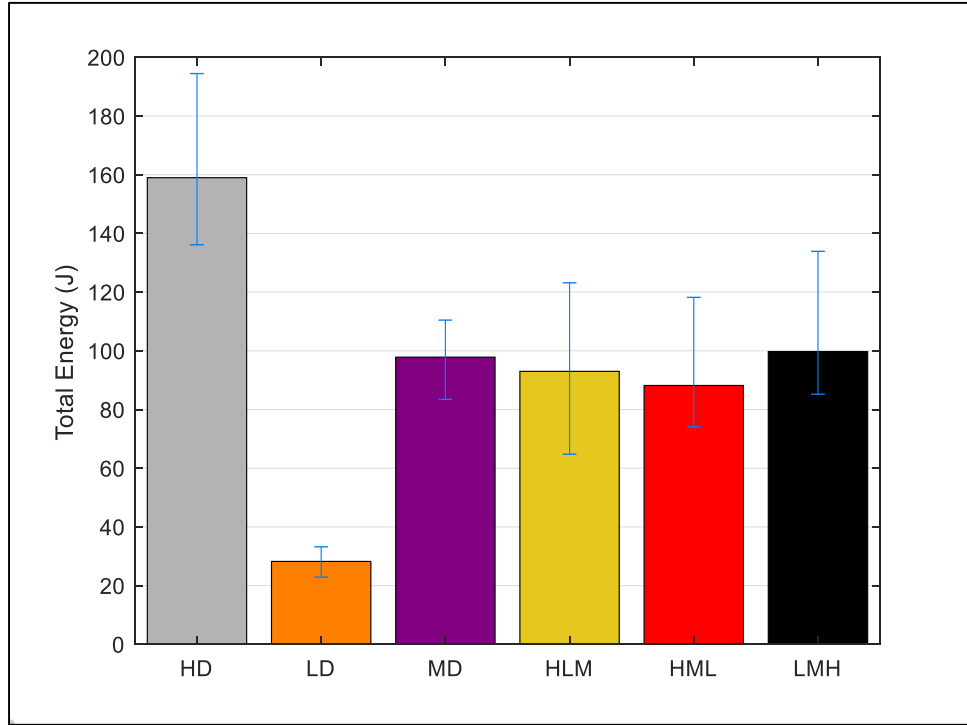
Figure 70. Total Energy Absorption for Cymat Low Velocity Impact Panels
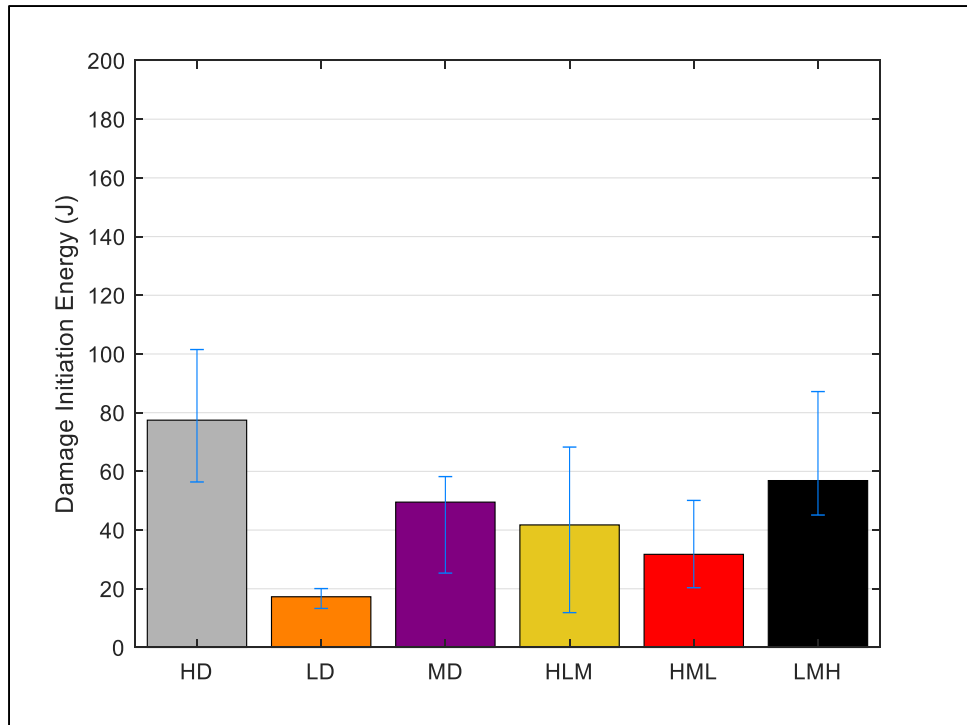
Figure 71. Damage Initiation Energy for Cymat Low Velocity Impact Panels
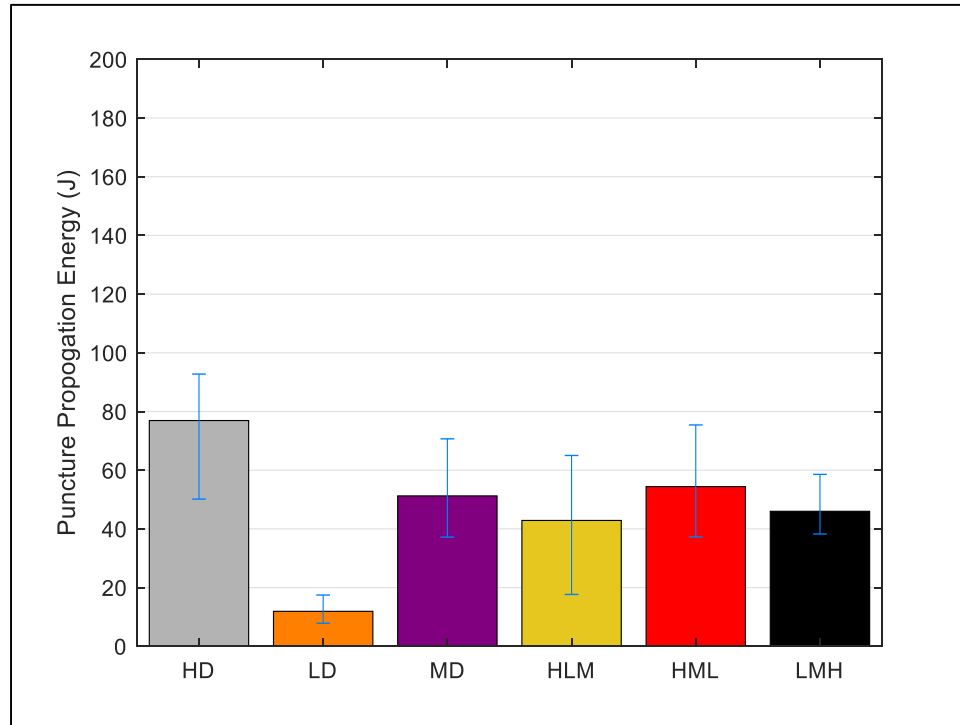
Figure 72. Puncture Propagation Energy for Cymat Low Velocity Impact Panels

Table 6. Peak Load, Total Energy Absorption, Damage Initiation Energy, Puncture Propagation Energy for Cymat Configurations

Panel Configuration	Peak Load (N)	Total Energy (J)	Damage Initiation Energy (J)	Puncture Propagation Energy (J)
HD	5786	158.99	77.45	76.93
LD	1329	28.24	17.28	11.92
MD	3867	97.84	49.52	51.25
HD-LD-MD	3178	93.01	41.75	42.88
HD-MD-LD	3556	88.19	31.73	54.42
LD-MD-HD	5392	99.76	56.87	46.00

As expected samples made with lowest density (LD) layers exhibited substantially less impact mitigation characteristics (Table 7). A 77% and 82% decrease was observed for peak load and total energy absorption, respectively, largely credited to the decreased material under the impact zone. Decreases in peak load, and energy absorption (total, damage initiation, and propagation) ranging from 7-45% and 37-45%, respectively, were observed in MD, HD-LD-MD,

and HD-MD-LD composites were observed when comparing to HD panels. From resulting analysis utilizing HD panels provide more impact mitigation to penetration versus all other configurations by a large margin (26-84%) in various puncture phases.

Table 7. Percent Decrease for Peak Load, Total Energy Absorption, Damage Initiation Energy, and Puncture Propagation

Panel Configuration	Peak Load (N) Percent Decrease	Total Energy (J) Percent Decrease	Damage Initiation Energy (J) Percent Decrease	Puncture Propagation Energy (J) Percent Decrease
HD	0.00	0.00	0.00	0.00
LD	77.04	82.24	77.69	84.51
MD	33.17	38.46	36.06	33.38
HD-LD-MD	45.08	41.50	46.09	44.25
HD-MD-LD	38.53	44.53	59.03	29.26
LD-MD-HD	6.82	37.26	26.58	40.20

Failure patterns for front and back surface (Fig. 59 A-F) show typical failure zone (circular penetration zone) on the front surface with the exception of panel with lowest density top layer (Fig. 59(B)), due to the initial strike face being primarily made of thin foil with minimal structural framework located directly under. Back surface failure zones for medium and high density (Fig. 59(D, F)) show large failure zone relative to the indenter diameter (20 mm), due to previously mention plug/cone formation from collapse material. Failure pattern on back face surfaces for panels with lowest density foam had a less pronounced failure zone that was consistently smaller than medium and high density layers. Fracturing of panels surfaces was observed predominantly in panels with medium and high density bottom layer. It is unclear as to if the fracture zones are created from the plug formation or the bending deflection of the panes during low velocity impact. Delamination between the layers was also observed for the previously mentioned configurations, but were more prominent in panels with highest density lower layer.
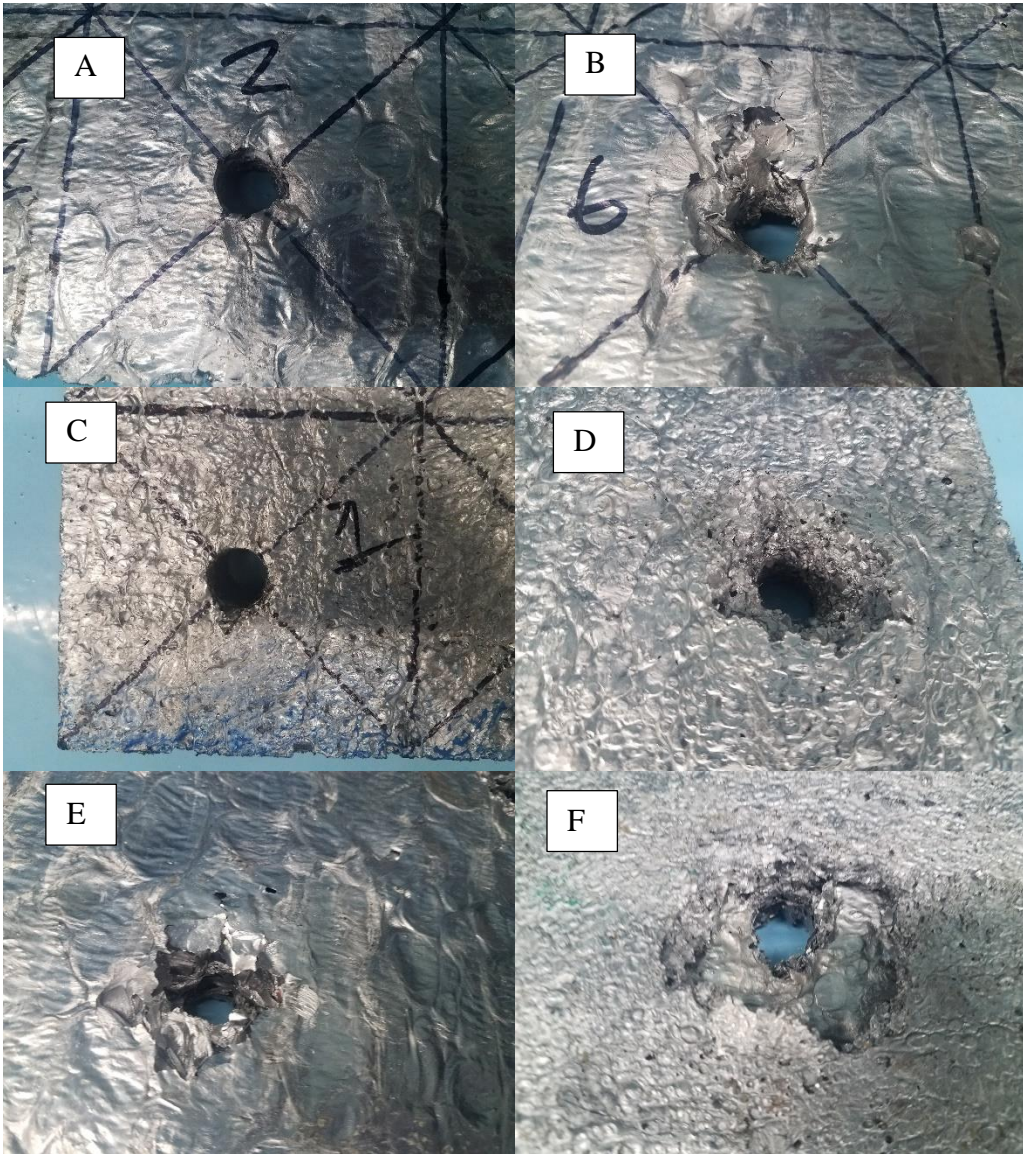
Figure 73. Cymat Failure Surfaces for Front (A-C) and Back Surfaces (D-F)

CHAPTER VI: DIRECT IMPACT OF FUCNTIONALLY GRADED METALLIC FOAMS - RESULTS/DISCUSSION

Direct impact tests were conducted on Duocel pure metallic foams and Duocel metallic/polymer infused composites to characterize the response of both uniform and functionally graded metallic foam and metallic/polymer composites. Strain-rate for all samples was maintained at ~ 500/s by varying velocity of impact striker in the REL Tension/Compression SHPB test equipment. Resultant analysis provides insight on the energy absorption capabilities of pure Foam-iT™ 3lb polymer infused metallic foams under direct compression impact loading.

Dynamic Stress-Strain relations (Fig. 74), for non-infused variations show typical responses like quasi-static compression of foam material. Three prominent regions are observed, an initial linear increase in strength, followed by a plateau region, trailed by a densification region. Compressive response of Foam-it 3lb yielded the lowest initial stiffness, followed by DNIL2, DNIH2L2H2 and DNIL2H2L2 which has approximately the same initial stiffness. Panels made from 3-layers of highest density Duocel foam (DNIH2) exhibited the highest initial stiffness before plateau region due to thickness of the framework providing greater resistance to deformation during impact. Plateau region of Foam-it 3lb remained relatively constant until 60% strain where densification regions starts. DNIH2, DNIL2, DNIH2L2H2, and DNIL2H2L2 did not exhibit a well-defined plateau region consistent with quasi-static compression, but rather show a hardening or slight densification that accumulates over increasing compressive strain. Comparison of

uniform panel configuration compared to functionally graded panels show a decrease and increase in response relative to DNIH2 and DNIL2 respectively.
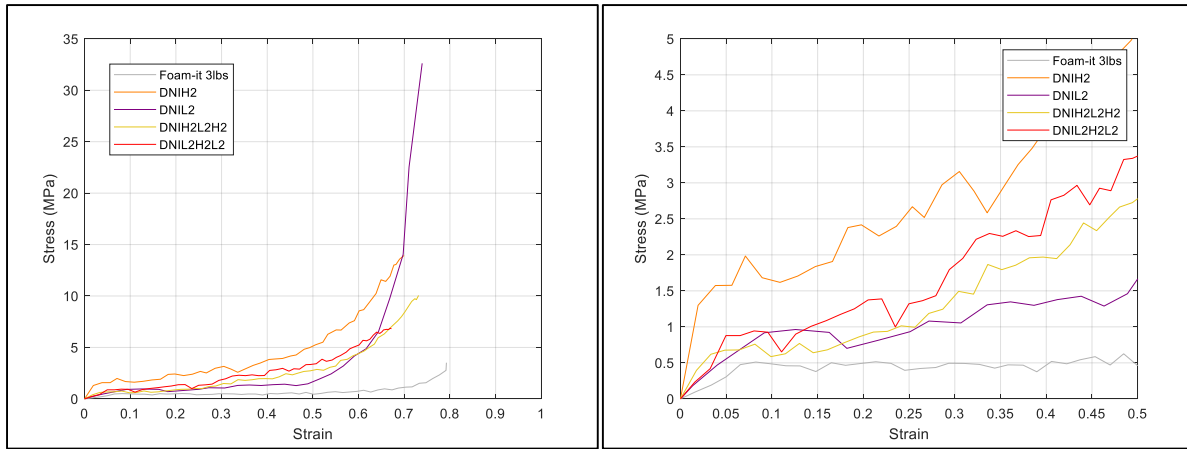
Figure 74. Dynamic Stress-Strain for Foam-it 3lb and Non-Infused Uniform and Functionally Graded Configurations

Samples with infusion had increased compressive load capacity with respect to non-infused variation of same stacking sequence (Fig. 75). As stated previously, the Foam-it 3lb provide increase resistance to strut movement in buckling/bending collapse. At up to 50% strain the trend seen in the strength of the configuration is consistent with non-infused variations with the exception of initial stiffness. DIL2 samples exhibited an increased initial stiffness that were previously consistent in the non-infused samples.
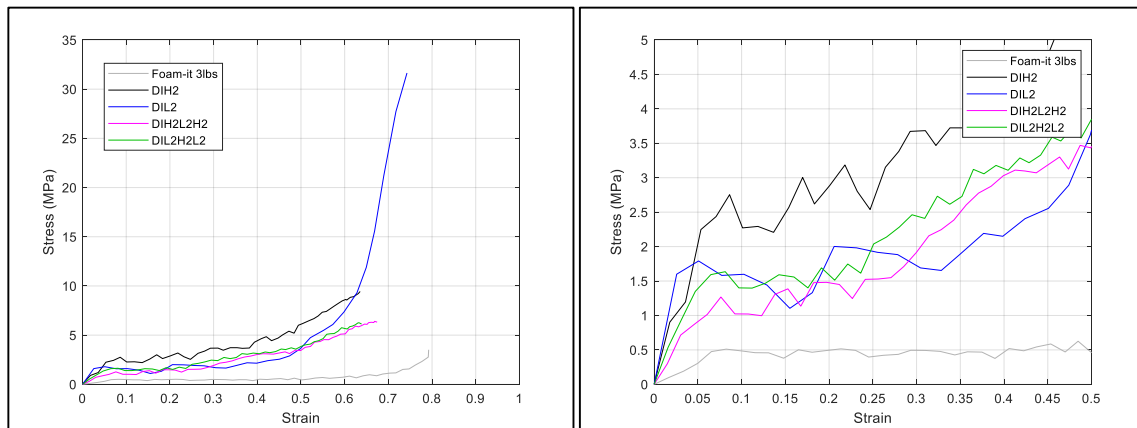
Figure 75. Dynamic Stress-Strain for Foam-it 3lb and Infused Uniform and Functionally Graded Configurations

From high speed imaging (Fig. 76) it is clear that compression during impact is localized in areas with lower strength, and was seen for all samples tested. Samples with uniform properties had localized deformation at random locations relative to thickness, due to the inconsistent properties of the metallic foam through the thickness. Functionally graded samples had localized compression in area with 4-6% RD foam for all tested samples, however the location within the 4-6% RD and the relative location to impact was not consistent. I.E. several samples had more compression in the 4-6% RD in the layer closest to the impact location and others had more deformation in area located further away. Based on computational simulation during quasi-static compression this is due to direction and thickness of the framework struts.
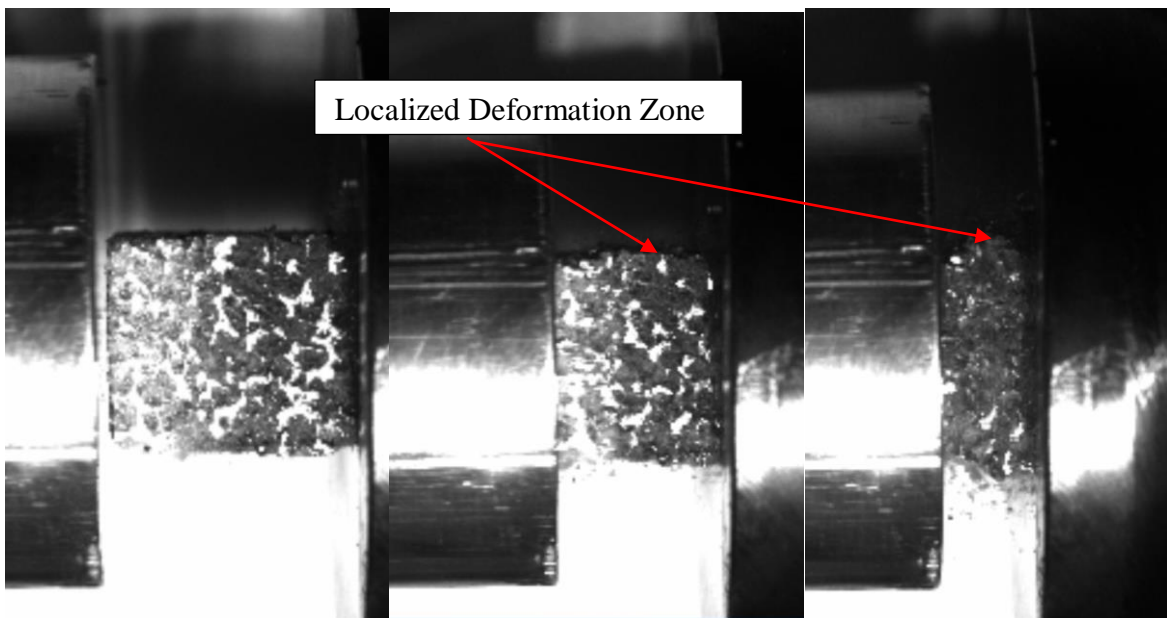
Figure 76. Localized Compression of Metallic Foam/Metallic-Polymer Composite Layers

Specific energy absorption was calculated with respect to compressive strain of the material to correct for difference in aspect ratio and impact velocity. Foam-it 3lb samples provided higher specific energy absorption (Fig. 77) as compared to all uniform and functionally graded materials with and without infusion up to approximately 65% strain for non-infused and 55% for

infused. Once densification starts in DNIL2 samples the specific energy absorption surpasses that of the Foam-it 3lb. At 45% strain of the metallic foam configurations the DNIH2 had the highest specific energy absorption, followed by DNIL2, DNIL2H2L2, and finally DNIH2L2H2. While DNIH2 configuration exhibited the highest specific energy up to approximately 65% and 67% strain densification of DNIL2 surpasses DNIH2 and DNIL2H2L2. Absorption characteristics of DNIH2L2H2 lags behind all other configurations, however based on the trend would inevitably surpass all configurations at about 80-90% strain. Consistent trends of specific energy absorption were seen in infused variations (Fig. 78). However, the densification of DIL2 started at 50% strain as opposed to 63% strain. This increase allowed the DIL2 configuration to surpass the energy absorption capabilities of Foam-it 3lb at approximately 58%. Higher energy absorption was seen for all infused configurations compared to non-infused.
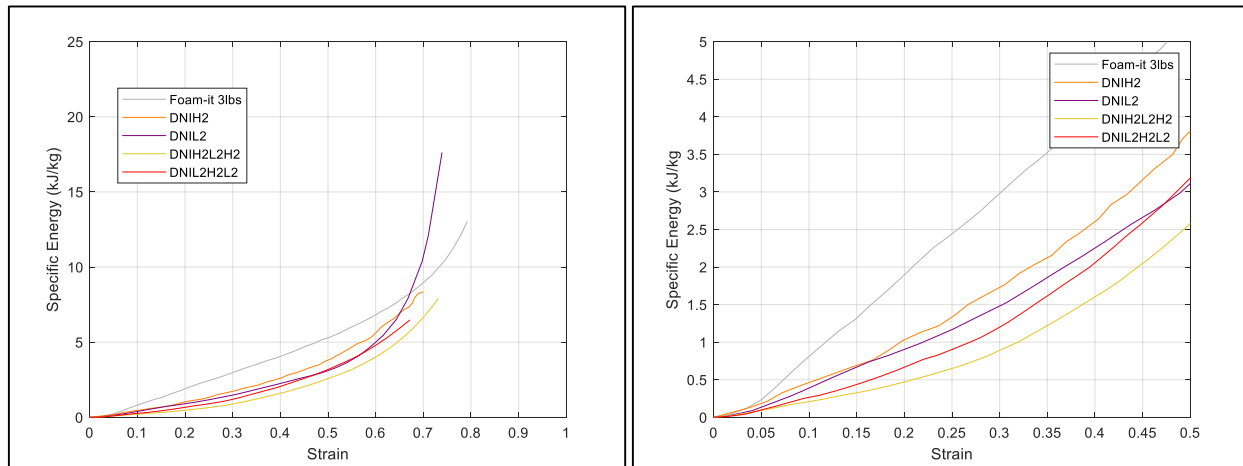
Figure 77. Compressive Specific Energy Absorption for Foam-it 3lb and Non-Infused Uniform Density and Non-Infused Functionally Graded Configurations
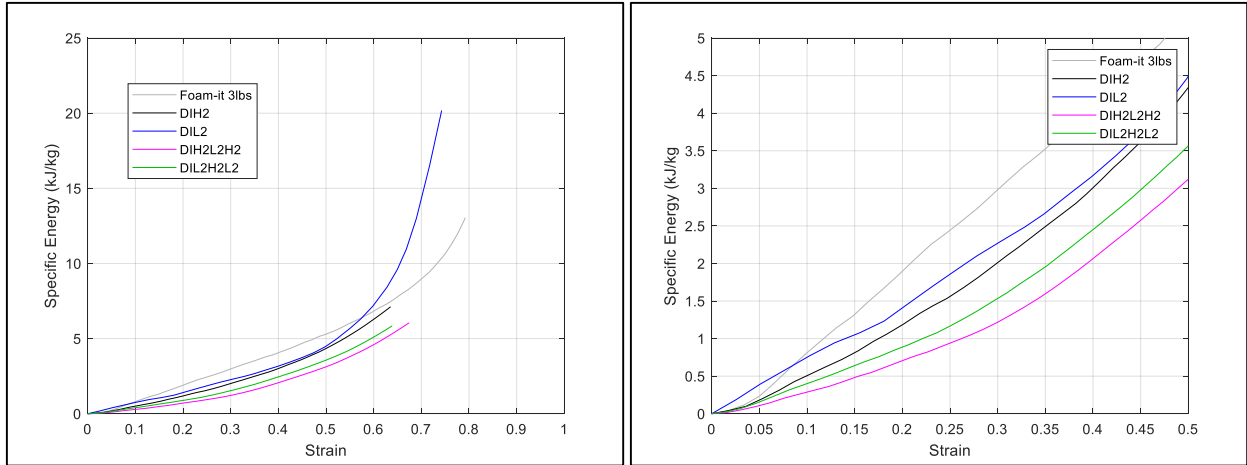
Figure 78. Compressive Specific Energy Absorption for Foam-it 3lb and Infused Uniform Density and Infused Functionally Graded Configurations

Stress-strain and energy absorption comparison of infused variations to non-infused show increases within the plateau region in all cases (Fig. 79-82). However, in all cases a shift during the densification region was seen in the strength of the material. In essence the strength of the non-infused variation exceeded that of the infused variations. This shift on response is due to the change in dominate material. In the initial and plateau region the composite material response dominates the overall constitutive (stress-strain) relationships, and once densification starts the metallic foam dominates the response.
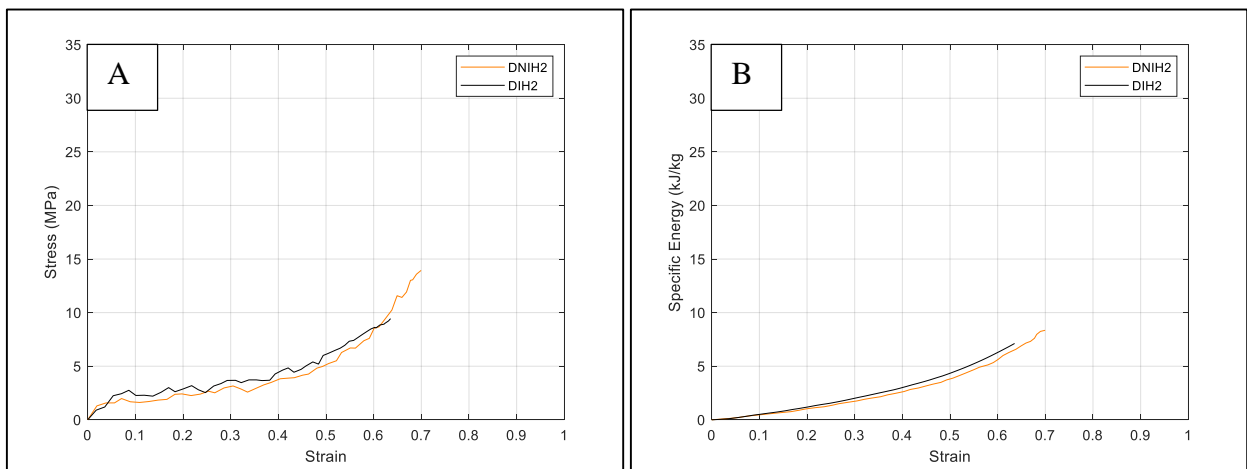
Figure 79. Dynamic Stress-Strain (A) and Specific Energy (B) Comparison of DNIH2 and DIH2 Configuration
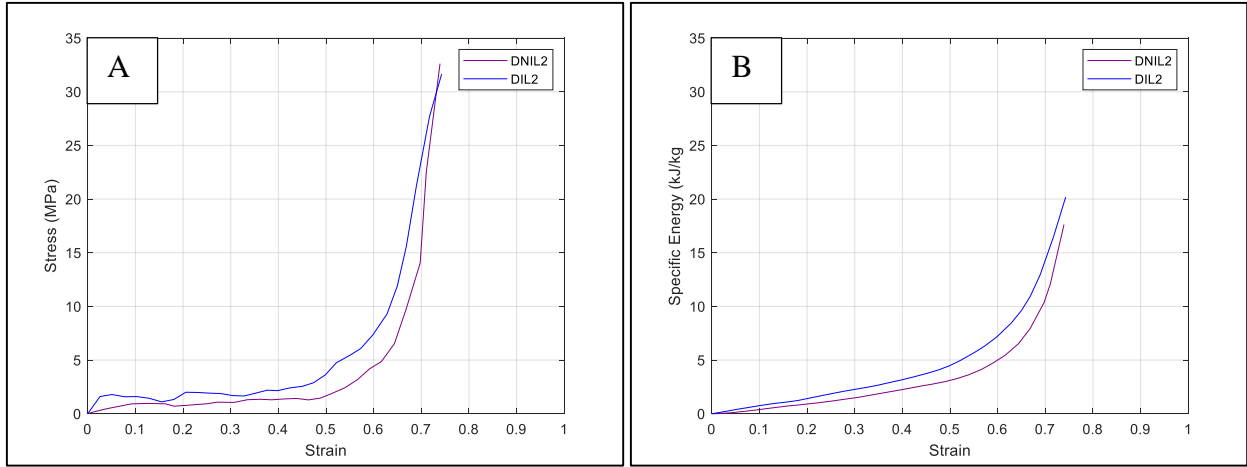
Figure 80. Dynamic Stress-Strain (A) and Specific Energy (B) Comparison of DNIL2 and DIL2 Configuration
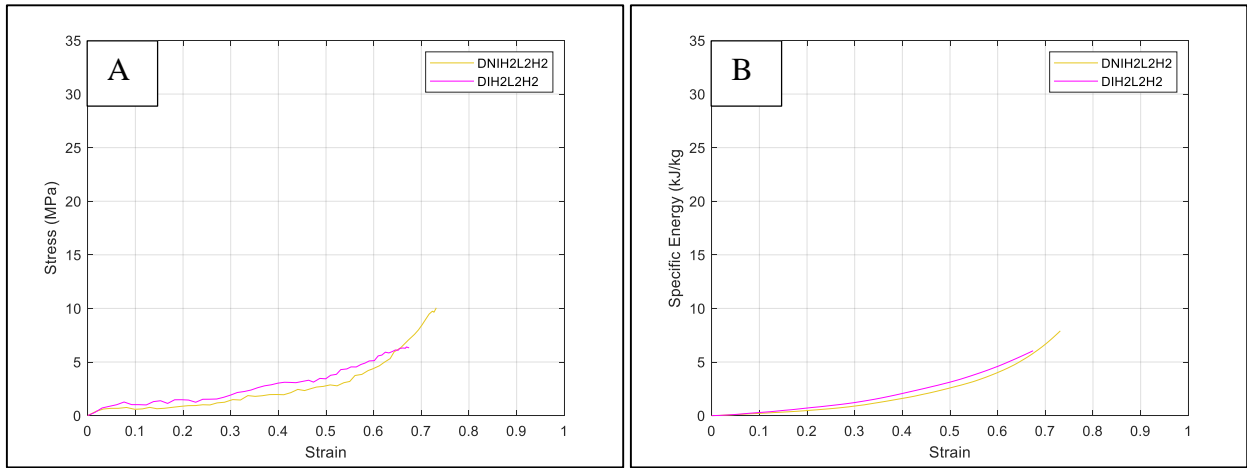
Figure 81. Dynamic Stress-Strain (A) and Specific Energy (B) Comparison of DNIH2L2H2 and DIH2L2H2 Configuration
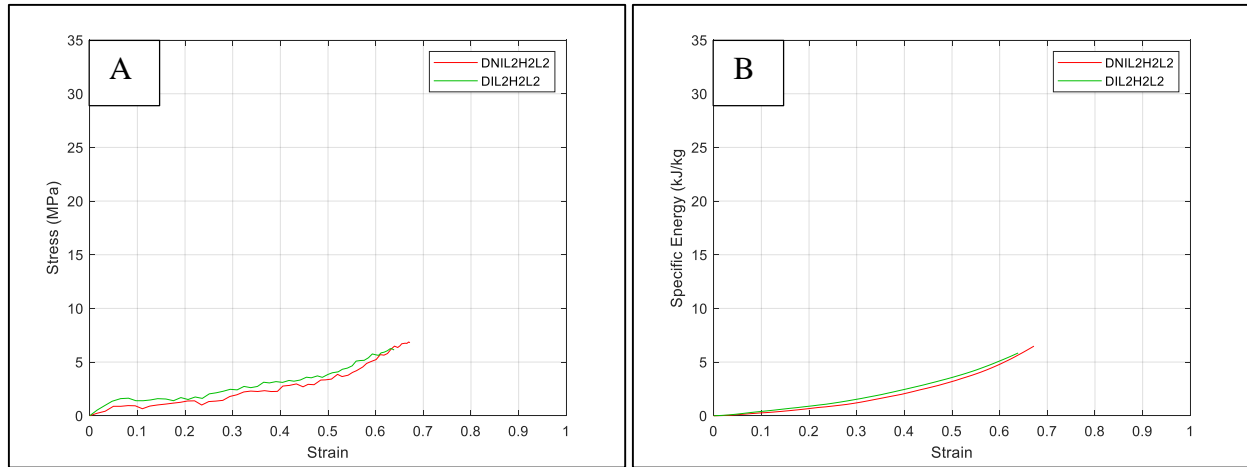
Figure 82. Dynamic Stress-Strain (A) and Specific Energy (B) Comparison of DNIL2H2L2 and DIL2H2L2 Configuration

Density of all material configurations can be seen in Figure 83. Only slight increases were observed due to the low density of the Foam-it 3lb material with the exception of DNIL2 compared to DIL2 configurations. Composite panels were manufactured and bonded using the same technique as low-velocity samples. As previously stated the bonding agent added a significant amount of mass due to its high density. Plateau and specific plateau strength increased for all metallic/polymer foam variations as compare to non-infused (Fig. 84-85, Table 8). This increase in strength is due to the role that the Foam-it 3lb plays on the compressive properties and the mechanism of deformation in each region (initial, plateau, and densification) of the compressive response. Increases ranging from 18%-89% and 11%-50% (Table 9) were seen when comparing non-infused and infused variations. DIH2 specimens only provided an 18% and 11% increase in plateau strength and specific plateau strength, respectively, revealing that the response is largely dominated by the metallic foam. An 89% and 39% increase was observed for DIL2 samples for plateau strength and specific plateau strength, respectively. This can be attributed to the added benefits of the composite response during the different regions (initial, plateau, and densification). DIH2L2H2 specimens' strength and specific strength increased by 76% and 50%, respectively.

111

The increased strength is due to not only the deformation mechanisms, but also the functionally gradation of the composite material; which previously had failure zone located at areas of lower density that are now infused slowing the progression of compressive collapse. Functionally graded samples, DIL2H2L2 did not exhibits as high of an increase in plateau strength and specific plateau strength (49% and 25%) as the DIH2L2H2 samples on average providing more incite to the role functionally gradation plays in the dynamic compressive response.
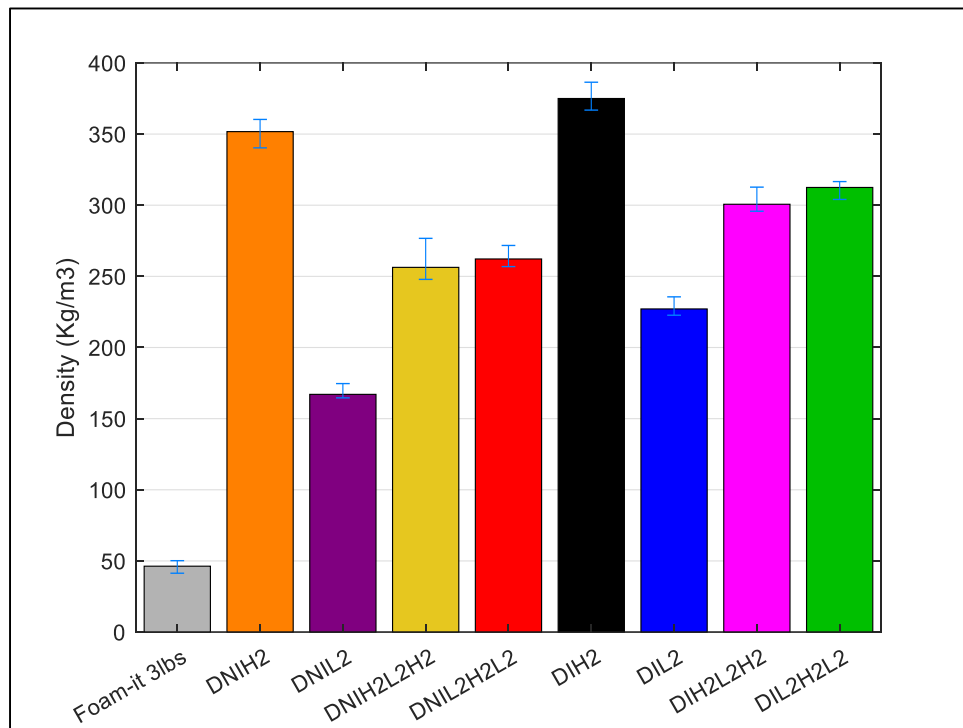
Figure 83. Density of Foam-it 3lb, and Non-Infused and Infused Uniform and Functionally Graded Configurations
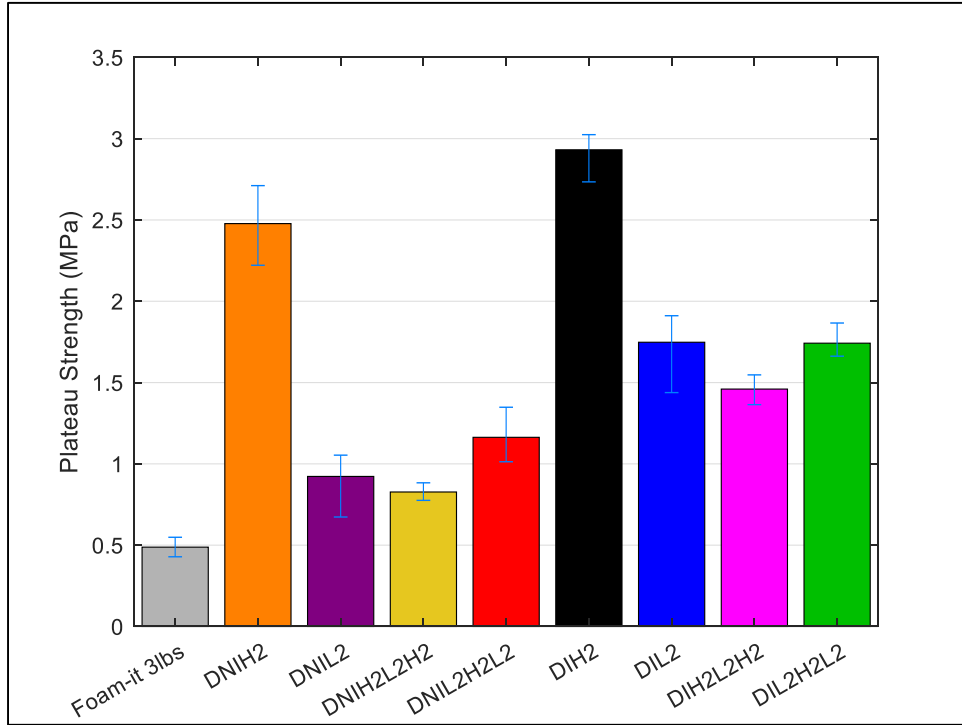
Figure 84. Plateau Strength of Foam-it 3lb, and Non-Infused and Infused Uniform and Functionally Graded Configurations
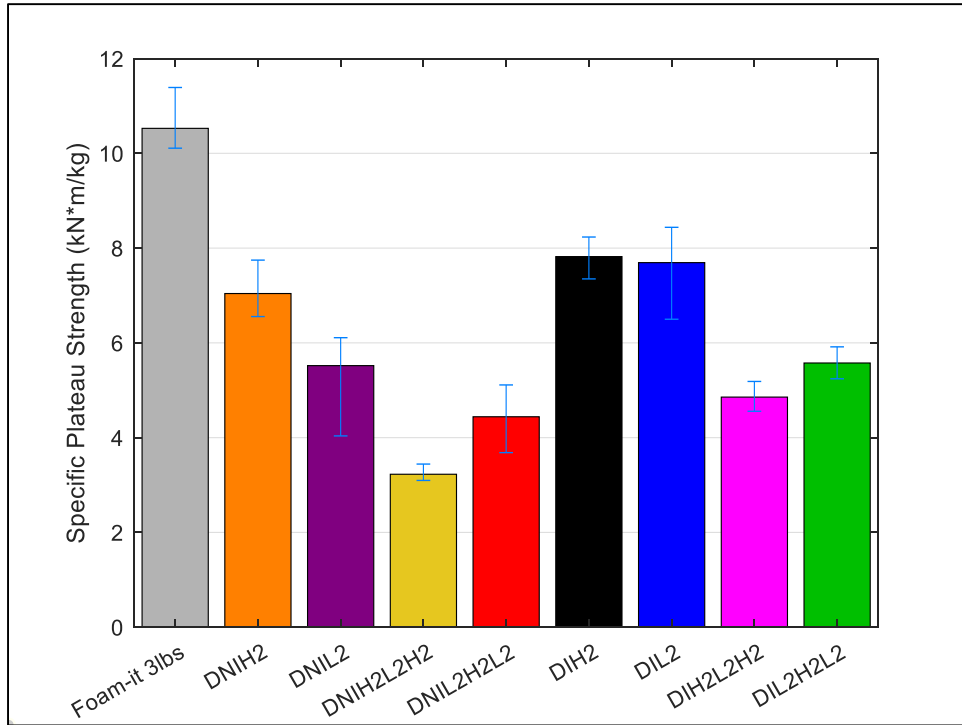
Figure 85. Specific Plateau Strength of Foam-it 3lb, and Non-Infused and Infused Uniform and Functionally Graded Configurations

Table 8. Density, Plateau Strength, and Specific Plateau Strength for Metallic Foam and Metallic/Polymer Foam Composite Uniform and Functionally Graded Composites

Panel Configuration	Density (kg/m³)	Plateau Strength (MPa)	Specific Plateau Strength (kN*m/kg)
Foam-it 3lb	46.30	0.49	10.52
DNI(H2)3	351.72	2.48	7.04
DNI(L2)7	167.07	0.92	5.52
DNIH2(L2)2H2	256.31	0.83	3.23
DNIL2(H2)2L2	262.21	1.16	4.44
DI(H2)3	374.99	2.93	7.82
DI(L2)7	227.10	1.75	7.69
DIH2(L2)2H2	300.67	1.46	4.86
DIL2(H2)2L2	312.48	1.74	5.58

Table 9. Percent Increase for Density, Plateau Strength, and Specific Energy for Metallic/Polymer Foam Composites to Non-Infused Metallic Foam Under Direct Impact Compression

Panel Configuration % Increase	Density (kg/m³)	Plateau Strength (MPa)	Specific Plateau Strength (kN*m/kg)
DI(H2)3-->DNI(H2)3	6.6	18.3	11.0
DI(L2)7-->DNI(L2)7	35.9*	89.4	39.3
DIH2(L2)2H2-->DNIH2(L2)2H2	17.3	76.5	50.4
DIL2(H2)2L2-->DNIL2(H2)2L2	19.1	49.7	25.5

* Density increase due to bond agent

CHAPTER VII: SPLIT HOPKINSON PRESSURE BAR RESULTS/DISCUSSION

7.1 Split Hopkinson Pressure Bar Experimental Results/Discussion

Split Hopkinson Pressure Bar tests were performed to understand the effects of the polymeric infusion on the dynamic properties of pure Al 6101-T6 metallic foam. High speed camera images revealed consistent localized deformation mechanism present in quasi static experimentation. Figure 86-87 shows a typical SHPB sample of 4-6% RD metallic foam and 4-6% RD metallic/polymer foam, and the localized deformation present on the right side of the specimen. As previously stated this is due to the inconsistent strut thickness causing areas of lower strength. Observation of high speed images show that more localized deformation is present in metallic foam samples as compared to infused variations, showing that the infusion process allows for a more uniform distribution of stress as it propagates through the material. Global strain was validated using DIC analysis and strain-time can of a typical SHPB experiment can be seen in Figure 88.
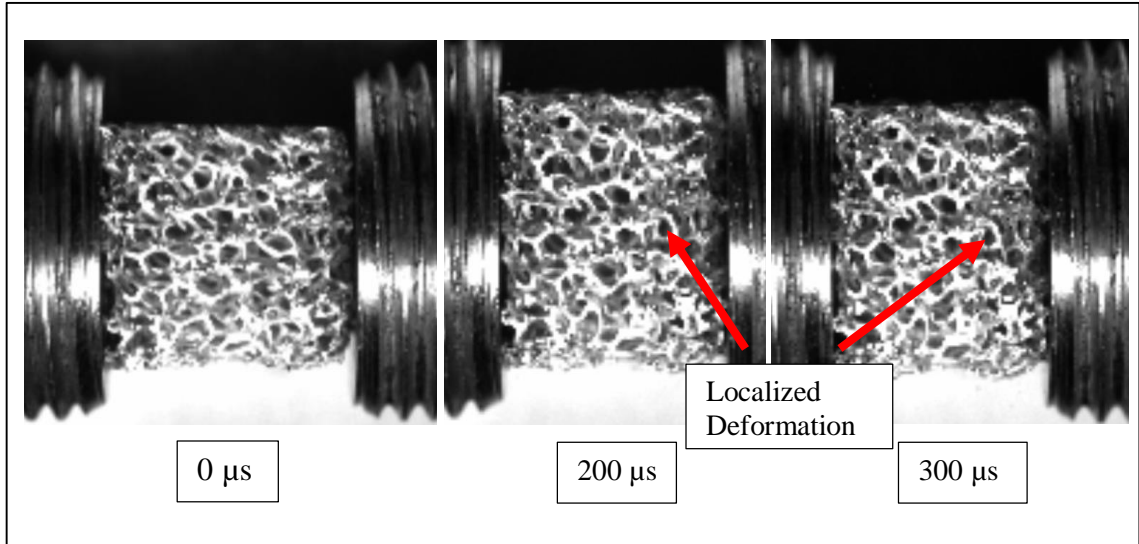
Figure 86. Split Hopkinson Pressure Bar Compression of 4-6% RD Duocel Metallic Foam
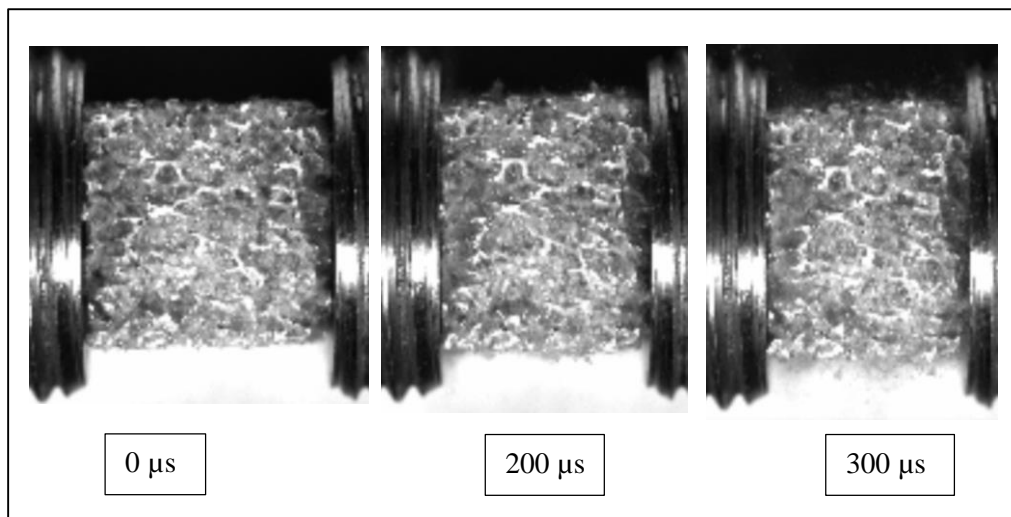
Figure 87. Split Hopkinson Pressure Bar Compression of 4-6% Foam-it!™ Infused Composite
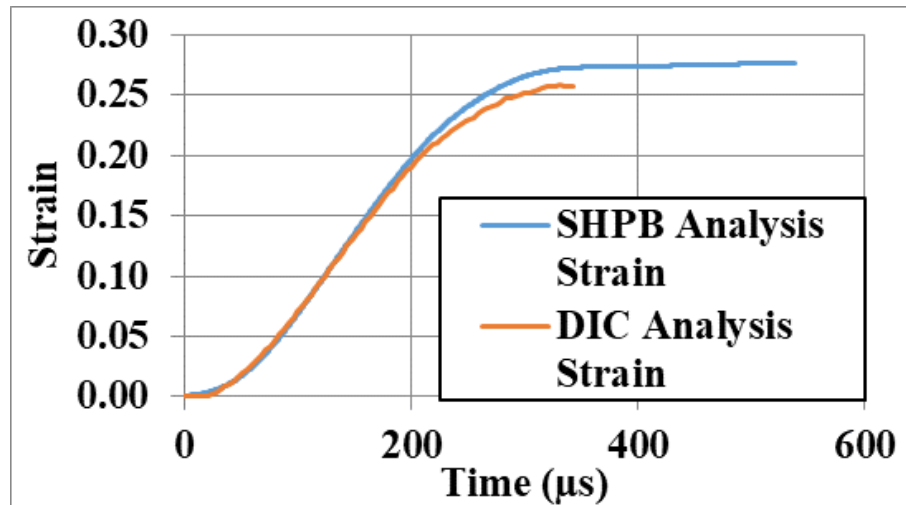
Figure 88. Digital Image Correlation and Conventional Split Hopkinson Pressure Bar Strain Comparison

Typical scatter expected in composite materials was observed in the dynamic stress-strain response of all the materials tested. Figure 89 displays the dynamic stress-strain response of the 10-12% Foam-it!™ infused composite at 1750/s strain rate. As can be seen small changes in initial stiffness of the material are present. Variation in plateau strength can clearly be seen for the 15 specimens plotted. Plateau strength was defined as the average strength between 10% strain at 20% strain for 1100/s and 1450/s strain-rate (unable to achieve 30% strain), and between 10% strain and 30% strain for the 1750/s strain-rate. These variations in initial strength and stiffness were present in all the evaluated sample types. The variation in response can be attributed to inconsistencies these types of materials. During curing the Foam-it!™ should be freely allowed to expand. Any restriction could cause variation in the density of the materials, and is likely why the Foam-it!™ material has large variation in both the quasi static and dynamic response. The metallic foam is also inconsistent due to the manufacturing method. These variations were seen for both relative densities of metal, and is also likely the cause of variation in dynamic properties. Overall larger variations were seen in the Foam-it!™ 3lb material versus the pure metallic and

117

infused composite materials, likely due to the Foam-it!™ 3lb exhibiting more brittle type failure during compression.
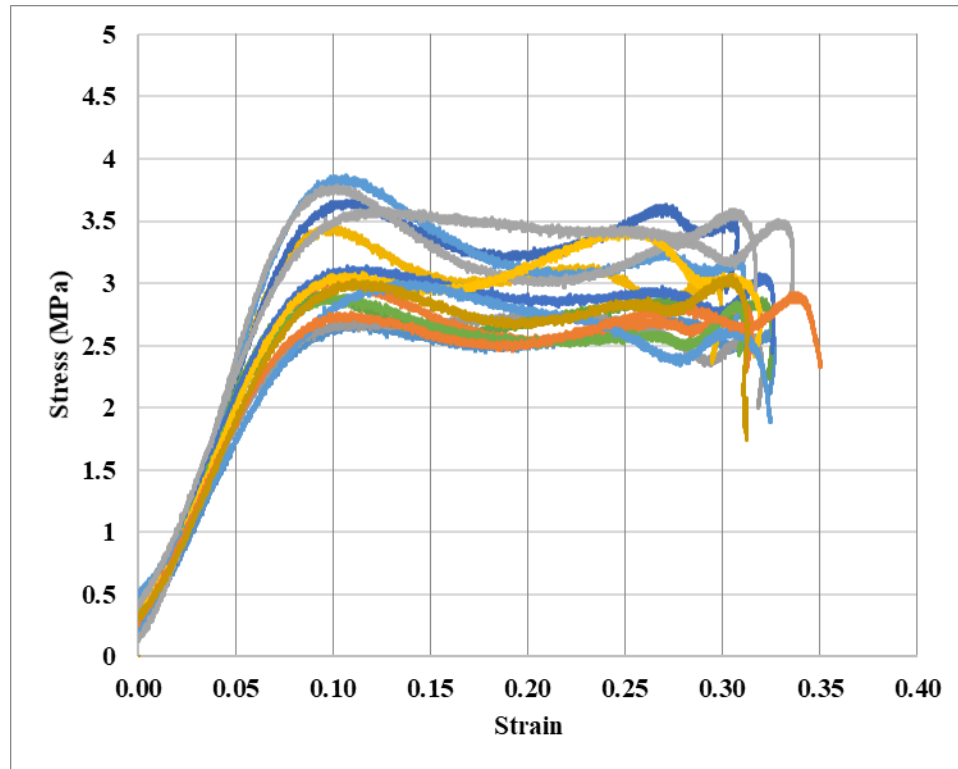
Figure 89. Typical Scatter in the Stress-Strain Response of 10-12% Foam-it!™ Infused Composite

Dynamic stress-strain trends showed negligible changes in strength and specific energy at both 10% and 20% strain for 4-6% metallic foam and 10-12% metallic foam with increasing strain-rate. The Foam-it!™ 3lb material, and both 4-6% Foam-it!™, and 10-12% Foam-it!™ composite had an overall decreasing trend in strength and specific energy at 10% and 20% strain as strain-rate was increased. However, the trend comparing base metal material to infused composite material shows an increase in both plateau strength and specific energy. Figures 90-94 show the average dynamic compression stress-strain response of each material at three strain-rates.
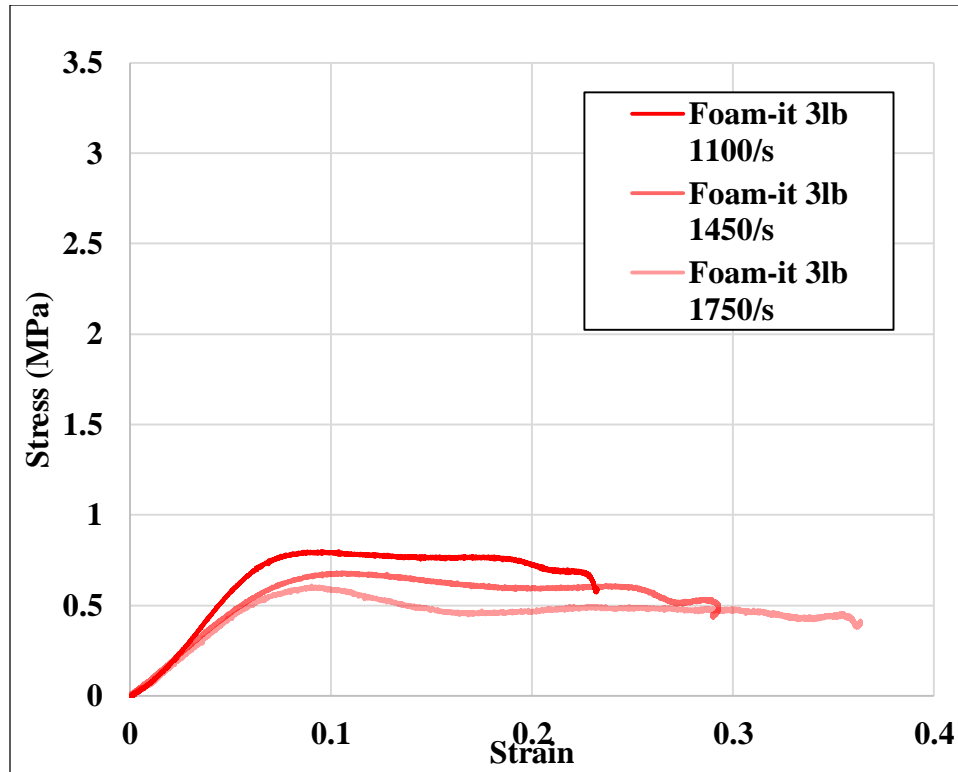
Figure 90. Foam-it!™ 3lb Dynamic Compression Stress-Strain Responses
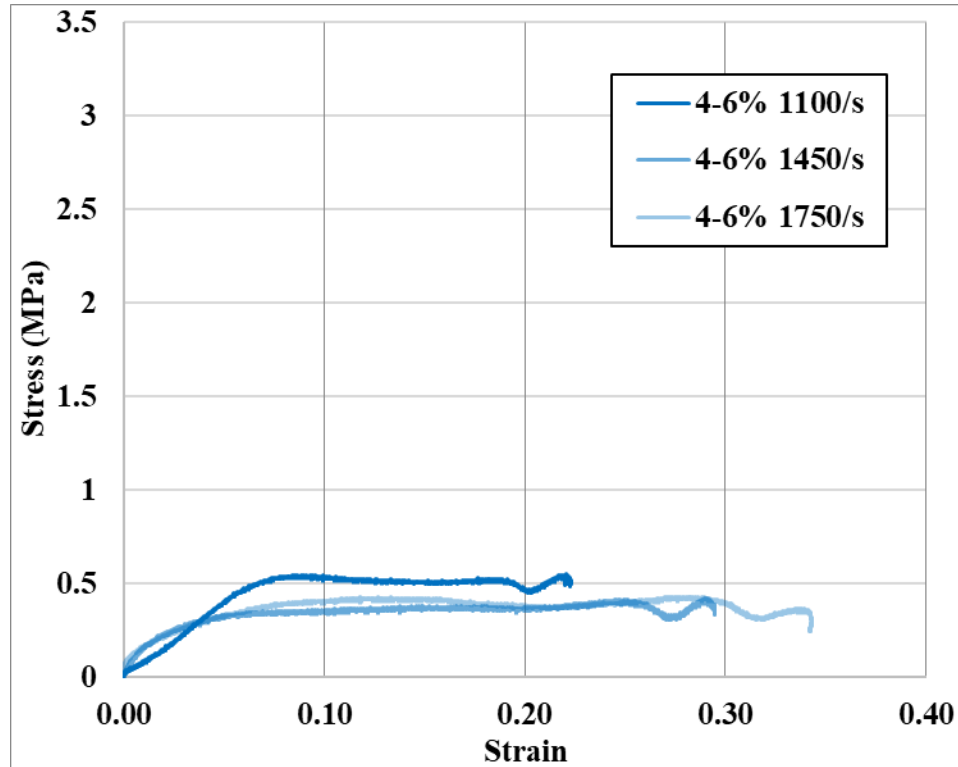
Figure 91. 4-6% Relative Density Dynamic Compression Stress-Strain Responses

119
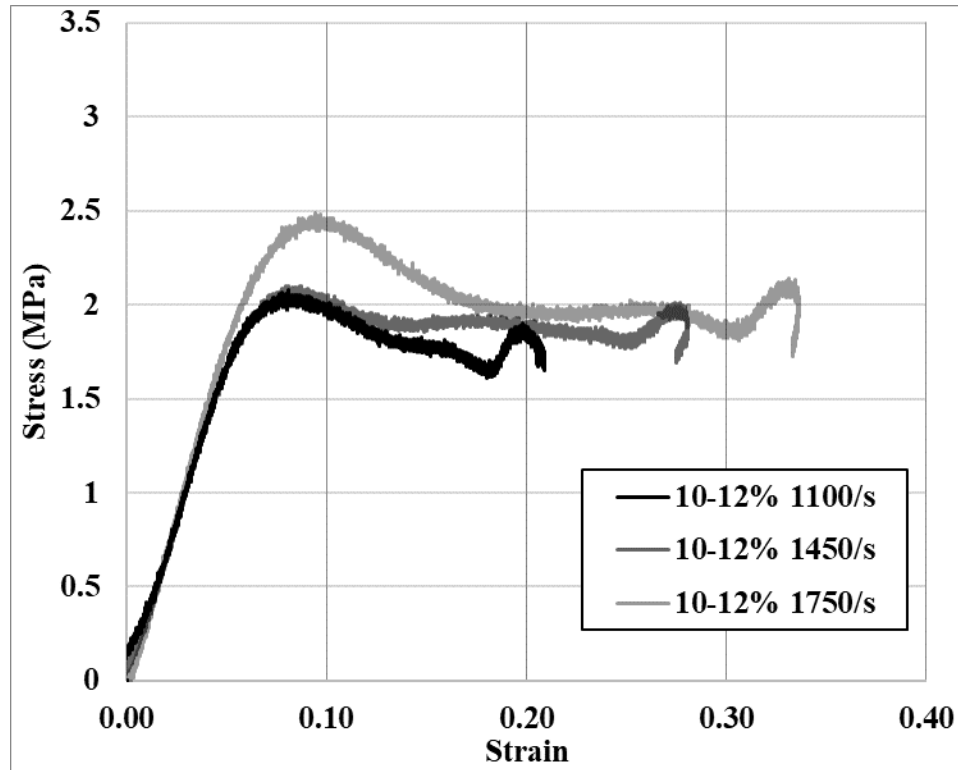
Figure 92. 10-12% Relative Density Dynamic Compression Stress-Strain Response
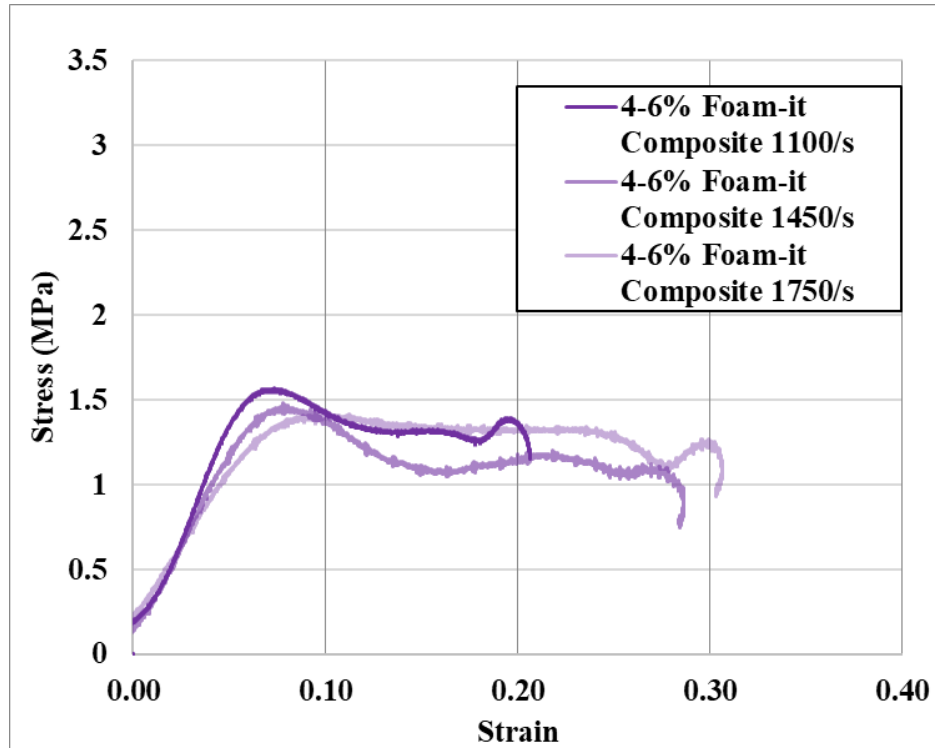
Figure 93. 4-6% Foam-it!™ Infused Composite Dynamic Compression Stress-Strain Response
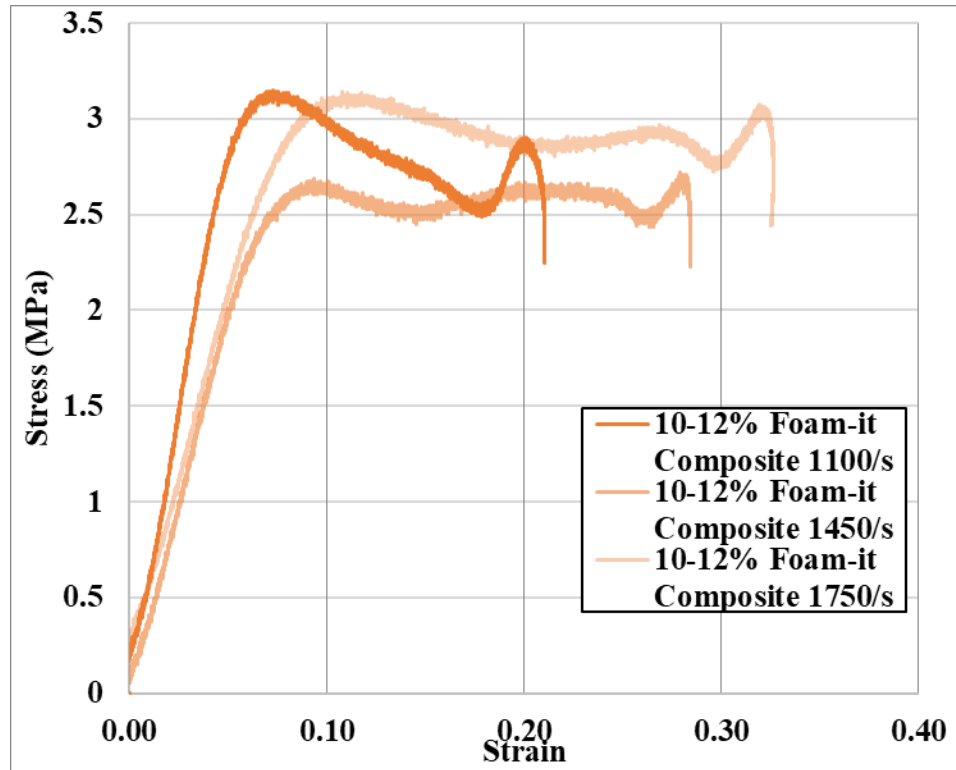
Figure 94. 10-12% Foam-it!™ Infused Composite Dynamic Compression Stress-Strain Response

Increase in strength and specific energy when comparing the response of the metallic foam to the infused composite material were seen in all cases analyzed at the same strain rate and when comparing the quasi static response to the maximum response at high strain-rate. The increase in response when comparing 4-6% RD to 4-6% Foam-it!™ composite ranged from 200% to 220%, 85% to 229% and 111% to 153% for the plateau strength, specific energy at 10% strain and 20% strain respectively. In all cases the 1100/s exhibited the highest average plateau strength and specific energy for the infused composite material. When comparing the quasi static response to the dynamic response (1100/s) for the plateau strength, specific energy at 10% and 20% an increase of 298%, 282%, and 223% was seen respectively. The substantial increase in strength can be attributed to the added resistance to the metallic framework motion and crushing of infused polymeric foam during dynamic compression. The average response of the Foam-it!™ 3lb, 4-6%,

121

and 4-6% Foam-it!™ infused composite for plateau strength, specific energy at 10% strain, and

specific energy at 20% strain for both quasi static and dynamic response can be seen in figures 95-

97. Increases when comparing 4-6% RD and 4-6% Foam-it!™ infused composite are summarized

in Table 10.
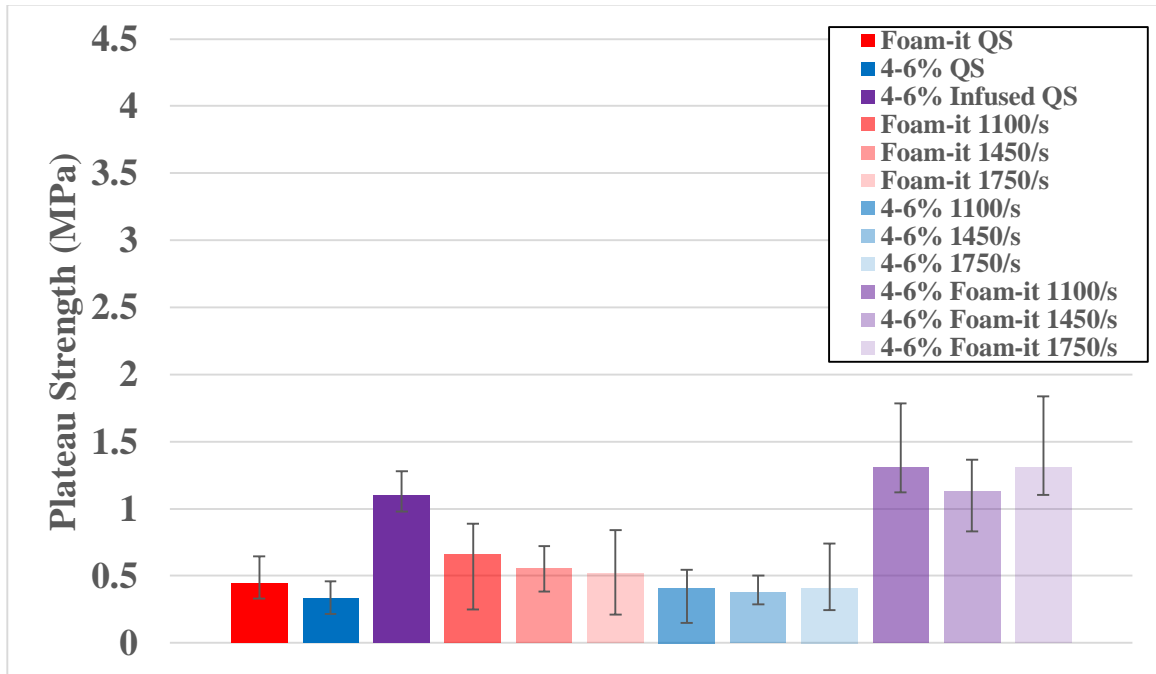
Figure 95. 4-6% Plateau Strength for Quasi Static and Dynamic Response of Foam-it!™ 3lb, 4-6% Relative Density, and 4-6% Foam-it!™ Infused Composite Materials
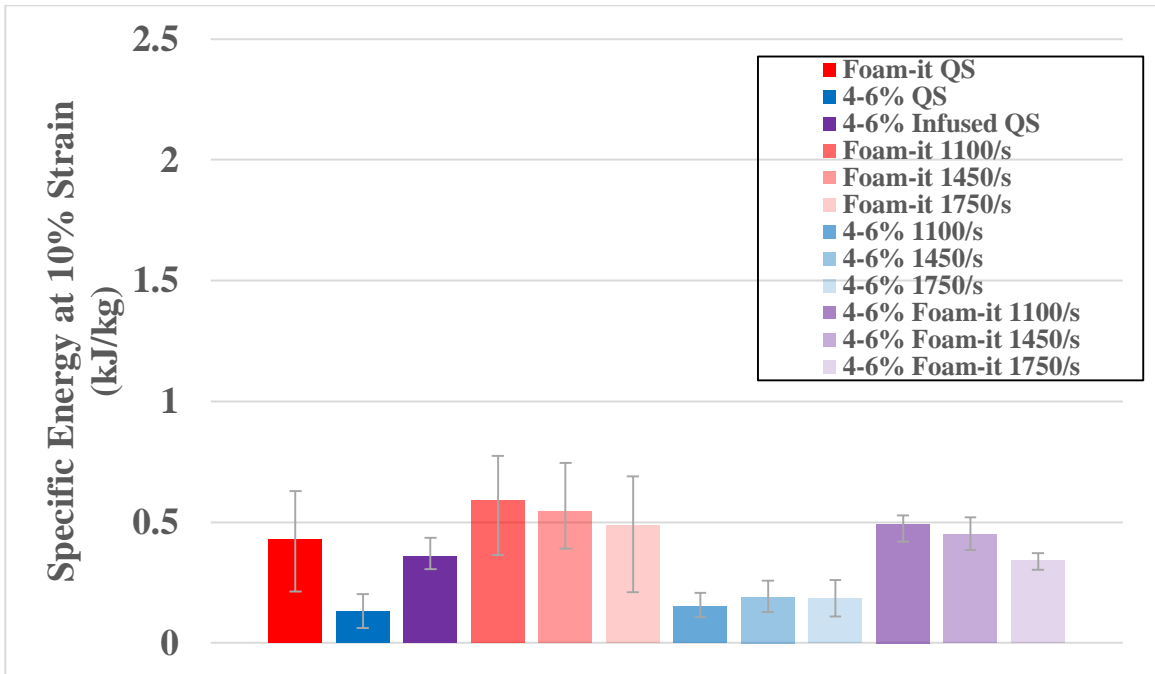
Figure 96. 4-6% Specific Energy at 10% for Quasi Static and Dynamic Response of Foam-it!™ 3lb, 4-6% Relative Density, and 4-6% Foam-it!™ Infused Composite Materials
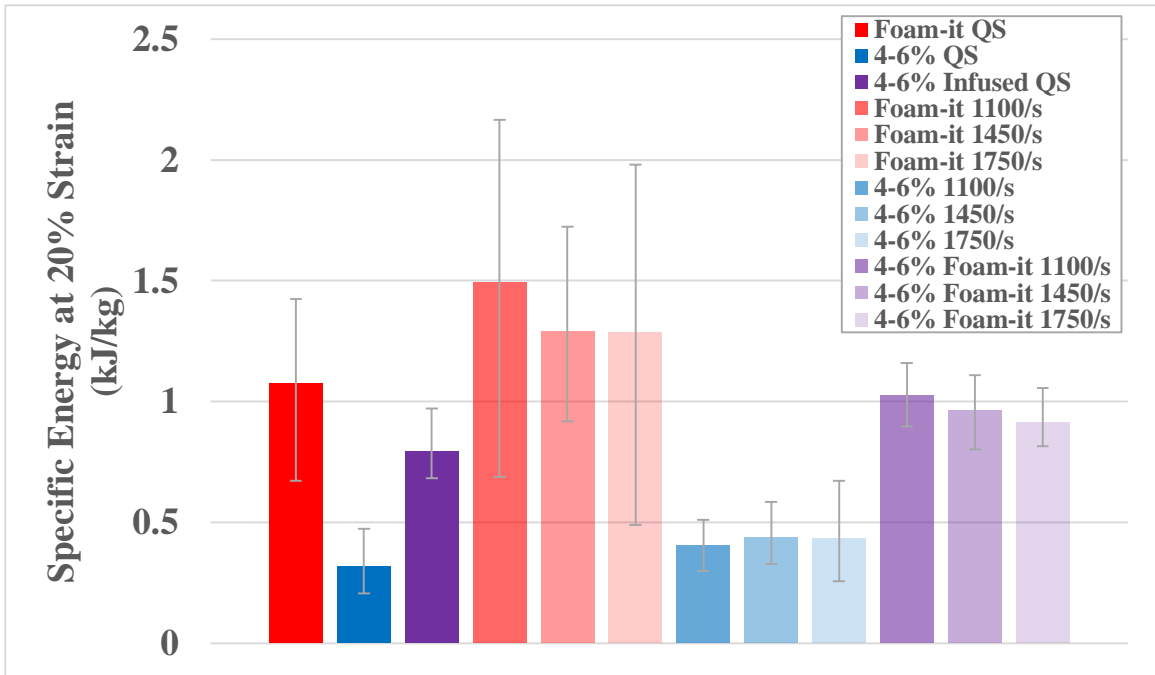
Figure 97. 4-6% Specific Energy at 10% for Quasi Static and Dynamic Response of Foam-it!™ 3lb, 4-6% Relative Density, and 4-6% Foam-it!™ Infused Composite Materials

Table 10. Comparison of 4-6% RD to 4-6% Foam-it!™ Infused Composite Materials, and Quasi Static to Dynamic SHPB Comparison

Plateau Strength (MPa)	4-6% RD	4-6% Foam-it!™ Infused Composite	Percent Increase
1100/s	0.44	1.31	220%
1450/s	0.38	1.13	200%
1750/s	0.41	1.30	217%
Specific Energy (kJ/kg) at 10% Strain			
1100/s	0.15	0.49	229%
1450/s	0.19	0.45	135%
1750/s	0.18	0.34	85%
Specific Energy (kJ/kg) at 20% Strain			
1100/s	0.41	1.03	153%
1450/s	0.44	0.96	120%
1750/s	0.43	0.91	111%
Quasi Static - Dynamic SHPB (1100/s)	Quasi Static	4-6% Foam-it!™ Infused Composite (1100/s)	
Plateau Strength (MPa)	0.32	1.31	298%
Specific Energy (kJ/kg) at 10% Strain	0.13	0.49	281%
Specific Energy (kJ/kg) at 20% Strain	0.32	1.03	224%

The 10-12% RD metallic foam response did not have nearly as sizable increases in the plateau strength and specific energy as the 4-6% RD. It is believed that this is due to the response of the 10-12% RD metallic foam dominating the overall dynamic response of the material. However, increase in plateau strength and specific energy were seen when comparing the 10-12% RD to the 10-12% Foam-it!™ infused composite material at the same strain rate as well as when comparing the quasi static response to the dynamic response. An increase of 27% to 45%, 20% to 53%, and 10% to 23% was seen for the plateau strength, specific energy at 10% strain, and 20% strain respectively (Fig. 98-100). Similarly, at 1100/s strain-rate, the infused composite material had the highest plateau strength and specific energy. When comparing the quasi static response to the dynamic response (1100/s) for the plateau strength, specific energy at 10% and 20% strain a

42%, 21%, and 14.5% increase in response was observed, respectively (Fig. 98-100). Comparison of SHPB plateau strength and specific energy can be seen in Table 11.
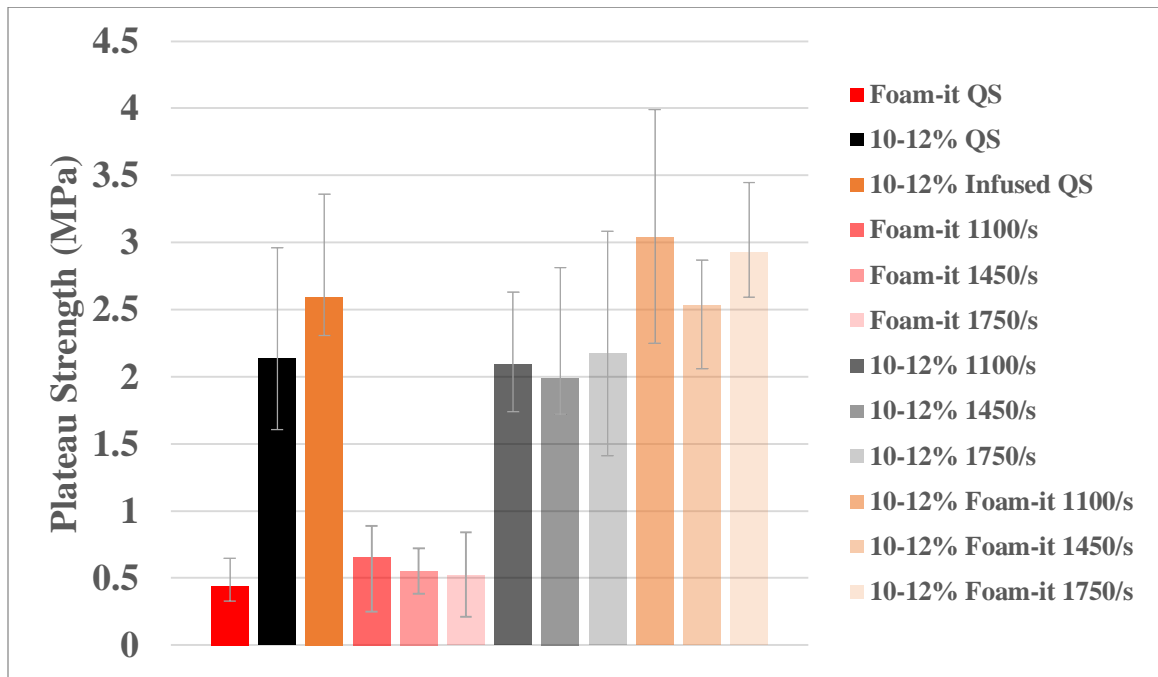
Figure 98. 10-12% Plateau Strength for Quasi Static and Dynamic Response of Foam-it!™ 3lb, 10-12% Relative Density, and 10-12% Foam-it!™ Composite Materials
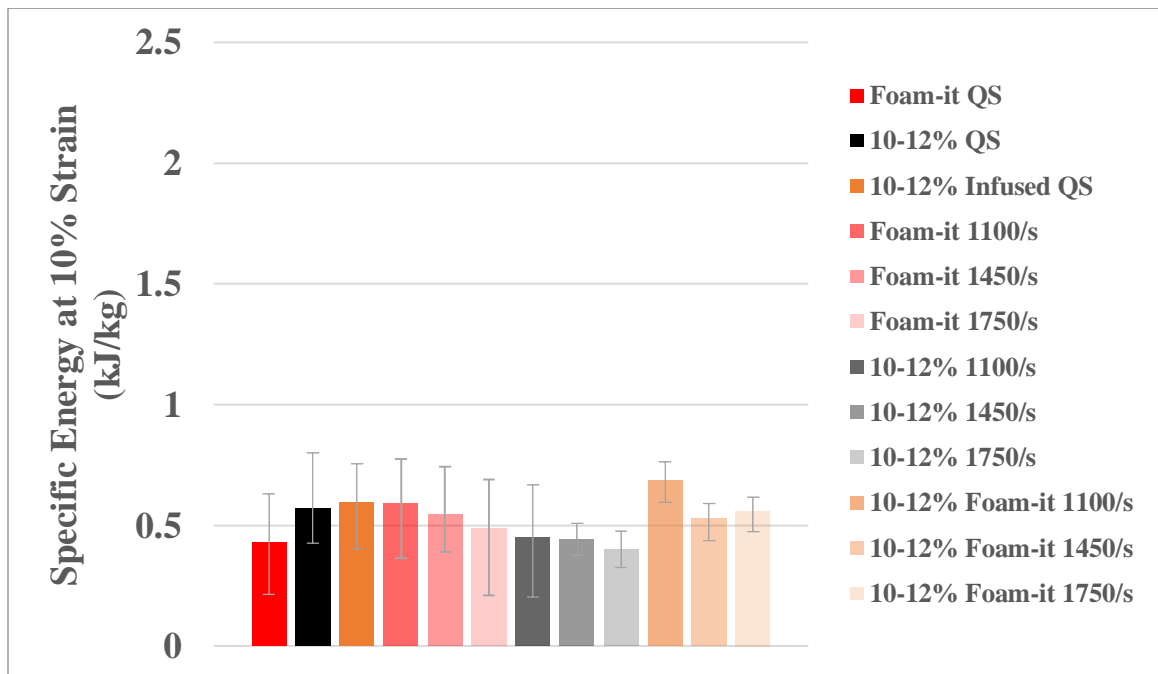
Figure 100. 10-12% Specific Energy at 20% for Quasi Static and Dynamic Response of Foam-it!™ 3lb, 10-12% Relative Density, and 10-12% Foam-it!™ Composite Materials

Table 11. Comparison of 10-12% RD to 10-12% Foam-it!™ Infused Composite Materials, and Quasi Static to Dynamic SHPB Comparison

Plateau Strength (MPa)	10-12% RD	10-12% Foam-it!™ Infused Composite	Percent Increase
1100/s	2.09	3.04	45%
1450/s	2.09	2.53	27%
1750/s	2.17	2.93	35%
Specific Energy (kJ/kg) at 10% Strain			
1100/s	0.45	0.69	53%
1450/s	0.44	0.53	20%
1750/s	0.40	0.56	40%
Specific Energy (kJ/kg) at 20% Strain			
1100/s	1.21	1.49	23%
1450/s	1.17	1.29	10%
1750/s	1.18	1.41	20%
Quasi Static - Dynamic SHPB (1100/s)	Quasi Static	10-12% Foam-it!™ Infused Composite (1100/s)	
Plateau Strength (MPa)	2.14	3.04	42%
Specific Energy (kJ/kg) at 10% Strain	0.57	0.69	21%
Specific Energy (kJ/kg) at 20% Strain	1.30	1.49	14.5%

126

Based on analyzed data the infusion of the polymeric increase the quasi static and dynamic properties of the pure metallic foam. The 4-6% metallic foam exhibited the highest increase in mechanical properties in both the quasi static and dynamic loading conditions. The increase in mechanical properties was not as high when comparing the 10-12% RD to 10-12% Foam-it!™ infused composite as the 4-6% RD to 4-6% Foam-it!™ infused composite material. It is conceivable that the higher stiffness of the 10-12% RD metallic foam framework is dominating the overall response for this composite configuration. If a higher density polymeric foam is used for infusion in the 10-12% Foam-it!™ composite it is highly likely that it will show the same increases exhibited by the 4-6% Foam-it!™ composite. Future studies will encompass incorporation of infused metallic foams in functionally graded materials (bio-inspired design), as well as variation in polymeric foam density to further understand the effects of polymeric infusion in metallic foams.

7.2 Split Hopkinson Pressure Bar Computational Results/Discussion

Computational simulations for dynamic loading were done using Dynamic Explicit option in Abaqus CAE to understand the slight performance increase in experimental results. Simulations were conducted using the same Johnson-Cook parameters and polymer foam tabular constitutive relationship used in quasi-static computational analysis. Resulting simulations revealed several findings. Firstly, an increase in stress was observed for all sample configurations as compared to quasi static loading simulations for the metallic framework. Secondly, the infused samples exhibited higher stress levels when compared to non-infused variations of similar metallic framework configuration. Lastly, when comparing non-staggered configurations to staggered configurations a decrease in strength was observed consistent with quasi-static computational results. Figure 101 A-F shows computational simulations for six variations. Based on the stress

127

levels at the edge of pores the stress achieved during dynamic compression within the metallic framework was theoretically found to be 486 MPa, 565 MPa, 432 MPa, 445 MPa, 433 MPa, and 461 MPa for non-staggered at 1100/s, non-staggered at 1750/s, staggered at 1100/s, staggered at 1750/s, infused staggered at 1100/s, and infused staggered at 1750/s, respectively. Based on resulting comparison a large increase in strength was observed when comparing quasi-static non-staggered configurations to SHPB simulations. It was also observed that the infusion did not produce a substantial increase in strength when compared to non-infused variation simulations. This is in stark contrast to experimental results which show considerable increase in strength. It is believed that the discrepancy is due to several of the underlying failure mechanism that are present in experimental results no being present in computational simulations. However, based upon the results several conclusions can be drawn. The first is that the slight increase in strength observed in dynamic SHPB compression for all samples is due largely to the metallic framework and the interaction of the polymer and metallic framework for the infused variations. It can also be concluded that as pores are randomly distributed the response becomes more isotropic. Lastly, it can be concluded that several additional failure mechanisms are present in the experimental results that have yet to be characterized by such simplified models.
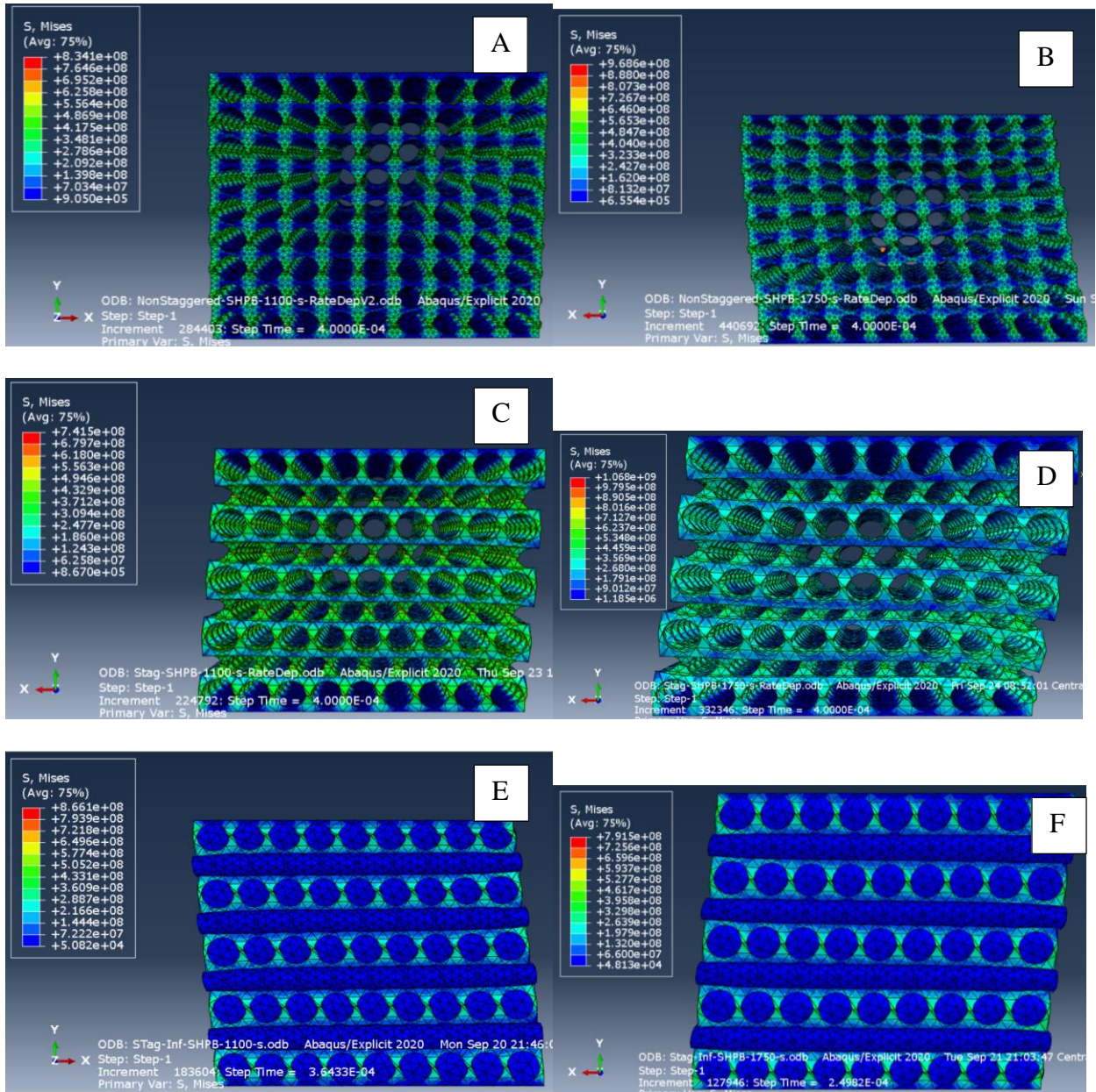
Figure 101. (A) Non-Staggered SHPB 1100/s, (B) Non-Staggered SHPB 1750/s, (C) Staggered 1100/s SHPB, (D) Staggered SHPB 1750/s, (E), Staggered Infused SHPB 1100/s, (F) Staggered Infused SHPB 1750/s

129

CHAPTER VIII: SHOCK TUBE RESULTS/DISCUSSION

8.1 Shock Tube Experimental Results/Discussion for DUOCEL

Shock loading of sample configurations for Duocel and Cymat panels was conducted on simply supported beam specimen. High speed photography was used to capture failure mechanisms and obtained out-of-plane deformation. During shock loading beam samples exhibited several deformation mechanisms, front plate indentation, multi-layer compression, interlayer slip, and bending deformation. Initial indentation was seen in all samples but was more pronounced in configurations with lowest density closest to initial strike face. Compression of initial layers (multi-layer compression) was seen in configurations with lowest density nearest to the loading zone (DNIL2, DNIL2H2L2, DIL2, DIL2H2L2) as well as one sample of DIH2L2H2. Figures 102 and 103 show typical samples that exhibited aforementioned failure mechanisms.
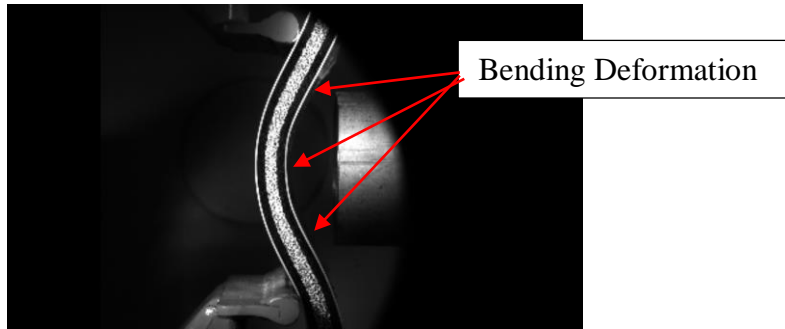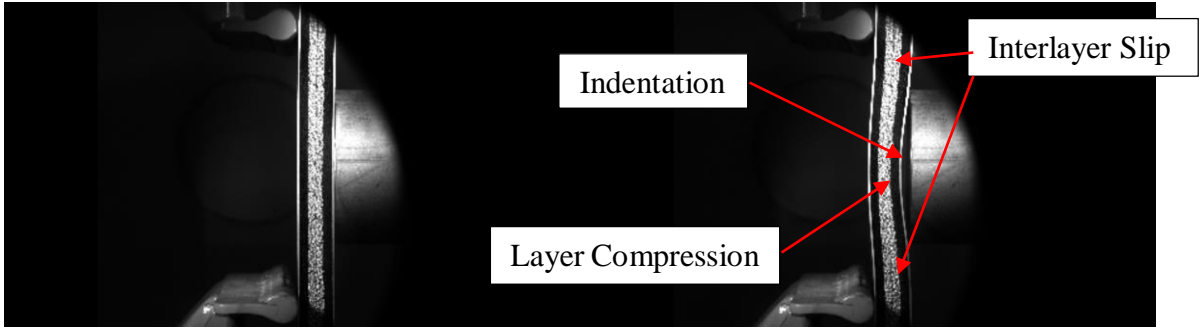
Figure 102. DNIH2L2H2 Beam Sample During Shock Loading
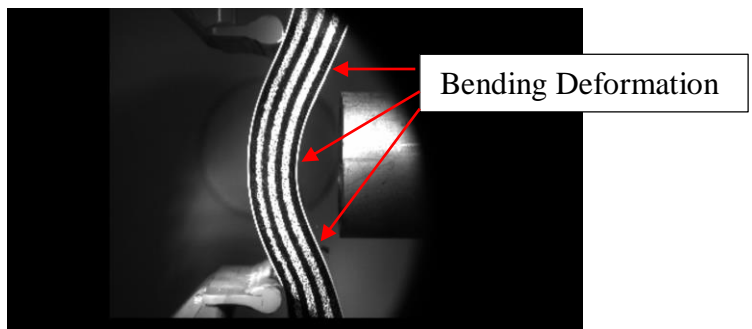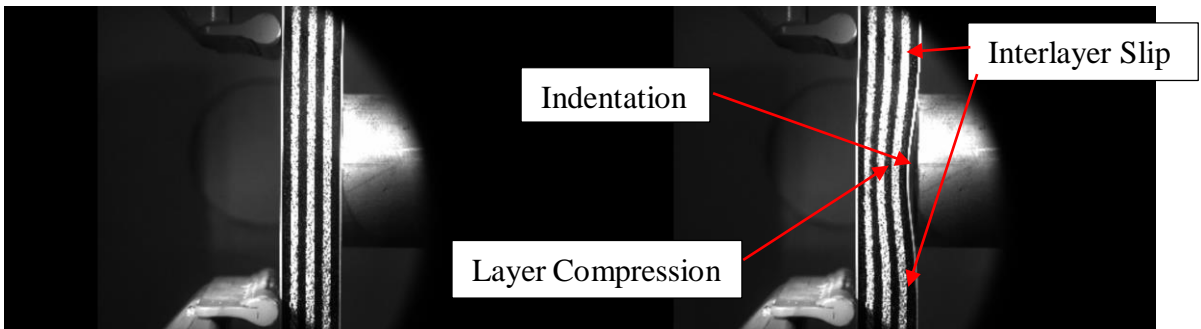
Figure 103. DIL2 Beam Sample During Shock Loading

Pressure waves were monitored using Kulite HKS-HP-375-5000SG transducers to obtain incident and reflected pressure profiles. Figure 104 shows typical pressure profiles for DNI and DI samples. Due to the repeatability of the shock tube experimentation minimal variations between each test was observed. Reflected pressure, which deforms samples, shows a slightly higher initial pressure for samples made of DNIH2 then all other samples, however during the later portion of loading (~0.8 ms - ~1.6 ms) DNIL2 samples exhibited equal pressure. Configurations of DNIH2L2H2, DNIL2H2L2, and DNIL2 displayed a decreasing initial reflected pressure. Infused configurations had similar initial pressure profiles until ~0.6 ms at which point DIH2 and DIL2 show higher reflected pressure while DIH2L2H2 and DIL2H2L2 samples decay at a faster rate. Based on the pressure signals samples made with highest density metallic foam only show increased initial resistance when compared to other configurations however during the duration of the loading become less resistant when comparing non-infused samples.
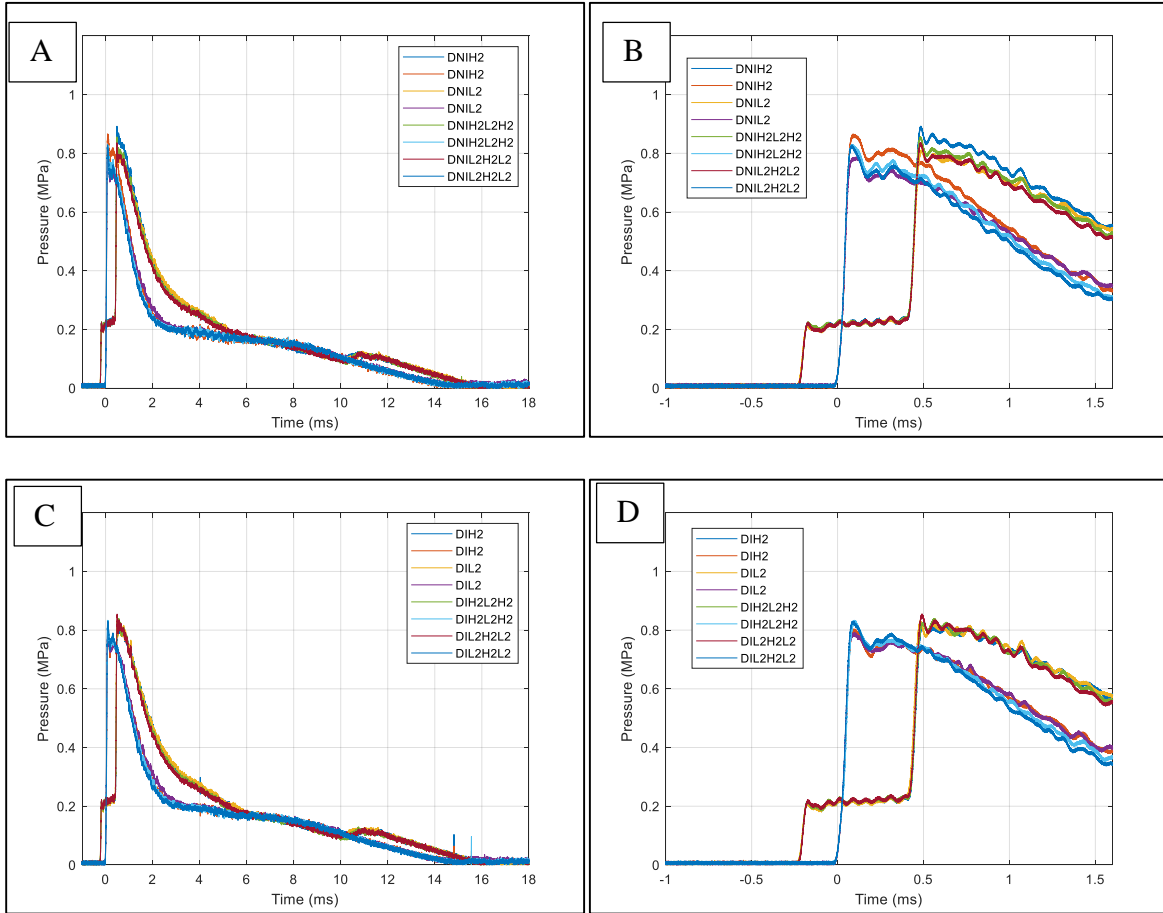
Figure 104. (A, B) Pressure Profiles for DNI (C, D) Pressure Profiles for DI Samples

Digital image correlation was used to obtain displacement of each layer of beam samples. The exception to this is the interfaces with same density at the middle of functionally graded samples. Deformation was only obtained at the interfaces with varying mechanical properties. The omission is due to the inability to track the interface due to it being obscured during deformation. Figure 105 shows typical automatic tracked features at multiple layers of a beam sample used for analysis. As a note interfaces designation increases with distance from shock loading strike face, i.e. interface 1 is closer to the strike face as compared to interface 2.
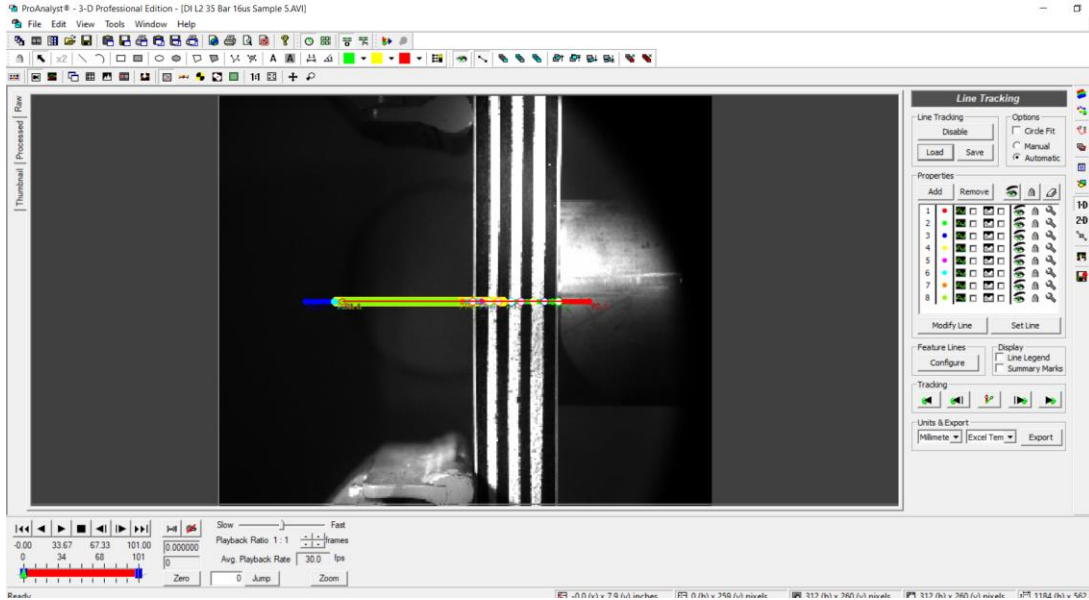
Figure 105. 1-Dimensional Line Tracking Digital Image Correlation of Beam Samples

From resulting DIC analysis, compression of beam sample layers was obtained to identify the dominate modes of failure. DNIH2 samples exhibited a very slight initial compression approximately 100 µs, during the indentation phase (Fig. 106). After which all layer interfaces move in unison showing no additional compression of the panel.
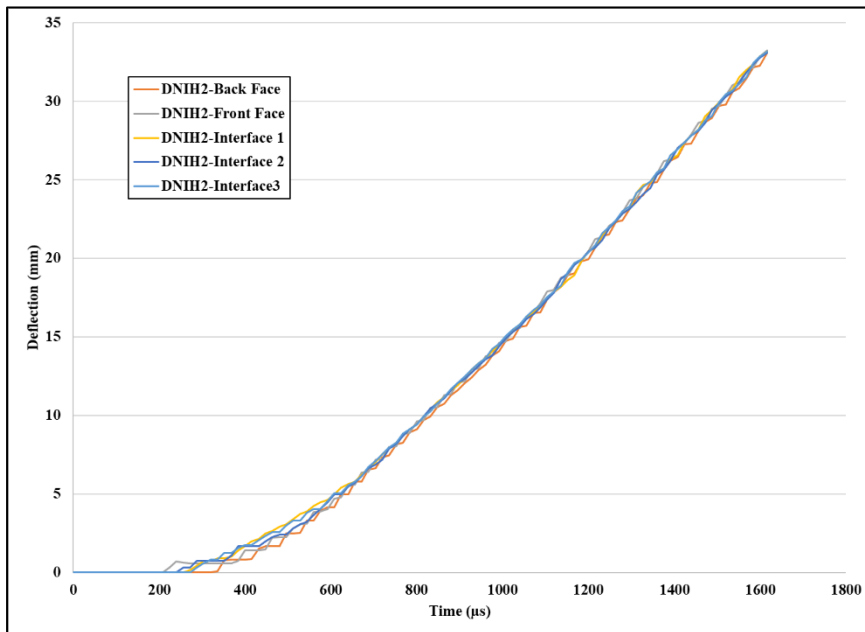
Figure 106. Deflection-Time for DNIH2 Interfaces

134

Samples made with 7-layers of lowest density foams shows a progressive collapse of the initial 3-4 layers and slight collapse of layers 5 and 6 during shock loading (Fig 107). This allowed samples to absorb the shock pressure and not transmit as much to the back face sheet.
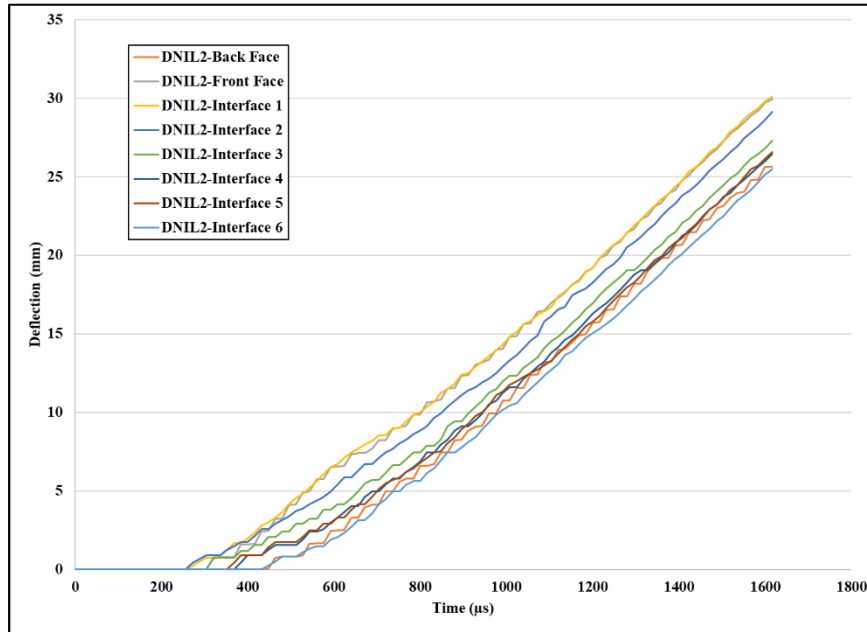
Figure 107. Deflection-Time for DNIL2 Interfaces

During shock loading samples made into DNIH2L2H2 exhibited compression of the lowest density layer only after slight indentation of the initial strike face. From Figure 108 it can be seen that the front face and interface 1 move in unison while interface 2 and the back face have a delayed displacement as well as move together. The conclusion of this phenomenon is that the middle layers of lowest density Duocel metallic foam are compressing throughout the duration of the shock loading, and assisting in reducing the transmission of the shock pressure to the back face.
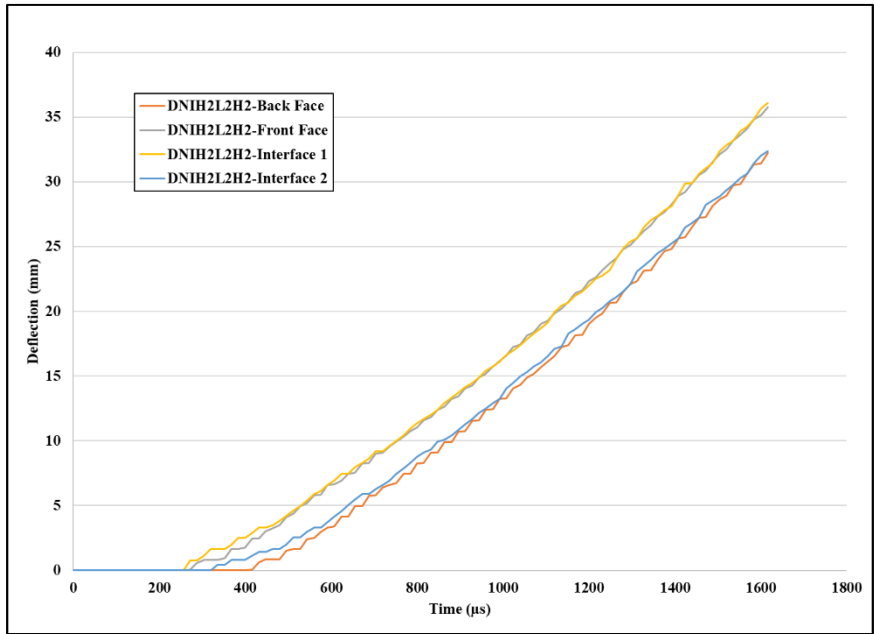
Figure 108. Deflection-Time for DNIH2L2H2 Interfaces

DNIL2H2L2 configurations showed initial collapse of lowest density layer closest to the strike face. Figure 109 illustrates the displacement of the front face and interface 1 being subjected to the shock pressure. It can also be seen that interface 1 and interface 2 (opposite sides of high density middle layers) do not move in unison meaning there is a slight compression of these layers as a whole. This again reduces the ability of the shock pressure to reach the back face.
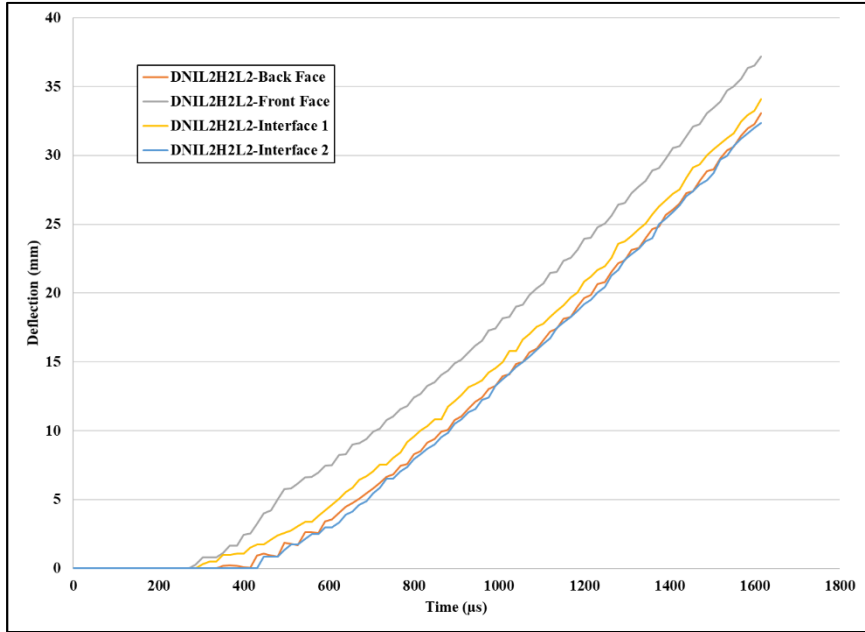
Figure 109. Deflection-Time of DNIL2H2L2 Interfaces

Similar trends for DIH2 samples were seen when compared to DNIH2 samples. No compression was seen in all samples during shock loading, as noted by the displacement of each interface being identical (Fig. 110). Essentially the shock pressure was immediately transmitted to the back face causing large deformation.
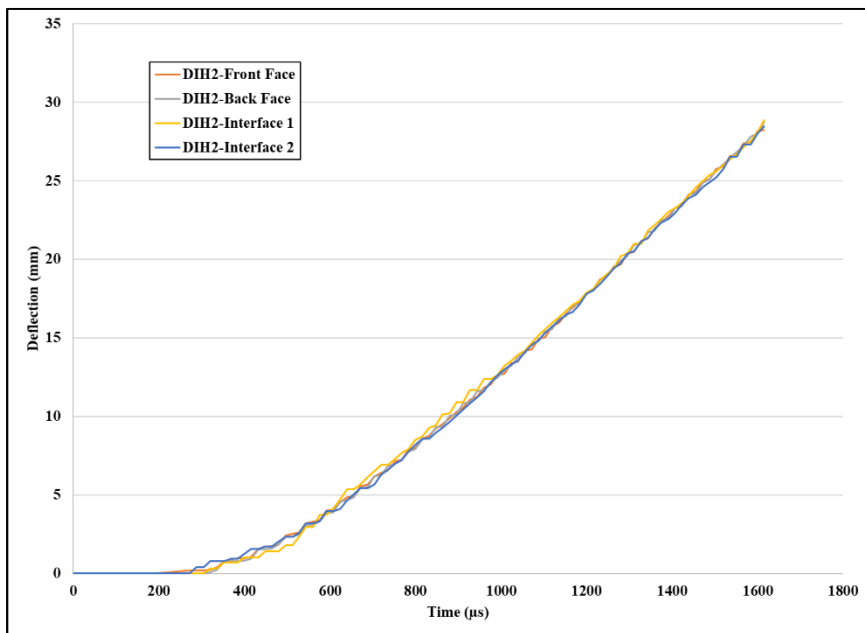
Figure 110. Deflection-Time for DIH2 Interfaces

Infused configurations made with low density Duocel foams showed two types of responses. The first response (Fig. 111 (A)) resembled that of high density non-infused and infused variation in which no compression was observed. This was only seen in one of the three samples. The second response (Fig. 111 (B)) resembled that of the non-infused DIL2 samples in which there is a progressive collapse of layers closest to the shock pressure. Samples exhibiting this response reduce the back face deflection as compared to samples that did not exhibit this response and did not have catastrophic failure.
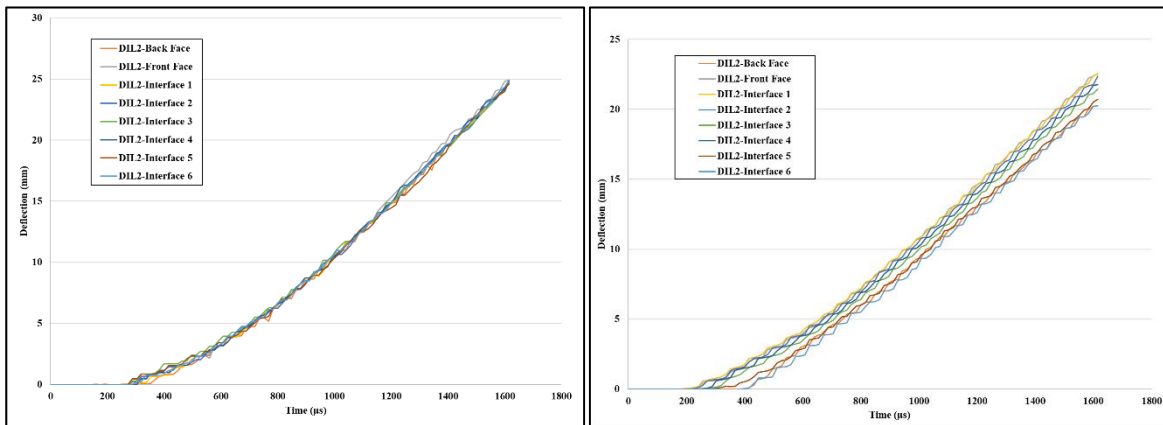
Figure 111. (A) Deflection-Time for DIL2 without Inter Layer Compression, (B) Deflection-Time for DIL2 Samples with Layer Compression

DIH2L2H2 exhibited similar response as DIL2 samples. Two of the three samples showed the first response (Fig. 112 (A)) in which no collapse of any layer was observed. The remaining sample had collapse of the high density layer closest to the shock load. It is believed that this is due to inconsistencies in the infusion process.
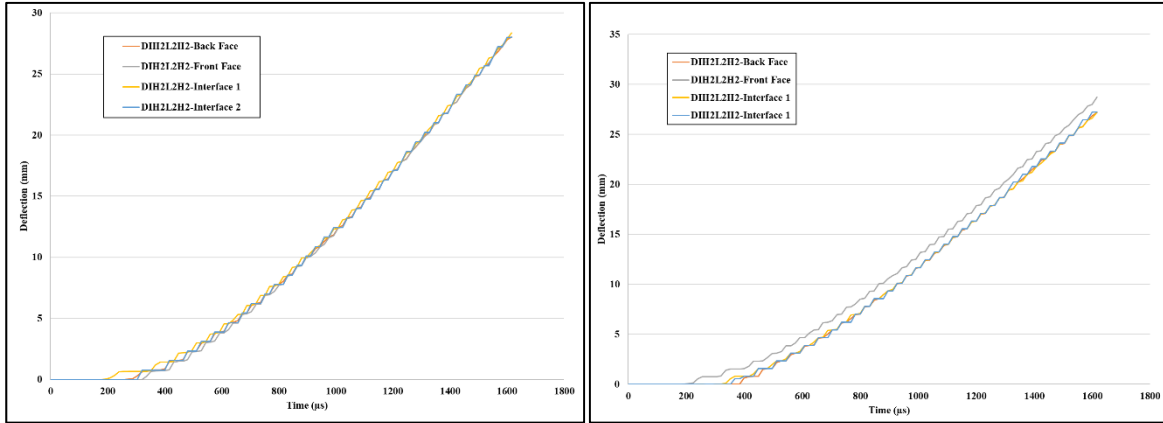
Figure 112. (A) Deflection-Time for DIH2L2H2 Interfaces without Collapse, (B) Deflection-Time for DIH2L2H2 Interfaces with Collapse

Samples configuration of DIL2H2L2 exhibited consistent response as DIL2H2L2. Two of the three samples showed no compression while the remaining sample showed compression of the high density middle layer. A possible explanation for the middle layer collapse is the inconsistent expansion of the polymer foam creating areas with less infusion.
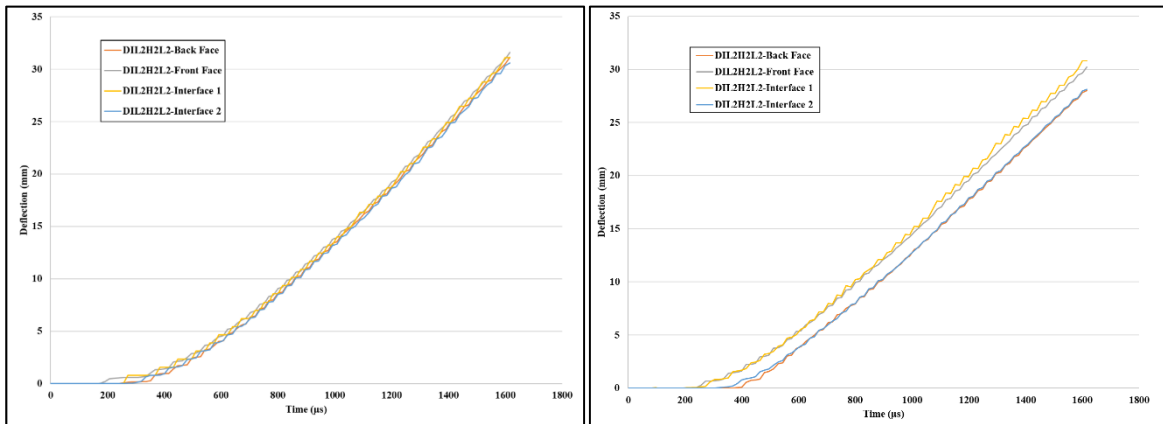
Figure 113. (A) Deflection-Time for DIL2H2L2 Interfaces without Collapse, (B) Deflection-Time for DIL2H2L2 Interfaces with Collapse

Back face deflection comparison can be seen in Figure 114. Based on resulting DIC it can be seen that DNIL2 and DIL2 configurations experienced the smallest amount of back face deflection. The large thickness of the beam allowed for increased resistance to bending during shock loading.

139

DIL2H2L2 samples exhibited the highest deflection when compared to other non-infused samples, followed by DNIH2 and DNIH2L2H2 samples. Infused variations showed identical trends when comparing back face deflection. Average values as well as percent reduction in back face sheet deflection can be seen in Table 12. Based on the analysis configurations made with lowest density foams show improved mitigation of pressure wave transmission to back face sheets.
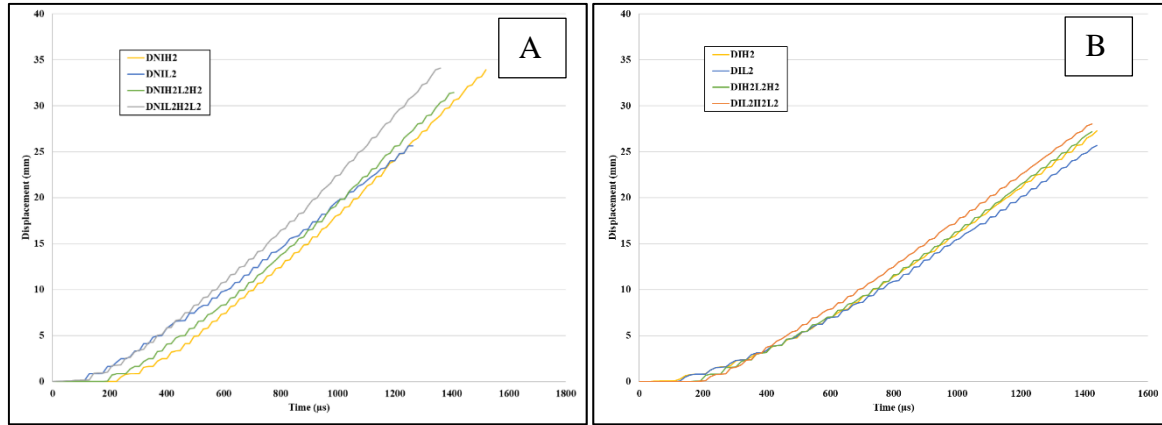
Figure 114. (A) Deflection-Time Comparison for DNI Configurations, (B) Deflection-Time for DI Configurations

Table 12. Back Face Sheet Deflection and Percent Reduction in Deformation

Sample Configuration	End Deflection at 1.6 ms (mm)	% Reduction in Deformation
DNIH2	33.11	0.88
DNIL2	25.70	23.07
DNIH2L2H2	31.45	5.85
DNIL2H2L2	33.41	0
DIH2	27.53	5.36
DIL2	23.60	18.85
DIH2L2H2	27.23	6.39
DIL2H2L2	29.09	0

Load-displacement (back face sheet) for each configuration can be seen in Figure 115. Load-displacement trends for all configuration are similar. An initial spike is observed then a steady decay as more displacement occurs. However, non-infused samples show a larger variance in load bearing capacity as compared to infused variations. Highest load capacity was seen in

140

DNIH2 samples followed by DNIH2L2H2, DIL2, and DIL2H2L2. From the results of the non-infused variations the effects of functionally grading can be seen. Based on the results configurations with lower density middle layers has a higher load bearing capacity than those with higher density middle layers. However, the bending strength is still lower than that of panels made with only high density layers. It is also noteworthy that the initial resistance of the infused variations is slightly higher than those of the non-infused variations as well as the strength of the panels.
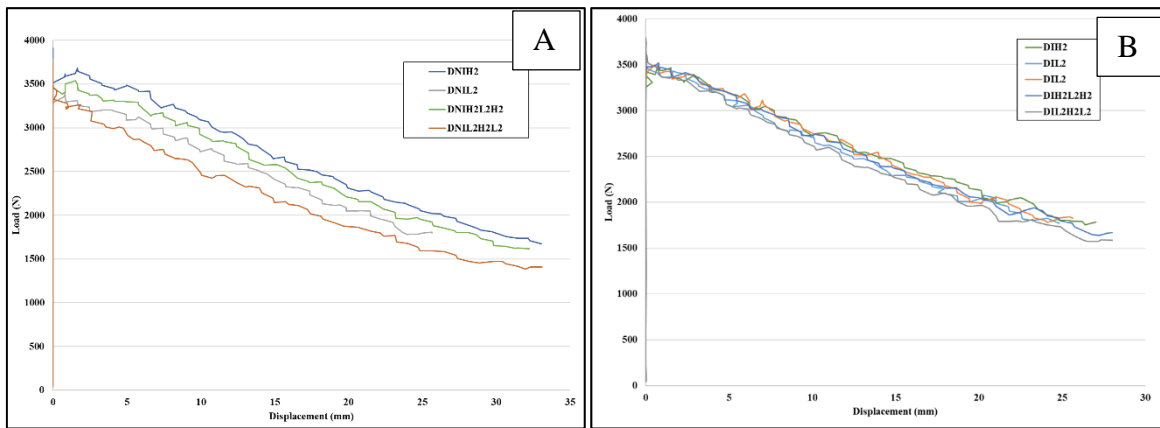
Figure 115. (A) Load-Deflection Comparison for DNI Configurations, (B) Load-Deflection for DI Configurations

Deformation energy of the beam samples was calculated by numerical integration of the Load-Displacement curves. From the analysis it can be seen that with respect to the non-infused configurations made of DNIH2 and DNIH2L2H2 absorb energy at a faster rate (Fig. 116). This is due to the decreased resistance to transmission of the shock pressure to the back face. In essence the shock pressure is almost immediately transmitted to the back face sheet. By comparison the DNIL2 and DNIL2H2L2 samples absorption happens at a slower rate. This is due to differing reasons. The increase resistance to bending as well as the compression of the DNIH2 samples slows the amount of energy that is transmitted to the back layer due to compression of initial layers causing decrease deflection. However, in the case of the DNIL2H2L2 samples the compression

141

of the initial layer of the panel caused a slower progression of energy absorption. Infused variations show a change in energy absorption rates by comparison to non-infused variations. Two samples for DIL2 are shown (Fig. 116 (B)) to illustrate the variance in response to shock loading. As can be seen the energy absorption rate of DIH2 samples was lowest by comparison to other configurations. This was followed by DIL2 samples that exhibited low energy absorption. Samples of DIH2L2H2, DIL2H2L2, and DIL2 with high energy absorption all show similar deformation energy absorption, due to previously mentioned reason for difference in shockwave transmission as well a resistance to bending.
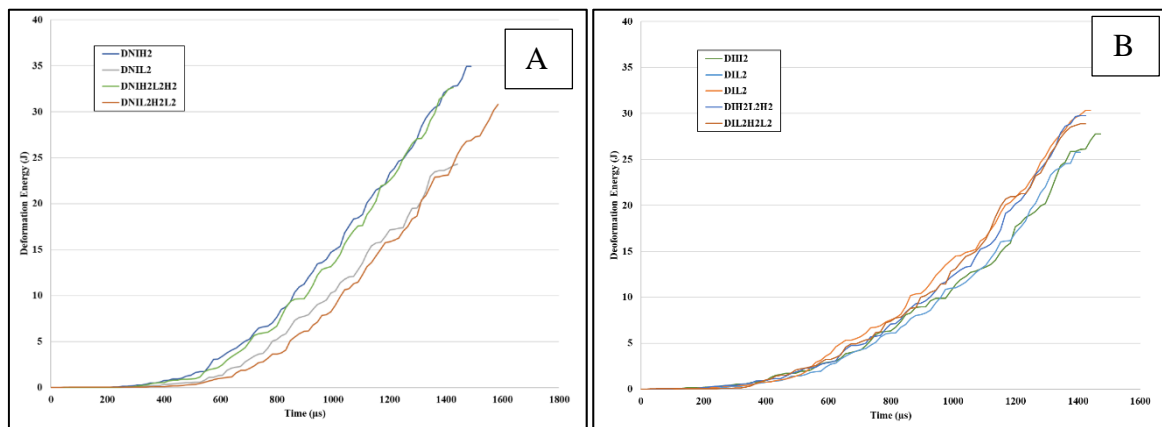
Figure 116. (A) Deformation Energy-Time Comparison for DNI Configurations, (B) Deformation Energy-Time for DI Configurations

Deformation energy versus displacement of the back face sheet center location can be seen in Figure 117. From the comparison of the non-infused samples it can be seen that the trends are similar in terms of energy absorbed at a particular displacement. This shows that regardless of the configuration the energy absorption at a particular displacement will be nearly identical. The exception to this is the later response of the DNIL2H2L2 at approximately 18 mm of displacement. Comparison of the infused variation reveals that samples made with lowest density metallic foam are able to absorb more energy at the same displacement by comparison to all other configurations. This response was seen in two of the three samples tested and were the only surviving samples

throughout all shock testing for Duocel configurations. Figure 118 shows damage samples for all

configurations tested. Based on the resulting analysis the functionally gradation of non-infused

Duocel configurations does not appear to have a pronounced effect in the overall performance

when comparing the energy absorption. This is due to a combination of the strength of the panel

which is based on the stacking sequence, the lag time for the pressure wave to be transmitted to

the back face, and the compression of the different layers of the panel.   In essence some

configurations are able to deflect but not compress where other are able to compress but no deflect.

This essentially causes the response to be very similar when comparing the deformation energy

versus displacement. When infusion is taken into account it increases the ability of the lower

density variation to resist the shock pressure in the initial layer given it higher strength while also

aiding in resistance to back face deflection due to the longer shock wave transmission time. This

allows the lowest density panels to not only absorb more energy at the same back face deflection

but increase the likelihood of a surviving panel during shock loading. Based on the resulting

analysis infusion can be used to aid in the resistance of a metallic foam panel when subjected to

blast loading.
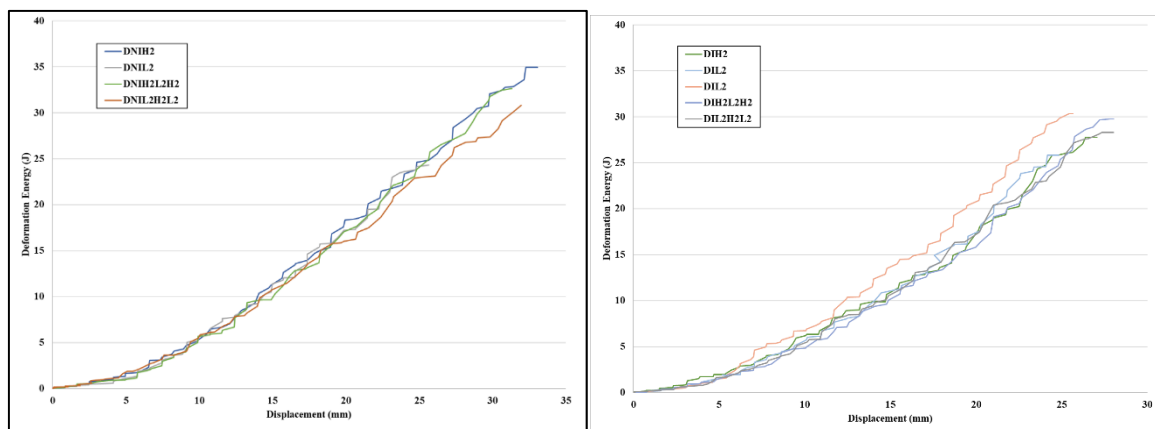
Figure 117. (A) Deformation Energy-Displacement Comparison for DNI Configurations,
(B) Deformation Energy-Displacement for DI Configurations
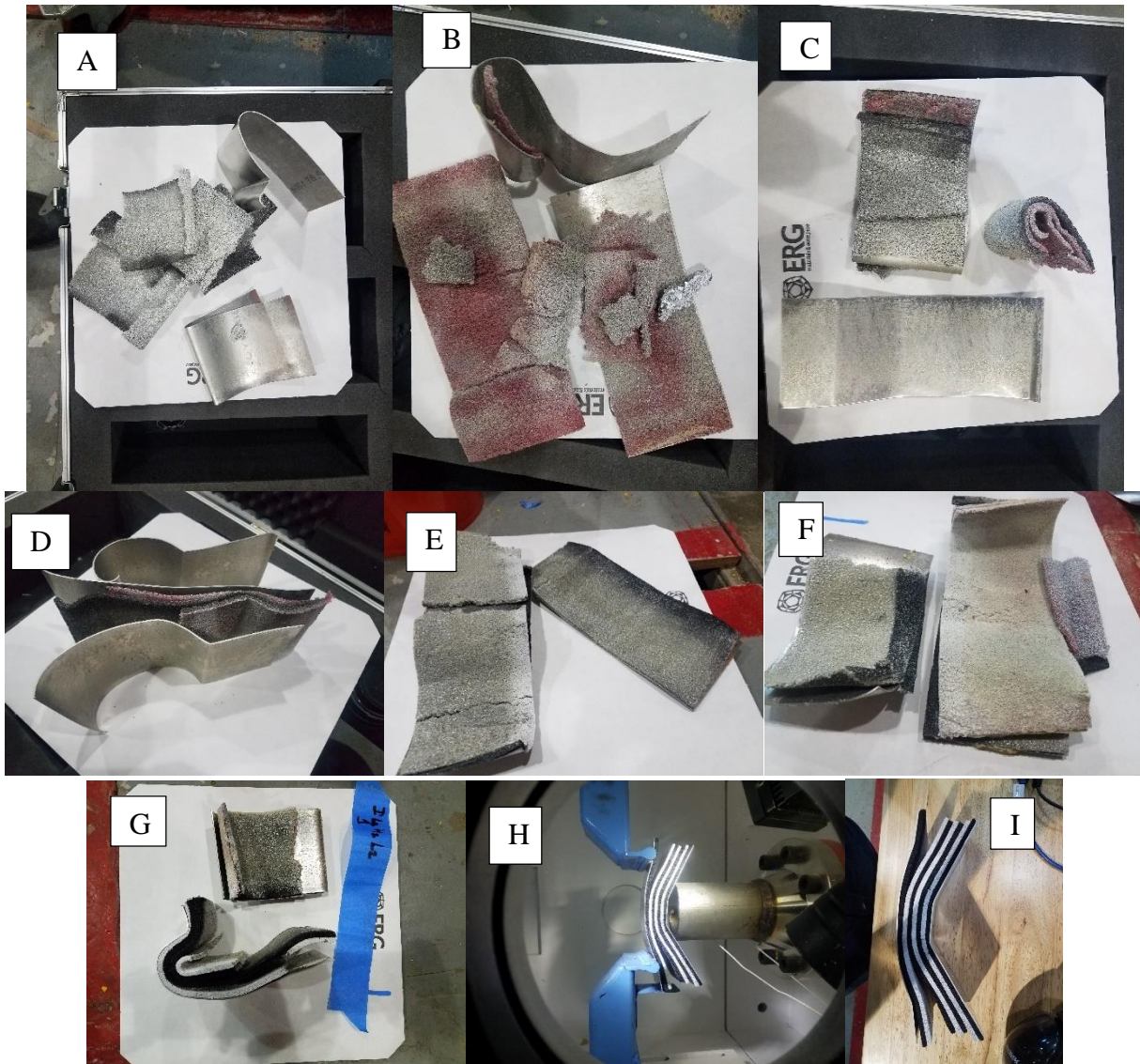
Figure 118. Non-Infused and Infused Specimens Subjected to Shock Loading (A) DNIH2, (B) DNIL2, (C) DNIH2L2H2, (D) DNIL2H2L2, (E) DIH2, (F) DIH2L2H2, (G) DIL2H2L2, (H, I) DIL2

Final decision on the effectiveness of Duocel non-infused and infused samples was based on three parameters total deflection of back face center point, specific energy, and acceleration of the back face center point (Fig. 119-121). These three parameters give a better understanding of the mitigation capabilities of each panel at a particular point. Due to inconsistencies in back face center point deflection comparisons of specific energy and acceleration were made at about 20 mm maximum deflection. From Figure 119 it can clearly be seen that the end displacement of the back

144

face sheet for DNIL2 and DIL2 are the lowest when comparing the non-infused and infused variations. DNIH2L2H2 and DIH2L2H2 exhibited the second lowest deflection showing that with functionally gradation desirable mitigation of blast loading can be achieved. Sample configurations with only highest density foams show increased deflection by comparison to previously mentioned configurations due to the ability of the metallic framework to resist compression and transmitted the applied force to the back face. Samples made with L2H2L2 stacking sequence has the lowest resistance to bending deflection which provides insight to the appropriate stacking sequence for metallic foam blast protective systems.
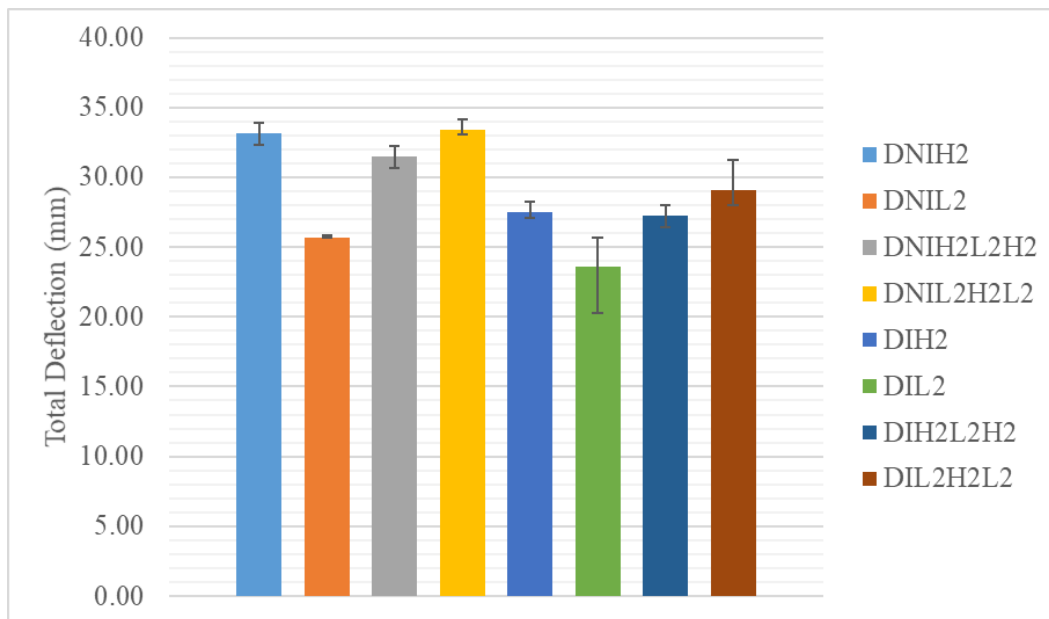
Figure 119. Back Face Sheet End Deflection (mm)

The specific energy absorption was also calculated from the load-displacement curves at 20 mm maximum back face sheet deflection (Fig. 120). When comparing non-infused samples, the DNIH2L2H2 stacking sequence shows slightly more energy absorption then all other configurations and is followed by the DNIL2 non-infused configuration. DNIH2 and DNIL2H2L2 samples exhibited lower specific energy absorption. For beams with only high density layers (DNIH2) the previously mentions reasons for increased back face deflection are the cause of the

145

decreased energy absorption. The DNIL2H2L2 configurations decrease in energy absorptions is due initial compression of the first layer of 4-6% Duocel foam, followed by rigid motion of the subsequent layers. In the case of infused variations, the trend is not consistent. The highest energy absorption was obtained by the DIL2H2L2 configurations. However, uniform low density configurations (DIL2) only shows a slight decrease (1.4%) in energy absorption. Samples made with DIH2L2H2 stacking sequence exhibited the lowest energy absorption which is in contrast to the center point end deflection.
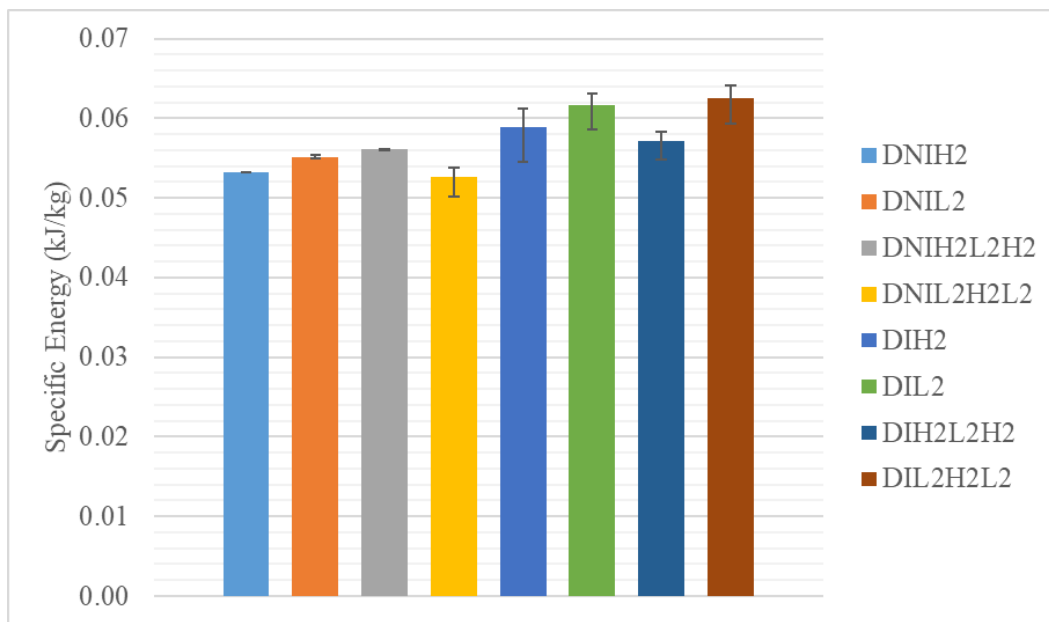
Figure 120. Specific Energy Absorption at 20 mm Back Face Sheet deflection of Shock Loaded Duocel Non-Infused and Infused Beams

Acceleration of the back face sheet center point allows for a better understanding of the force transmitted to the back face as well as the energy transmitted to the back face. Based on resulting analysis of non-infused beam panels the highest acceleration at 20 mm of displacement was the uniform high density panels, followed by DNIH2L2H2. This shows that the shock loading is transmitted better to the back face sheets as compared to other configurations. The lowest acceleration was obtained by the DNIL2 panels showing the ability of the panels to compress while

absorbing the shock pressure and not transmit the force to the back plate. When comparing the infused variations, the DIL2 configurations had substantially lower acceleration as compared to all other configurations, clearly illustrating the superior mitigation potential of panels made with the lowest density foam. Panels made with DIH2L2H2 stacking sequence show slight decrease in acceleration as compared DIH2 beams. This clearly shows the capabilities of functionally graded panels to not only be superior in certain cases but also the placement of material is critical when designing blast mitigation panels.
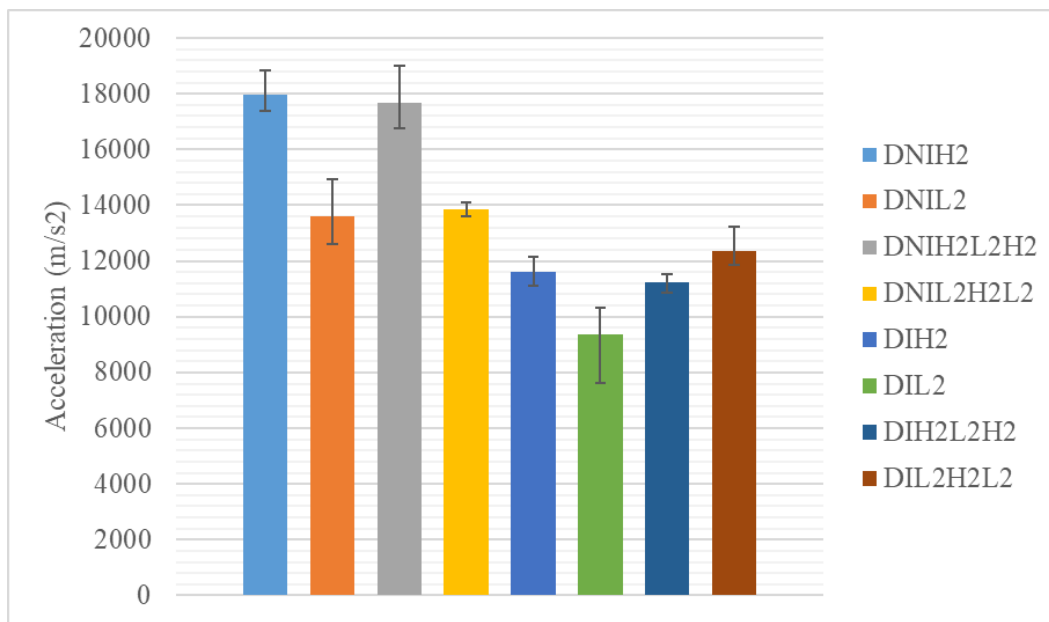
Figure 121. Back Face Sheet Acceleration at 20 mm deflection of Duocel Non-Infused and Infused Beams

Based upon the three criterion (back face end displacement, specific energy absorption at 20 mm, and back face acceleration at 20 mm deflection) samples made with lowest density configurations (DNIL2 and DIL2) are more ideal for blast mitigation due to the ability to decrease force transmitted to the back face as well as absorb energy during shock loading. It can also be concluded that the infused technique does increase the absorption potential of metallic foam panels. However, the increases are not consistent with different functionally graded stacking

147

sequences. It can also be concluded that stacking sequences with lowest density middle layer overall are a more suitable than configurations with highest density middle layers.

8.2 Shock Tube Computational Results/Discussion

Computational modeling was done using Abaqus CAE Explicit Dynamic to compare results obtained from experimental and finite element analysis (FEA). Simply supported beams with similar dimensions were subjected to idealized blast loading waves similar to experimental pressure waves. Due to the complexity of the experimental setup and sample configuration several simplifications were made to the computational model. The first simplification that was made is that the metallic foam framework was simplified into a solid material with the same constitutive relationship obtained from experimental SHPB analysis. The second simplification is that configurations with the same density have no layering in the simulation. Lastly, the pressure as applied to a square surface area rather than a circular surface area. This was done to represent the shock loading more accurately on the experimental sample surface which loads a rectangular section after the initial deflection of beam samples. Functionally graded samples were layered with similar staking sequence as experimental samples (Fig. 122). Constitutive relations with strain-rate dependency ((Daoud, Jomma, Chatelain, & Bouzid, 2015) were used for aluminum 6061. Empirical constitutive relationships for Duocel metallic foam and Duocel/Foam-iT!™ 3 composites used in simulations were obtained from linear fit (Elastic region) and polynomial curve fit (plastic region) from experimental stress-strain data from quasi-static and SHPB analysis.

Figure 122. Finite Element Analysis Functionally Graded Stacking Sequence

Same element size was used for all FEA simulations to ensure no mesh size dependency in the results of the analysis (Fig. 123). Boundary condition for the beam samples restricted out of plane motion of the beam. In essence the beam is only allowed to move in the same directions as the pressure wave plane (Fig. 124). Two rollers were placed 152.4 mm apart to replicate the experimental setup. Rollers were fully constrained during the simulation.
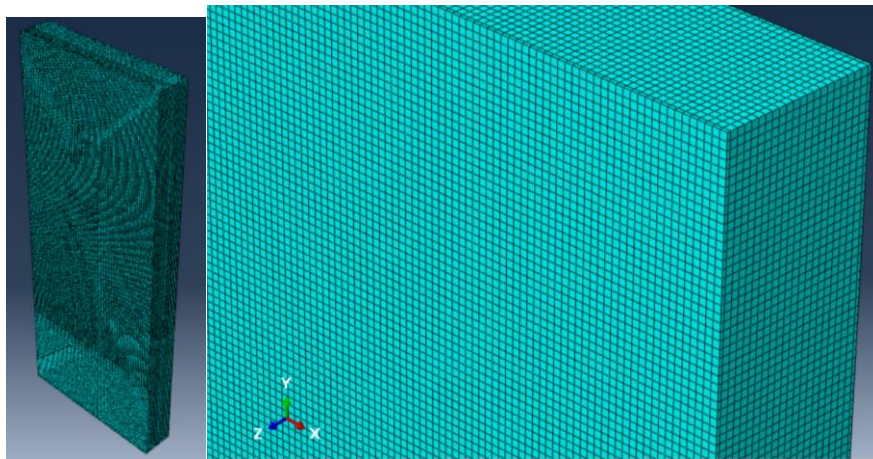
Figure 123. Finite Element Analysis Mesh Size
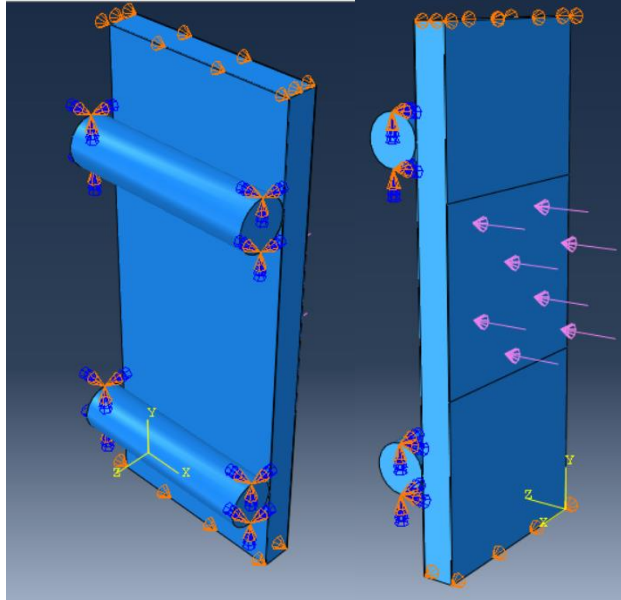
Figure 124. Finite Element Analysis Boundary Conditions

Figure 125 shows a typical Von Mises stresses for a shock loading FEA simulation. From the simulation the shape of deflection is consistent with the experimentation, however the overall deflection at the back face was inaccurate.
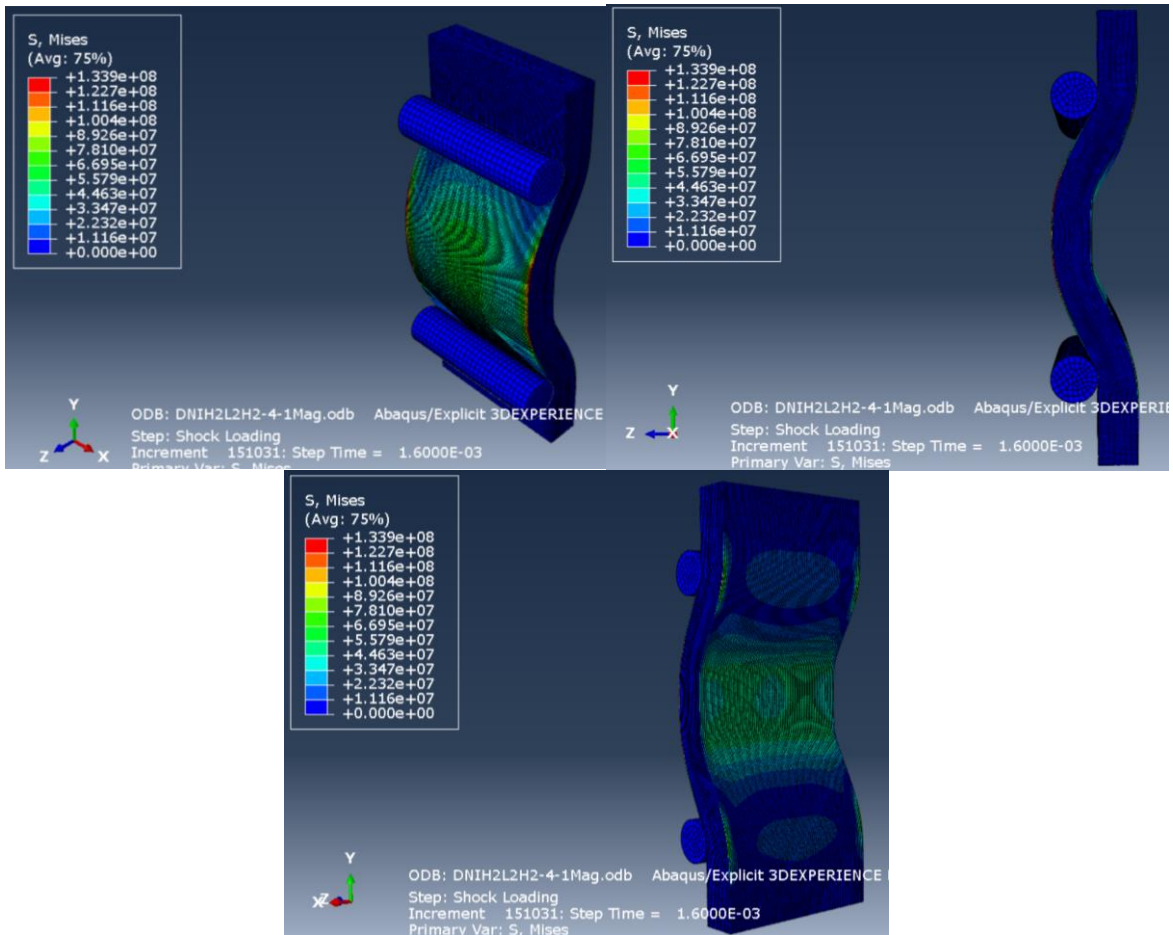
Figure 125. Finite Element Analysis Von Mises Stress

Figure 126-130 show a comparison of deflection at the back face during shock loading for experimental DIC analysis and FEA simulations. Large variations were seen when comparing the experimental back face sheet deflection as compare to FEA simulations for non-infused variations. This can be attributed to several causes. First the simulation does not take into account the bonding between the two layer since the rectangular specimen is one solid piece that has been partitioned. This was done due to the lack of parameters for bonding strength between layers. This causes the simulation to neglect any slip between the layers as the sample bends from the shock loading. This is inconsistent with the experimentation which has been shown to have slipping at the interface between layers. This is the primary cause for the deflection to initially be consistent, but deviate

as shock loading continues. The simulation also showed little difference between DNIH2L2H2 and DNIL2H2L2 samples.
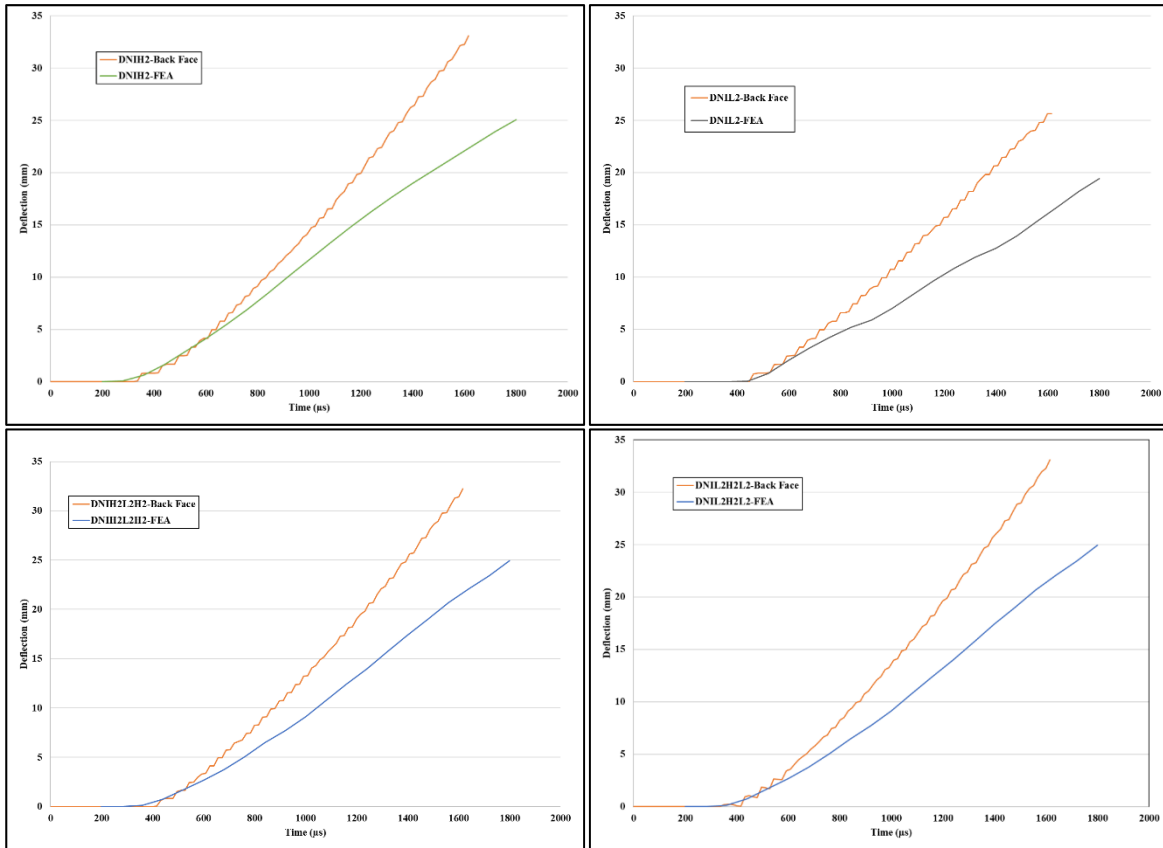
Figure 126. Experimental and FEA Back Face Sheet Deflection-Time for DNI Configuration

Computational analysis of infused variations shows a more consistent deflection at the back face sheet as compared to experimental results. The likely cause is that the bonding agent used provided better adhesion for infused samples due to the increased surface area as compared to non-infused samples. Figure 127-130 clearly show the increase accuracy of the FEA simulation by comparison to the non-infused. While the simulation is reasonable accurate it still fails to capture several mechanisms present in the experimentation. Compression of layers, interface slip, increase resistance during bending, and metallic framework-polymer infusion interactions are all not present in the simulation. However, it can be used to serve as an approximation of the response of infused panels subjected to blast loading.
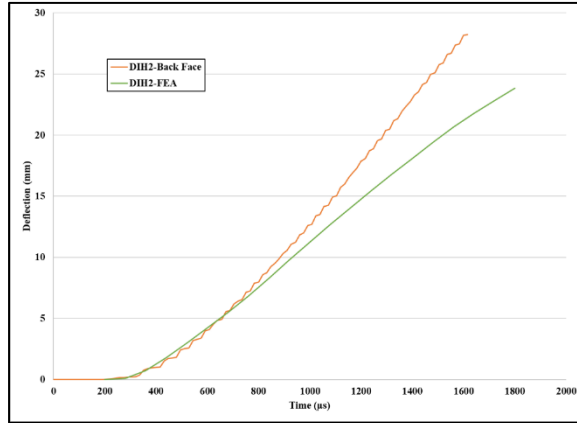
Figure 127. Experimental and FEA Back Face Sheet Deflection-Time for DIH2 Configuration
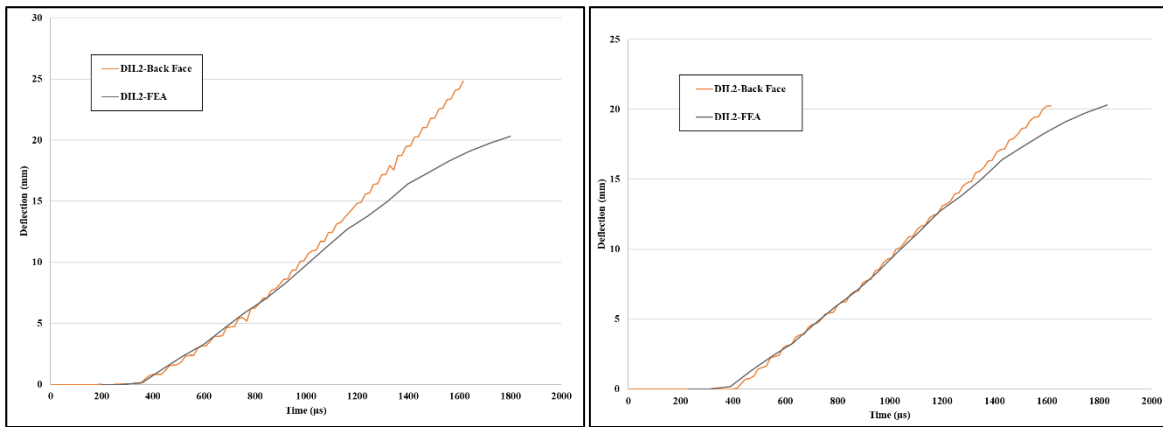
Figure 128. Experimental and FEA Back Face Sheet Deflection-Time for DIL2 Configuration
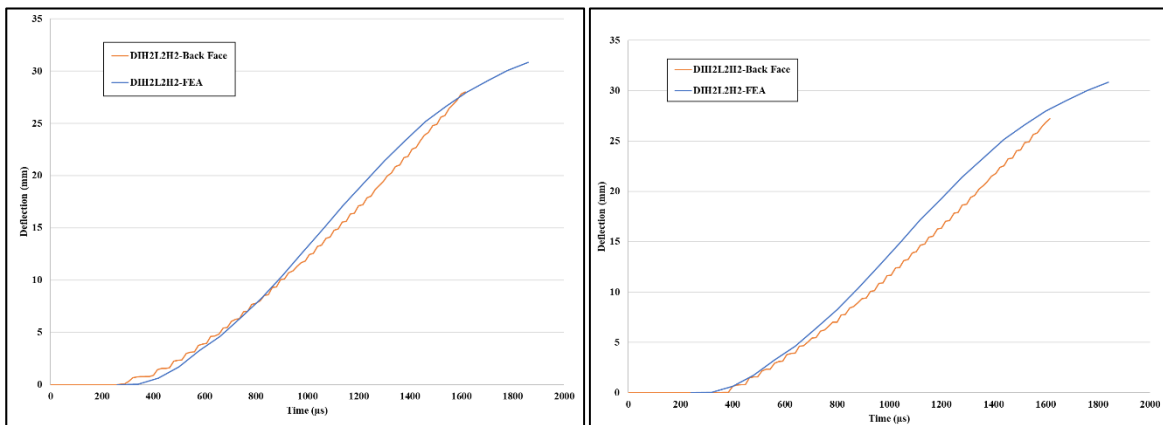
Figure 129. Experimental and FEA Back Face Sheet Deflection-Time for DIH2L2H2 Configuration

153
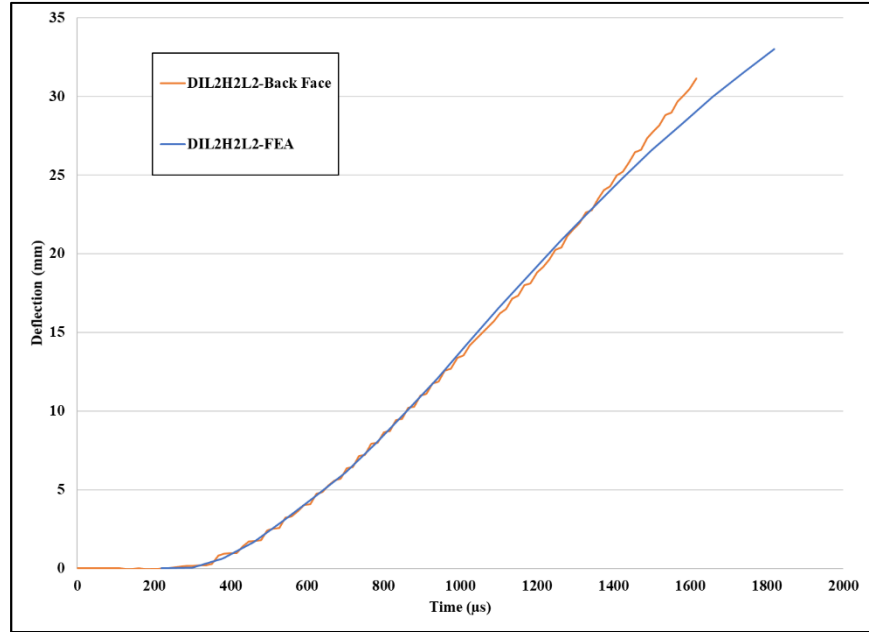
Figure 130. Experimental and FEA Back Face Sheet Deflection-Time for DIL2H2L2 Configuration

8.3 Shock Tube Experimental Results/Discussion for CYMAT Metallic Foam

Resulting analysis of Cymat beam samples subjected to shock loading provided valuable insight of the effects of functional gradation. Samples have similar damage mechanisms to those of Duocel configurations with the exception of inter layer slip. An additional mechanism that was not present in Duocel foams seen in Cymat metallic foams is the presence of fracture within the layers. This was present in all samples during shock loading but was more pronounce in denser layers as opposed to lower density layers. Figure 131 shows a typical high density Cymat metallic foam that has been subjected to a shock wave. As can be seen from the images only a small amount of deflection is present during loading.

Figure 131. Cymat Highest Density Configuration High Speed Images During Shock Loading

Large deformation was observed from high speed images of Cymat panels with only lowest density foams (Fig. 132). Deformation was largest in these samples as compared to all other configurations. Small indentations were also observed located at the center point of beam samples at the strike face.
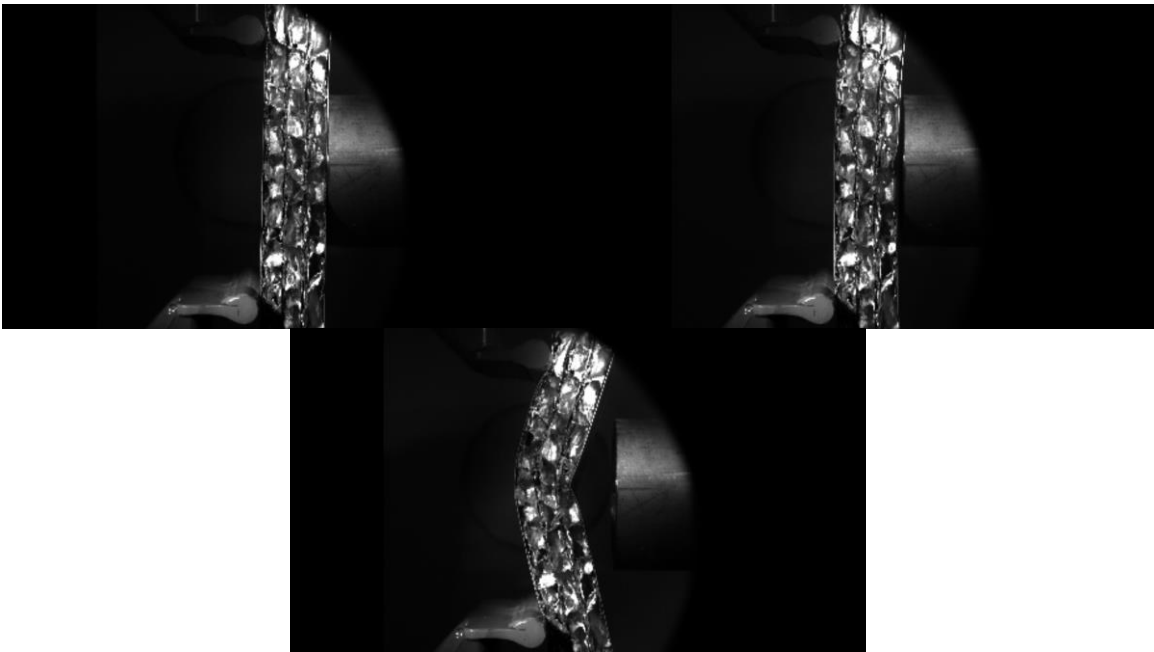
Figure 132. Cymat Lowest Density Configuration High Speed Images During Shock Loading

Cymat BWR configurations showed increase resistance to shock loading inconsistent with previous findings (Wang, Gardner, & Shukla, 2009). When panel configuration with lowest density were placed closer to the front face sheet and higher density on the back face sheet (RWB,

Fig. 134) larger deformation and damage was observed then the reverse (BWR, Fig. 133) of the configuration. This inconsistent results from previous finding is likely due to the ability of the metallic framework to transmit the pressure to the back face sheet as well as low bending strength of Cymat metallic foams. In the BWR configuration the initial high density plate is able to resist the shock loading while the back face provides additional resistance to bending with less fracturing of the framework. By comparison the RWB samples had lower resistance at the initial loading face sheet and more fracturing of the high density back layer which have decreased bending strength.
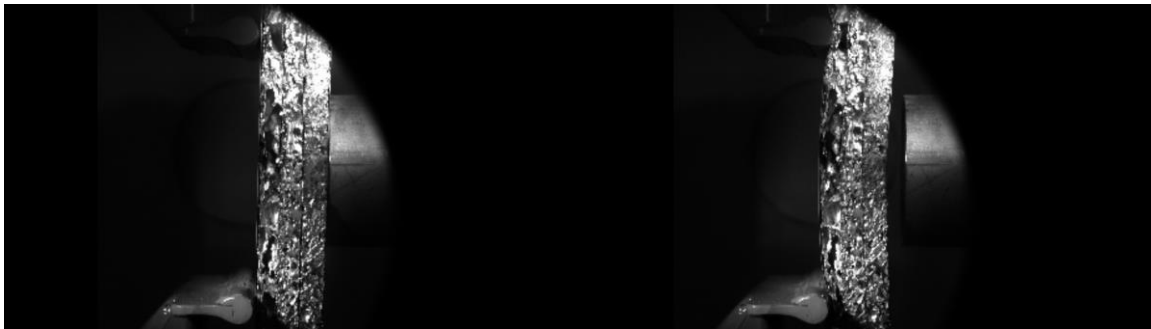
Figure 133. Cymat BWR High Speed Image During Shock Loading
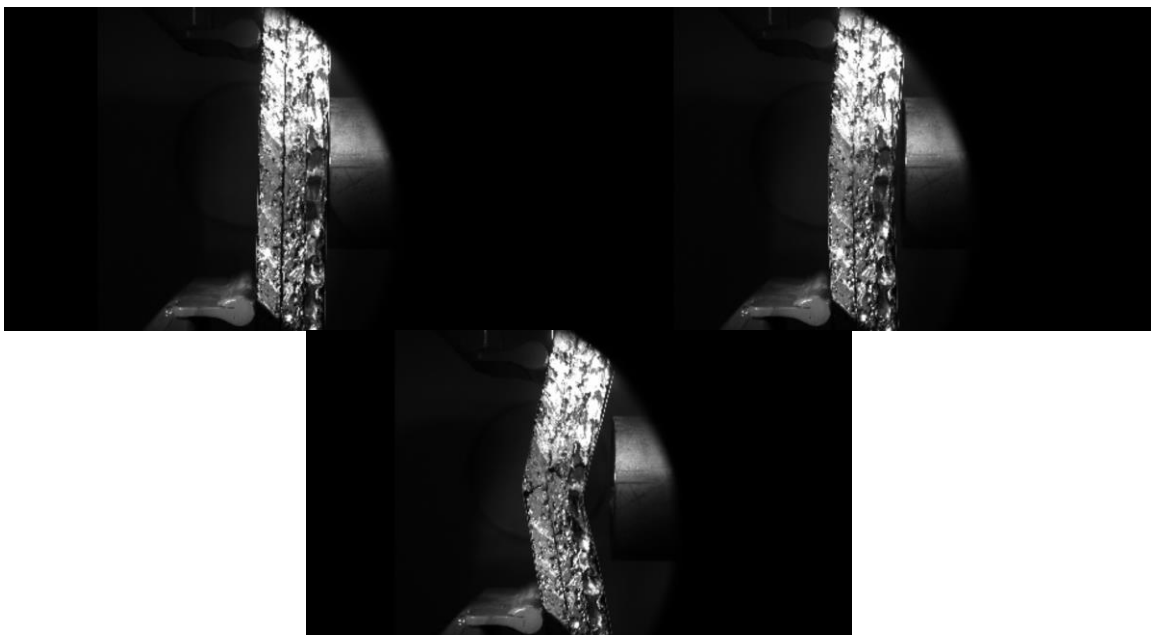
Figure 134. Cymat RWB High Speed Images During Shock Loading

Displacement-time response of all Cymat configurations can be seen in Figure 135 from resulting DIC analysis. Samples made from only highest density (Blue) showed the lowest back face sheet deflection, followed by medium density samples (White). Samples with BWR configurations and BRW had nearly similar responses with the BRW configuration being slightly more resistant to back face deflection. These were then followed by RWB and samples made with only lowest density foams.
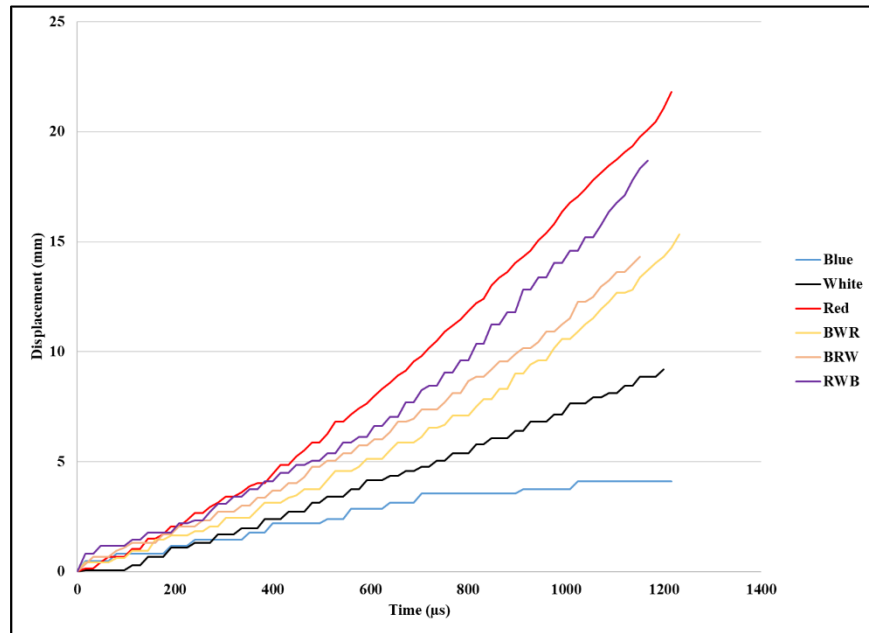
Figure 135. Deflection-Time for Cymat Shock Tube Loaded Samples

Load-displacement curves for Cymat configurations can be seen in figure 136. The response of high density panels clearly shows a much shorter response during blast loading. It was also observed that one out of the three samples were able resist the shock loading without having complete catastrophic failure. By comparison the lowest density panels had a much longer response when subjected to shock loading. This allowed the samples to absorb more energy (Fig. 137) over the duration of the loading event. Based on the trends when comparing the deformation

energy-displacement curves configurations made with RWB stacking sequence would inevitably

surpass all other configurations at ~ 27 mm of deflection.
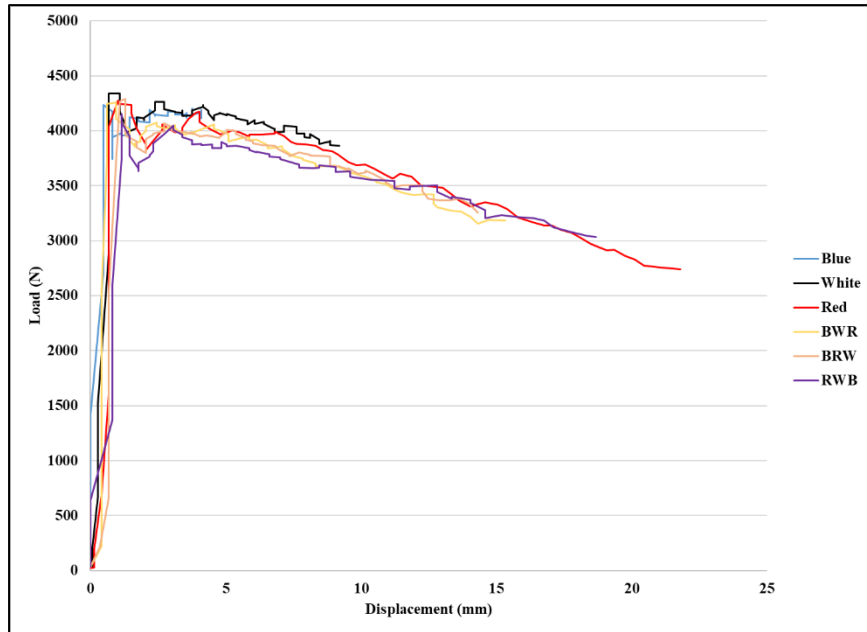
Figure 136. Load-Displacement for Cymat Shock Tube Loaded Configurations
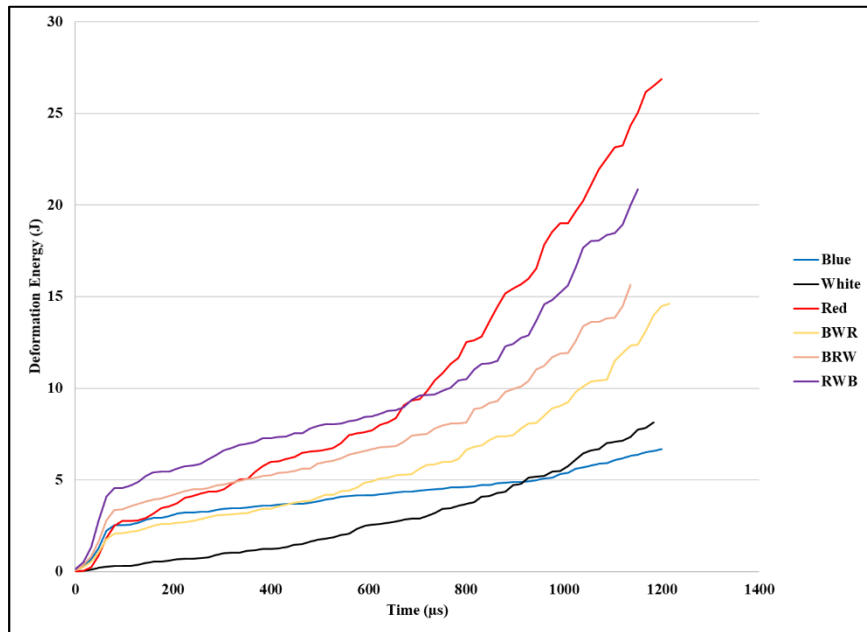
Figure 137. Deformation Energy-Time for Cymat Shock Tube Loaded Configurations

158

Deformation energy-displacement shows varying initial trends but appears to converge at ~ 18 mm (Fig. 138). Based on the responses the RWB configuration absorbed more energy till ~ 15 mm. However, assuming the trends remain consistent configurations made with BWR and BRW would surpass RWB. This assumption does not take into account any damage of the layers that inevitably would be present at different displacement for each sample. For this reason, the assessment of the Cymat samples is based on the response of the configuration throughout the duration of the experimental time constraints. Based on the assessment functionally graded configurations with increasing density through the thickness relative to the front and back face sheet are more ideal for absorbing energy during a shock loading scenario.
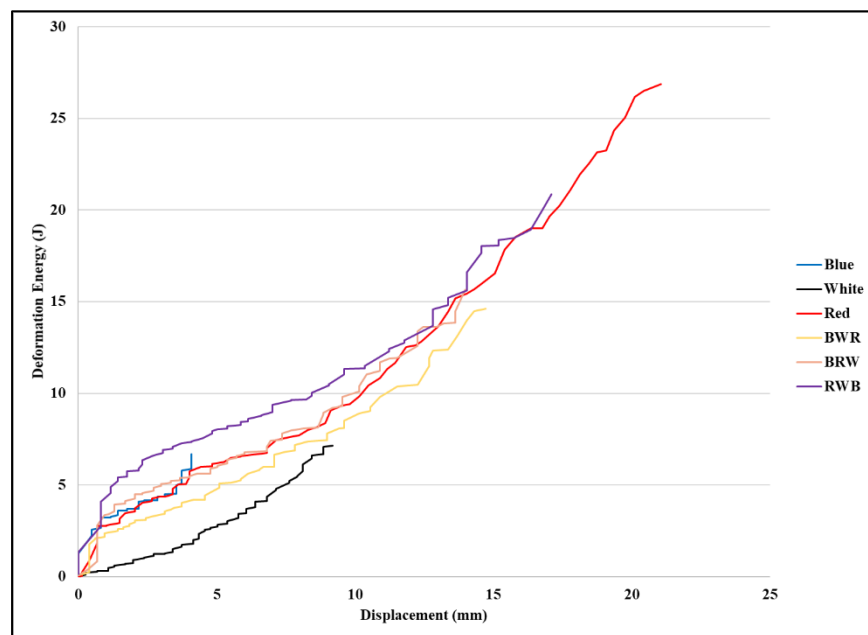
Figure 138. Deformation Energy-Displacement for Cymat Shock Tube loaded Configurations

Back face sheet end deflection for Cymat configurations at approximately 1.6 ms can be seen in figure 139. From the DIC analysis it is clear that the HD 3 layer configurations have higher resistance to blast loading when compared to all other configurations. However, this comes at the cost of the overall weight of the panels. The lowest density foam had considerable more deflection

than all other configurations. Functionally graded configurations show a unique trend differing from other researchers that found that placement of the lowest density foam closest to blast loading exhibited less back face deflection due to compression of the low density layers. In this study it was observed that placing the highest density foam nearest to the front face provided more resistance to back face sheet deflection. It was also found that having decreasing properties in strength provided better resistance to bending deflection.
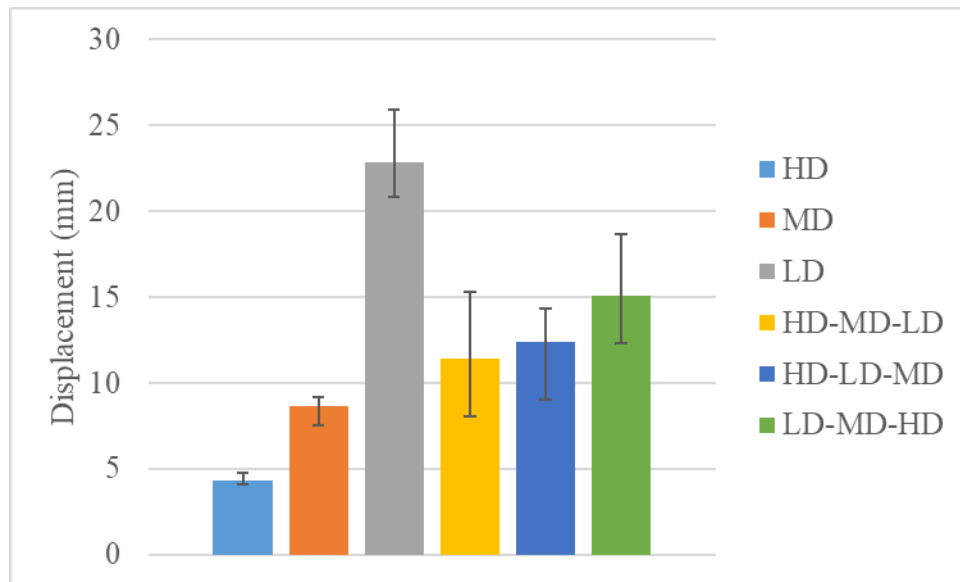
Figure 139. Center Point End Displacement for Cymat Shock Loaded Beams

Due to the low back face sheet deflection of panels with 3 layers of highest density Cymat metallic foam comparisons were made up to 5 mm of deflection. Figures 140 and 141 show the specific energy and acceleration at the back face sheet at 5 mm of displacement. When comparing specific energy panels made with lowest density foam had highest energy absorption during shock loading due to its low density. Second highest specific energy was observed in LD-MD-HD configurations, consistent with (Wang, Gardner, & Shukla, 2009), in which it was shown that having the lowest density layer closets to the shock front had better blast mitigating properties. Other configurations of functionally graded Cymat beams (HD-LD-MD, and HD-MD-LD) had

160

higher specific energy absorption as compared to 3 layer HD and MD beams, illustrating the advantages of using functionally graded materials to mitigate shock loading. The center point back face sheet acceleration was highest in 3 layer LD configurations. This is obviously due to the poor strength of the metallic framework as compared to other configurations. The acceleration of the 3 layer HD beams was considerable lower (more than half) than all other configurations. When comparing functionally graded configurations Samples made with highest density front layer (HD-MD-LD, and HD-LD-MD) show less back face acceleration. Due to the increase initial resistance of the front layer the transmitted force to the back face is decreased. This is again in contrast to other author (Wang, Gardner, & Shukla, 2009). The difference in response is due to the low compressibility of metallic foams during shock loading versus that of polymeric foams used in other published literature. This low compressive nature changes the mechanics of how the beam absorb energy from compression of internal core layer to resistance to bending and fracture. While there was a slight increase in specific energy absorption ~28% when comparing the highest density foam to functionally graded configurations it has still been decided that using 3 layers of highest density Cymat metallic foams provides considerable more protection in a blast scenario due to its increased resistance to bending within the analyzed deflection range. It is also noteworthy that this assessment is likely to change due to fracture observed at the back layers. In essence at a certain point the 3 layer HD samples will lose all load bearing capacity while other configurations will still be able to deform. Based on resulting analysis of functionally graded Cymat configurations HD-MD-LD is more ideal for shock mitigation due to its decreased displacement and acceleration. Testing a various shock pressure would provide a better understanding of each panels' capabilities under shock loading for more accurate comparisons.
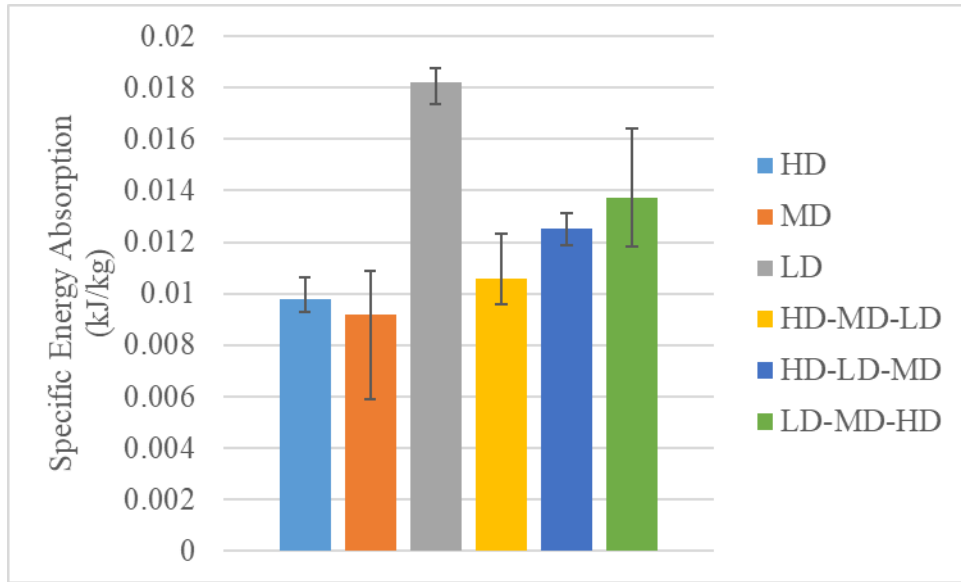
Figure 140. Specific Energy for Cymat Shock Loaded Beams
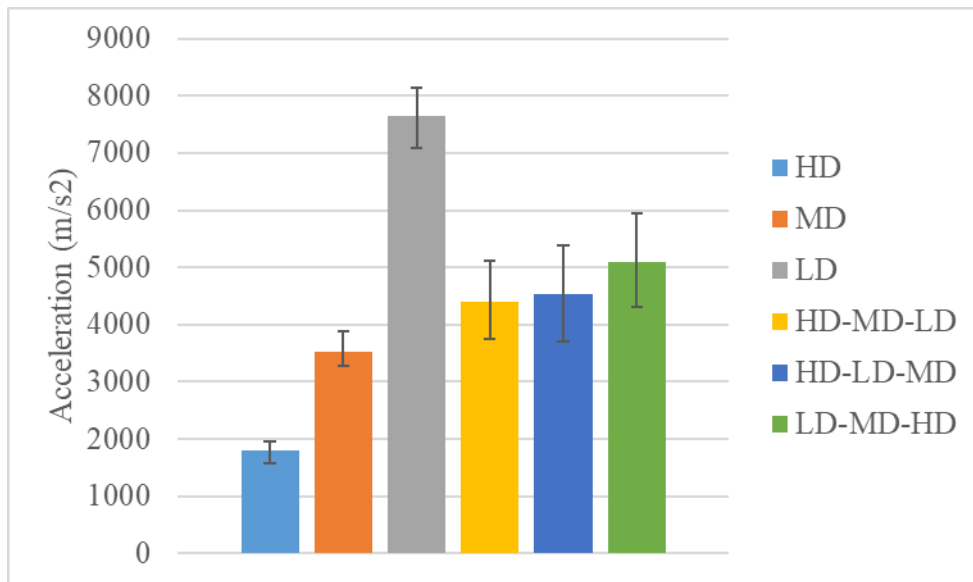
Figure 141. Back Face Center Point Acceleration for Cymat Shock Loaded Beams

CHAPTER IX: CONCLUSION AND RECOMMENDATIONS

9.1 Quasi-Static

Compression testing of various Duocel metallic foams and polymer infused Duocel metallic foam was performed showing the benefits polymer infusion can have on the compressive strength and specific energy absorption of metallic foams.

- Digital image correlation technique was implemented to obtain global strain of both non-infused and infused metallic foams.

- Manufacturing process for infusion of metallic foams with a rapid setting polyurethane was established.

- Highest compressive strength observed in 10-12%/Foam-iT™! composites

- Larger increase in strength and specific energy found in 4-6%/Foam-iT™! When compared to 4-6% Duocel metallic foam.

- 10-12%/Foam-iT™! composite exhibited increased mechanical properties (strength and specific energy), though not as high as 4-6%/Foam-iT™! composites

- Estimated strength using rule of mixtures did not agree with experimental plateau strength of 4-6% Foam-iT™! composite, provide insight that an additional mechanism is present during compression.

- Proposed mechanism which increased strength is buckling resistance to metallic foam framework.

- Computational results show that localized deformation is due to void size and frame work strength.

- FEA simulation with randomly positioned voids and size show a more isotropic response then non-staggered and staggered configurations.

- Infusions of metallic foam increased stress in composite metallic framework allowing more stress in metal framework during compression.

- Polymer foam helped resist metal framework deformation and buckling.

9.2 Low-Velocity

- Increase resistance to punch shear penetration for peak load, total energy absorption, damage initiation energy, and puncture propagation energy was seen in all comparison of non-infused configurations when compared to the infused variation of the same stacking sequence.

- Highest increase in peak load, total energy absorption, damage initiation energy, and puncture propagation energy observed when comparing DNIL2 to DIL2.

- Damage zone of all samples exhibited typical compression cup and fracture of metal framework for all tested samples.

- Damage zone larger for infused variation when compared to non-infused variations showing more material interacts during penetration of hemispherical tup.

- Peak load highest in DNIL2H2L2 and DIL2H2L2 functionally graded samples with highest density in the middle showing significant improvements due to stacking sequence.

- Uniform density 4-6% non-infused and infused composite demonstrated highest total energy, damage initiation energy, and puncture propagation energy due to increased time duration of penetration resistance.

- Cymat samples made with only high density layers had highest peak load followed by functionally graded samples with low density, medium density, and high density stacking sequence.

- Peak load obtained during punch shear penetration is affected more by density of layer furthest from initial impact zone.

- Highest density configuration had the highest total energy absorption, damage initiation energy, and puncture propagation energy and was followed by LD-MD-HD configurations with the exception of puncture propagation energy.

- Stacking sequence changes displacement need to obtain peak strength during low velocity impact and can be used to absorb more energy in the right configuration.

- Most ideal functionally graded configuration is LD-MD-HD.

- Fracture zone on back face of panels larger than penetration indenter for all samples, but the degree of damage dependent on density furthest from indentation location. Higher density panels exhibited more damage.

9.3 Direct Impact

- Direct impact testing on all non-functionally graded and functionally graded panels as well as Foam-iT!™ 3.

- Foam-iT!™ 3 had highest specific energy under direct impact loading until ~ 0.67 strain for non-infused configuration and ~ 0.58 for infused configurations, but ultimately was surpassed by DNIL2 and DIL2 configurations.

- Initial response of functionally graded lower than both H2 and L2 non-infused and infused configurations.

- Highest plateau strength increase observed when comparing DNIL2 to DIL2 configurations.

- Specific plateau strength increase highest when comparing DNIH2L2H2 configurations to DIH2L2H2.

9.4 Split Hopkinson Pressure Bar

- Digital image correlation strain evolution matched response obtained from conventional SHPB analysis using stress pulses.

- Large scatter present in dynamic stress-strain response, likely due to inconsistencies in metallic foam density.

- Slight strain-rate sensitivity seen in all non-infused and infused specimens subjected to dynamic SHPB compression.

- Increases in plateau strength and specific energy seen for all comparison of non-infused variations when compared to infused variations.

- Comparison of plateau strength and specific energy shows increase for all non-infused configurations compared to infused configurations, but was considerably higher in 4-6%/Foam-iT!™ composites.

- FEA simulation showed minimal rate dependency and increase in stress in metal framework can be attributed to material property of metal framework. Simulation is in disagreement with experimental results which show rate effects in all cases.

- Computational simulation missing mechanism which captures the rate effects of the polymer infusion and interaction of the metallic framework with the infused polymer.

9.5 Shock Tube

- Simply supported beam samples subjected to shock loading were tested to obtain the role functionally grading and infused play on the dynamic behavior of metallic foams.

- Configuration made with DNIH2 and DIH2 exhibited no compression during shock loading. Samples made with DNIL2 configurations show progressively collapse of layer closes to front face. Non-infused configurations made with 4-6% and 10-12% show compression of 4-6% layers only. Infused samples with only 4-6% metallic framework showed two type of response progressive collapse and no collapse. Samples of DIH2L2H2 and DIL2H2L2 both had samples that displayed no collapse of any layers as well as collapse of the first 10-12% layer in DNIH2L2H2 and middle 10-12% layer in DIL2H2L2 during shock loading.

- Deflection-time show decreasing trend for L2H2L2, H2, H2L2H2, and L2 configurations.

- Load-displacement show increase strength trend for H2, H2L2H2, L2, and L2H2L2 for non-infused functionally graded configurations.

- Load-displacement similar for all infused variations.

- Deformation energy-time and deformation energy-displacement highest for infused 4-6% Duocel composites.

167

- Most ideal configurations for shock loading mitigation is infused 4-6%/Foam-iT!™ composites due to the energy absorption at the same back face deflection and its ability to endure the entire shock loading event without having catastrophic failure.

- Simulations for DNI shock loading show inaccurate representation of back face sheet center point deflection. Better experimental-FEA agreement was seen in DI simulations.

- Inaccuracies in DNI and higher accuracy in DI results, with the additional information obtain from high speed photography which show interface slip and lack of bonding between DNI versus DI configurations it can be concluded that the model does not capture this deformation mechanism. It can also be concluded that the bonding between infused configurations is higher than non-infused variations due to higher surface area contact.

- Most accurate FEA results obtain in DIL2H2L2 when compared to experimental deflection-time curves.

- Cymat beam panels made with lowest density foam had highest back face deflection and lowest in panels with highest density layers.

- Deformation energy initially highest in LD-MD-HD configurations but is ultimately surpassed by 3 layer LD panels.

- Most ideal configuration for absorbing shock loading is LD-MD-HD consistent with (Wang, Gardner, & Shukla, 2009) where it was observed that panels with lowest density nearest to shock loading absorbed more energy throughout the duration of the loading.

9.6 Recommended Future Works

Recommendations for continuation of characterizing metallic polymer composites using Duocel metallic foam and Foam-iT!™ polyurethane foam are as follows-

- FEA analysis of a 3D CT scanned model with and without infusion for quasi-static and SHPB so a direct comparison with experimental results can be obtained.

- Infusion of different layers to understand the effects on blast mitigation.

- Investigation of bonding strength for non-infused and infused panels to obtain an additional mechanism that can be used in FEA simulations.

- Additional metallic foam densities and stacking sequences to create most ideal configuration.

- Variations in low velocity impact speeds to characterize the response of panels at various impact energies.

- Modification to direct impact system to allow for equilibrium during compression to be obtained.

- Modification to direct impact system to allow for increased compression-rate range to allow for a broader strain-rate range of testing.

- Additional high speed cameras to obtain back face surface strain as well as increased video capture time to obtain first failure point of each configuration.

- Investigation into the effects of infusion of different densities on the dynamic properties of metallic foam/polymer composites to obtain the ideal ratio.

REFERENCES

Abdullah, R. (2008). The High Velocity Impact Response of Novel Fibre-Metal Laminates.

Alamy. (2008, March 7). *Building Damaged Terror Bomb Blast Explosion Century Bazaar Worli 1993 Bombay Mumbai Maharashtra India*. Retrieved 1 10, 2020, from Alamy: https://www.alamy.com/stock-photo-building-damaged-terror-bomb-blast-explosion-century-bazaar-worli-85278117.html

Alamy. (2019, April 10). *Holes from Bullets and Shell Fragments in the Body of a Padded Armored Vehicle*. Retrieved 1 10, 2020, from Alamy: https://www.alamy.com/holes-from-bullets-and-shell-fragments-in-the-body-of-a-padded-armored-vehicle-image264774155.html?pv=1&stamp=2&imageid=1D101FAC-FA25-4E9C-88AA-63D6CA9D5797&p=532964&n=11&orientation=0&pn=1&searchtype=0&IsFromSearch=1&srch=foo%3Dbar%

Anderson, J. D. (2012). *Moedrn Compressible Flow With Historical Perspective Third Edition.* New York: McGraw-Hill.

ASTM Standard. (2018, September). ASTM Standard: D3763-06, Standard Test Method for High Speed PunctureProperties of Plastics Using Load and Displacement Sensors. ASTM International, D20 Plastics D20.10 Mechanical Properties.

Chen, W., & Song, B. (2011). *Split Hopkinson (Kolsky) Bar: Design, Testing and Applications.* Springer.

Chen, W., Zhang, B., & Forrestal, M. J. (1998). A Split Hopkinson Bar Technique for Low Impedance Materials. *Experimental Mechanics*, 81-85.

Chintapalli, R. K., Mirkhalaf, M., Dastjerdi, A. K., & Barthelat, F. (2014). Fabrication, Testing and Modeling of a New Flexible Armor Inspired from Natural Fish Scales and Osteoderms. *9*.

Cymat Technologies Ltd. (2019, 1 1). *Cymat Technologies*. Retrieved 1 10, 2020, from Defense and Military Cymat Technologies: http://www.cymat.com/industries-defense-military/

Daniel, I. M. (2010). Impact Response and Damage Tolerence of Composite Sandwich Structures. *Chapter 7 191-232*.

Dannemann, K. A., & Lankford Jr., J. (2000). High Strain Rate Compression of Closed-Cell Aluminium Foams. *Material Science & Engineering A, A293 (157-164)*.

Daoud, M., Jomma, W., Chatelain, J. F., & Bouzid, A. (2015). A Machining Based Methodology to Identify Material Constitutive Law for Finite Element Simulation. *International Journal of Advance Manufaturing Technology*, 2019-2033: DOI 10.1007/s00170-014-6583-z.

David, B. (2014, December 31). *Tanks Encyclopedia*. Retrieved 1 1, 2020, from M1 Abrams Main Battle Tank - Tanks Encyclopedia: https://tanks-encyclopedia.com/coldwar/US/M1_Abrams.php

Defense, U. S. (2019, September 11). *A 9/11 Reflection: The Pentagon in Photos*. Retrieved 1 10, 2020, from Defense: https://www.defense.gov/explore/story/Article/1939053/a-911-reflection-the-pentagon-in-photos/

Deshpande, V. S., & Fleck, N. A. (2000). High Strain Rate Compressive Behaviour of Aluminium Alloy Foams. *24 (277-298)*.

Deshpande, V., & Fleck, N. (2000). Isotropic Constitutive Models of Metallic Foams. *48: 1253-83*.

172

Edwin Raj, R., Parameswaran, V., & Daniel, B. (2009). Comparison of Quasi-Static and Dynamic Compression Behavior of Closed-Cell Aluminum Foam. *Materials Science and Engineering A*, 11-15.

ERG Materials and Aerospace. (2020, September 12th). *The Basics of Duocel Foam*. Retrieved from The Basics of Duocel Foam - ERG Areospace: http://ergaerospace.com/technical-data/the-basics-of-duocel-foam/

Fang, Q., Zhang, J., Zhang, Y., Liu, J., & Gong, Z. (2015). Mesoscopic Investigation of Closed-Cell Aluminum Foams on Energy Absoprtion Capability Under Impact. *124 (409-420)*.

Fı´la, T., Zlamal, P., Jirousek, O., Falta, J., Koudelka, P., Kytyr, D., . . . Valach, J. (2017). Impact Testing of Polymer-filled Auxetics Using Split. *19*(DOI: 10.1002/adem.201700076).

Frew, D. J., Forrestal, M. J., & Chen, W. (2002). Pulse Shaping Techniques for Testing Brittle Materials with a Split Hopkinson Pressure Bar. *Experimental Mechanics*, 42(1), pp. 93-106.

Gardner, N., Wang, E., Kumar, P., & Shukla, A. (2012). Blast Mitigation in a Sandwich Composite Using Graded. *52 (119-133)*(DOI 10.1007/s11340-011-9517-9).

Gibson, L. J., & Ashby, M. F. (1997). *Cellular Solids Structures and Properties Secon Edition.* Cambridge: The Press Syndicate of the Universty of Cambridge.

Gibson, R. F. (2007). *Principles of Comppsite Material Mechanics Second Edition.* Boca Raton: CRC Press Taylor and Francis Group.

Hassan, M. Z., Guan, Z. W., Cantwell, W. J., Langdon, G. S., & Nurick, G. N. (2012). The Influence of Core Density on the Blast Resistance of Foam-Based Sandwich Structures. *50 (9-16)*.

Huang, J., Durden, H., & Chowdhury, M. (2011). Bio-Inspired Armor Protective Material Systems for Ballistics Mitigation. *Materials and Design*.

Jing, L., Wang, Z., Shim, V. P., & Zhao, L. (2014). An Experimental Ctudy of the Dynamic Response of Cylindrical. *71 (60-72)*.

Karen, I., Yazici, M., & Shukla, A. (2016). Designing Foam Filled Sandwich Panels for Blast Mitigation Using a Hybrid Evolutionary Optimization Algorithm. *158 (72-82)*.

Karkaria, B. (2015, July 30). *How the 1993 Blasts Changed Mumbai Forever*. Retrieved 1 10, 2020, from British Broadcasting Corporation: https://www.bbc.com/news/world-asia-india-33713846

Langdon, G. S., Karagiozova, D., Theobald, M. D., Nurick, G. N., Lu, G., & Merrett, R. P. (2010). Fracture of Aluminum Foam Core Sacrifical Cladding Subjected to Air-Blast Loading. *37 (638-651)*.

Li, Z., Zheng, Z., & Yu, J. (2019). Low-Velocity Perforation Behavior of Composite Sandwich Panels with Aluminun Foam Core. *15(1) 92-109*.

Liu, H., Cao, Z. K., Luo, H. J., Shi, J. C., & Yao, G. C. (2013). Performance of Closed-Cell Aluminum Foams Subjected to Impacy Loading. *570 (27-31)*.

Liu, X. R., Tian, X. G., Lu, T. J., & Liang, B. (2014). Sandwich plates with functionally graded metallic foam cores. *84 (61-72)*.

Markaki, A. E., & Clyne, T. W. (2000). Characterization of Impact Response of Metallic Foam/Ceramic Laminates. *Material Science and Techology*, Vol 16. 785-791.

McCormack, T., Miller, R., Kesler, O., & Gibson, L. J. (2001). Failure of Sandwhich Beams with Metallic Foam Cores. *38 (28-29): 4901-20*.

McKittrick, J., Chen, P.-Y., Tombolato, L., Novitskaya, E., Trim, M., Hirata, G., . . . Meyers, M. (2010). Energy Absorbent Natural Materials and Bioinspired Design Strategies: A Review. *30 (2010) 331-342 DOI:10.1016/j-msec.2010.01.011*.

Merrett, R. P., Langdon, G. S., & Theobald, M. D. (2013). The Blast and Impact Loading of Aluminum Foam. *44 (311-319)*.

Mohan, K., Yip, T. H., Idapalapati, S., & Chen, Z. (2011). Impact Response of Aluminum Foam Core Sandwich Structures. *Material Science and Engineering A*, 94-101.

Multi-National Corps - Iraq Publ. (2005, April 3). *DVIDS - Images This Shrapnel Lacerated Protective Vest and Body Armor*. Retrieved 1 1, 2020, from Defence Visual Information Distribution Service Hub: https://www.dvidshub.net/image/4631/shrapnel-lacerated-protective-vest-and-body-armor

Nelms, M. (2018). Computational Modeling of Damage Mechanisms in Mineralized Biological Tissue. *University of Mississippi, Oxford Mississippi*.

Olsson, R. (1998). Theory of Small Mass Impact on Sandwich Panels. Mechanics of Sandwich Structures. *pp.231-238*.

Peroni, M., Solomos, G., & Pizzinato, V. (2013). Impact Behaviour Testing of Aluminum Foam. *53 (74-83)*.

Porter, M. M., Ravikumar, N., Barthelat, F., & Martini, R. (2017). 3D-printing and Mechanics of Bio-Inspired Articulated and Multi-Material. *73 (114-126)*.

Pramanik, B., & Mantena, P. (2009). Punch-Shear Characteristics of Nanoclay and Grahpite Pleatelet Reinforced Vinyl Ester Plates, Laminated Face Sheets and Sandwich Composites Under Low Velocity Impact. *ASME Early Career Technical Journal*, 8(1), 66-73.

Pramanik, B. (2014). High-Strain Rate Tensile Characterization Of Graphite Platelet Reinforced Vinyl Ester Based Nanocomposites Using Split-Hopkinson Pressure Bar. *Electronic Theses and Dissertation*, 689.

Qin, Q., Xiang, C., Zhang, J., Wang, M., Wang, T. J., & Poh, L. H. (2017). On Low-Velocity Impact Response of Metal Foam Core Sandwich Beam: A Dual Beam Model. *176 (1039-1049)*.

Rajaneesh, A., Sridhar, I., & Rajendran, S. (2014). Relative Performance of Metal and Polymeric Foam Sandwich Plates Under Low Velocity Impact. *International Journal of Impact Engineering*, 126-136.

Reyes, G. (2008). Static and Low Velocity Impact Behavior of Composite Sandwich Panels with an Aluminum Foam Core. *42 (1659-1670)*.

Shield Technology Inc. (2018, July 27). *Tactical Bulletproof Vest: Cons and Downfalls (and a Better Option)*. Retrieved 1 1, 2020, from Shield Technology Inc.: https://shieldtechnologyinc.com/tactical-bulletproof-vest-cons-and-downfalls-and-a-better-option/

Srushti Engineering Innovations PVT. LTD. (2020, March). Shock Tube Assembly and Operation. *Shock Tube Assembly and Operation*. Bengaluru, India: Srushti.

Sun, G., Wang, E., Wang, H., Xiao, Z., & Li, Q. (2018). Low-Velocity Impact Behaviour of Sandwich Panels with Homogeneous and Stepwise Graded Foam Cores. *Materials and Design*, 160 (1117-1136).

Wang, E., & Shukla, A. (2010). Analytical and Experimental Evaluation of Energies During Shock Wave Loading. *International Journal of Impact Engineering, 37 (1188-1196)*.

Wang, E., Gardner, N., & Shukla, A. (2009). The Blast Resistance of Sandwich Composites with Stepwise Graded Cores. *International Journal of Solids and Structures, 46 (3492-3502).*

Wang, Z., Li, Z., Ning, J., & Zhao, L. (2009). Effect of Heat Treatment on Crushing Behavior and Energy Absorbing Performance of Aluminum Alloy Foams. *30 (977-982).*

Weaire, D. (2009). Kelvin's Ideal Foam Structure. *Journal of Pyhsics: Conference Series 158* (pp. 1-5). Journal of Physics Conference.

Wegst, U. K., & Ashby, M. F. (2004). The Mechanical Efficieny of Natural Materials. *Philosophical Magazine*, 84(21), 2167-2186.

Writer, S. (2019, July 8). *M1 Abrams Main Battle Tank (MBT).* Retrieved 1 1, 2020, from Militry Factory: https://www.militaryfactory.com/armor/detail.asp?armor_id=1

Yang, B., Tang, L., Liu, Y., Liu, Z., Jiang, Z., & Fang, D. (2013). Localized Deformation in Aluminum Foam During Middle Speed Hopkinson Bar Impact Tests. *560 (734-743).*

Yang, X., Ma, J., Shi, Y., & Yang, J. (2017). Crashworthiness Investigation of the Bio-Inspired Bi-Directionally Corrugated Core Sandwich Panel Under Quasi-Static Crushing Load. *135 (275-290).*

Yazici, M., Wright, J., Bertin, D., & Shukla, A. (2014). Experimental and Numerical Study of Foam Filled Corrugated Core Steel Sandwich Structures Subjected to Blast Loading. *110 (98-109).*

Yazici, M., Wright, J., Bertin, D., & Shukla, A. (2015). Preferentially Filled Foam Core Corrugated Steel Sandwich Structures for Improved Blast Performance. *82 (061005-1-061005-13).*

Yu, J., Wang, E., Li, J., & Zheng, Z. (2008). Static and Low-Velocity Impact Behavior of Sandwich Beams with Closed Cell Aluminum-Foam Core in Three-Point Bending. *35 (885-894)*.

VITA

Damian Stoddard

EDUCATION	Ph.D. Mechanical Engineering	2021

University of Mississippi – University, MS, USA
Dissertation: Dynamic Characterization of Bio-Inspired Functionally
Graded Polymer Infused Metallic Foams for Blast and Impact Hazard
Mitigation

M.S. Mechanical Engineering   2014
University of Mississippi – University, MS, USA
Thesis: Microstructure, Quasi-Static, And High-Strain Rate Dynamic
Characterization of Metakaolin and Fly Ash Based Geopolymers For
Structural Applications

B.S. Mechanical Engineering   2010
Prairie View A&M University - Prairie View, TX, USA

EXPERIENCE   Laboratory Instructor   2016-Present
Dept. of Mechanical Engineering
University of Mississippi – University, MS, USA

Honor Thesis Advisor   2019-Present
Dept. of Mechanical Engineering
University of Mississippi – University, MS, USA
Honor Students: Ivy Turner, Tallulah Jones, Greer Lauber
Benjamin Rhoads

Research Assistant – ERDC-GSL   2012-2013
Engineer Research and Development Center (ERDC)
Vicksburg, MS, USA

Graduate Teaching/Research Assistant   2011-2015
Dept. of Mechanical Engineering
University of Mississippi – University, MS, USA

HONOR AND AWARDS	School of Engineering – Outstanding Teaching Award	2021
	ERDC-GSL – Research Assistantship	2012-2013
	Senator of Mechanical Engineering, Graduate Student Council, University of Mississippi	2014
SOCIETY MEMBERSHIPS	NSBE – National Society of Black Engineers ASME – American Society of Mechanical Engineers	

JOURNAL PUBLICATIONS

Scott, N. R., Stoddard, D. L., Nelms, M. D., Wallace, Z., Turner, I., Turner, L., Croom, M., Franklin, K., Sandifer, S., Ali Al-Fahdi, M. S., Butler, T., Rajendran, A. M., (2021) "Experimental and Computational Characterization of Glass Microsphere-Cementitious Composites", Cement And Concrete Research, Vol. 152 (Feb 2022) https://doi.org/10.1016/j.cemconres.2021.106671

Stoddard, D., Ukyam, S. B., Tisserat, B., Turner, I., Baird, R., Serafin, S., Torrado, J., Chaudhary, B., Piazza, A., Tudor, M., and Rajendaran, A. M. (2020). "High Strain-Rate Dynamic Compressive Behavior and Energy Absorption of Distiller's Dried Grains and Soluble Composites with Paulownia and Pine Wood using a Split Hopkinson Pressure Bar Technique", BioRes. 15(4), 9444-9461

Suman Babu Ukyam, Raju P. Mantena, Damian L. Stoddard, Arunachalam M. Rajendran, Robert D. Moser (2021). "Dynamic Flexural Modulus and Low-Velocity Impact Response of Supercomposite™ Laminates with Vertical Z-Axis Milled Carbon Fiber Reinforcement" Material Science and Applications, Vol.12 No.04(2021), Article ID:108584,19 pages, 10.4236/msa.2021.124010

Ivy Turner, Rowan Baird, Sofia Serafin, Birendra Chaudhary, Jose Torrado Damian Stoddard, (2019). "High Strain-Rate Sensitivity and Energy Absorption of DuroProtect, A Fiber-Reinforced Ballistics Composite", Journal of UAB ECTC, Volume 18 pp. 8-14

Birendra Chaudhary, Suman Babu Ukyam, Damian Stoddard, (2019). "Comparative Analysis and Dynamic Response of Garolites Under Temperature Spectrum Using Low Velocity Impact", Journal of UAB ECTC, Volume 18

Rowan Baird, Mason Tudor, Damian Stoddard, (2019). "Dynamic Compressive Behavior and Energy Absorption of Ethylene Polyurethane Diene Monomer Foam Using Split Hopkinson Pressure Bar Technique", Journal of UAB ECTC, Volume 18

Damian Stoddard, Suman Babu Ukyam, R. Mantena Prabhakar, Arunachalam Rajendran, (2018). "Energy Absorption of Pultruded Glass-Graphite/Epoxy Hybrid Composites under High Strain-Rate Induced Transverse Tension", Open Journal of Composite Materials, Vol.08 No.02(2018), Article ID:83751,11 pages 10.4236/ojcm.2018.82004

Maharshi J. Dave, Tejas S. Pandya, Damian Stoddard, Jason Street (2018). "Dynamic Characterization of Biocomposites Under High Strain Rate Compression Loading with Split Hopkinson Pressure Bar and Digital Image Correlation Technique", International Wood Products Journal, DOI: 10.1080/20426445.2018.1482673

Maharshi J Dave, Tejas Pandya, Damian Stoddard, (2018). "Dynamic and Damping Properties of Novel Bio-Composites Using the Hammer Excitation Vibration Technique", Wood Research, 63(2) 215-226

Shah, A. J., Pandya, T. S., Stoddard, D., Ukyam, S. B., Street, J., Wooten, J., Mitchell, B., (2017). "Dynamic Response of Wood Based Bio-Composites Under High-Strain Rate Compressive Loading", Wood and Fiber Science, Vol.49 No.4 pp.444-452 ref.10

Seyed Soheil Daryadel, P. Raju Mantena, Kiyun Kim, Damian Stoddard, A.M. Rajendran, (2016). "Dynamic Response of Glass Under Low-Velocity Impact and High Strain-Rate SHPB Compression Loading", Journal of Non-Crystalline Solids, 432-439
http://dx.doi.org/10.1016/j.jnoncrysol.2015.10.043
0022-3093/

CONFERENCE PRESENTATIONS	D. L. Stoddard, P. Raju Mantena, P. G. Allison, R. D. Moser, (2013). "Microstructure, Quasi-Static, and High-Strain Rate Dynamic Characterization of Metakaolin and Fly Ash Based Geopolymers for Structural Applications", Mid-South Annual Engineering and Science Conference
	D. L. Stoddard, P. Raju Mantena, P. G. Allison, R. D. Moser, (2014). "Microstructure, Quasi-Static, and High-Strain Rate Dynamic Characterization of Metakaolin and Fly Ash Based Geopolymers for Structural Applications", Mid-South Annual Engineering and Science Conference, 2014 American Society of Mechanical Engineers (ASME) Early Career Technical Conference (ECTC)
	D. L. Stoddard, K. Kim, P. Raju Mantena, (2014). "Low-Velocity Impact Characterization of Armored Glass", 2014 American Society of Mechanical Engineers (ASME) Early Career Technical Conference (ECTC)